



The  
University  
Of  
Sheffield.

Department  
of  
Mechanical  
Engineering

# **Study of accelerating and decelerating turbulent flows in a channel**

A dissertation submitted in partial fulfilment of the requirements for the degree of

Doctor of Philosophy

**Akshat Mathur**

Supervised by Professor Shuisheng He

Department of Mechanical Engineering

The University of Sheffield

January 2016



# Abstract

Accelerating and decelerating turbulent channel flows are investigated to study the response of the turbulence dynamics. The objective of these investigations is to further enhance the understanding on the behaviour of turbulence and wall friction under transient conditions. Large-Eddy Simulations (LES) are carried out for step-like accelerating flows with significantly higher ratios of Reynolds number than previously covered. An experimental investigation is carried out for ramp-like accelerating flows using Particle-Image Velocimetry (PIV) and Constant-Temperature Anemometry (CTA) techniques to reproduce and validate the findings in numerical simulations. Step- and ramp-like decelerating flows are studied using Direct Numerical Simulations (DNS), the results of which are compared with observations in accelerating flows.

Step-like high  $Re$ -ratio and ramp-like accelerating flows are shown to exhibit essentially the same three-stage laminar-turbulent *transitional* response as that described in He & Seddighi (*J. Fluid Mech.* 715:60-102, 2013), resembling bypass transition of boundary layer flows. The first stage is characterised by elongation and enhancement of streaks. The growing instabilities of the streak structures lead to breakdown and formation of isolated turbulent patches in the second stage, which grow in time and eventually merge with each other. The third stage is marked by the entire wall surface being covered by the newly generated turbulence. It is shown in the present study that the features of transition become more striking when the  $Re$ -ratio increases – the elongated streaks in the pre-transitional period become increasingly longer and stronger, and the turbulent spots generated at the initial stage at the onset of transition become increasingly sparse. In a slower ramp-like flow excursion, on the other hand, the onset of transition is delayed making the flow development slower. In a step-like acceleration, a new boundary layer is formed instantly over the wall which develops into the flow with time. In a ramp-like case, however, the boundary layer development is shown to be described as an integral consequence of a continuous change of the flow. During the pre-transition stage, the

---

time-development of the boundary layer in the step- and ramp-like accelerating flows bears strong resemblance to a time-developing laminar boundary layer described by the solution to Stokes' first problem and can be represented by its analytical solution with a small correction.

The streamwise fluctuation velocity profile in a high  $Re$ -ratio accelerating flow is shown to exhibit two peaks immediately following the onset of transition. A conditional sampling technique, based on a  $\lambda_2$ -criterion, is used to show that the two peaks are separate contributions of the *active* and *inactive* regions of turbulence generation. The peak closer to the wall is attributed to the 'newly' generated turbulence in the active region; while the peak farther from the wall is attributed to the enhanced streaks in the inactive region.

Decelerating flows are shown to be also characterised by a time-developing boundary layer, similar to that in accelerating flows, bearing strong resemblance to the time-developing laminar boundary layer. The mean flow and wall friction in the early stages of the transient can be represented by the laminar analytical solution of the Stokes' first problem. The streamwise fluctuations are shown to respond immediately following the commencement of the transient, while the response of the 'real' turbulence is shown to respond after a delay. Although the decay of turbulence and flow structures appear to be a gradual development herein, the decelerating flows may also undergo a transition process. However, the mechanism and stages of any such process are not clear in the present investigation.

In addition, a brief investigation on the performance of the low-Reynolds number Launder-Sharma  $k$ - $\varepsilon$  model in predicting unsteady turbulent flows is undertaken using different CFD codes. It is shown that the model performance itself is robust and insensitive to the numerical/coding framework, while slight changes in the formulation of the model have significant effect on the performance of the model.

# Acknowledgements

I would like to express my sincere gratitude towards my supervisor, Professor Shuisheng He, for providing me the opportunity to pursue this research and has since been a source of invaluable guidance and inspiration. Completion of my project would not have been possible without his constant support and encouragement.

I am also very grateful of my colleagues and fellow researchers, in particular Dr. Mehdi Seddighi-Moornani, Dr. Wei Wang, Dr. Sam Gorji, Dr. Yu Duan, Dr. Kui He and Mr. Xiao Zhang, who have been extremely helpful and resourceful. I would also like to thank all my other friends in Sheffield (*notably VP, PP, DM, MR, BS, GG & CB*) who have made the past four years truly enjoyable and memorable.

I would like to acknowledge the technical staff of the Corporate Information and Computing Services (CiCS) of The University of Sheffield, who have been immensely resourceful in troubleshooting high-performance calculations on HPC cluster *iceberg*. My sincere thanks to the technical staff of the Mechanical Engineering Fluids Lab, especially Mr. Wayne Oxley, who have helped me in operation, maintenance and repair of the experimental flow loop facility.

Above all and beyond, I am deeply grateful to my parents and my sister who have supported me and encouraged me to learn throughout my life, and have been the impetus for me to pursue higher education and research.



# Contents

<b>Abstract</b> .....	<b>i</b>
<b>Acknowledgements</b> .....	<b>iii</b>
<b>List of Figures</b> .....	<b>viii</b>
<b>List of Tables</b> .....	<b>xv</b>
<b>Nomenclature</b> .....	<b>xvi</b>
<b>Chapter 1 Introduction</b> .....	<b>1</b>
1.1 Objectives of the Present Study .....	2
1.2 Thesis Structure .....	3
<b>Chapter 2 Literature Review</b> .....	<b>4</b>
2.1 Unsteady Turbulent Flows.....	4
2.1.1 Periodic flows .....	5
2.1.2 Non-Periodic flows .....	7
2.2 Bypass Transition .....	11
2.3 RANS Turbulence Modelling.....	14
<b>Chapter 3 Numerical Methods</b> .....	<b>17</b>
3.1 RANS, DNS and LES.....	17
3.2 Direct Numerical Simulation.....	20
3.2.1 Governing Equations .....	21
3.2.2 Spatial and Temporal Discretization.....	23
3.2.3 Boundary and Initial Conditions.....	26
3.2.4 Fractional Step Method.....	26
3.3 Large-Eddy Simulation .....	29
3.3.1 Smagorinsky Model.....	31
3.3.2 Dynamic Germano-Lilly Model.....	32
3.3.3 Wall-Adapting Local Eddy-viscosity (WALE) Model.....	35
3.4 Statistical Calculation.....	36
3.5 Code Validation.....	38
3.5.1 DNS Validation .....	38

---

3.5.2	Steady-State LES Validation.....	38
3.5.3	Unsteady-Flow LES Validation .....	44
3.5.4	Steady-State LES Validation at High $Re_\tau$ .....	46
<b>Chapter 4 Experimental Rig and Measurement Techniques .....</b>		<b>49</b>
4.1	Flow Loop Facility .....	49
4.2	Particle-Image Velocimetry .....	53
4.3	Constant-Temperature Anemometry.....	57
4.4	Data Processing.....	61
4.5	Data Validation .....	63
4.5.1	Steady-State Validation .....	63
4.5.2	Unsteady Flow Comparison.....	66
4.5.3	Uncertainty in Experimental Data .....	68
<b>Chapter 5 Large-Eddy Simulation of Step-Accelerating Flows .....</b>		<b>70</b>
5.1	Present Simulation Cases .....	71
5.2	Instantaneous Flow Response.....	73
5.3	Correlations of Flow Transition.....	80
5.3.1	Uncertainty in the Predictions of the Transitional Reynolds Numbers .....	84
5.4	Ensemble-Averaged Flow Response.....	89
5.4.1	Boundary layer development.....	89
5.4.2	Response of r.m.s. fluctuating velocities.....	93
5.5	Summary .....	107
<b>Chapter 6 Experimental Investigation of Ramp-Accelerating Flows .....</b>		<b>109</b>
6.1	Present Experimental Cases.....	110
6.2	Ensemble-Averaged Flow Response.....	112
6.2.1	Response of friction coefficient and wall shear stress.....	113
6.2.2	Boundary layer development.....	118
6.2.3	Response of mean and r.m.s. fluctuating velocities .....	125
6.3	Instantaneous Flow Response.....	131
6.4	Correlations of Flow Transition.....	136
6.5	Summary .....	140
<b>Chapter 7 Direct Numerical Simulation of Decelerating Flows .....</b>		<b>142</b>
7.1	Present Simulation Cases .....	143

---

7.2	Ensemble-Averaged Flow Response.....	144
7.2.1	Response of friction coefficient.....	144
7.2.2	Boundary layer development.....	146
7.2.3	Turbulence decay.....	154
7.2.4	Turbulence spectra intensity and velocity auto-correlations .....	159
7.3	Instantaneous Flow Response.....	166
7.4	Summary .....	171
<b>Chapter 8 Low-Reynolds Number Modelling – Launder-Sharma <math>k-\varepsilon</math> Model .....</b>		<b>173</b>
8.1	Low-Reynolds Number Modelling.....	173
8.2	Launder-Sharma Model.....	174
8.3	Model Performance of Different RANS Codes.....	178
8.4	Model Sensitivity.....	182
8.5	Model Performance for Unsteady Channel Flow.....	185
8.6	Summary .....	187
<b>Chapter 9 Conclusions .....</b>		<b>189</b>
9.1	Accelerating Flows .....	189
9.2	Decelerating Flows.....	191
9.3	Launder-Sharma $k-\varepsilon$ Model .....	192
9.4	Suggestions for Future Work.....	193
<b>References.....</b>		<b>195</b>
<b>List of publications.....</b>		<b>205</b>
<b>Appendix A.....</b>		<b>206</b>
<b>Appendix B.....</b>		<b>210</b>

# List of Figures

Figure 3.1 Staggered grid arrangement in the present code. ....	24
Figure 3.2 Simulation procedure adopted in the present code. ....	28
Figure 3.3 Validation of present steady-state simulation at $Re_\tau = 180$ performed using <i>CHAPSim</i> against DNS data of Moser <i>et al.</i> [153] at $Re_\tau = 180$ (Denoted 'MKM').....	39
Figure 3.4 Validation of present steady-state simulation at $Re_\tau = 420$ performed using <i>CHAPSim</i> against DNS data of Moser <i>et al.</i> [153] at $Re_\tau = 395$ (Denoted 'MKM').....	40
Figure 3.5 Comparison of mean velocity between steady state LES against DNS for steady channel flow at a) $Re_b = 7400$ , and b) $Re_b = 12600$ . ....	41
Figure 3.6 Comparison of r.m.s. fluctuating velocity between steady state LES against DNS for steady channel flow at a) $Re_b = 7400$ , and b) $Re_b = 12600$ . Streamwise, wall-normal and spanwise components are denoted by black, blue and red colours, respectively. ....	41
Figure 3.7 Comparison of Reynolds and viscous stresses between steady state LES against DNS for steady channel flow at a) $Re_b = 7400$ , and b) $Re_b = 12600$ . Reynolds and viscous stresses are denoted by red and black colours, respectively.....	42
Figure 3.8 Modified activity parameter ( $s^*$ ) for the three SGS models at steady flow of a) $Re_b = 7400$ , and b) $Re_b = 12600$ .....	44
Figure 3.9 Resolved-stress indicator ( $LES_{IQ_\tau}$ ) for the three SGS models for steady flow at a) $Re_b = 7400$ , and b) $Re_b = 12600$ .....	44
Figure 3.10 Comparison of friction coefficient development for present LES cases using the three sub-grid models against the DNS cases of He & Seddighi [7, 8] – a) case HS13, and b) case HS15. ....	45
Figure 3.11 Comparison of mean velocity between present LES against DNS of Lee & Moser [158] (denoted 'LM') for steady channel flow at a) $Re_\tau = 950$ , and b) $Re_\tau = 2050$ . ....	47
Figure 3.12 Comparison of r.m.s. fluctuating velocity between present LES against DNS of Lee & Moser [158] (denoted 'LM') for steady channel flow at a) $Re_\tau = 950$ , and b) $Re_\tau = 2050$ . ....	47
Figure 3.13 Comparison of Reynolds and viscous stresses between present LES against DNS of Lee & Moser [158] for steady channel flow at a) $Re_\tau = 950$ , and b) $Re_\tau = 2050$ . ....	48

Figure 3.14 LES quality parameters for the present simulations at $Re_\tau = 950$ (dashed) and 2050 (solid) — a) Modified activity parameter ( $s^*$ ), and b) Resolved-stress indicator ( $LES_IQ_\tau$ ). .....	48
Figure 4.1 Schematic view of the channel.....	50
Figure 4.2 Schematic arrangement of the flow loop facility (Gorji [60]).....	51
Figure 4.3 Operational and inherent curves of the control valve. ....	52
Figure 4.4 PIV system components (Dantec Inc.).....	53
Figure 4.5 Different camera-laser orientations for the two PIV configurations: (a) vertical-PIV ( $xy$ plane), and (b) parallel-PIV ( $xz$ plane).....	55
Figure 4.6 Constant-Temperature Anemometer circuit diagram.....	58
Figure 4.7 Dantec 55R47 glue-on film probes (Dantec Inc.).....	58
Figure 4.8 Removable panel for film sensors.....	59
Figure 4.9 Calibration curves for film sensors.....	61
Figure 4.10 Comparison of outer-scaled present experimental data with DNS data of Lee & Moser [158] for steady channel flows at $Re_b = 2800, 9800$ and $20100$ .....	64
Figure 4.11 Comparison of inner-scaled present experimental data with DNS data of Lee & Moser [158] for steady channel flows at $Re_b = 2800, 9800$ and $20100$ .....	66
Figure 4.12 Comparison of present unsteady flow case E1 with flow case S29-76 of Gorji [60]. 67	
Figure 4.13 Repeatability ( $\sigma$ ) of the bulk velocity of steady flows at different Reynolds numbers for a) single, and b) multiple realizations. ....	68
Figure 4.14 Repeatability ( $\sigma$ ) of the CTA output for steady flows at different Reynolds numbers for a) single, and b) multiple realizations. ....	69
Figure 5.1. Three dimensional isosurfaces for cases (a) U3 and (b) U6. Streak structures are shown in blue/green with $u'/U_{b0} = \pm 0.35$ and vortical structures are shown in red with $\lambda_2/(U_{b0}/\delta)^2 = -5$ .....	75
Figure 5.2. Visualization of streak instability and breakdown in case U3 using a sliding window. 3D iso-surface streak structures are shown in blue/green with $u'/U_{b0} = \pm 0.65$ , and vortical structures are shown in red with $\lambda_2/(U_{b0}/\delta)^2 = -80$ .....	77
Figure 5.3. Streamwise velocity autocorrelations at several time instants during the transient for case U3 (a, b) and U6 (c, d) in the streamwise (a, c) and spanwise directions (b, d) at $y^+ = 10$ ..	78
Figure 5.4. Time development of $(\lambda'_{2,rms})_{max}/(U_{b0}/\delta)^2$ for cases U3 and U6.....	80

Figure 5.5. Dependence of equivalent critical Reynolds number on initial turbulence intensity.	82
Figure 5.6. Relationship between the transition period Reynolds number critical Reynolds number.....	84
Figure 5.7. Deviations in friction coefficient development for multiple realizations for flow cases U3-U6.....	85
Figure 5.8. Deviations observed in the equivalent critical Reynolds number.....	85
Figure 5.9. Friction coefficient developments using different domain lengths for cases U3-U6..	86
Figure 5.10. Effect of domain length on a) critical Reynolds number, b) r.m.s. fluctuation of critical Reynolds number, and c) transition period Reynolds number.....	88
Figure 5.11. Development of the perturbation velocity profiles for the present cases during the pre-transition period compared with the Stokes' solution.....	92
Figure 5.12. Development of the perturbation friction coefficient ( $C'_{f,du}$ ).....	92
Figure 5.13. R.M.S. Fluctuating velocity profiles at several time instants during the transient for cases U3 (a)-(c) and U6 (d)-(f). Profiles of $u'/U_{b0}$ (a, d); $v'/U_{b0}$ (b, e); $w'/U_{b0}$ (c, f).....	94
Figure 5.14. Instantaneous flow for case U3 at $t^{+0} = 89.8$ (a) is-surface structures of $u'/U_{b0} = \pm 0.35$ ; (b) iso-surface structures of $\lambda_2/(U_{b0}/\delta)^2 = -5$ ; (c) contours of streamwise fluctuation velocity $u'/U_{b0}$ at $y^{+0} = 5$ ; (d) active region of turbulence production (shown in grey) determined using equation (5.15).....	97
Figure 5.15. Conditionally-averaged mean velocity profiles of the active ( $\bar{u}_a$ ) and inactive ( $\bar{u}_i$ ) regions, along with domain-averaged ( $\bar{u}_d$ ) for a) case U6 at $t^{+0} = 67.5$ , and b) case U3 at $t^{+0} = 84.1$ . Also shown are the initial ( $\bar{u}_0$ ) and final ( $\bar{u}_1$ ) steady flow profiles, for comparison.....	98
Figure 5.16. Conditionally-averaged streamwise fluctuation energy profiles of the active ( $u_a'^2$ ) and inactive ( $u_i'^2$ ) regions, along with domain-averaged ( $u_d'^2$ ) for a) case U6 at $t^{+0} = 67.5$ , and b) case U3 at $t^{+0} = 84.1$ . Also shown are the domain-averaged initial ( $u_0'^2$ ) and final ( $u_1'^2$ ) steady flow profiles, for comparison.....	99
Figure 5.17. Conditionally-averaged streamwise fluctuation velocity profiles of the active ( $u'_{a,rms}$ ) and inactive ( $u'_{i,rms}$ ) regions, along with domain-averaged ( $u'_{d,rms}$ ) for a) case U6 at $t^{+0} = 67.5$ , and b) case U3 at $t^{+0} = 84.1$ . Also shown are the domain-averaged initial ( $u'_{rms,0}$ ) and final ( $u'_{rms,1}$ ) steady flow profiles, for comparison.....	100
Figure 5.18. R.M.S streamwise fluctuating velocity profiles at several time instants during the transient for (a) inactive and (b) active regions for case U6.....	101

Figure 5.19. R.M.S streamwise fluctuating velocity profiles at several time instants during the transient for (a) inactive and (b) active regions for case U3. ....	102
Figure 5.20. Conditionally-averaged maximum energy growth for a) case U6, and b) case U3. ....	103
Figure 5.21. Peak location of the conditionally-averaged energy for a) case U6, and b) case U3. ....	103
Figure 5.22. Domain- and conditionally-averaged a) maximum streamwise fluctuations, and b) the $y$ -location of their peaks, for cases U1, U2, U4 and U5. (Symbols: Line – domain-averaged; $\circ$ – inactive region; $\Delta$ – active region; Colours: green – U1; blue – U2; red – U4; black – U5). ....	106
Figure 6.1 Variation of bulk Reynolds number obtained from integration of PIV data for the present experimental cases. ....	111
Figure 6.2. Variation of bulk velocity for the cases E1-E3 and their reproduced simulation cases. ....	112
Figure 6.3. Response of the friction coefficient during the transient for cases a) E1, b) E2, and c) E3. ....	115
Figure 6.4. Response of the wall shear stress during the transient for cases a) E1, b) E2, and c) E3. ....	116
Figure 6.5. Development of the perturbation velocity profiles ( $u^{\wedge}$ ) compared with the laminar boundary-layer development for time varying perturbation for cases a) E1, b) E2, and c) E3. ....	120
Figure 6.6. Development of the modified friction coefficient for cases E1-E3 and their respective reproduced simulation cases, along with the laminar boundary-layer solution for time-varying velocity. ....	122
Figure 6.7. Development of the a) momentum thickness Reynolds number ( $Re_{\theta}$ ), and b) shape factor ( $H$ ) for case E1, E1D and E1L compared with that of step-acceleration case (HS13) of He & Seddighi [7], and bypass transitional flow cases (T3A and T3B) of Roach & Brierley [180]. ....	123
Figure 6.8. Development of the a) momentum thickness Reynolds number ( $Re_{\theta}$ ), and b) shape factor ( $H$ ) for case E1, E2, E3 and their respective reproduced simulation cases. ....	124
Figure 6.9. Transient development of mean, fluctuating and Reynolds stress components for case E1, E1D and E1L. Symbols denote the experimental data of E1; red and blue lines represent the numerical data of E1D and E1L, respectively. All quantities are in absolute units: $m/s$ for (a)-(c); and $m^2/s^2$ for (d). All subplots share the same legend, which is split into subplots (a) and (c). ....	126

Figure 6.10. Transient development of mean, fluctuating and Reynolds stress components for case E2 and E2L. Symbols denote the experimental data of E2; blue lines represent the numerical data of E2L. All quantities are in absolute units: $m/s$ for (a)-(c); and $m^2/s^2$ for (d). All subplots share the same legend.....	128
Figure 6.11. Transient development of mean, fluctuating and Reynolds stress components for case E3 and E3L. Symbols denote the experimental data of E3; blue lines represent the numerical data of E3L. All quantities are in absolute units: $m/s$ for (a)-(c); and $m^2/s^2$ for (d). All subplots share the same legend.....	129
Figure 6.12. Development of the scaled r.m.s. velocity profiles at several time instants in the pre-transition period for a) streamwise component ( $urms'^{\wedge}$ ), and b) wall-normal component ( $vrms'^{\wedge}$ ). The profiles are shifted by an amount proportional to time ( $t^{+0}$ ).....	130
Figure 6.13 Contour plots of streamwise velocity fluctuations, $u'$ ( $m/s$ ), at several instants during the transient at wall distance of $y = 2$ mm for cases a) E1, b) E1D, and c) E1L.....	132
Figure 6.14 Contour plots of streamwise velocity fluctuations, $u'$ ( $m/s$ ), at several instants during the transient at wall distance of $y = 2$ mm for cases a) E2, and b) E2L.....	133
Figure 6.15. Streamwise velocity auto-correlations ( $R_{11}$ ) at several time instants for case E1D (a,b) and E2L (c,d) in the streamwise (a,c) and spanwise directions (b,d) at $y^{+0} = 5$ . Subplots (a-b) share a legend; while (c-d) share a legend.....	135
Figure 6.16. Dependence of equivalent critical Reynolds number on initial turbulence intensity for the present cases E1-E7 and their reproduced simulation cases.....	138
Figure 6.17. Relationship between transition period Reynolds number and critical Reynolds number for the present experimental cases E1-E7 and their reproduced simulation cases. ....	139
Figure 7.1. Transient response of friction coefficient (Inset shows the cases S1-S4 in a different scale). .....	145
Figure 7.2. Mean velocity profiles of cases D1, D4, D5 and D7 at several time instants (Legend entry with symbols represent end of deceleration period). .....	147
Figure 7.3. Development of the perturbation velocity profiles at several time instants for the present base case D1, the cases 'S14' and 'S03' of He & Seddighi [8] and the Stokes' solution. (The profiles are shifted at an amount proportional to the time).....	147
Figure 7.4. Development of the modified friction coefficient ( $C'_{f\ du}$ ) for the base case (D1), and the accelerating cases 'S14' and 'S03' of He & Seddighi [8]. .....	149

Figure 7.5. Development of the perturbation velocity profiles at several time instants for selected decelerating cases (The profiles are shifted at an amount proportional to the time).	150
Figure 7.6. Development of the modified friction coefficient for present decelerating cases, along with the linearly accelerating case (RAMP) of Seddighi <i>et al.</i> [59].	151
Figure 7.7. Development of the perturbation velocity profiles at several time instants for (a) case D4, and (b) case D7, along with the laminar boundary layer solution.	152
Figure 7.8. Development of the modified friction coefficient for cases a) D4, and b) D7, along with the laminar boundary-layer solution for time-varying velocity.	153
Figure 7.9. Development of maximum r.m.s. fluctuating velocities for a) streamwise component; b) wall-normal and spanwise components. c) All three components shown in different scale.	156
Figure 7.10. Development of a) turbulent kinetic energy; b) streamwise, c) wall-normal and d) spanwise fluctuating velocities at wall-normal location of $y^{+0} = 5$ .	157
Figure 7.11. Development of the budget terms of $u'^2$ integrated over channel half-height, normalised with $u_{\tau 0}^4/\nu\delta$ – a) production, b) dissipation, and c) pressure-strain terms.	158
Figure 7.12. Development of the pre-multiplied streamwise wavenumber spectra of the streamwise velocity at $y^{+0} = 5$ for cases a) D1, and b) D7.	161
Figure 7.13. Development of the pre-multiplied spanwise wavenumber spectra of the streamwise velocity at $y^{+0} = 5$ for cases a) D1, and b) D7.	163
Figure 7.14. Development profiles of the two-point auto-correlation of the streamwise velocity in the streamwise (a, c) and spanwise (b, d) directions at $y^{+0} = 5$ for cases D1 (a, b) and D7 (c, d).	165
Figure 7.15. Flow structures in 3D iso-surface plots in cases a) D1, b) D4, and c) D7. Streaks are shown in blue/green with $u'/U_{b1} = \pm 0.3$ , and vortical structures are shown in red with $\lambda_2/(U_{b1}/\delta)^2 = -5$ .	167
Figure 7.16. Development of $(\lambda'_{2,rms})_{max}/(U_{b1}/\delta)^2$ for cases D1, D4 and D7 during the transient.	170
Figure 8.1 Comparison of friction coefficient predicted using different CFD codes for steady pipe flows.	179
Figure 8.2 Comparison of mean velocity predicted using different CFD codes for steady pipe flows.	180

---

Figure 8.3 Reynolds stress predicted using different CFD codes compared with experimental data of He [131] for an unsteady pipe flows. Experimental data points: — ( $\Delta$ ) $y = 1.9$ mm; ( $\times$ ) $y = 5.4$ mm; (+) $y = 9.4$ mm; (o) $y = 21.4$ mm.....	181
Figure 8.4 Comparison of wall shear stress predicted using different CFD codes with experimental data of He [131] for an unsteady pipe flow. ....	182
Figure 8.5 Comparison of different LS model interpretations for steady pipe flow at $Re_b = 45000$ .....	184
Figure 8.6 Comparison of different LS model interpretations for a 5 second ramp-up pipe flow. ....	184
Figure 8.7 Comparison of prediction of wall shear stress response using UDF-LS and Fluent-LS implementations for a) ramp-accelerating case E2, and b) step-accelerating case U3. The inset in subplot (b) shows the early response using a different scale. ....	186
Figure 8.8 Comparison of prediction of wall shear stress response using UDF-LS and Fluent-LS implementations for a) ramp-decelerating case D7, and b) step-decelerating case D1. The inset in subplot (b) shows the early response using a different scale. ....	186

# List of Tables

Table 3.1 Domain and grid size for DNS and LES steady-state simulations used for validation. .	40
Table 3.2 $Re_\tau$ obtained for LES simulations using different sub-grid models. ....	40
Table 3.3 Mesh parameters for DNS and LES at high $Re_\tau$ steady-state simulations. ....	47
Table 4.1 Calibration constants obtained for the present test run cases. ....	61
Table 4.2 $Re_\tau$ obtained for LES simulations using different sub-grid models. ....	65
Table 5.1. Present accelerating flow cases with the DNS cases of He & Seddighi [7, 8] for comparison. ....	71
Table 5.2. Simulation parameters for additional simulations of cases U3-U6. ....	72
Table 6.1. Variation of Reynolds number for the present experimental cases. ....	111
Table 6.2. Simulation parameters used to reproduce the experimental flow cases. ....	112
Table 6.3. Critical and completion times of transition for different cases determined using the measured friction coefficient development. ....	117
Table 6.4. Critical and completion times of transition for the reproduced simulation cases determined using the friction coefficient developments of the simulations. ....	118
Table 7.1. Simulation parameters based on initial and final flow conditions. ....	143
Table 7.2. Decelerating flow cases investigated in the present study. ....	143
Table 8.1 Launder-Sharma implementation cases in the present study. ....	183

# Nomenclature

## *Symbols*

$A, B, C$	Constants
$C_f$	Friction coefficient
$C_S, C_d, C_W$	Subgrid-scale constants
$C_\mu$	Eddy viscosity constant
$D_\varepsilon$	Additional term in $k$ -transport equation
$d_{PIV}$	Length of interrogation area
$E_\varepsilon$	Additional term in $\varepsilon$ -transport equation
$E_{ij}$	Error residual tensor
$f_1, f_2, f_\mu$	Damping functions
$H$	Shape factor
$k$	Turbulent kinetic energy
$L_x, L_z$	Computational domain in streamwise and spanwise directions
$\mathcal{L}_{ij}$	Leonards stress tensor
$M$	Magnification factor
$\mathcal{M}_{ij}$	Subgrid model kernel
$N_l$	Number of data points used for ensemble-/temporal-averaging
$N_x, N_y, N_z$	Number of mesh points in streamwise, wall-normal and spanwise directions
$p$	Pressure
$P_k$	Production of kinetic energy
$R_1, R_2, R_3$	Internal resistances of Constant Temperature Anemometer
$R_S, R_L$	Resistances of the sensor element and its leading cables
$Re$	Reynolds number
$Re_b$	Reynolds number based on channel half-height and bulk velocity
$Re_{cr}$	Critical Reynolds number
$Re_t$	Equivalent Reynolds number

---

$Re_{turb}$	Fully-turbulent Reynolds number
$Re_{\tau}$	Reynolds number based on channel half-height and friction velocity
$Re_{\theta}$	Momentum-thickness Reynolds number
$\mathbf{S}$	Symmetric part of velocity-gradient tensor
$S_{ij}$	Strain-rate tensor
$S_{ij}^d$	Traceless symmetric part of the square of strain-rate tensor
$t$	Time
$Tu_0$	Initial turbulence intensity
$u, v, w$	Streamwise, wall-normal and spanwise velocities
$U_b$	Bulk velocity
$U_{conv}$	Convective velocity
$U_{\infty}$	Free-stream velocity
$u_{\tau}$	Friction velocity
$u', v', w'$	Fluctuating streamwise, wall-normal and spanwise velocities
$u'_{rms}, v'_{rms}, w'_{rms}$	Streamwise, wall-normal and spanwise r.m.s. fluctuating velocities
$\overline{u'v'}$	Reynolds shear stress
$x, y, z$	Streamwise, wall-normal and spanwise directions
$\alpha_{ij}, \beta_{ij}$	Subgrid model kernels
$\gamma$	Intermittency; Dimensionless rate parameter
$\Delta$	Filter width
$\tilde{\Delta}$	Test filter width
$\Delta Re_{cr}$	Equivalent transition-period Reynolds number
$\Delta t$	Duration of time
$\Delta x, \Delta y, \Delta z$	Grid spacing in streamwise, wall-normal and spanwise directions
$\delta$	Channel half-height; Displacement thickness
$\delta_{ij}$	Kronecker's delta
$\varepsilon$	Dissipation rate
$\tilde{\varepsilon}$	Modified dissipation rate
$\eta$	Stokes' similarity parameter

---

$\theta$	Momentum thickness
$\kappa$	von Kármán constant
$\lambda_2$	Second-largest eigenvalue of symmetric tensor, $S^2 + \Omega^2$
$\lambda'_2$	Root-mean-square of fluctuation of $\lambda_2$
$\mu, \nu$	Dynamic and kinematic viscosity
$\mu_t, \nu_t$	Turbulent dynamic and kinematic viscosity
$\mu_{sgs}, \nu_{sgs}$	Subgrid-scale dynamic and kinematic viscosity
$\rho$	Density
$\sigma$	Temporal relaxation factor; Repeatability
$\tau^R$	Residual stress
$\tau_w$	Wall shear stress
$\omega$	Vorticity; Specific dissipation rate
$\Omega$	Anti-symmetric part of velocity-gradient tensor

### **Subscripts**

0, 1	Initial and final states
<i>a</i>	Active region-averaged
<i>b</i>	Bulk value
<i>c</i>	Centreline value
<i>cr</i>	Critical state
<i>d</i>	Domain-averaged
<i>du</i>	Pertaining to perturbation flow
<i>i</i>	Inactive region-averaged
<i>i, j, k, l</i>	Dummy variables
<i>lam</i>	Pertaining to laminar flow
<i>loc</i>	Locally-averaged
<i>max</i>	Maximum value
<i>p-cr</i>	Homogenous plane-averaged at critical state
<i>rms</i>	Root mean square value
<i>Stokes</i>	Pertaining to the solution of Stokes' first problem

---

*turb* Fully turbulent state

***Superscripts***

+ Inner scaling  
\* Outer scaling  
^ Perturbing velocity component  
0, 1 Initial and final states

***Abbreviations***

CCD Charged-Coupled Device  
CFD Computational Fluid Dynamics  
CTA Constant-Temperature Anemometer  
DAQ Data Acquisition  
DNS Direct Numerical Simulation  
FOV Field of View  
FST Free-Stream Turbulence  
IA Interrogation Area  
LES Large-Eddy Simulation  
LRN Low-Reynolds Number  
LS Launder-Sharma model  
PIV Particle-Image Velocimetry  
PVC Poly-Vinyl Chloride  
RANS Reynolds-Averaged Navier Stokes  
RMS Root-Mean-Square  
TS Tollmien-Schlichting  
UDF User-Defined Function  
WALE Wall-Adapting Local Eddy-viscosity model



# Chapter 1

## Introduction

---

Wall-bounded unsteady turbulent flows are encountered frequently in a wide range of engineering and natural systems such as arterial blood flow, tracheal air flow, coolant flow in nuclear power plants, combustion engines, air flow inside railway tunnels, etc. Understanding the flow physics of such flows has proved to be of crucial importance in the design and prediction of such systems. Examples of such applications include development of leak detection techniques based on accurate prediction of unsteady wall shear stress [1, 2]; turbulence modelling of pulsatile stenotic flows [3, 4], enhancement of convective heat transfer in turbulent flows [5, 6].

In addition to the practical importance, unsteady flows also have the potential to provide an insight into the fundamental physics. The response of turbulence to unsteady flow conditions exhibits the underlying physics of turbulence that is not explicitly observed in steady turbulent flows. Thus, unsteady turbulent flow remains a topic of interest to researchers for many years. A brief review of the past studies is presented later, in Chapter 2.

## 1.1 Objectives of the Present Study

The eventual goal of the present research is to enhance the knowledge of turbulence dynamics and wall shear stress in unsteady flows; and potentially contribute to the development of analytical or empirical formulations for turbulence- and friction-modelling. The motivation of the present study arises from the recent numerical studies of He & Seddighi [7, 8] which have presented a new perspective on the turbulence dynamics in unsteady turbulent flows. It was reported that the transient flow following a rapid increase of flow rate from an initially turbulent flow is a laminar-turbulent bypass transition and three-stage response of turbulence to flow acceleration bears strong resemblance to the three regions of bypass transition flow of the boundary layer. The *time-developing boundary layer* generated at the wall in the transient flow was shown to be similar to the time-developing laminar boundary layer; with the early response of mean flow and wall friction represented by analytical solutions of the laminar flow.

The present thesis aims to supplement this study by investigating the effects of a high-Reynolds number ratio and a ramp-type flow acceleration on flow transition. Furthermore, the thesis also aims to complement the study of accelerating flows by investigating the response of turbulence and wall friction in a temporally-decelerating channel flow. In addition, a brief study on the performance and implementation of a RANS turbulence model is also presented in this thesis.

The specific objectives covered in the present thesis are:

- i) To implement subgrid-scale (SGS) models in the *in-house* Direct Numerical Simulations (DNS) code, *CHAPSim* [7-9], to conduct Large-Eddy Simulations (LES) of high Reynolds number flows.
- ii) To use the LES code to investigate the effect of high-Reynolds number ratio on the response of turbulence and the *unsteady-flow transition* phenomenon in step-like accelerating flows.
- iii) To produce experimental measurements of wall friction and turbulence in ramp-like accelerating flows; to study the effect of gradual acceleration on the response of

turbulence and *unsteady-flow transition*; and to cross-validate the findings of experimental and numerical data.

- iv) To investigate the response of turbulence and mean flow in temporally-decelerating turbulent channel flow using DNS.
- v) To implement the low-Reynolds number Launder-Sharma  $k-\varepsilon$  model [10] in the commercial CFD solver ANSYS Fluent using user-defined custom functions; to evaluate its performance in predicting unsteady turbulent flows against other CFD codes and its sensitivity to model parameters.

## 1.2 Thesis Structure

The present thesis consists of nine chapters. Chapter 2 presents a summary of a literature reviews of relevant studies on unsteady turbulent flows and boundary-layer bypass transition phenomenon, followed by a brief overview of RANS turbulence modelling. The numerical schemes used for the present investigations are presented in Chapter 3. This chapter discusses the DNS code, *CHAPSim* [7-9], which has been used herein. Also discussed in this chapter are the SGS models which have been implemented in the DNS code to conduct LES for the present study. Chapter 4 discusses the experimental flow-loop facility, measurement devices and techniques which have been used in the present study.

The effect of high-Reynolds number ratio on the unsteady-flow transition phenomena in a step-like accelerating flow is investigated in Chapter 5 using LES. Chapter 6 presents an experimental study of unsteady-flow transition in a ramp-like accelerating flow. Chapter 7 details a DNS investigation on the turbulence dynamics in a temporally-decelerating flow. Chapter 8 presents a brief study on the performance and mathematical formulation/implementation of RANS turbulence model of Launder & Sharma [10]. Finally, Chapter 9 provides the conclusions of the present investigations and discusses potential future work.

## Chapter 2

# Literature Review

---

Unsteady turbulent flows are encountered frequently in engineering and natural systems. In addition to having practical importance, unsteady flows also have the potential to provide an insight into the fundamental physics of turbulence that is usually absent in steady turbulent flows. Hence, researchers have maintained an on-going interest in the study of unsteady turbulent flows. This chapter presents review of such studies from the literature.

### 2.1 Unsteady Turbulent Flows

The study of unsteady turbulent flows is generally classified in two categories: periodic and non-periodic flows. Periodic flows are further divided into two categories – pulsating flows, having a non-zero mean flow; and oscillatory flows, having a zero mean flow. Non-periodic flows are generally classified into accelerating and decelerating flows; or by the rate of change in flow rates. Very high magnitude flow accelerations and decelerations are considered as a step change in flow; while slow accelerations and decelerations are generally referred to as ramp-up and ramp-down flows.

As the present study is concerned with step- and ramp-like non-periodic flows, the literature review presented herein focusses on the developments in the studies of non-periodic flows. Nevertheless, a brief review of studies of periodic flows is also presented.

### 2.1.1 Periodic flows

Gerrard [11] presented one of the early qualitative studies of pulsating turbulent pipe flow. It was reported that the turbulent intensity decreased during the accelerating phase and laminarization was observed, while the turbulent intensity increased during the deceleration phase. More detailed experimental studies were presented in Mizushima *et al.* [12, 13], which studied the generation and propagation of turbulence. The generation of turbulence was characterised using a critical pulsation period,  $T_c$ . It was shown that for flows with a pulsation period longer than  $T_c$ , the turbulence bursting period was independent of the pulsation. The authors also showed that the propagation of turbulence was independent of the pulsation period and scaled with the wall parameters.

Comprehensive experimental studies of periodic pipe flows were presented by Ramaprian & Tu [14-16] for a range of pulsation frequencies and amplitudes. It was reported that in addition to Strouhal number, the ratio of pulsation frequency to mean bursting frequency also affected the behaviour of turbulent flow at transitional Reynolds numbers. They reported that the time-mean turbulent flow was strongly affected by the imposed unsteadiness. A *turbulent Stokes number* ( $= \omega D / u_\tau$ ) was proposed to characterise turbulent periodic flow, which is based on the interaction between imposed pulsations and turbulent bursting process. Five regimes of periodic turbulent flow were identified using this parameter – namely quasi-steady, low-frequency, intermediate frequency, high frequency and rapid oscillations.

Most of the aforementioned studies reported that the time-mean flow was influenced by the imposed unsteadiness. However, some studies have reported otherwise. Ohmi *et al.* [17] reported an experimental investigation of pulsatile pipe flow for a wide range of frequencies,

amplitudes and Reynolds numbers. The authors showed a similarity between the instantaneous and the time-mean velocities of the pulsatile flows and those of corresponding steady flows. Tardu *et al.* [18] reported an experimental study of pulsatile channel flows for a range of frequencies, amplitudes and Reynolds numbers. In contrast to previous studies of Mizushima *et al.* [12, 13], it was reported that with the exception of large amplitude pulsations, the time-mean velocity and wall shear stress were not influenced by the imposed unsteadiness. This, however, was consistent with the findings of Ohmi *et al.* [17, 19] and is considered an established consensus. Further experimental studies investigating the role of coherent structures in pulsatile turbulent flows were presented by Tardu *et al.* [20-23].

More recently, He & Jackson [24] presented an experimental investigation of periodic pipe flow for a range of imposed frequencies. For higher frequencies, the flow showed a slug-like behaviour in the core region, with the velocity amplitudes remaining constant throughout the oscillation. This 'frozen' region decreased with decreasing frequencies, and completely disappeared when the frequency was very low. The maximum amplitude of the velocity modulations occurred at a location near the wall, which moved further away from the wall as the frequency reduced. Due to redistribution of turbulence energy from axial to radial components, a difference in the response of turbulence was noted for the RMS turbulence fluctuations of the two components. It was shown that the propagation of turbulence from the wall to the core introduced a delay in the response on turbulence, which was independent of the frequency of the imposed modulation. In the core region, the amplitude of modulation of both axial and radial RMS turbulence fluctuations reduced with an increase of the oscillation frequency, eventually becoming zero, implying a frozen turbulence condition.

Other notable works on periodic turbulent flows include experimental investigations of Hino *et al.* [25], Shemer *et al.* [26, 27], Mao & Hanratty [28-30], Brereton *et al.* [31, 32] and numerical studies of Scotti & Piomelli [33, 34] and Cotton *et al.* [35-39]. Extensive reviews on the subjects

have also been reported by Brereton & Mankbadi [40], Gündoğdu & Çarpınlioğlu [41] and Nabavi & Siddiqui [42].

### 2.1.2 Non-Periodic flows

One of the earliest experimental investigations on the transient response of turbulence following a step-change in flow was presented by Maruyama *et al.* [43]. It was reported that the generation and propagation of 'new' turbulence are the dominant process in the step-increase flow cases, whereas the decay of 'old' turbulence is the dominant process in the step-decrease flow cases. The response of turbulence was reported to undergo a delay, which was longer in the centre of the pipe. It was concluded that the turbulence is generated close to the wall and thereafter propagates to the centre.

He & Jackson [44] presented a comprehensive experimental investigation of linearly accelerating and decelerating flows. The response of turbulence was reported to be characterised by three delays, namely the delays associated with turbulence production, energy redistribution and its propagation. It was further shown that the streamwise velocity is the first to respond in the wall region followed by the transverse components, while all components responded approximately at the same time in the core region. Consistent with the earlier studies, it was concluded that turbulence responds first in the near-wall region and then, due to the action of turbulence diffusion, propagates to the core of the flow. It was shown that the delays associated with the decelerating flows were smaller in comparison to those associated with accelerating flows. The shorter delay was attributed to shorter turbulence timescales (such as  $\nu/u_\tau^2$ ) at higher Reynolds numbers at the beginning of the transient in decelerating flows. Overall, turbulence was shown to produce a two-stage response – an initial slow response followed by a rapid one. Similar results of delayed response and propagation of turbulence was also reported by the experimental investigation of Greenblatt & Moss [45], with much higher initial and final Reynolds numbers and higher acceleration rates. However, in contrast to previous studies, it was reported a second peak of turbulence intensity is generated

in the later stages of acceleration, originating in a region away from the wall (at  $y^+ \sim 300$ ) and gradually moving towards the wall.

Early studies on the response of wall shear stress include experimental investigations of Shuy [46] and Kurokawa & Morikawa [47]. In contrast to previous theoretical predictions, it was observed that the turbulent stresses were always smaller than the quasi-steady values in accelerating flows, and always greater than the quasi-steady values in decelerating flows. More recent detailed studies on wall shear stress response include the numerical investigations of He *et al.* [48], Ariyaratne *et al.* [49] and He & Ariyaratne [50]; and the experimental investigation of He *et al.* [51]. It was reported that the unsteady wall shear stress can be either larger or smaller, depending on the balance of two factors acting during the transient, namely the flow inertia and the delays in the response of turbulence. Depending on this balance, the transient behaviour of wall shear stress was divided into distinct phases. The first phase is marked by a strong inertial effect and a sharp change in the wall shear stress from the quasi-steady values. In the second phase, the near-frozen turbulence counters the effect of inertia, reducing the rate of change of the wall shear stress. Turbulent production and decay begin to respond in the third phase, where the wall shear stress asymptotically approaches the quasi-steady value.

Ariyaratne *et al.* [49] also reported that decelerating flows show a sharp decrease of wall shear stress to negative values in later stages of flow deceleration, implying a flow separation at the wall caused by plug-like behaviour of the core of the flow. Similar results were also reported by the numerical investigation of Coleman *et al.* [52] and Talha [53] for strongly decelerated flows. Spatially-evolving boundary layer flows subjected to adverse pressure gradient (APG) have been shown to share similarities with temporally-decelerating wall-bounded flows. It has been well-documented that the imposition of an APG leads to instability in the flow. Experimental studies of boundary layers subjected to APG like Krogstad & Skåre [54] and Nagano *et al.* [55] reported flow separation at the wall, causing an inflection point in the near-wall velocity profile.

DNS of ramp-up and ramp-down turbulent channel flows following a step-change in the driving pressure gradient was reported by Chung [56] and Seddighi *et al.* [57]. The response of turbulence was reported to be anisotropic in the early stages of the transient. For ramp-up flow, the energy in streamwise component was reported to be more than the quasi-steady values, while that in the transverse components was less than the quasi-steady values. On the other hand, this trend was reversed in ramp-down flows. This was attributed to the redistribution of energy from the streamwise component to the transverse components. Similar findings of anisotropic response of turbulence were also reported by a LES investigation of accelerating flows by Jung & Chung [58].

A recent DNS study of He & Seddighi [7] has proposed a new interpretation of the behaviour of transient turbulent flow. It was reported that the transient flow following a rapid increase in flow rate of a turbulent flow is effectively a laminar-turbulent transition similar to bypass transition in a boundary layer. With an increase in flow rate, the flow does not progressively evolve from the initial turbulent flow to a new one, but undergoes a process with three distinct phases of *pre-transition* (laminar in nature), *transition* and *fully-turbulent*. These resemble the three regions of boundary layer bypass-transition, namely, the buffeted laminar flow, the intermittent flow and fully developed regions, respectively. The initial response to the sudden change in flow is the formation of a thin layer of high strain-rate at the wall which grows into the flow with time. This *time-developing boundary layer* was shown to be similar to the time-developing laminar boundary-layer, and can be represented by the solution of Stokes' first problem. The turbulent structures present at the start of the transient, like the 'free-stream turbulence' (FST) in boundary layer flows, act as a perturbation to the time-developing laminar boundary layer. Elongated streaks of high and low streamwise velocities are formed, which remain stable in the pre-transition period. In late pre-transition period, the growing instabilities lead to breakdown of these streak structures and generate local packets of turbulence, thereby triggering onset of transition. In the transition period, isolated turbulent spots are generated which eventually grow in both streamwise and spanwise directions and merge with one another

eventually occupying the entire wall surface. The critical times of onset and completion of transition are clearly identifiable from the development of the friction coefficient. The time of minimum friction coefficient approximately corresponds to the appearance of first turbulent spots and, hence, the onset of transition; while the time of first peak corresponds to a complete coverage of wall with newly generated turbulence and, hence, the completion time. The new perspective presented by the authors explains the well-accepted features of accelerating flow established from previous studies [43, 44, 51, 57, 58].

Further, He & Seddighi [8] investigated various step-increase accelerating flows with initial and final Reynolds numbers ranging from 2800 to 12600. The Reynolds number ratio of the transient flow ranged from 1.1 to 4.5 (or the *initial turbulent intensity*, equivalent to FST of boundary layer flow, ranging from 15.3% down to 3.8%). It was reported that the response of high and low *Re*-ratio transients was in strikingly different patterns. The response in a high *Re*-ratio transient was characterised by three clear and distinct processes resembling the typical three regions of bypass transition. In low *Re*-ratio transients, however, the transition process was indiscernible from the instantaneous flow structures. The streaks were weaker and the turbulence spots were hardly identifiable, making the process appear like a progressive evolution of flow rather than a transition. Nevertheless, the mean and turbulent flow statistics showed unambiguously that the transient was characterised by the laminar-turbulent transitional response. It was shown that the critical time of transition showed a power-relationship with the initial turbulence intensity; while the transition period was linearly correlated with the critical time of transition.

Seddighi *et al.* [59] reported DNS of slower ramp-type accelerating flow. It was reported that despite having quantitative differences in its mean and instantaneous flows with those in a step-increase flow, the ramp flow shows the same three-stage transitional response. It was shown that, unlike in step-change where the new boundary layer is generated instantly over the walls,

the boundary layer development in a linearly changing flow develops gradually as an integral consequence of continuous changes in the flow.

Similar findings of transitional behaviour of linear-like accelerating flows was also reported by a recent experimental investigation of Gorji [60]. Turbulence measurements, obtained with the means of Particle-Image Velocimetry (PIV) and Laser-Doppler Velocimetry (LDV), were reported to respond in a similar three-stage manner. Although, the investigation lacked direct wall friction measurement, the equivalent critical and transition period Reynolds numbers were obtained from wall-normal and streamwise fluctuating velocities, and were shown to exhibit similar trends as those of the numerical data of He & Seddighi [8].

The present thesis partly aims at supplementing these studies of transitional response of accelerating flows [7, 8, 59, 60] by investigating the effects of a high-Reynolds number ratio and linear flow accelerations on the flow transition. Hence, a brief review of recent research and concepts pertaining to bypass transition flows is presented next.

## 2.2 Bypass Transition

Transition to turbulence has long been an interest to researchers. Since the first experimental investigation of Reynolds [61], there has been a great deal of research studying transition in pipes, channels and external boundary layers using theoretical, experimental and numerical methods. Understanding the underlying flow physics in transition mechanisms has direct engineering applications such as the prediction, and hence control, of wall shear stress, mixing processes, heat transfer, etc.

Transition to turbulence in flat plate boundary layers can occur via two mechanisms, namely, either a natural or bypass transition. The natural transition is observed in flows with small disturbances, represented by FST or turbulence intensity,  $Tu \ll 1\%$ . The transition occurs via the generation of two-dimensional Tollmien-Schlichting (TS) waves which travel in streamwise

direction eventually leading to three-dimensional instability followed by complete breakdown to turbulence (Kleiser & Zang [62]). The natural transition is a slow process, occurring at high Reynolds numbers ( $Re_x \sim 10^6$ , based on free-stream velocity and distance from the leading edge). When the level of  $Tu$  is more than 1%, the disturbances in the flow develop rapidly, bypassing the generation of TS waves. The breakdown to turbulence, hence, occurs much earlier ( $Re_x < 10^5$ ). This mechanism of transition is referred to as bypass transition (due to Morkovin [63]).

In bypass transition, the flow undergoes three regions of development, namely, the buffeted laminar boundary layer region, the intermittent transitional region and the fully-developed turbulent flow region (Jacobs & Durbin [64]). The first region is characterised by the enhancement of the spanwise-alternating elongated structures of positive and negative streamwise fluctuations, referred to as Klebanoff modes (due to Kendall [65]). The amplitude of perturbations grows downstream leading to instability and eventual breakdown of these structures. In the second region, the streaks break down to form localised turbulent patches, which increase in size and eventually merge with each other further downstream. The turbulence structures covering the entire span of boundary layer marks the final region of the transition process.

The formation of the streak structures can be explained by the *transient growth theory* [66, 67], which refers to the linear growth of the disturbances prior to their viscous decay downstream. Physical explanation of the process is given by the *lift-up* mechanism of Landahl [68], where a pair of stable, counter-rotating, streamwise-oriented vortices transfer momentum across the boundary layer, enhancing the streamwise velocity perturbation. Jacobs and Durbin [64] showed that the streamwise perturbations in the free-stream decay further downstream, while those in the boundary layer are enhanced and undergo a transition process. It was shown that high-frequency disturbances are filtered by the boundary layer; while the low-frequency disturbances penetrate into the boundary layer, which are then amplified further downstream.

The amplification of these disturbances has been known to grow to as high as 25% of the free-stream velocity (Alfredsson & Matsubara [69]).

Although the mechanisms of generation and enhancement of streak structures have been well established now, the mechanism of turbulent burst formation and the role of streak structures are still not well understood. Two typical instability modes have been identified, namely the sinuous and varicose modes. The former is reported to be caused by the spanwise inflections of the mean flow and can be visually identified as the streamwise-propagating low-speed structures with antisymmetric spanwise-waviness (Swearingen & Blackwelder [70]). On the other hand, the latter is reported to be caused by Kelvin-Helmholtz-like instability of the wall-normal inflectional velocities and can be identified by the generation of spanwise-symmetric repetitive *horseshoe*-shaped vortical structures propagating in the streamwise direction (Asai *et al.* [71]). The faster-growing sinuous mode is reported to be the dominating and more common instability [72-76]. The varicose mode, on the other hand, is considered relatively more stable due to its lower amplification rate. Asai *et al.* [71] reported that the growth of sinuous mode led to the formation of a chain of quasi-streamwise vortices with vorticity of alternate signs; while the varicose mode evolves into hairpin vortices made up of a pair of counter-rotating streamwise vortices.

Andersson *et al.* [77], based on secondary instability analysis of the *optimal* boundary layer streaks, reported that the critical streak amplitude for breakdown to turbulence is 26% and 37% for the sinuous and varicose instability modes, respectively. These values were further confirmed by computational investigations of Brandt & Henningson [78]. Diverging from the theoretical predictions, Vaughan & Zaki [79] and Mandal *et al.* [80] have reported critical streak amplitude of  $\sim 10\%$ . However, Arnal *et al.* [81] have shown that streak amplitudes as low as  $\sim 5\text{--}7\%$  are sufficient to trigger transition.

Westin *et al.* [82] showed that streamwise energy growth in the streak structures was in linear proportion to the downstream Reynolds number ( $u'_{max}{}^2 \sim Re_x$ ). This was later confirmed by

experimental investigations of Andersson *et al.* [83], Matsubara & Alfredsson [84] and Fransson *et al.* [85]. Based on theoretical prediction and confirmation by experiment, Andersson *et al.* [83] proposed a relationship between critical Reynolds number of transition and the FST. The relationship was later validated by the experimental investigations of Fransson *et al.* [85]. Narasimha *et al.* [86] suggested a power-law relation between transition zone Reynolds number and critical Reynolds number. Fransson *et al.* [85] later argued the existence of a minimum length of transition zone and, hence, proposed a linear relationship.

Recently, application of LES to transitional flows has become an active field of research due to its relatively less computational costs. Piomelli *et al.* [87] reported that flow backscatter effects are important features in modelling of transitional flows. Ducros *et al.* [88] showed that the SGS model to be used in modelling transitional flows should be able to appropriately dissipate fluctuations in smallest resolved scales and turn itself off in the absence of small-scale fluctuations. Schlatter *et al.* [89] argued that a successful SGS model also needs to faithfully predict the physically dominant structures and their mechanism even at low grid resolutions, such as formation of  $\Lambda$ -vortices and hairpin structures. The dynamic Smagorinsky model in its original form [90], the spatially-averaged form [91] and the Lagrangian-averaged form [92], have been applied successfully by many researchers in transitional channel and boundary layer flows [90, 92-94]. LES of bypass transition has been reported by several researchers, including Voke & Yang [95] using the constant Smagorinsky model; Péneau *et al.* [96] using the mixed dynamic model [97]; Calo [98] and Hughes *et al.* [99] using the variational multiscale (VMS) method [100], and; Schlatter [101] and Schlatter *et al.* [102] using the approximate deconvolution model (ADM) [103].

## 2.3 RANS Turbulence Modelling

Accurate predictions of turbulence and wall shear stress using DNS or LES are not always feasible in engineering applications due to the considerable computational requirements of

such techniques. The competence of the less-expensive Reynolds-Averaged Navier-Stokes (RANS) modelling techniques has gained interest of researchers for decades.

The RANS models are generally classified by the modelling scheme, i.e. the quantities/equations used to model turbulence. The most simplified examples of such models are the zero-equation mixing-length model of Prandtl [104]; the one-equation models of Prandtl [105] and Spalart & Allmaras [106]; and the two-equation  $k$ - $\varepsilon$  and  $k$ - $\omega$  models. Although researchers have proposed many different variations of two-equation models, most of the formulations are modifications of the original  $k$ - $\varepsilon$  model of Jones & Launder [107] and the  $k$ - $\omega$  model of Wilcox [108]. Other notable formulations include the Reynolds Stress Model of Launder *et al.* [109] and Speziale *et al.* [110]; the  $k$ - $\varepsilon$ - $v^2$  model of Durbin [111]; the  $v^2$ - $f$  model of Parneix *et al.* [112]; and the  $\gamma$ - $Re_\theta$  transition model of Langtry & Menter [113].

One of the early assessment of RANS models was reported by Sarkar & So [114]. The authors compared the performance of ten two-equation formulations against DNS and experimental data for Couette flow, channel flow, boundary layer flow and flow over backward step. The authors reported that the models which correctly produced the asymptotic behaviour of turbulence kinetic energy ( $k$ ) and its dissipation rate ( $\varepsilon$ ) very close to the wall generally performed better in predicting overall flow features.

Other comparative studies were reported for boundary layer flows by Patel *et al.* [115]; for natural convection cavity flows by Betts & Dafa'Allah [116]; and for fully-developed turbulent pipe flows by Hrenya *et al.* [117, 118] and Thakre & Joshi [119, 120]; and for mixed convection flows by Kim *et al.* [121]. It was reported that the performance of two-equations formulations of Launder & Sharma [10], Yang & Shih [122], Chien [123], Myong & Kasagi [124] and Wilcox [108] usually performed better than other models.

Studies concerning unsteady turbulent flows such as that of Scotti & Piomelli [34] for pulsating channel flows, and that of Khalegi *et al.* [125] for accelerating pipe flows reported that the  $k$ - $\varepsilon$

$v^2$  model performed superior to the other two-equation formulations. Recently, Gorji *et al.* [126] presented a comparative study for accelerating turbulent channel flows, and concluded that the  $k$ - $\varepsilon$  formulations of Launder & Sharma [10] and the  $\gamma$ - $Re_\theta$  model of Langtry & Menter [113] produced consistently better results compared to other two- and four-equation formulations. The authors observed that the delay in the response of the Reynolds stress and decoupling it from the response of turbulent kinetic energy are the most important features that the model should account for.

It is noted that the  $k$ - $\varepsilon$  model due to Launder & Sharma [10], although initially proposed for swirling flows, has been reported to predict several types of turbulent flows reasonably well. However, some researchers using commercial CFD solvers have reported poor and inconsistent performance of this model in comparison to other formulations [127-130]. Chapter 8 presents an evaluation of this model for steady and unsteady turbulent pipe flows, using the commercial CFD solver ANSYS Fluent and the *in-house* RANS code, TRANPIPE due to He [131].

## Chapter 3

# Numerical Methods

---

The Navier-Stokes equations, which are named after a French engineer and physicist Claude-Louis Navier and a British mathematician and physicist George Stokes, have been used to describe the motion of viscous fluids for nearly 170 years. However it was not until 1949 that numerical simulation was proposed to be used for turbulence studies. The major problem in computation is that there are closed analytical solutions to these nonlinear equations for very few problems. Therefore, various numerical techniques are employed in order to get an approximate solution.

The numerical techniques can be broadly classified into three categories – namely, the Reynolds-Averaged Navier-Stokes (RANS) approach, the Large Eddy Simulation (LES) approach and the Direct Numerical Simulation (DNS) approach. This chapter is a review of these different classifications and the various numerical methods used in the present study.

### **3.1 RANS, DNS and LES**

The governing equations for fluid flow are given by the Navier-Stokes equations as conservation of mass, momentum and energy. For an incompressible flow, the momentum and mass conservation equations in differential form read,

$$\text{Momentum equation:} \quad \frac{\partial u_i}{\partial t} + u_j \frac{\partial u_i}{\partial x_j} = -\frac{1}{\rho} \frac{\partial p}{\partial x_i} + \nu \frac{\partial^2 u_i}{\partial x_j \partial x_j} \quad (3.1)$$

$$\text{Continuity equation:} \quad \frac{\partial u_i}{\partial x_i} = 0 \quad (3.2)$$

The numerical techniques that are used to study turbulent flows are classified into three groups as below:

- Reynolds-Averaged Navier-Stokes (RANS)
- Direct Numerical Simulation (DNS)
- Large-Eddy Simulation (LES)

The RANS method is based on the classical approach by Osborne Reynolds that the instantaneous quantities can be decomposed into a mean and a fluctuating part. Thus, the velocity  $u_i$  and pressure  $p$  can be written as:

$$\begin{aligned} u_i &= \bar{u}_i + u'_i \\ p &= \bar{p} + p' \end{aligned} \quad (3.3)$$

where the overbar ( $\bar{\phantom{x}}$ ) denotes the time-averaged component and the prime ( $\prime$ ) denotes the fluctuating component. Thus, the time-average of the fluctuating component is zero ( $\overline{\phi'} = 0$ ).

The RANS equations are obtained by substituting equation (3.3) into the governing equations (3.1) and (3.2) and subsequently time-averaging the equations. The resulting Reynolds-averaged equations read:

$$\text{Momentum equation:} \quad \frac{\partial \bar{u}_i}{\partial t} + \bar{u}_j \frac{\partial \bar{u}_i}{\partial x_j} = -\frac{1}{\rho} \frac{\partial \bar{p}}{\partial x_i} + \nu \frac{\partial^2 \bar{u}_i}{\partial x_j \partial x_j} - \frac{\partial \overline{u'_i u'_j}}{\partial x_j} \quad (3.4)$$

$$\text{Continuity equation:} \quad \frac{\partial \bar{u}_i}{\partial x_i} = 0 \quad (3.5)$$

The above transformation results in additional nonlinear terms of fluctuating velocity components, i.e. the final term in RHS of equation (3.4). The six unknown terms, namely  $-\overline{u'u'}$ ,  $-\overline{v'v'}$ ,  $-\overline{w'w'}$ ,  $-\overline{u'v'}$ ,  $-\overline{u'w'}$  and  $-\overline{v'w'}$ , are referred to as Reynolds stresses. Additional transport equations for these terms may be written, but they will result in further higher order unknown terms (such as  $\overline{u'_i u'_j u'_k}$ ). This results in a problem as there are more unknowns than equations. In such a case, the equations are said to be ‘unclosed’. This is often referred to as the *closure problem of turbulence*.

Turbulence modelling is employed to resolve the issue, which models the Reynolds stress with either empirical values or additional variables. The Reynolds Stress Model (RSM) solves the modelled transport equations for individual Reynolds stresses. Alternatively, the Boussinesq hypothesis is used to couple the Reynolds stress to the mean flow with the help of a proportionality constant – the ‘turbulent viscosity’ or ‘eddy viscosity’. This turbulent viscosity is further defined with the help of turbulence models. Zero-equation mixing length models are the most common empirical models that do not require any further equations. The most-widely used models are the two-equation  $k$ - $\varepsilon/\omega$  models, where transport equations of two additional variables, namely the turbulent kinetic energy  $k$  and the dissipation rate  $\varepsilon$  (or specific dissipation rate,  $\omega$ ), are solved. These variables are then used to define the turbulent viscosity. A detailed discussion on the  $k$ - $\varepsilon$  modelling is presented in Chapter 8.

The direct numerical simulation (DNS) approach solves the Navier-Stokes equations directly without time-averaging. Thus, DNS does not require modelling of turbulence as it solves all the temporal and spatial scales of the motions. The foundation of this approach was laid by Orszag & Patterson [132] who performed computation of isotropic turbulence on a  $32^3$  grid using a spectral method. The computing resources then did not allow DNS of wall-bounded flows. DNS of channel flows was first presented by Kim *et al.* [133] and Moser & Moin [134]. Since then, DNS has been widely used to simulate turbulence in pipe and channel flows. However, the number of grid points required for DNS is exponentially proportional to the Reynolds number of

the flow (i.e.  $N \propto Re^{9/4}$ ), which makes the computational cost of DNS extremely high at moderate and high Reynolds number range. For this reason, DNS is rarely used in any practical applications and is more often used in fundamental study of the physics of the flow. The present study uses this approach to study decelerating channel flows using the in-house code, *CHAPSim* [7-9]. Further details about the code and the methods used are presented in §3.2.

An intermediate approach between DNS and RANS is Large-Eddy Simulation (LES). LES uses a spatial-filtering approach where the large-scale eddies are resolved using the filtered Navier-Stokes equations and the smaller isotropic eddies are modelled. The influence of smaller scales on the larger scales is accounted for with a ‘subgrid-scale (SGS)’ model. The computational grid for this approach does not resolve the small scales, therefore the computational cost is only a fraction of DNS. The first successful LES study of channel flow was presented by Deardorff [135] on a computational grid of  $24 \times 20 \times 14$ , and an eddy-viscosity based SGS model of Smagorinsky [136]. The accuracy of an LES is dependent on the quality of the spatial filter and the underlying SGS model applied. The near-wall behaviour of SGS models also deserves special attention. A dynamic procedure of SGS modelling was first proposed by Germano *et al.* [90], which adjusts the model coefficient to the local-flow conditions e.g. reducing the model contribution in the vicinity of the walls or laminar flow regions. For the purpose of the present study, SGS calculations are implemented on the code *CHAPSim*. The resulting computational code, named *CHAPSim\_LES*, is used for the study of high-Reynolds number ratio accelerating flows. Further details about the method and SGS models used are given in §3.3.

## 3.2 Direct Numerical Simulation

Direct numerical simulations (DNS) are the most accurate method of simulation and are often referred to as numerical experiments. But due to high computational cost of this approach, it is mostly used for studying fundamental physics of the flow. The present study uses this approach to study turbulence dynamics in decelerating flows. An in-house DNS code, *CHAPSim* [7-9] is

employed here. The code uses a hybrid-discretization scheme where the continuity restraint is enforced using a Fractional-Step Method (Kim & Moin [137]; Orlandi [138]). The pressure is taken out of the momentum equations, and the momentum equations are solved for intermediate velocities. The pressure is calculated via solving the Poisson equation to reinforce the continuity constraint by an efficient 2D FFT solver due to Orlandi [138]. In order to solve a spatially-developed flow in a channel, periodic boundary conditions are applied to the streamwise and spanwise directions and a no-slip boundary condition is applied on the top and bottom walls. The code is parallelised using the message-passing interface for use on a distributed-memory computer cluster.

### 3.2.1 Governing Equations

To solve the governing equations (3.1) and (3.2), the present DNS code uses specific parameters to remove the dimension from the equations – the centreline velocity of laminar Poiseuille flow ( $U_P$ ), the channel half-height ( $\delta$ ), time scale ( $\delta/U_P$ ) and pressure-scale ( $\rho U_P^2$ ). Using these parameters, the dimensionless forms of variables in the equations are as below,

$$\begin{aligned} x^* &= \frac{x}{\delta} & u^* &= \frac{u}{U_P} \\ t^* &= \frac{t}{\delta} U_P & p^* &= \frac{p}{\rho U_P^2} \end{aligned} \quad (3.6)$$

Note that the superscript (\*) indicates dimensionless form of the parameter. So the dimensionless governing equations read,

x-momentum:

$$\frac{\partial u^*}{\partial t^*} + u^* \frac{\partial u^*}{\partial x^*} + v^* \frac{\partial u^*}{\partial y^*} + w^* \frac{\partial u^*}{\partial z^*} = -\frac{\partial \bar{p}^*}{\partial x^*} - \frac{\partial p'^*}{\partial x^*} + \frac{1}{Re_P} \left( \frac{\partial^2 u^*}{\partial x^{*2}} + \frac{\partial^2 u^*}{\partial y^{*2}} + \frac{\partial^2 u^*}{\partial z^{*2}} \right) \quad (3.7)$$

y-momentum:

$$\frac{\partial v^*}{\partial t^*} + u^* \frac{\partial v^*}{\partial x^*} + v^* \frac{\partial v^*}{\partial y^*} + w^* \frac{\partial v^*}{\partial z^*} = -\frac{\partial p'^*}{\partial x^*} + \frac{1}{Re_P} \left( \frac{\partial^2 v^*}{\partial x^{*2}} + \frac{\partial^2 v^*}{\partial y^{*2}} + \frac{\partial^2 v^*}{\partial z^{*2}} \right) \quad (3.8)$$

z-momentum:

$$\frac{\partial w^*}{\partial t^*} + u^* \frac{\partial w^*}{\partial x^*} + v^* \frac{\partial w^*}{\partial y^*} + w^* \frac{\partial w^*}{\partial z^*} = -\frac{\partial p'^*}{\partial x^*} + \frac{1}{Re_p} \left( \frac{\partial^2 w^*}{\partial x^{*2}} + \frac{\partial^2 w^*}{\partial y^{*2}} + \frac{\partial^2 w^*}{\partial z^{*2}} \right) \quad (3.9)$$

Conservation of mass:

$$\frac{\partial u^*}{\partial x^*} + \frac{\partial v^*}{\partial y^*} + \frac{\partial w^*}{\partial z^*} = 0 \quad (3.10)$$

where  $Re_p$  is the Reynolds number based on channel half-height ( $\delta$ ) and laminar Poiseuille centreline velocity ( $U_p$ ).

$$Re_p = \frac{U_p \delta}{\nu} \quad (3.11)$$

In the present simulations, a constant mass flow approach is used to drive the flow. The three velocity components are kept periodic in the streamwise and spanwise directions, but pressure cannot be periodic in the streamwise direction as a mean pressure gradient is needed to drive the flow. In the equation (3.7) pressure gradient is split into two parts  $\left( \frac{\partial p^*}{\partial x^*} = \frac{\partial \bar{p}^*}{\partial x^*} + \frac{\partial p'^*}{\partial x^*} \right)$ . The latter  $\left( \frac{\partial p'^*}{\partial x^*} \right)$  is the fluctuation pressure and is periodic in the streamwise and spanwise directions like velocity, but the former  $\left( \frac{\partial \bar{p}^*}{\partial x^*} \right)$  is the mean pressure gradient and requires careful formulation.

Simulations at a steady state can be performed using two different flow constraints, namely enforcing either a constant pressure force ( $\partial \bar{p} / \partial x = \text{constant}$ ), or a constant mass flow rate ( $\partial Q / \partial t = 0$ , where  $Q = \iint u \cdot dy \cdot dz$ ). In the present study, the latter condition is used to drive the steady flow. By integrating the x-momentum equation (3.7) over the flow domain and equating the rate of change of mass flowrate to zero, we can get the formulation for the mean pressure gradient,

$$\frac{\partial \bar{p}^*}{\partial x^*} = + \frac{1}{Vol. Re_p} \iiint \frac{\partial^2 u^*}{\partial x_j^* \partial x_j^*} dx dy dz \quad (3.12)$$

The above formulation acts as a source term for the momentum equation and is evaluated at every time step based on results of previous time step.

For an unsteady simulation, an unsteady source term,  $\left(-\frac{\partial \bar{p}^*}{\partial x^*}\right)_u$ , is added to the above formulation (3.12). The source term for the unsteady simulation reads,

$$\frac{\partial \bar{p}^*}{\partial x^*} = + \frac{1}{Vol. Re_P} \iiint \frac{\partial^2 u^*}{\partial x_j^* \partial x_j^*} dx dy dz + \left(-\frac{\partial \bar{p}^*}{\partial x^*}\right)_u \quad (3.13)$$

where,  $\left(-\frac{\partial \bar{p}^*}{\partial x^*}\right)_u = \frac{\partial}{\partial t^*} \int Q dx = \frac{dQ}{dt} L_X^*$ , and  $L_X^*$  is the non-dimensional domain length in the streamwise direction.

### 3.2.2 Spatial and Temporal Discretization

The governing equations need to be discretized in time and space before using the computational methods. The differential equations here are approximated by a system of algebraic equations at discrete locations in time and space. The Finite-Difference Method (FDM) is the most popular approach for spatial discretization in DNS calculations. The present code uses a second-order central finite-difference scheme to discretize the governing equations in space. Central-difference discretization on *collocated grid* exhibits a weak coupling between the pressure and velocity fields which can result in *checkerboard-like* instability (Patankar [139]). This error is also known as ‘odd-even decoupling’. Instead, a *staggered grid* approach is used in the present code, i.e. the pressure is located at the cell centre and the velocities are located at cell surfaces. Staggered arrangement using second-order finite-difference has been shown to conserve kinetic energy and is the commonly used scheme for DNS and LES [140, 141]. Figure 3.1 illustrates this method in two dimensions.

Uniform grids are adopted for the periodic streamwise and spanwise directions; however the grid in wall-normal direction is non-uniform to better resolve the high-gradient regions near the wall. The *tanh* function method [142] is used for this purpose.

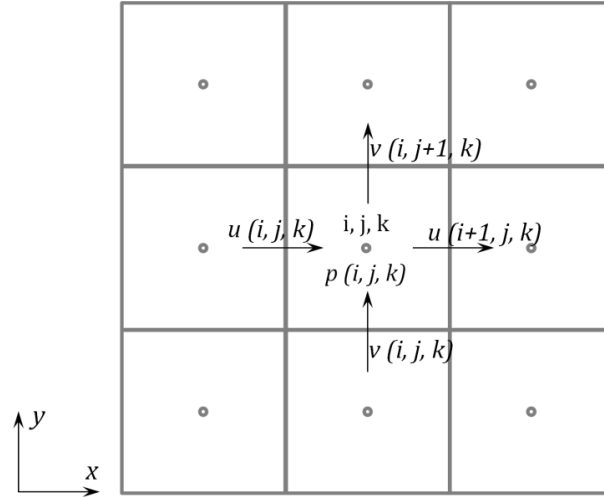


Figure 3.1 Staggered grid arrangement in the present code.

An important factor to be considered in temporal discretization of the governing equations of DNS is the physics of the flow. Accuracy over a wide range of turbulent eddy sizes requires an accurate time resolution. The time step ( $\Delta t$ ) needs to be of the order of Kolmogorov time scale ( $t_K$ ) in order to resolve the smallest eddies,

$$t_K = \left( \frac{\nu}{\varepsilon} \right)^{1/2}, \quad \text{where } \varepsilon \sim \frac{u_\tau^2 U_b}{\delta} \quad (3.14)$$

$$\Delta t \sim \frac{\delta}{u_\tau} Re_b^{-1/2} \quad \text{or} \quad \Delta t^+ \sim Re_\tau \cdot Re_b^{-1/2}$$

Although fully-implicit discretization schemes are unconditionally numerically stable, the time step used in such schemes should satisfy the above condition to resolve the physics of turbulent flows. Choi and Moin [143] performed DNS with such fully-implicit discretization scheme and concluded that for their turbulent plane channel flow of  $Re_\tau = 180$  the time step needs to be smaller than  $0.2 \nu / u_\tau^2$  in order to sustain turbulence, which is appreciably lower than Kolmogorov time scale. Such time step restrictions on fully-implicit schemes can require very high computational resources. In addition, as the convective terms in the governing equation are nonlinear, implicitly discretized equations have to be solved using iterative techniques which require comparatively lot more computational time. Thus, even though implicit techniques may seem attractive due to their numerical stability, they can prove to be highly computationally expensive in practice.

On the other hand, the numerical stability of the fully-explicit discretization schemes becomes more important. The physics of turbulent flows is effectively resolved in such schemes as the stability criteria usually constraint the time steps to be lower than the Kolmogorov time scales (Coleman & Sandberg [144]). Stability analysis for explicit treatment of the convective terms leads to the stability condition known as the *Courant-Friedrich-Lewy* (CFL) criterion, which needs to be satisfied,

$$\Delta t \leq \left[ \frac{|u_1|}{\Delta x} + \frac{|u_2|}{\Delta y} + \frac{|u_3|}{\Delta z} \right]^{-1} \quad (3.15)$$

The numerical stability condition associated with explicit treatment of the diffusion terms is referred to as viscous stability criterion,

$$\Delta t \leq \frac{1}{2\nu} \left[ \frac{1}{\Delta x^2} + \frac{1}{\Delta y^2} + \frac{1}{\Delta z^2} \right]^{-1} \quad (3.16)$$

This condition is usually more restrictive than the previous one, particularly in the presence of very fine grid near the wall. However, the viscous stability criterion can be bypassed by using implicit scheme for the viscous terms, while the convective terms can be treated explicitly to retain a higher temporal resolution. It is common practice in incompressible DNS of wall-bounded flows to use such *semi-implicit* approach (i.e. implicit time-advancement for the viscous terms and explicit time-advancement for the convective terms) as such schemes provide the computationally-cheapest trade-off between fully-implicit and fully-explicit schemes (Moin & Mahesh [145]). The present code utilises a similar approach where the time step is determined solely by the CFL criterion, with the step sizes up to  $\sim 0.75 \nu / u_\tau^2$  in the present DNS/LES simulations. There are two sets of semi-implicit second-order schemes in the present code: i) Adams-Bashforth and Crank-Nicolson, ii) Runge-Kutta and Crank-Nicolson. The linear (viscous) terms in both schemes are integrated by a second-order implicit Crank-Nicolson scheme, whereas, the nonlinear (convective) terms are integrated using either Adams-Bashforth or a low-storage third-order Runge-Kutta explicit scheme. This hybrid scheme is used with the Fractional Step Method to enforce the continuity constraint, as shown in the §3.2.4.

### 3.2.3 Boundary and Initial Conditions

There are two types of boundary conditions used in the present DNS code. The first is the periodic boundary condition which is used in streamwise and spanwise directions. Here, the value of the quantity is simply set equal at the first and last surfaces. The second condition is the no-slip condition, which is applied in the wall-normal directions for both top and bottom walls.

The initial condition for a steady simulation does not affect the result as the aim is to achieve a fully-developed channel flow. In the present code, a laminar parabolic Poiseuille profile ( $u(y) = 4(1 - |y|^2)$ , where  $y$  is the distance from the centre of the channel) is defined as the streamwise velocity profile. A random non-zero disturbance is also added to this velocity profile. For unsteady simulations, the initial conditions hold a lot of importance as the purpose is to study the temporal evolution of a spatially-developed unsteady flow. In the present research, a steady simulation is performed at a particular Reynolds number first, until it reaches a fully-developed statistically-steady condition. Then this flow field is subjected to unsteady flow conditions in a separate simulation to study its temporal evolution.

### 3.2.4 Fractional Step Method

A difficulty in solving the Navier-Stokes solution arises from the lack of an independent equation for the pressure whose gradient is involved in the momentum equations. There are several numerical methods to treat this problem, known as pressure-correction methods. The present code uses an alternative method known as the Fractional Step Method. This method was first formulated by Yanenko [146] and was subsequently implemented for the Navier-Stokes equations by Kim and Moin [137]. The modified method of Orlandi [138] is used in the present code, which incorporates the hybrid semi-implicit discretization scheme. The three steps of the Runge-Kutta method using this approach in discretized form read [9, 137, 138],

$$\text{Step 1:} \quad \hat{u}_i = u_i^n + \Delta t \left[ \gamma_1 H_i^n + \zeta_1 H_i^{n-1} + \frac{\alpha_1}{2Re} L_{jj} (\hat{u}_i + u_i^n) - \alpha_1 (G_i p^m + S_i^n) \right] \quad (3.17)$$

$$L_{jj}\phi^a = \frac{-1}{\alpha_1\Delta t}D(\hat{u}_i) \quad (3.18)$$

$$\frac{u_i^a - \hat{u}_i}{\Delta t} = -\alpha_1 G_i \phi^a \quad (3.19)$$

$$p^a = p^n + \phi^a - \frac{\alpha_1\Delta t}{2Re}L_{jj}\phi^a \quad (3.20)$$

$$\text{Step 2: } \hat{\hat{u}}_i = u_i^a + \Delta t \left[ \gamma_2 H_i^a + \zeta_2 H_i^n + \frac{\alpha_2}{2Re} L_{jj}(\hat{u}_i + u_i^a) - \alpha_2 (G_i p'^a + S_i^a) \right] \quad (3.21)$$

$$L_{jj}\phi^b = \frac{-1}{\alpha_2\Delta t}D(\hat{\hat{u}}_i) \quad (3.22)$$

$$\frac{u_i^b - \hat{\hat{u}}_i}{\Delta t} = -\alpha_2 G_i \phi^b \quad (3.23)$$

$$p^b = p^a + \phi^b - \frac{\alpha_2\Delta t}{2Re}L_{jj}\phi^b \quad (3.24)$$

$$\text{Step 3: } \hat{\hat{\hat{u}}}_i = u_i^b + \Delta t \left[ \gamma_3 H_i^b + \zeta_3 H_i^a + \frac{\alpha_3}{2Re} L_{jj}(\hat{\hat{u}}_i + u_i^b) - \alpha_3 (G_i p'^b + S_i^b) \right] \quad (3.25)$$

$$L_{jj}\phi^{n+1} = \frac{-1}{\alpha_3\Delta t}D(\hat{\hat{\hat{u}}}_i) \quad (3.26)$$

$$\frac{u_i^{n+1} - \hat{\hat{\hat{u}}}_i}{\Delta t} = -\alpha_3 G_i \phi^{n+1} \quad (3.27)$$

$$p^{n+1} = p^b + \phi^{n+1} - \frac{\alpha_3\Delta t}{2Re}L_{jj}\phi^{n+1} \quad (3.28)$$

where  $H_i$  is the discretized operator for the non-linear terms;  $L_{ii}$ ,  $G_i$  and  $D$  are the discretized Laplacian, gradient and divergence operators, respectively. The source term  $S_i$ , here, is the mean pressure gradient terms which drives the flow as defined in §3.2.1. The coefficients,  $\gamma_i$ ,  $\zeta_i$  and  $\alpha_i$  for three steps are defined as below,

$$\begin{array}{lll} \gamma_1 = 8/15 & \zeta_1 = 0 & \alpha_1 = \gamma_1 + \zeta_1 = 8/15 \\ \gamma_2 = 5/12 & \zeta_2 = -17/60 & \alpha_2 = \gamma_2 + \zeta_2 = 2/15 \\ \gamma_3 = 3/4 & \zeta_3 = -5/12 & \alpha_3 = \gamma_3 + \zeta_3 = 1/3 \end{array} \quad (3.29)$$

For the purpose of computer programming, the equations (3.17), (3.21) and (3.25) are factorized by an approximate method, due to Beam and Warming [147]. Using this factorization technique, a three-component non-solenoidal intermediate velocity is calculated from equations (3.17), (3.21) and (3.25). The divergence-free velocity field is then calculated using the pressure corrections solved from the Poisson equations (3.19), (3.23) and (3.27). For this purpose, an efficient Fast Fourier Transform solver developed by Orlandi [138] is used in the present code. The pressure at the next time-step is then calculated using the equations (3.20), (3.24) and (3.28). The solution process for the present code is illustrated in a flow chart in Figure 3.2.

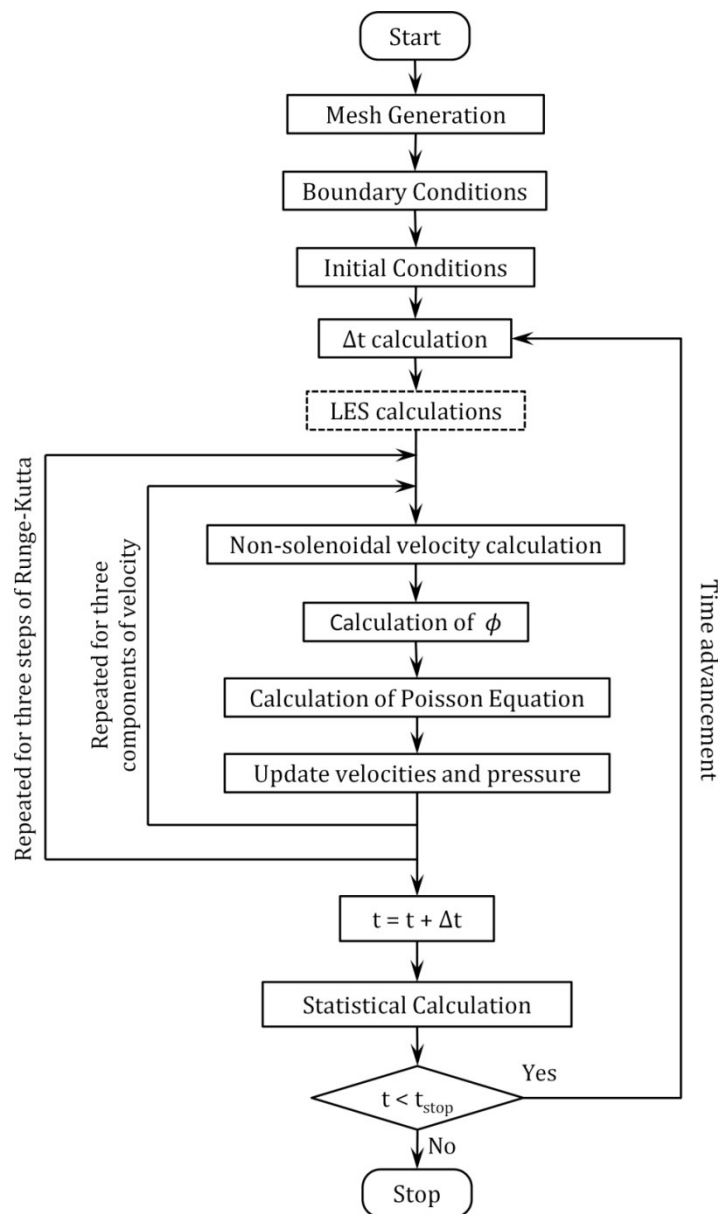


Figure 3.2 Simulation procedure adopted in the present code.

### 3.3 Large-Eddy Simulation

For practical applications, it is often necessary to simulate high Reynolds number flows, which cannot be achieved by the computationally-expensive DNS approach or the low-accuracy RANS approach. Large-eddy simulation (LES) technique is motivated by the shortcomings of the above approaches. Here, the small-scale eddies, which are considered to be generally isotropic in nature are modelled and the large scale eddies, which are characteristic of the flow are resolved by the governing equations. A spatial-filtering operation is defined to decompose the velocity into the sum of a resolved (or filtered) component and a sub-grid (or residual) component. The spatial filter is generally of the same order as the computational grid. As the smaller eddies are to be modelled, the computational grid for LES has a lesser spatial resolution than for DNS. Hence, the computational cost of LES is drastically reduced, with an acceptable decrease in accuracy. It is considered that in a good implementation of LES, 80% of the turbulent kinetic energy is accounted for by the resolved scale and the rest resides in sub-grid scale (Pope [148]).

The spatial filtering operation for velocity leads to two components,

$$u_i = \bar{u}_i - u_i' \quad (3.30)$$

Note that this decomposition is based on spatial-filtering and is different from the RANS approach which is based on temporal averaging. The governing equations for LES are achieved by decomposing the governing equations (3.1) and (3.2), and then spatially-averaging the resulting equations. The resulting equations, also known as resolved or filtered governing equations, read,

$$\text{Momentum equation:} \quad \frac{\partial \bar{u}_i}{\partial t} + \frac{\partial}{\partial x_j} (\bar{u}_i \bar{u}_j) = -\frac{1}{\rho} \frac{\partial \bar{P}}{\partial x_i} - \frac{\partial \tau_{ij}^R}{\partial x_j} + \nu \frac{\partial^2 \bar{u}_i}{\partial x_j \partial x_j} \quad (3.31)$$

$$\text{Continuity equation:} \quad \frac{\partial \bar{u}_i}{\partial x_i} = 0 \quad (3.32)$$

$$\tau_{ij}^R = \overline{u_i u_j} - \bar{u}_i \bar{u}_j \quad (3.33)$$

where  $\tau_{ij}^R$ , the residual stress is the difference between the filtered product of velocity and the product of filtered velocity, and is analogous to the Reynolds-stress of the RANS approach. The residual stress is the influence of sub-grid scale on the resolved scale. The anisotropic residual stress tensor is defined by,

$$\tau_{ij}^r = \tau_{ij}^R - \frac{1}{3} \tau_{kk}^R \delta_{ij} \quad (3.34)$$

This anisotropic part is modelled by a sub-grid scale (SGS) model and the isotropic part is included in the modified filtered pressure,

$$\bar{P} = \bar{p} + \frac{1}{3} \rho \tau_{kk}^R \quad (3.35)$$

The sub-grid scale (SGS) models are based on the eddy-viscosity hypothesis, where the anisotropic residual stress is assumed to be related to the filtered rate-of-strain with a proportionality constant, the sub-grid scale viscosity ( $\nu_{sgs}$ ). Thus, the sub-grid contribution term in the resolved governing equation (3.31) can be expressed like the viscous term in the equation.

For the purpose of this study, LES approach has been implemented in the in-house code, *CHAPSim*. The code is incorporated with a switch for LES calculations using an SGS model. The underlying numerical methods are the same as those employed in DNS calculations (described in §3.2). The sub-grid calculations for the residual stresses and viscosity are done prior to every Runge-Kutta step using the results based on the previous step. Appropriate sub-grid contribution is then accounted for in the resolved-scale calculations in equations (3.17)-(3.28).

Three SGS models, namely, the Smagorinsky model, the Germano-Lilly Dynamic model and the Wall-Adapting Local Eddy-viscosity (WALE) model have been implemented in the present computational code. The modified LES code, *CHAPSim\_LES*, has been used in the present study to investigate accelerating flows with high Reynolds number ratios. The following sub-sections will briefly describe these models.

### 3.3.1 Smagorinsky Model

The Smagorinsky model [136] is a linear eddy-viscosity, based on the mixing-length hypothesis.

The residual stress is related to the filtered rate of strain by,

$$\tau_{ij}^r = -2\nu_{sgs}\bar{S}_{ij} \quad (3.36)$$

The SGS viscosity is given by,

$$\nu_{sgs} = l_s^2 |S| = (C_s \Delta)^2 |\bar{S}| \quad (3.37)$$

$$|\bar{S}| = \sqrt{2S_{ij}S_{ij}} \quad (3.38)$$

where  $l_s$  is the Smagorinsky lengthscale (analogous to the mixing lengthscale) and  $|\bar{S}|$  is the filtered strain rate magnitude. The model constant,  $C_s$  is known as the Smagorinsky coefficient and usually has the value,  $C_s \approx 0.1 - 0.12$ . The characteristic filter width,  $\Delta$ , is of the same order of magnitude as the size of the computational grid and is defined by,

$$\Delta = (\Delta x \cdot \Delta y \cdot \Delta z)^{1/3} \quad (3.39)$$

Thus, the anisotropic residual stress is modelled as,

$$\tau_{ij}^r = -2 (C_s \Delta)^2 |\bar{S}| \bar{S}_{ij} \quad (3.40)$$

A major drawback of this SGS model is that the computed SGS viscosity has a non-zero value at solid boundaries, which is contrary to the knowledge that there is zero turbulence at the wall. This problem is resolved by introduction of a damping function in the model definition. A van Driest-style damping function is most commonly used for this purpose,

$$D = [1 - \exp(-y^+/A^+)^2]^2 \quad (3.41)$$

where  $y^+$  is the dimensionless distance from the wall ( $y^+ = yu_\tau/\nu$ ), and  $A^+=25$ . In the present code, the Smagorinsky model with the van Driest damping function, given by equation (3.46), is implemented as one of the choices for SGS models.

There are two other major issues with the Smagorinsky model. Firstly, the model constant is an *a-priori* input and does not depend on the local conditions of the flow. A single constant value cannot be used to represent various turbulent flows. And second, this model does not permit any backscatter of energy i.e. transfer of energy from sub-grid scale to the resolved scale. Since  $\nu_{sgs}$  is always positive in this model, the energy transfer is limited to only one direction. These issues are dealt with use of a dynamic procedure of calculating the model constant.

### 3.3.2 Dynamic Germano-Lilly Model

A dynamic procedure for calculating the model constant was first proposed by Germano *et al.* [90]. In this model, the model constant is not assigned *a-priori* but is computed from the local flow variables. For the purpose of dynamic calculation, a ‘test filter’ ( $\tilde{\Delta}$ ) is introduced, which is larger than the computational filter (generally taken as  $\tilde{\Delta} = 2\Delta$ ). The residual stresses resulting from the two filtering procedures are defined in similar functional form as in the Smagorinsky model, i.e. equation (3.40), but the model constant is computed dynamically. Applying this test filter on the LES governing equations, (3.31) and (3.32), we get,

$$\text{Momentum equation:} \quad \frac{\partial \tilde{u}_i}{\partial t} + \frac{\partial}{\partial x_j} (\tilde{u}_i \tilde{u}_j) = -\frac{1}{\rho} \frac{\partial \tilde{p}}{\partial x_i} - \frac{\partial T_{ij}}{\partial x_j} + \nu \frac{\partial^2 \tilde{u}_i}{\partial x_j \partial x_j} \quad (3.42)$$

$$\text{Continuity equation:} \quad \frac{\partial \tilde{u}_i}{\partial x_i} = 0 \quad (3.43)$$

$$T_{ij} = \overline{\tilde{u}_i \tilde{u}_j} - \tilde{u}_i \tilde{u}_j \quad (3.44)$$

where  $T_{ij}$  is the residual stress corresponding to the test filter. The two residual stresses are defined in a fashion similar to equation (3.40),

$$\tau_{ij}^d = \tau_{ij}^R - \frac{1}{3} \tau_{kk}^R \delta_{ij} = -2 C_d \bar{\Delta}^2 |\bar{S}| \bar{S}_{ij} \quad (3.45)$$

$$T_{ij}^d = T_{ij} - \frac{1}{3} T_{kk} \delta_{ij} = -2 C_d \tilde{\Delta}^2 |\tilde{S}| \tilde{S}_{ij} \quad (3.46)$$

Germano *et al.* [90] proposed a resolved stress (also known as Leonard stress) tensor,  $\mathcal{L}_{ij}$ , which is related to the two residual stresses by the *Germano identity*,

$$\mathcal{L}_{ij} = T_{ij} - \widetilde{\tau}_{ij} = \widetilde{u}_i \widetilde{u}_j - \widetilde{u}_i \widetilde{u}_j \quad (3.47)$$

where  $\mathcal{L}_{ij}$  represents the contributions to sub-grid stresses by length scales larger than the computational filter ( $\Delta$ ) but smaller than the test filter ( $\widetilde{\Delta}$ ). The anisotropic part of the resolved stress can be written as,

$$\mathcal{L}_{ij}^d = \mathcal{L}_{ij} - \frac{1}{3} \mathcal{L}_{kk} \delta_{ij} = C_d \alpha_{ij} - \widetilde{C_d \beta_{ij}} \quad (3.48)$$

where  $\alpha_{ij} = -2\widetilde{\Delta}^2 |\widetilde{S}| \widetilde{S}_{ij}$  and  $\beta_{ij} = \overline{\Delta^2 |\overline{S}| \overline{S}_{ij}}$ . Assuming that the model parameter is uniform over the test filter width, it can be taken out of the test-filtering operator. This leads to the ‘Smagorinsky definition’ of deviatoric part of the resolved stress,

$$\mathcal{L}_{ij}^S = T_{ij}^d - \widetilde{\tau}_{ij}^d = C_d (\alpha_{ij} - \widetilde{\beta}_{ij}) \quad (3.49)$$

Local values of the parameter,  $C_d$ , are computed to minimise the error between the deviatoric stress and its Smagorinsky prediction, resulting from the approximation  $\widetilde{C_d \beta_{ij}} = C_d \widetilde{\beta}_{ij}$ . The error is calculated by residual  $E_{ij}$ ,

$$E_{ij} = \mathcal{L}_{ij}^d - \mathcal{L}_{ij}^S \quad (3.50)$$

Germano *et al.* [90] proposed contraction of equation (3.56) with the resolved strain rate tensor,  $\overline{S}_{ij}$ , to obtain a value of  $C_d$  by solving,

$$\frac{\partial E_{ij} \overline{S}_{ij}}{\partial C_d} = 0 \quad (3.51)$$

Lilly [91] proposed an improved method of solving for  $C_d$ , where the residual tensor is contracted with itself, which is equivalent to solving parameter  $C_d$  by a least-square method,

$$\frac{\partial E_{ij} E_{ij}}{\partial C_d} = 0 \quad (3.52)$$

This yields the definition of the model parameter,  $C_d$ ,

$$C_d = -\frac{1}{2} \frac{\mathcal{M}_{ij} \mathcal{L}_{ij}^d}{\mathcal{M}_{kl} \mathcal{M}_{kl}} = -\frac{1}{2} \frac{\mathcal{M}_{ij} \mathcal{L}_{ij}}{\mathcal{M}_{kl} \mathcal{M}_{kl}} \quad (3.53)$$

where  $\mathcal{M}_{ij} = \alpha_{ij} - \widetilde{\beta}_{ij}$ .

The resulting Germano-Lilly model (also referred to as the dynamic Smagorinsky model) yields an eddy viscosity which does not need an *a-priori* value and is computed dynamically corresponding to the local flow conditions. There is no need of a near-wall damping function with this model as the model parameter automatically reduces in laminar flow regions. It can also assume a negative value which can be interpreted as backscatter of energy.

Since there is no bound on the values of the model parameter,  $C_d$ , prolonged negative values or ‘zero-denominator’ often lead to numerical instability of the simulation. It is a usual practice to average the numerator and denominator of equation (3.53) either spatially or temporally to get a reasonable value of model parameter [90, 91]. Commercial CFD solvers ANSYS Fluent [149] and Code\_Saturne [150] use a spatial-averaging approach to resolve the issue. The numerator and denominator are averaged in homogeneous directions (i.e. wall parallel direction). In the absence of a homogeneous direction a local spatial-average (using the adjoining mesh elements) is performed. ANSYS Fluent also employs a clipping operation ( $0 < C_d < 0.053$ ) to keep the values bounded. ANSYS CFX [151], in addition of clipping, uses a temporal relaxation for  $C_d$ ,

$$C_d^{n+1} = \sigma C_d^{n+1} + (1 - \sigma) C_d^n \quad (3.54)$$

where  $C_d^{n+1}$  is the relaxed value at the current time step,  $C_d^{n+1}$  is the value at the current time step computed from equation (3.53),  $C_d^n$  is the relaxed value at the previous time step and  $\sigma$  is the relaxation factor ( $\sigma \approx 0.1$ ).

In the present code, it is found that the model definition using equation (3.53) resulted in numerical instability due to large, prolonged negative values of  $C_d$ . Both spatial-averaging and temporal-relaxation techniques are implemented in the current code to resolve this issue.

### 3.3.3 Wall-Adapting Local Eddy-viscosity (WALE) Model

The Smagorinsky model (both constant and dynamic form) is based on the local strain rate, which is an arbitrary choice of velocity scale. Nicoud & Ducros [152] noted that the Smagorinsky model relates the sub-grid dissipation (proportional to the eddy viscosity) only to the strain rate of the smallest resolved scale of motion but not to its rotational rate. The authors argued that the energy is concentrated in regions of high vorticity, which these models do not account for.

Nicoud and Ducros [152] proposed a novel model based on both the strain and rotational rates. The authors begin with the traceless symmetric part of the square of the velocity gradient tensor,

$$\bar{S}_{ij}^d = \frac{1}{2}(\bar{g}_{ij}^2 + \bar{g}_{ji}^2) - \frac{1}{3}\delta_{ij}\bar{g}_{kk}^2 \quad (3.55)$$

where  $\bar{g}_{ij}$  is the resolved velocity gradient tensor,

$$\bar{g}_{ij} = \frac{\partial \bar{u}_i}{\partial x_j} \quad (3.56)$$

The equation (3.55) can be re-written in terms of the strain rate and the rotational rate,

$$\bar{S}_{ij}^d = S_{ik} + \bar{S}_{kj} + \bar{\Omega}_{ik} + \bar{\Omega}_{kj} - \frac{1}{3}\delta_{ij}(\bar{S}_{mn}\bar{S}_{mn} - \bar{\Omega}_{mn}\bar{\Omega}_{mn}) \quad (3.57)$$

where  $\bar{S}_{ij}$  is the resolved strain rate (symmetric part of the velocity gradient tensor) and  $\bar{\Omega}_{ij}$  is the resolved rotational rate (anti-symmetric part of the velocity gradient tensor),

$$\bar{S}_{ij} = \frac{1}{2}\left(\frac{\partial \bar{u}_i}{\partial x_j} + \frac{\partial \bar{u}_j}{\partial x_i}\right), \quad \bar{\Omega}_{ij} = \frac{1}{2}\left(\frac{\partial \bar{u}_i}{\partial x_j} - \frac{\partial \bar{u}_j}{\partial x_i}\right) \quad (3.58)$$

With use of Cayley-Hamilton theorem and equation (3.63), the second invariant of  $\bar{S}_{ij}^d$  can be approximated (assuming incompressibility) as,

$$\overline{S_{ij}^d S_{ij}^d} = \frac{1}{6}(S^2 S^2 + \Omega^2 \Omega^2) + \frac{2}{3}S^2 \Omega^2 + 2IV_{S\Omega} \quad (3.59)$$

where  $S^2 = \overline{S_{ij} S_{ij}}$ ,  $\Omega^2 = \overline{\Omega_{ij} \Omega_{ij}}$  and  $IV_{S\Omega} = \overline{S_{ik} S_{kj} \Omega_{jl} \Omega_{li}}$ .

Making use of this identity, Nicoud and Ducros [152] proposed the Wall-Adapting Local Eddy-viscosity (WALE) model,

$$v_{sgs} = (C_w \Delta)^2 \frac{(\overline{S_{ij}^d S_{ij}^d})^{3/2}}{(\overline{S_{ij} S_{ij}})^{5/2} + (\overline{S_{ij}^d S_{ij}^d})^{5/4}} \quad (3.60)$$

where  $C_w$  is the model parameter ( $C_w \approx 0.5 - 0.6$ ).

The model is designed to produce the correct wall asymptotic behaviour ( $y^3$ ) for wall-bounded flows. The viscosity naturally goes to zero at the wall, hence, does not require a damping function. The model is said to account for all turbulent structures relevant for the kinetic energy dissipation since the spatial operator is associated with both the local strain rate and the rotational rate. The model also produces zero eddy-viscosity in case of pure shear flow and, hence, can potentially reproduce transitional flows [152].

The WALE model with the model parameter,  $C_w = 0.5$ , has been implemented in the present LES computational code, *CHAPSim\_LES*.

### 3.4 Statistical Calculation

The present computational code employs dedicated subroutines to carry out statistical calculations. According to the Ergodic hypothesis, ensemble averaging of a steady state simulation can be replaced by averaging over homogeneous space and time.

For steady state calculations, the computation is initially carried out for some time steps in order to obtain statistical equilibrium of the flow. Then the results are averaged over the homogeneous directions (streamwise and spanwise) and then over time to obtain statistical

quantities. The time interval between two instants is kept  $t \approx 50 \nu/u_\tau^2$ . The time-averaging is performed until the averaged values converged, i.e. they did not change as new data is included. The total averaging time is kept about  $t \approx 4000 \nu/u_\tau^2$ . The statistics used to check convergence are mean velocity, r.m.s. fluctuating velocity and the Reynolds stress.

For unsteady state calculations, ensemble averaging is employed instead of temporal averaging. Multiple unsteady simulations are carried out starting from independent flow fields of the same steady simulations. To ensure complete independence from each other, the time interval between two flow fields of steady simulation is kept roughly  $t \approx 500 \nu/u_\tau^2$ . Quantities at every temporal point are averaged over the homogeneous plane and over repeated runs.

The ensemble-averaged mean velocity, r.m.s. of fluctuating velocity and shear stress for a particular wall-normal location,  $j$ , are given by,

$$U(j) = \frac{1}{N_l N_x N_z} \sum_{l=1}^{N_l} \sum_{k=1}^{N_z} \sum_{i=1}^{N_x} u(i, j, k, l) \quad (3.61)$$

$$u'_{rms}(j) = \sqrt{\frac{1}{N_l N_x N_z} \sum_{l=1}^{N_l} \sum_{k=1}^{N_z} \sum_{i=1}^{N_x} [u(i, j, k, l) - U(j)]^2} \quad (3.62)$$

$$u'v'(j) = \frac{1}{N_l N_x N_z} \sum_{l=1}^{N_l} \sum_{k=1}^{N_z} \sum_{i=1}^{N_x} [u(i, j, k, l) - U(j)]. [v(i, j, k, l) - V(j)] \quad (3.63)$$

where  $u(i, j, k, l)$  is the instantaneous velocity at grid location  $(i, j, k)$ ;  $N_x$  and  $N_z$  are the number of grid points in the streamwise and spanwise directions, respectively; and  $l = 1, 2, 3, \dots, N_l$  is the number of time-instants used in temporal-averaging (for steady state calculations), or the number of repeated runs used in ensemble-averaging (for unsteady state calculations). It should be noted that the present computational grid is staggered, which means that the velocities are on the surfaces. For the purpose of statistical calculation, all velocities are interpolated for the centre of the cells.

The homogeneous space-averaging is performed within the DNS/LES computational codes, with use of dedicated subroutines. These averaged values are then saved in binary file format for several time instants and/or several repeated runs. MATLAB script files are then used to read these binary files and perform the temporal-/ensemble-averaging accordingly.

## 3.5 Code Validation

The DNS code *CHAPSim* has been used and validated in a number of studies in the literature [7-9, 57, 59]. In the present study, this code is used to investigate decelerating channel flows. Whereas, the modified LES code, *CHAPSim\_LES* is used to investigate accelerating channel flows. In this section, these two computational codes are validated against benchmark channel flow data and against each other.

### 3.5.1 DNS Validation

Steady-state simulations at Reynolds numbers of  $Re_\tau = 180$  and  $Re_\tau = 420$  performed using *CHAPSim* are compared against the DNS data of Moser *et al.* [153] in Figure 3.3 and Figure 3.4, respectively. It should be noted that in the Figure 3.4, the present DNS data at  $Re_\tau = 420$  has been compared against data at  $Re_\tau = 395$  of Moser *et al.* [153]. Nevertheless, it can be seen that the present data is in good agreement with the benchmark data at both Reynolds numbers.

### 3.5.2 Steady-State LES Validation

The LES computational code, *CHAPSim\_LES*, developed for the present study is validated next against DNS data generated using *CHAPSim*. Steady-state simulations at Reynolds numbers  $Re_b = 7400$  and  $Re_b = 12600$  are carried out using the three aforementioned sub-grid models. DNS is also performed at LES resolution which essentially presents a ‘no-model’ LES case. The domain and grid sizes used in these simulations are presented in Table 3.1. The total number of elements of the LES is about one-fifth of that of the DNS.

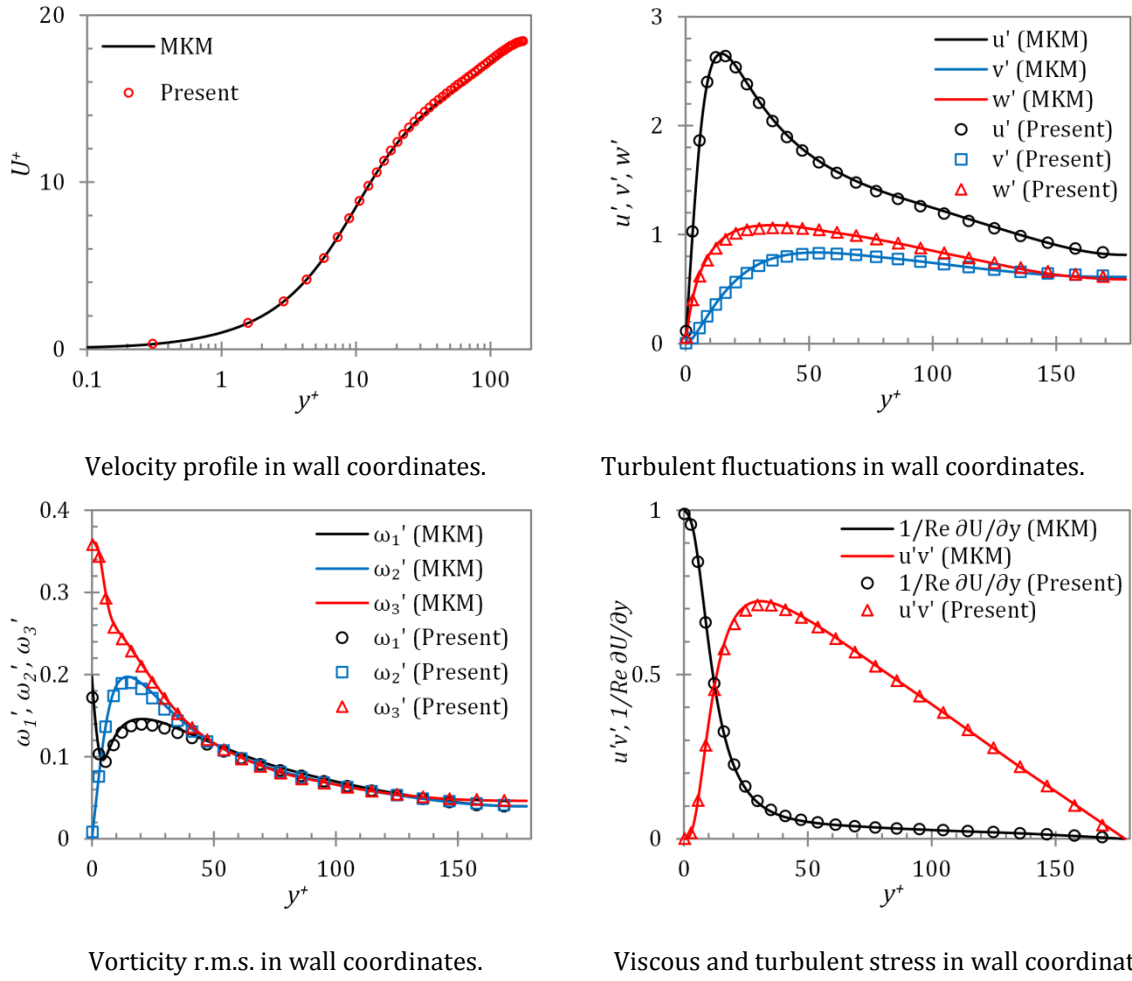


Figure 3.3 Validation of present steady-state simulation at  $Re_\tau = 180$  performed using *CHAPSim* against DNS data of Moser *et al.* [153] at  $Re_\tau = 180$  (Denoted 'MKM').

Table 3.2 shows the  $Re_\tau$  ( $= u_\tau \delta / \nu$ , where  $u_\tau$  is the friction velocity and  $\delta$  is the channel half-height) obtained using different sub-grid models in comparison to those from DNS. The three sub-grid models, the Smagorinsky model, the Germano-Lilly model and the WALE model have been denoted as 'LES1', 'LES2' and 'LES3', respectively. The no-model LES case has been denoted as 'LES0'. It is clear that all three sub-grid models over-predict the wall shear stress (hence, the friction velocity). Among the three models, the prediction of the LES2 model (Lilly [91]) is nearest to that of DNS, while that of LES1 model (Smagorinsky [136]) is farthest.

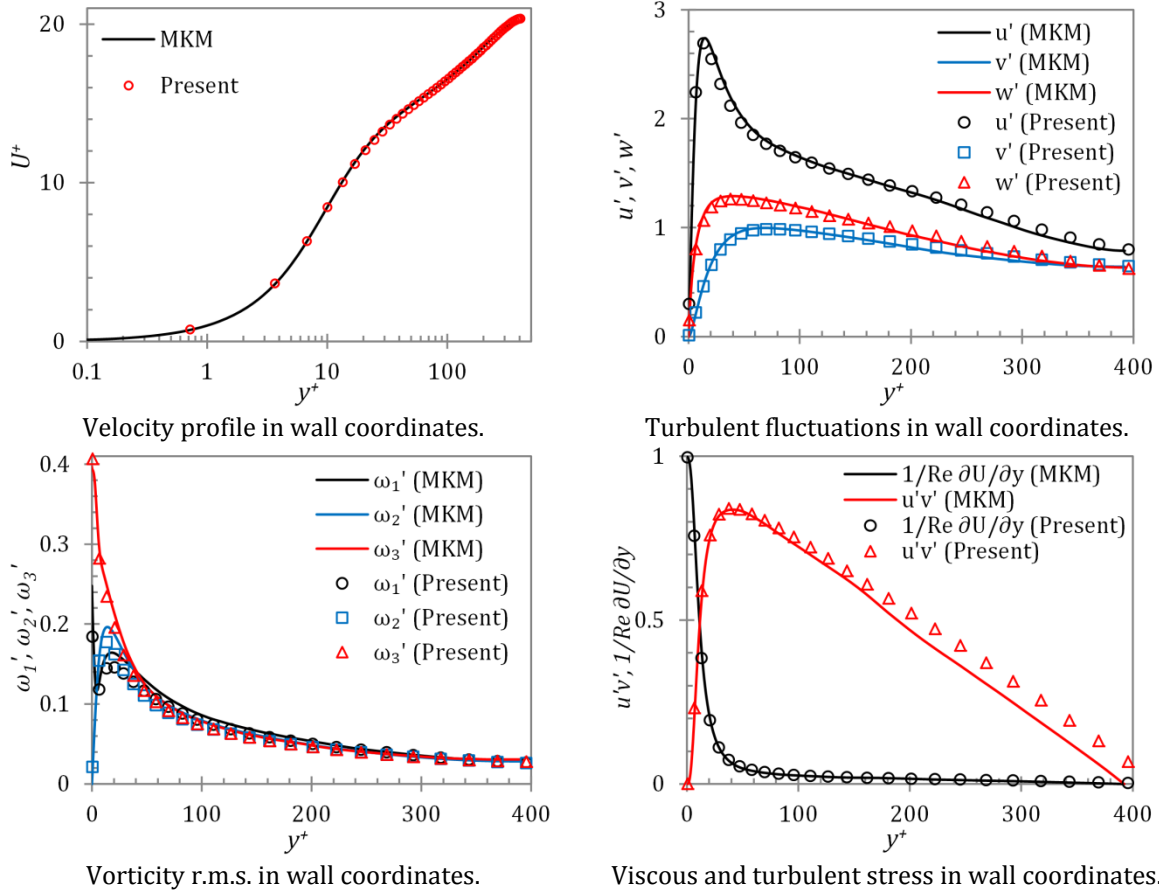


Figure 3.4 Validation of present steady-state simulation at  $Re_\tau = 420$  performed using *CHAPSim* against DNS data of Moser *et al.* [153] at  $Re_\tau = 395$  (Denoted ‘MKM’).

Simulation	$Re_b$	$L_x \times L_z$	$N_x \times N_y \times N_z$	Mesh size ( $\times 10^6$ )	$\Delta x^+$	$\Delta z^+$	$\Delta y_{min}^+ / \Delta y_c^+$
DNS	7400	$12.8 \times 3.5$	$512 \times 200 \times 200$	20.5	10	7	0.7 / 6.5
DNS	12600	$18 \times 5$	$1024 \times 240 \times 480$	117.9	12	7	0.5 / 9
LES	7400	$12.8 \times 3.5$	$192 \times 128 \times 160$	3.9	28	9	0.5 / 11
LES	12600	$18 \times 5$	$450 \times 200 \times 300$	27.0	27	11	0.6 / 15

Table 3.1 Domain and grid size for DNS and LES steady-state simulations used for validation.

Case	DNS	LES0	LES1	LES2	LES3
$Re_b = 7400$	413.1	449.9	436.3	428.9	430.8
$Re_b = 12600$	657.5	704.9	697.6	663.5	679.8

Table 3.2  $Re_\tau$  obtained for LES simulations using different sub-grid models.

A comparison of statistical profiles in wall units among these simulations is presented in Figures 3.5-3.7. It is seen that the performances of LES2 and LES3 are comparable to each other and are superior to that of LES1. Both the WALE and dynamic models are able to pretty accurately predict the mean velocity in the core of the flow, and the peaks of the streamwise velocity fluctuations and Reynolds stress; while the Smagorinsky model overestimates the same.

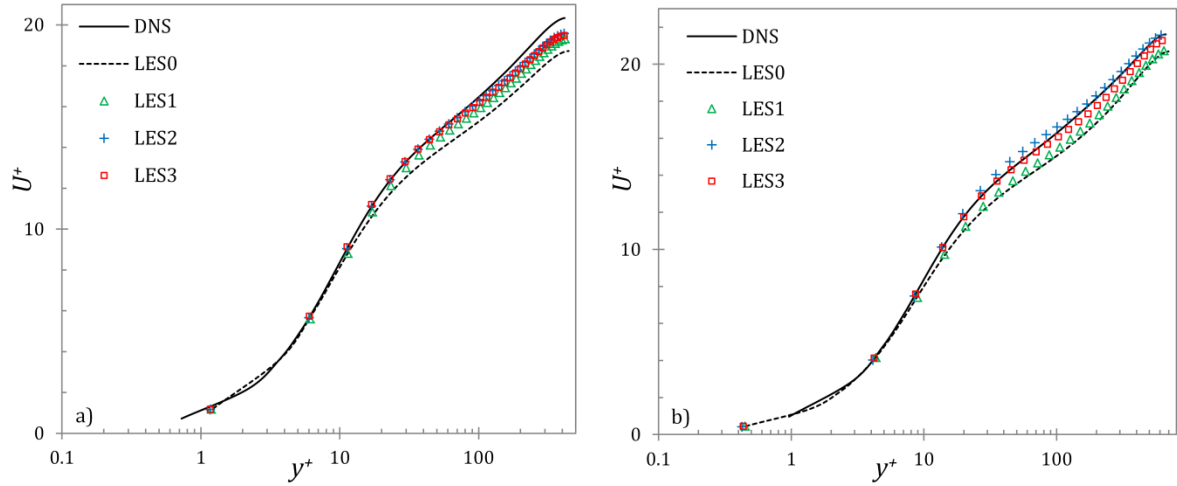


Figure 3.5 Comparison of mean velocity between steady state LES against DNS for steady channel flow at a)  $Re_b = 7400$ , and b)  $Re_b = 12600$ .

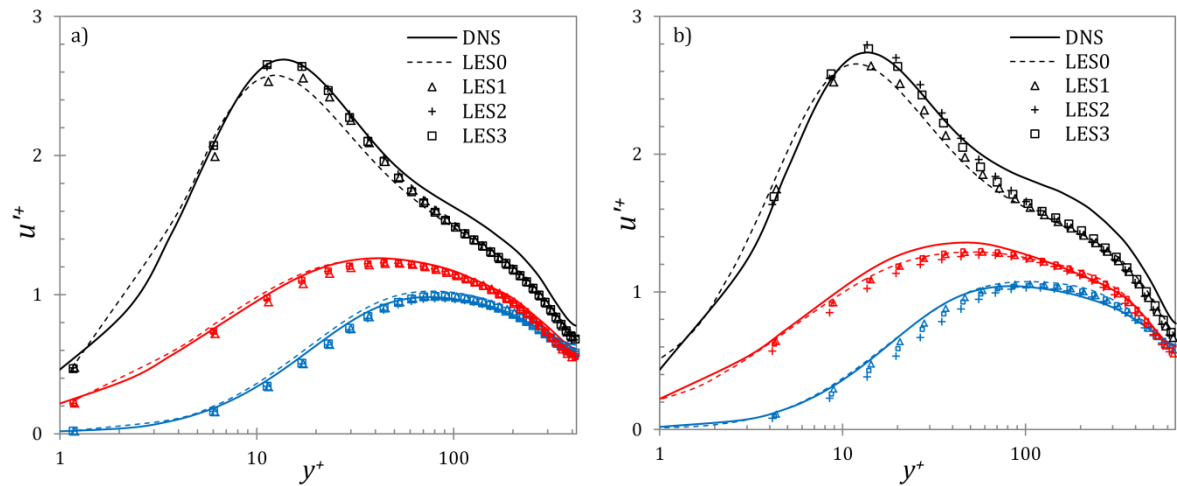


Figure 3.6 Comparison of r.m.s. fluctuating velocity between steady state LES against DNS for steady channel flow at a)  $Re_b = 7400$ , and b)  $Re_b = 12600$ . Streamwise, wall-normal and spanwise components are denoted by black, blue and red colours, respectively.

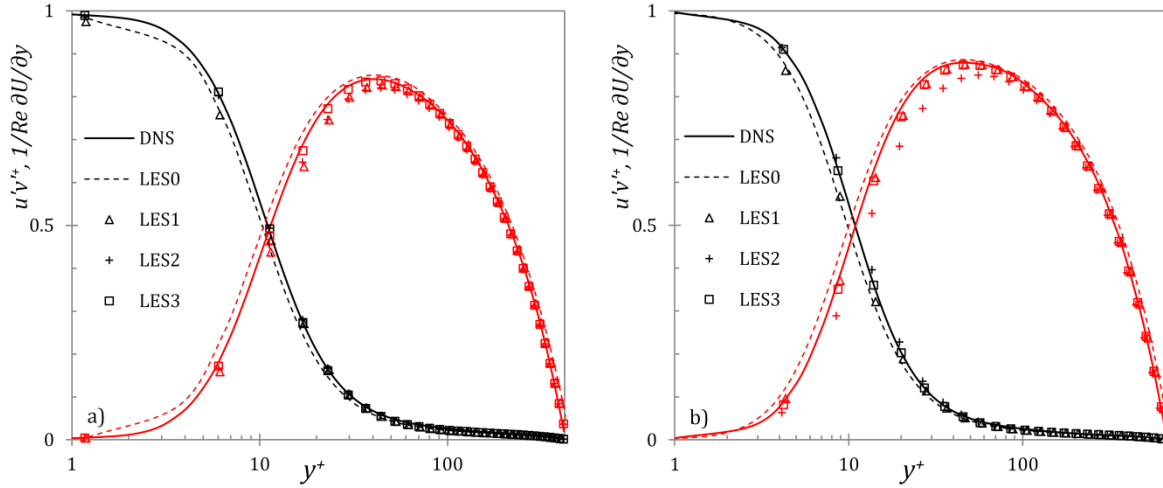


Figure 3.7 Comparison of Reynolds and viscous stresses between steady state LES against DNS for steady channel flow at a)  $Re_b = 7400$ , and b)  $Re_b = 12600$ . Reynolds and viscous stresses are denoted by red and black colours, respectively.

The inaccuracies in LES are the combined effect of numerical and model inaccuracies. The former are related to the grid resolution, while the latter refers to the performance of the SGS models in comparison to DNS. LES may be assessed via *a priori* tests, whereby predictions are compared to the corresponding filtered quantities from DNS calculations; or *a posteriori* tests which compare actual LES results with those from DNS or experiments. However, in most engineering applications, the use of DNS or experiments for validation itself contradicts the use of LES as a predictive tool. Hence, researchers have aimed at developing independent assessment measures to judge the quality of LES. Geurts & Fröhlich [154] introduced such an independent parameter to assess LES results, in the form of a subgrid activity parameter,

$$s = \frac{\langle \varepsilon_{sgs} \rangle}{\langle \varepsilon_{sgs} \rangle + \langle \varepsilon_{\mu} \rangle} \quad (3.64)$$

where  $\langle \varepsilon_{sgs} \rangle$  is the average subgrid-scale dissipation and  $\langle \varepsilon_{\mu} \rangle$  is the average molecular dissipation. The subgrid parameter can vary as  $0 \leq s \leq 1$ , with  $s = 1$  corresponding to LES at infinite Reynolds number and  $s = 0$  for DNS. Celik *et al.* [155] demonstrated that the dissipation can be written in terms of molecular viscosity,  $\nu$ , and the subgrid-scale viscosity,  $\nu_{sgs}$ . Hence, the equation (3.64) can be re-written as,

$$s \cong \frac{\langle v_{sgs} \rangle}{\langle v_{sgs} \rangle + \nu} \quad (3.65)$$

Further, Celik *et al.* [155] argued that the subgrid parameter of equation (3.65) is not sensitive to grid resolution as it does not take into account the numerical dissipation. The authors instead proposed an alternative parameter,

$$s^* \cong \frac{\langle v_{sgs} \rangle + \langle v_{num} \rangle}{\langle v_{sgs} \rangle + \langle v_{num} \rangle + \nu} \quad (3.66)$$

where  $\langle v_{num} \rangle$  is the average numerical viscosity. Celik *et al.* [156] suggested that the numerical viscosity may be approximated by the following empirical equation,

$$v_{num} = \sqrt{C_n} \left( \frac{h}{\Delta} \right)^2 v_{sgs} \quad (3.67)$$

where  $\Delta$  is the filter width,  $h = (\Delta x \Delta y \Delta z)^{1/3}$  is the grid size, and  $C_n \approx 1$  for  $h = \Delta$ . The authors [156] recommended value of this parameter to be  $s^* \sim 0.2$ , signifying an 80% contribution of molecular viscosity towards dissipation. Figure 3.8 presents this parameter for the three SGS models for steady flows at  $Re_b = 7400$  and  $12600$ . It is seen that all three SGS models show reasonable values for this parameter for both steady flows. In the viscous sublayer, the parameter goes to zero implying little or no SGS activity, while in the region farther away from the wall  $s^*$  is in the range 0.1-0.2. LES2 and LES3 are seen to bear the recommended value of 0.2, while the same for LES1 is lower. Zhang *et al.* [157] introduced another assessment indicator based on the comparison of resolved and modelled stresses,

$$LES_IQ_\tau = \frac{\tau}{\tau + \tau_{sgs}} \quad (3.68)$$

where  $\tau$  and  $\tau_{sgs}$  are the resolved and modelled stresses, respectively. The authors suggested that for wall-bounded flows, value of  $LES_IQ_\tau > 0.8$  indicates a sufficient grid resolution. Figure 3.9 presents this indicator for the three SGS models for steady flows at  $Re_b = 7400$  and  $12600$ . Again, LES2 and LES3 are seen to show reasonable values of this parameter signifying appropriate grid resolution for the two steady flows. LES1 shows comparatively low values in

region close to the wall implying a coarser grid resolution of that region. The LES assessment parameters confirm that the WALE and dynamic models give superior results to those by Smagorinsky model.

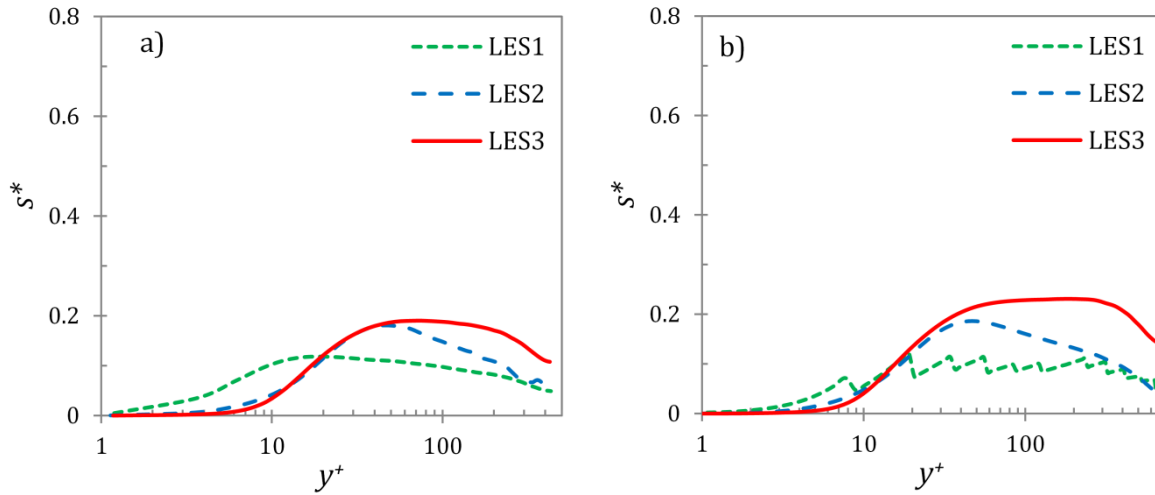


Figure 3.8 Modified activity parameter ( $s^*$ ) for the three SGS models at steady flow of a)  $Re_b = 7400$ , and b)  $Re_b = 12600$ .

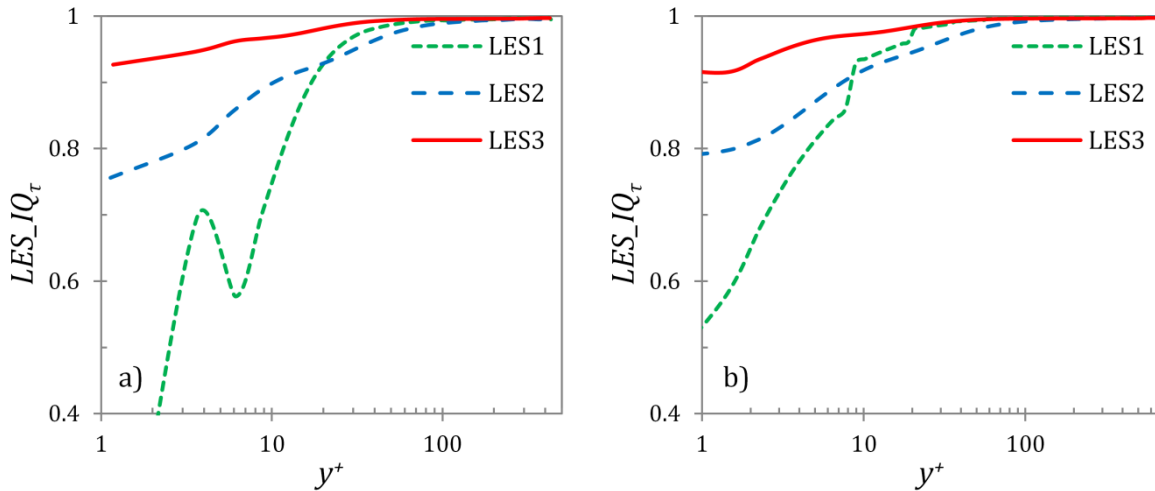


Figure 3.9 Resolved-stress indicator ( $LES\_IQ_\tau$ ) for the three SGS models for steady flow at a)  $Re_b = 7400$ , and b)  $Re_b = 12600$ .

### 3.5.3 Unsteady-Flow LES Validation

Validation for unsteady flow is presented to further compare the performance of the sub-grid models. Two accelerating flow cases are performed each using the above sub-grid models to reproduce two DNS flow cases of He & Seddighi [7, 8] (termed as HS13 and HS15, respectively). In case HS13, the flow is accelerated from a bulk Reynolds number of 2825 to 7404, while in

case HS15 from 2800 to 12600. The domain and grid sizes used in these LES simulations are the same as that provided in Table 3.1. Three realizations of the unsteady flow each starting from a different initial flow field are performed for each of the above three sub-grid models to facilitate the ensemble-averaging of the flow transient response. As described in He & Seddighi [7, 8], the time scale of the response of accelerating flows can be very well characterised by the friction coefficient development. Hence, a comparison of the predictions of this parameter by LES with those of DNS should be enough to determine the performance of the sub-grid models. Figure 3.10 presents the comparison of friction coefficient responses for the two cases with the DNS data of HS13 and HS15.

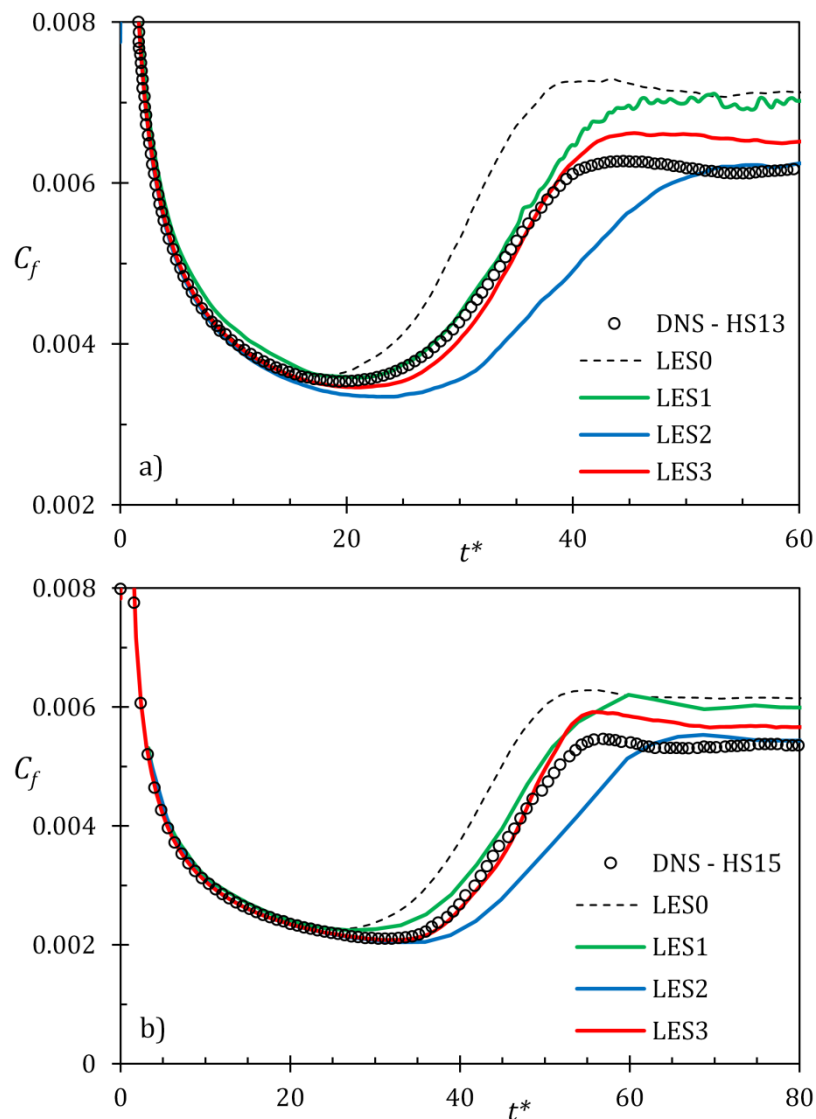


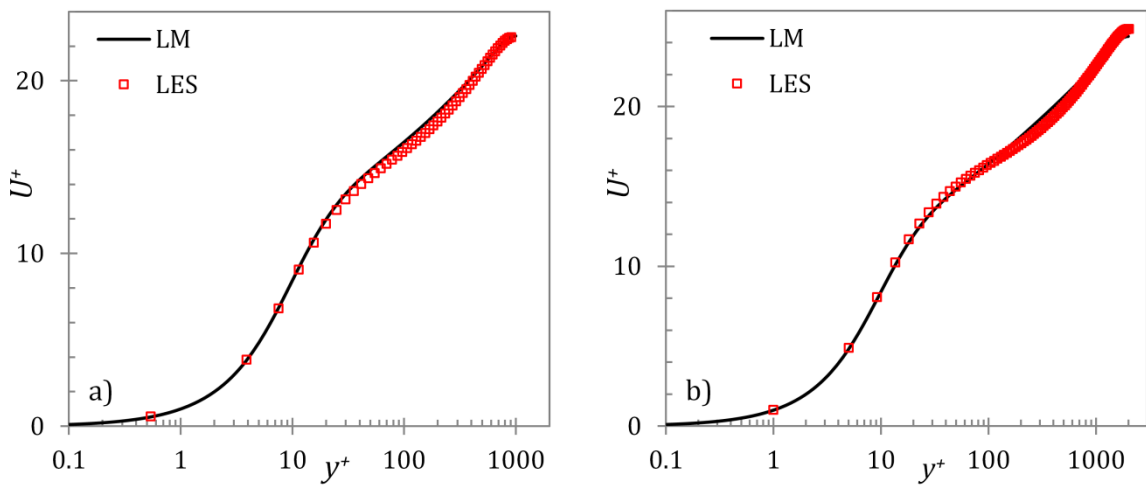
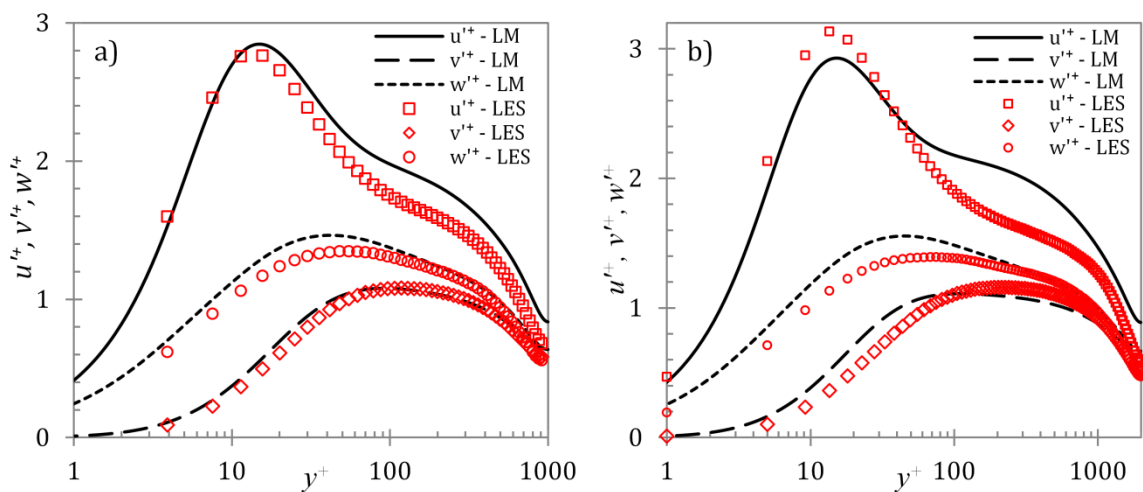
Figure 3.10 Comparison of friction coefficient development for present LES cases using the three sub-grid models against the DNS cases of He & Seddighi [7, 8] – a) case HS13, and b) case HS15.

It is seen that all three sub-grid models are able to roughly reproduce the critical time of minimum friction coefficient ( $t_{cr}^* = 19.4$  and  $31.2$  for HS13 and HS15, respectively, where  $t^* = tU_{b1}/\delta$ ). On the other hand, the recovery is predicted correctly only by LES1 and LES3. Although, LES2 precisely predicts the final value of friction coefficient, it overestimates its recovery period. Of LES1 and LES3, the prediction of the final value of the friction coefficient and the time of its first peak are predicted more accurately by LES3. Hence, it can be deduced that LES3 (WALE model of Nicoud & Ducros [152]) is most suitable for the present study of accelerating flow transition phenomena.

#### 3.5.4 Steady-State LES Validation at High $Re_\tau$

As discussed above, the performance of the WALE sub-grid model is more suitable than others for the present study. Hence, the LES of accelerating channel flows presented in Chapter 5 are performed using this model. To further evaluate the WALE model performance, steady channel flow LES simulations at higher  $Re_\tau$  are compared next against benchmark data. LES is performed for steady channel flow at  $Re_b = 18500$  and  $45000$  (roughly equivalent to  $Re_\tau = 950$  and  $2050$ , respectively). Table 3.3 compares the simulation parameters for the present LES with those of DNS of Lee & Moser [158] at  $Re_b = 19900$  and  $43400$  (equivalent to  $Re_\tau = 1000$  and  $1994$ , respectively). Figures 3.11-3.13 present the comparison between these simulations results. It is seen that the agreements between the data are satisfactory. The LES quality parameters,  $s^*$  and  $LES_IQ_\tau$ , for high- $Re_\tau$  simulations are presented in Figure 3.14. For steady flow at  $Re_\tau = 950$ , it is seen that both parameters show good values ( $s^* \sim 0.2$  and  $LES_IQ_\tau > 0.9$ ), implying a sufficient grid resolution and appropriate SGS activity. On the other hand, the parameters show relatively poor values for flow at  $Re_\tau = 2050$  ( $s^* \sim 0.4-0.45$  in the logarithmic region, and  $LES_IQ_\tau < 0.9$  in near-wall region). This is expected as the grid resolution for this flow case is kept at relatively much lower values (ref. Table 3.3) due to high computational costs.

Simulation	$Re_\tau$	$L_x \times L_z$	$N_x \times N_y \times N_z$	Mesh size ( $\times 10^6$ )	$\Delta x^+$	$\Delta z^+$	$\Delta y_{min}^+ / \Delta y_c^+$
DNS [158]	1000	$8\pi \times 3\pi$	$2304 \times 512 \times 2048$	2416	11	5	0.02 / 6.2
DNS [158]	1994	$8\pi \times 3\pi$	$4096 \times 768 \times 3072$	9664	12	6	0.02 / 8.2
LES	950	$24 \times 5$	$1200 \times 360 \times 540$	233	19	9	0.4 / 10
LES	2050	$72 \times 3$	$2400 \times 360 \times 360$	311	60	17	0.9 / 22

Table 3.3 Mesh parameters for DNS and LES at high  $Re_\tau$  steady-state simulations.Figure 3.11 Comparison of mean velocity between present LES against DNS of Lee & Moser [158] (denoted 'LM') for steady channel flow at a)  $Re_\tau = 950$ , and b)  $Re_\tau = 2050$ .Figure 3.12 Comparison of r.m.s. fluctuating velocity between present LES against DNS of Lee & Moser [158] (denoted 'LM') for steady channel flow at a)  $Re_\tau = 950$ , and b)  $Re_\tau = 2050$ .

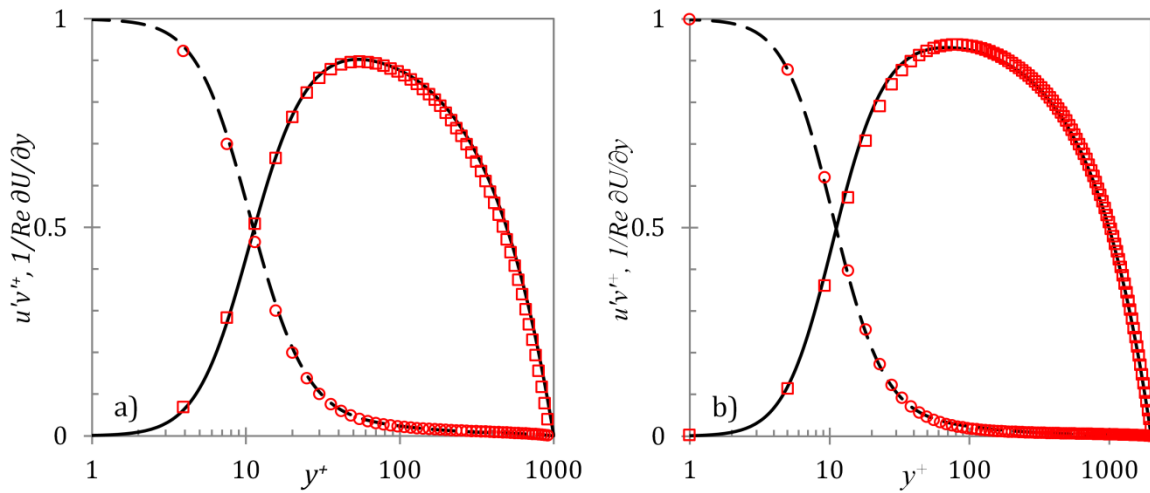


Figure 3.13 Comparison of Reynolds and viscous stresses between present LES against DNS of Lee & Moser [158] for steady channel flow at a)  $Re_\tau = 950$ , and b)  $Re_\tau = 2050$ .

Lines: (—)  $u'v'^+$  - LM; (- - -)  $1/Re \partial U/\partial y$  - LM. Symbols: ( $\circ$ )  $u'v'^+$  - LES; ( $\square$ )  $1/Re \partial U/\partial y$  - LES.

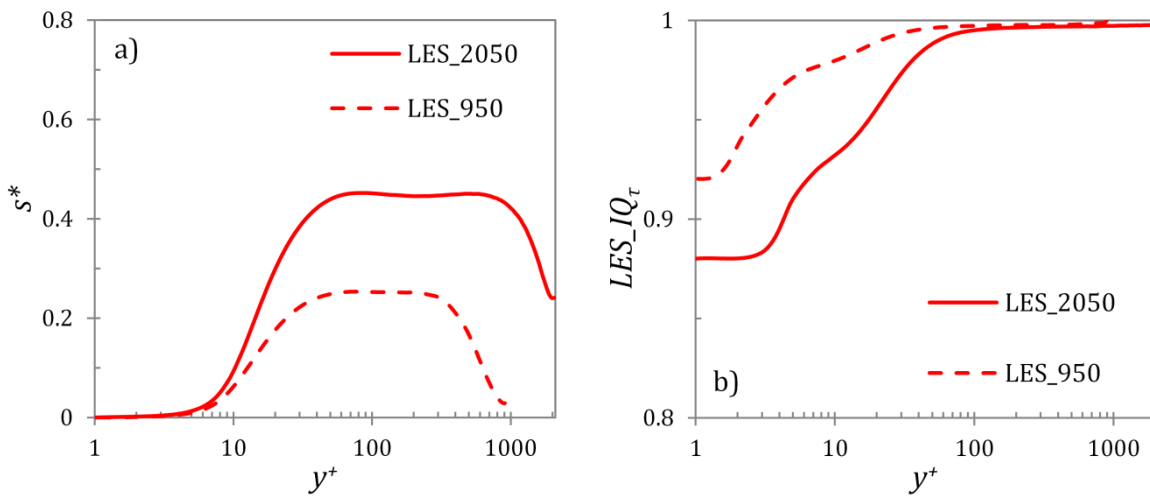


Figure 3.14 LES quality parameters for the present simulations at  $Re_\tau = 950$  (dashed) and 2050 (solid) — a) Modified activity parameter ( $s^*$ ), and b) Resolved-stress indicator ( $LES\_IQ_\tau$ ).

## Chapter 4

# Experimental Rig and Measurement Techniques

---

An experimental investigation of unsteady flow has been carried out in the present study. For this purpose, a water channel flow-loop facility has been used. Detailed measurements of instantaneous and bulk velocities were taken using a Particle-Image Velocimetry (PIV) system. Hotfilm glue-on sensors are installed in the facility and are used with a Constant-Temperature Anemometer (CTA) to measure the instantaneous wall shear stress. This chapter details the flow loop facility, measurement and data acquisition techniques, and data processing schemes used in the present study.

### 4.1 Flow Loop Facility

A water channel-flow loop facility, due to Gorji [60], has been used to study unsteady turbulent flow. Figure 4.1 shows a schematic view of the channel with corresponding coordinate system applied throughout this study. Dean [159] presented a review of channel flow studies and suggested that the minimum width to height ratio ( $W/H$ ) should be 7 to avoid secondary flows at mid-span plane. A detailed investigation of the effects of development length on smooth pipe and channel flows was presented by Monty [160]. It was concluded that the length to height

ratio ( $L/H$ ) of 130 was enough to produce a fully-developed mean and turbulence profiles in channels. The present flow loop facility follows these guidelines with width-to-height ratio ( $W/H$ ) of 7, and length-to-height ratio ( $L/H$ ) of 160. The physical size of length, width and height of the channel are 8, 0.35 and 0.05 m, respectively.

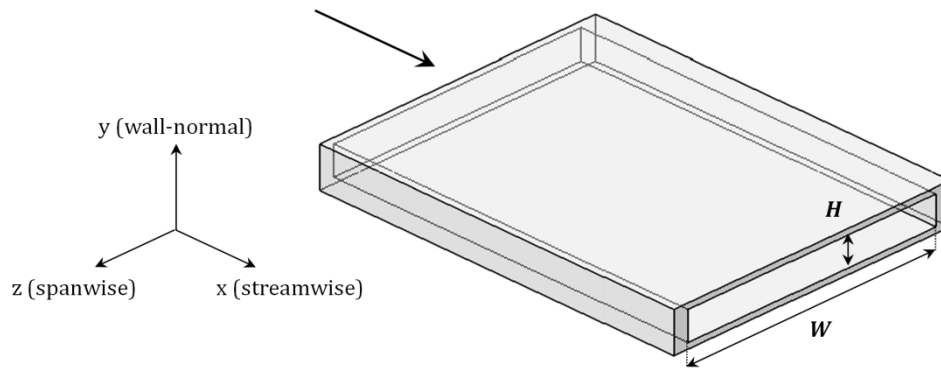


Figure 4.1 Schematic view of the channel.

Figure 4.2 illustrates the arrangement of the water flow loop facility. A 4-inch PVC pipeline feeds the channel from a header tank located 4.5 meters above the channel. A PVC honeycomb unit is placed before the test section to remove any possible swirls, thereby, enhancing the flow development. Water flows from the top tank through a manual ball valve, PVC pipeline, the channel test section, the control valve and a magnetic flow meter, before being discharged into a bottom tank. The outlet pipe from the test section is fully submerged into the bottom tank to minimise generation of bubbles in the system. The bottom tank, with a capacity of 3,000 litres, is sufficient to maintain a continuous flow loop. A four-inch bore 2.4 kW, three-phase, 4 pole centrifugal in-line pump delivers the discharged water from the bottom to the header tank. The delivery to the header tank is also submerged in water to reduce insertion of bubbles. In order to maintain a constant driving pressure gradient, an overflow pipeline is used to remove excessive water from the header tank back into the bottom tank.

The channel is constructed out of four transparent Perspex plates. However, a glass window is mounted onto one side of the measurement section to improve the optical access. The glass window is 700 mm long and at a distance of 500 mm from the outlet.

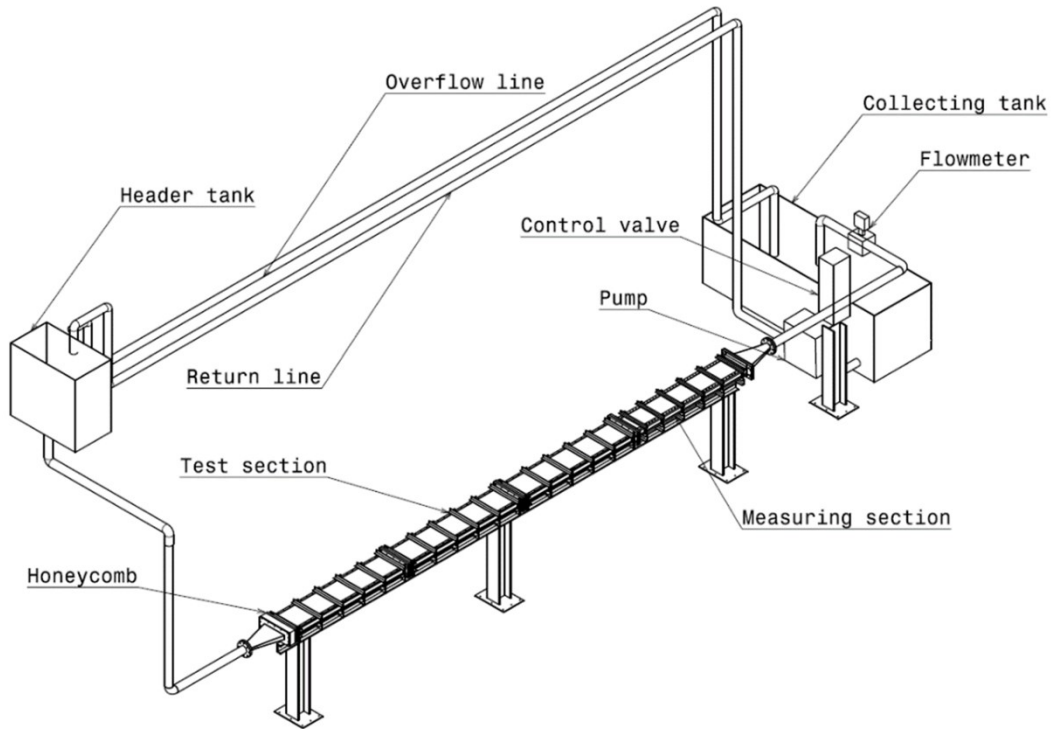


Figure 4.2 Schematic arrangement of the flow loop facility (Gorji [60]).

To reduce the possibility of bubbles in the channel, certain measures are taken. A column of half meter of water above the suction pipe was always maintained at the bottom tank to avoid cavitation. As the overflow pipe removed excess water from the header tank, the pipe delivers a mixture of water and air to the bottom tank. Hence, the overflow pipe at the bottom tank is arranged far from the suction pipe to allow water to settle and air to escape. A mesh screen is mounted on the outlet of the pump's delivery line at the header tank to entrap any bubbles and avoid their entrainment into the test section. The above measures completely remove all bubbles in the channel.

The flow is controlled by a 4-inch pneumatically-controlled globe valve which is located one meter downstream of the test section. A Siemens PS2 positioner was used to control the position of the valve trim by means of a 4-20  $mA$  signal. This current signal was generated through a Phoenix Contact three-way isolating amplifier supplied with the 0-10  $V$  signal from

the National Instruments (NI USB-6211) Data Acquisition (DAQ) device. The valve flow-lift characteristics was set at equal-percentage – i.e. changes in the flow being an equal percentage of existing flow for equal increment of the valve travel. This, however, is only an inherent feature of the valve by itself. The operational curve of the valve is characteristic of the configuration of the flow system. Figure 4.3 compares the operational curve of the valve in the present flow system with its inherent curve.

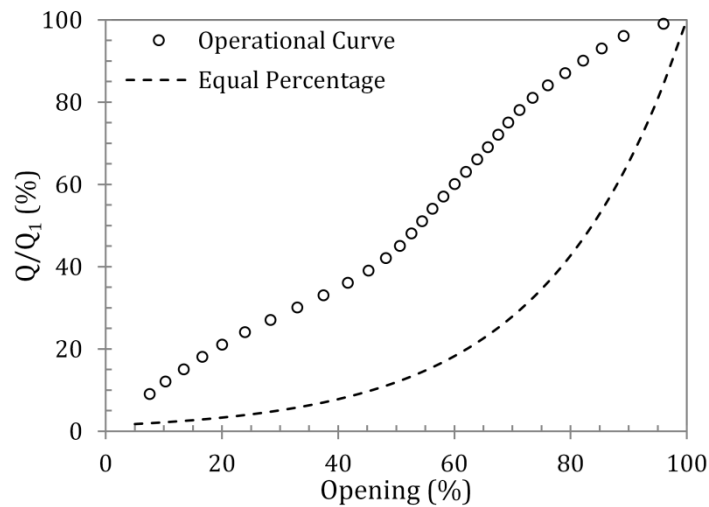


Figure 4.3 Operational and inherent curves of the control valve.

A 4-inch ISOMAG magnetic flowmeter, located further downstream of the control valve, is used to measure variations in the bulk flow. The output signal of the flowmeter was within 4-20 mA which was converted to a 0-10 V signal by means of a 250  $\Omega$  resistor. The output signal is connected to the DAQ device and was recorded through LabVIEW scripts.

For the purpose of this study, hot-film sensors are installed on a removable panel of the channel top wall. The hot-films are located in the measurement (final) section, roughly 200 mm before the outlet. A Constant-Temperature Anemometer system was set up to measure wall shear stress of unsteady flow. The Particle-Image Velocimetry system is located at the measurement section of the channel. The velocity measurement location is 7 meters downstream from the inlet of the channel, giving a development length of  $140H$ . The entire measurement section is

housed inside a custom-made 'dark room' to comply with the laser safety guidelines and to provide optimum lighting conditions for the PIV measurements.

## 4.2 Particle-Image Velocimetry

Particle-Image Velocimetry (PIV) is a non-intrusive optical measurement technique, which can provide instantaneous flow fields of two or three velocity components. A PIV system consists of three main components, laser pulse generator, Charge-Coupled Device (CCD) camera and post-processing software. A double-pulsed laser is used to generate two consecutive laser-sheets with a known time difference between them. The camera, usually located perpendicular to the laser sheet, is used to capture two consecutive frames synchronised with the laser pulses. The two frames are then processed using a software which employs advanced cross-correlation algorithms to yield an instantaneous velocity field. Figure 4.4 outlines the procedure of the PIV system.

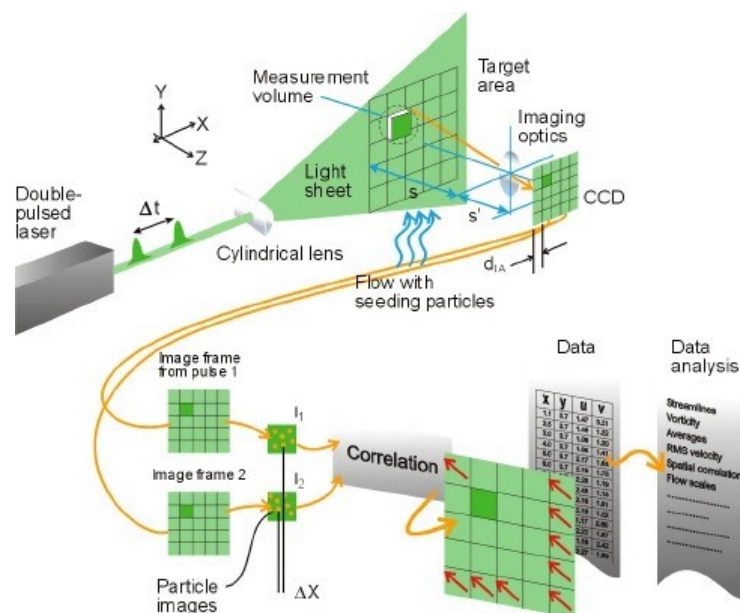


Figure 4.4 PIV system components (Dantec Inc.).

Post-processing software uses locations of tracer particles in the captured frames to compute cross-correlation. Due to this, there are three inherent assumptions associated with PIV

measurement and analysis: tracer particles follow the flow motion accurately; the tracer particles are distributed homogeneously; and, the particles have uniform distribution within the interrogation areas.

For the present study, the Dantec Dynamics integrated planar PIV system is employed. A Litron Nano-S-65 Nd-YAG (Yttrium-Aluminium-Garnet) laser, capable of generating pulsed laser light at a wavelength of 520 nm (green) with a maximum energy of 65 mJ per pulse, is used as the laser source. A Dantec Dynamics FlowSense 12-bit 4M CCD camera with the resolution of 2048 x 2048 pixels is used to capture the flow field images. The CCD camera is mounted with a Nikon AF Micro-Nikkor lens with a focal length of 60mm and a maximum aperture number of f/2.8D. Dantec DynamicStudio v3.31 software is used to post-process the images and the data. Synchronisation of the laser, camera and the computer is performed by a NI PCI-E 1427 DAQ card and a Dantec Dynamics timer box which is controlled by a NI PCI 6602 timer board. Silver-coated hollow glass spheres with a mean diameter of 14 $\mu$ m and unit specific gravity are used as tracer particles.

Two orientations of the camera-laser position were used for measurements in the present study. The first orientation (vertical; termed v-PIV hereafter), with the laser firing from the top, was used to capture the wall-normal statistical data ( $x$ - $y$  plane); whereas the second orientation (parallel; termed p-PIV hereafter), with laser firing from the side, was used to capture the instantaneous wall-parallel velocity field ( $x$ - $z$  plane). Figure 4.5 illustrates the two orientations employed in the present study.

Post-processing software computes the velocity field by the displacement of the tracer particles and the time difference between the laser pulses. Both images are divided into a number of interrogation areas (IAs). Groups of particles in each IA create a unique pattern in the first frame, and is needed to be searched in the second frame. The pattern detected in the first frame should be traced in the second frame within the IA at the same position as that in the first frame. Cross-correlation needs to be calculated at each position within the IA to give a correlation

function. A maximum correlation is obtained if the pattern is detected in the second frame. The displacement vector is calculated by the offset of the pattern in the second-frame IA with respect to that in the first frame. The velocity is, thus, calculated by this displacement and the time difference between the two laser pulses. The process is repeated over all IAs.

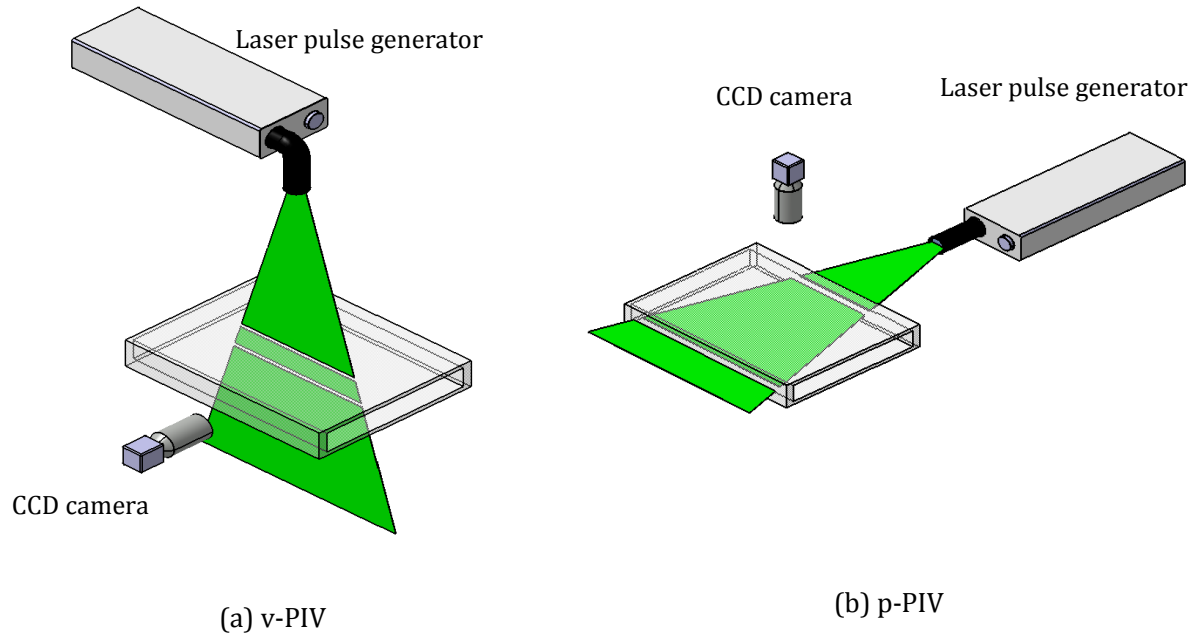


Figure 4.5 Different camera-laser orientations for the two PIV configurations: (a) vertical-PIV ( $xy$  plane), and (b) parallel-PIV ( $xz$  plane).

The accuracy of PIV measurements is affected by several factors such as particle's fidelity to the flow, light pulse timing, light sheet positioning, depth of field, and size of the interrogation areas. A number of thumb rules are suggested for PIV measurements by Keane and Adrian [161, 162] and Raffel *et al.* [163]. For example, the diameter of tracer particles is suggested to be more than 3 pixels to reduce inaccuracies in displacement calculation; the number of tracer particles within one IA is suggested to be 5-15 to produce strong cross-correlation; the maximum displacement of the particles between the laser pulses is suggested not to exceed 25% of the IA width to improve the process of the pattern detection.

A major challenge in measurement of unsteady flows arises from the fact that the optimal displacement of the particles between pulses can be hugely different for the initial and final

flows. Additionally, the measurement of velocity gradients of the streamwise velocity with larger field-of-view (FOV) sizes applies a constraint on the time difference between two pulses. Keane and Adrian [164] suggested a time constraint in order to obtain acceptable displacement detection for velocity gradients:

$$\frac{M \Delta U_y \Delta t}{d_{PIV}} < 0.03 \quad (4.1)$$

where  $M$  is the magnification factor,  $\Delta U_y = (\partial U / \partial y) \cdot d_{PIV} / 2$ ,  $\Delta t$  is the laser pulse separation time, and  $d_{PIV}$  is the length of the IA. The above expression limits the validity of measurements at locations in the near-wall region of high Reynolds number flows. For example, it can be shown that for a flow of Reynolds number  $Re_b = 2800$ , only the measurements above  $y^+ \approx 12$  are considered as valid, given that magnification factor ( $M$ ) and pulse separation time ( $\Delta t$ ) are 2.35 and 800  $\mu s$ , respectively. However, at Reynolds number of  $Re_b = 20000$ , only measurements above  $y^+ \approx 50$  are considered valid, given  $M$  and  $\Delta t$  are 2.35 and 300  $\mu s$ , respectively. In the present study of unsteady flows, the laser separation time used to capture the transient flow is maintained at a level suitable to that of the final flow. This is done as the present investigations are more concerned with the 'late' responses in the transient i.e. the response during the later stages of the transient period. It should be noted that although the appropriate recommendations for tracer particles (pixel resolution of particles; number of particles per IA; and displacement of particle in an image pair) are satisfied in the present investigation, the above criterion limits the reliability of PIV measurements in the high velocity gradient region near the wall leading to invalid results in that region.

In the present study, the *adaptive correlation* technique has been applied to compute the displacement field. In this method, the velocity vectors are iteratively calculated first with an initial larger IA, then narrowing to the final smaller IA size. For the v-PIV investigations reported here, the iterations were performed with an initial IA size of  $128 \times 128$  pixels and after three iterations, the final IA size of  $32 \times 32$  pixels. For p-PIV investigations, however, the initial IA size was kept  $256 \times 256$  pixels with a final IA size of  $64 \times 64$  pixels after three iterations. The

FOV sizes of the v-PIV and p-PIV configurations were about  $35 \times 35 \text{ mm}^2$  and  $75 \times 75 \text{ mm}^2$ , respectively.

A central difference scheme is adopted to estimate the time-derivative of displacement. Spurious velocity vectors are detected by performing a peak validation (Keane & Adrian [164]), i.e. the ratio of the highest consecutive correlation peaks should not exceed 1.2 otherwise the results is rejected. The rejected spurious vectors are replaced with a moving averaged value. The moving average is performed with 3 iterations and acceptance factor of 0.12 using  $5 \times 5$  neighbourhood vectors for the v-PIV investigations, and  $3 \times 3$  neighbourhood vectors for the p-PIV investigations. The specific parameters listed above for the v-PIV and p-PIV configurations are chosen based on the optimum calculation/correction of the velocity field.

### 4.3 Constant-Temperature Anemometry

Constant-Temperature Anemometry (CTA) is an intrusive technique which is capable of measuring velocities associated with fine structures of the flow. The working principle of this technique is based on cooling effect of a flow on a heated body. The two main components used in this technique are: the heated element which acts as a flow sensor, and the anemometer. In this technique, the sensor element is attached to one arm of the Wheatstone bridge and a servo-amplifier keeps the bridge in balance by controlling the current to the sensor.

Figure 4.6 illustrates the basic circuit for this technique. Here,  $R_S$  and  $R_L$  are the operational resistances of the sensor element and its leading support/cable, respectively.  $R_1$  and  $R_2$  are fixed resistances in the anemometer whose ratio ( $R_1/R_2$ ) is known as the bridge ratio. A variable resistor,  $R_3$ , is provided in one arm of the Wheatstone bridge to account for different sensor resistances and/or the required over-temperature for the sensor.  $R_3$  is adjusted to keep the ratio  $(R_S + R_L)/R_3$  same as bridge voltage and maintain the sensor temperature above the ambient fluid temperature. As the flow conditions change, the temperature and hence the

resistance of the sensor also change, making the bridge unbalanced. The error voltage ( $e_1 - e_2$ ) measures the corresponding change in the sensor resistance and forms the input to the amplifier. The amplifier has an output current,  $i$ , which is inversely proportional to the change in resistance. This current is fed back at the top of the bridge to restore the sensor resistance back to its original value and balance the bridge.

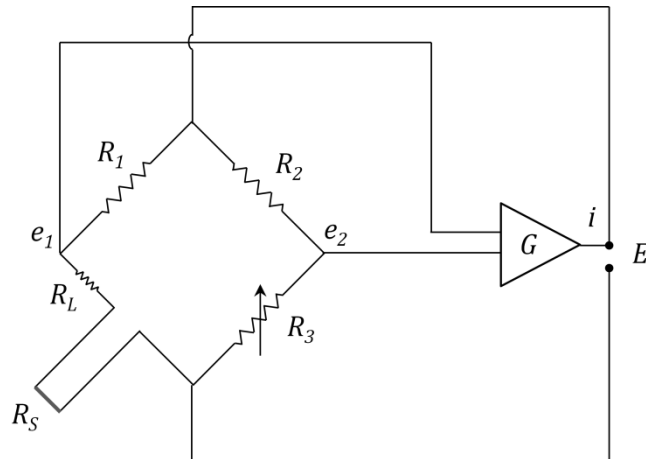


Figure 4.6 Constant-Temperature Anemometer circuit diagram.

In the present investigation, Dantec 55R47 glue-on film probes were used as sensor elements. The film probe, as shown in Figure 4.7, consists of a nickel heating film (0.9mm x 0.7mm x 0.001mm) deposited on a polyimide foil (8mm x 16mm x 0.05mm). A thin layer of quartz is deposited over the film to provide a protective coating. The film is connected to two nickel/gold-plated areas onto which the copper wires are soldered.

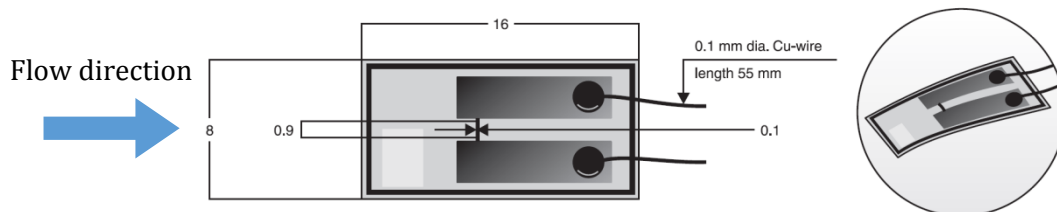


Figure 4.7 Dantec 55R47 glue-on film probes (Dantec Inc.).

Three such films are mounted on a removable panel on the top wall of the Perspex channel downstream of the measurement section. The films are placed at a distance of 50 mm from each other and about  $10H$  from the outlet of the test section to measure the instantaneous wall shear

stress. The sensors are grounded by a 108 mm long brass tube which is machined to be placed in a groove in the panel. The films are glued onto the surface of the panel by means of Loctite® 495 cyanoacrylate adhesive. The leading copper wires of the sensors are soldered to an electrical joint and then soldered to RG59 BNC cables. The soldered joints and connecting wires are sealed from exposure to water using Araldite® Rapid epoxy adhesive. The design of the removable panel for the sensor films is illustrated in Figure 4.8.

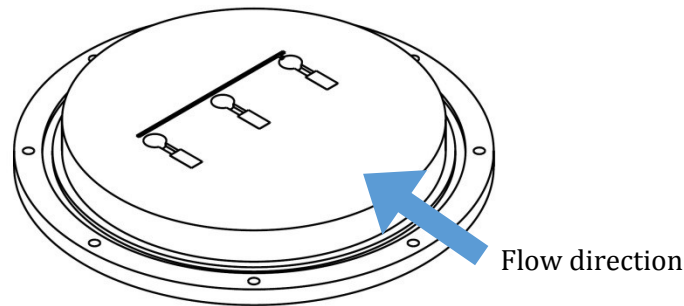


Figure 4.8 Removable panel for film sensors.

In this study, Dantec 54N81 Multichannel CTA system is used which has the capacity of 6 CTA channels, each with a bridge ratio ( $R_1/R_2$ ) of 1:20 and sensor resistance range of 4-20  $\Omega$ . The maximum output voltage of each CTA is 5 Volts with options of offset (0 or 0.9-2.2 V) and gain (1 or 2-5) for the output signal. An option of low-pass filters (1, 3, 10 kHz) is also available for the output. To increase the flow sensitivity in the present study, the offset is set to zero, the gain is set to maximum and a low-pass filter of 1 kHz is used to get CTA output. The output signal is connected to the DAQ device and is recorded through LabVIEW scripts. Of the three new film sensors installed for the purpose of the present investigation, only one of them was found to produce meaningful variation of the output signal with unsteady flow. The other two sensors produced high fluctuations of voltage which eventually decayed to a constant signal under unsteady flow conditions.

A relationship between skin friction and the heat convected from a heated platinum strip was first presented by Fage & Falkner [165]. Subsequently, Ludweig [166] designed the flush-mounted sensors based on this analogy and obtained an analytical solution to the heat-transfer

equations. Notable works using the film sensors include Liepmann & Skinner [167], Bellhouse & Schultz [168], and Menendez and Ramaprian [169]. With the assumption that the thermal boundary layer lies entirely within the laminar boundary layer, a steady state analysis yields,

$$\frac{I^2 R_S^2}{\Delta T} = A \tau_w^{1/3} + B \quad (4.2)$$

where  $R_S$  is the resistance of the sensor element,  $\Delta T$  is the difference in temperature between the sensor and ambient fluid, and A and B are calibration constants. For constant-temperature anemometry, equation (4.2) can be expressed as:

$$E^2 = A \tau_w^{1/3} + B \quad (4.3)$$

where  $E$  is the output voltage of the CTA system. The calibration constants, A and B, are determined *in situ* with measurements of flows with known wall shear stress.

A major problem in use of film sensors for water flow measurements is contamination of the sensor. Gradual build-up of scale, algae and minerals on the film results in a shift in the calibration curve and loss of flow sensitivity. Jimenez *et al.* [170] reported that if film probes are cleaned just before the test run, the surface contamination can be so fast that the data taken at the end of the run cannot not be made to correspond with those taken at the beginning. It was suggested that the films should be 'aged' with running water. Other means to reduce contamination of the sensors include the use of de-ionised water or treatment of the water with algae inhibitors.

In the present investigations, the method of 'ageing' or 'pre-contamination' is found to reduce the drift of the calibration curve. There are, however, still significant variations in calibration curves for separate test runs. Figure 4.9 shows the calibration curves for several independent test runs performed for the film sensor, and Table 4.1 presents the calibration constants obtained from these curves.

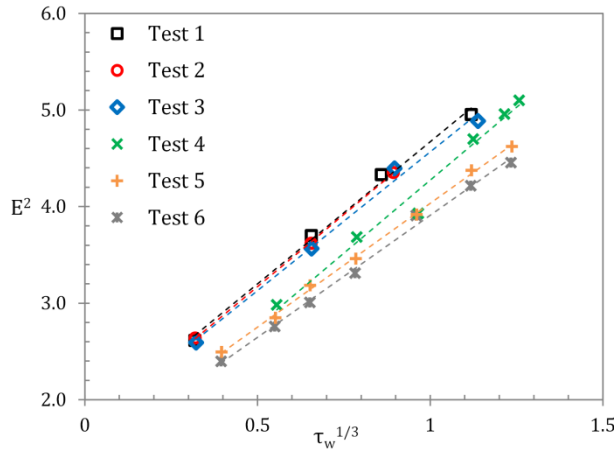


Figure 4.9 Calibration curves for film sensors.

Test Run	$A$	$B$
1	2.945	1.727
2	2.986	1.678
3	2.873	1.694
4	3.020	1.253
5	2.563	1.470
6	2.536	1.383

Table 4.1 Calibration constants obtained for the present test run cases.

Due to these variations in the calibration curves, a ‘dynamic calibration’ method is adopted to obtain calibration constants. For each unsteady run, the initial and final flows are maintained for significant amount of time (60 seconds) to ensure ‘steadiness’. The CTA output signals at these known ‘pseudo-steady’ flowrates serve as a calibration for that individual run. The wall shear stresses for the initial and final flows for each run are calculated dynamically from interpolated data of DNS. Thus, separate calibration curves are achieved for each of the repeated runs of an unsteady flow. The ensemble-averaging is performed on the skin friction or wall shear stress history.

## 4.4 Data Processing

The ensemble average statistical quantities are obtained for measurements of PIV and CTA. Dantec DynamicStudio v3.31 is used to acquire and analyse the images obtained in PIV, and record the velocity fields in a CSV file format. MATLAB scripts are used to read these files and perform averaging.

For steady state calculations, the statistical quantities are achieved by performing a streamwise-spatial and temporal averaging. For unsteady state calculation, temporal averaging is replaced

by ensemble averaging. The mean velocity, r.m.s. fluctuating velocity and shear stress at any wall normal location,  $j$ , are given by:

$$U(j) = \frac{1}{N_l N_x} \sum_{l=1}^{N_l} \sum_{i=1}^{N_x} u(i, j, t) \quad (4.4)$$

$$u'_{rms}(j) = \sqrt{\frac{1}{N_l N_x} \sum_{l=1}^{N_l} \sum_{i=1}^{N_x} [u(i, j, t) - U(j)]^2} \quad (4.5)$$

$$u'v'(j) = \frac{1}{N_l N_x} \sum_{l=1}^{N_l} \sum_{i=1}^{N_x} [u(i, j, t) - U(j)] \cdot [v(i, j, t) - V(j)] \quad (4.6)$$

where,  $N_x$  is the number of data points in streamwise direction.  $N_l$  is the number of time instants used for temporal-averaging (for steady state) or the number of repeated runs for ensemble-averaging (for unsteady state).

The output voltage signal from CTA was acquired with the National Instruments DAQ device and was recorded by LabVIEW scripts. The data recording rate in these scripts was fixed at 100 Hz. MATLAB scripts were used to read this data and calibrate the CTA signal using the ensemble-averaged velocity from PIV and determine the unsteady wall shear stress. The ensemble-averaged unsteady wall shear stress or skin friction is given by:

$$\bar{\phi}(t) = \frac{1}{N_l} \sum_{l=1}^{N_l} \phi(l, t) \quad (4.7)$$

where  $\phi(l, t)$  is the quantity at time instant,  $t$ , for  $l^{\text{th}}$  repeated run, and  $N_l$  is the number of repeated runs used for ensemble-averaging. For the present investigations, each unsteady flow case was repeated 60 times to facilitate the ensemble-averaging of PIV and CTA data.

## 4.5 Data Validation

The present flow facility and the PIV system have been previously employed and validated in Gorji [60]. In this section, the PIV measurements for steady flows are validated against benchmark DNS data from the literature. Subsequently, the unsteady flow measurements are compared the experimental data of Gorji [60] to demonstrate the repeatability of the experiments.

### 4.5.1 Steady-State Validation

Steady channel flow measurements are carried out at  $Re_b$  (based on bulk velocity and channel half-height) of 2800, 9800 and 20100 termed as S1, S2 and S3, respectively. Figure 4.10 compares the flow statistics obtained from S1-S3 against the DNS data of Lee & Moser [158] at  $Re_\tau = 180, 550$  and 2000 (roughly equivalent to  $Re_b = 2800, 10000$  and 20000, respectively). The flow profiles here are presented using outer-scaling – normalised with centreline velocity ( $U_c$ ) and channel half-height ( $\delta$ ). It should be noted that the data shown in Figure 4.10 has been clipped in the region  $y/\delta < 0.05$  as the data outside this region are considered as unreliable. It is seen that the present data is in close agreement with DNS data. Although measurements very close to the wall could not be made, the peaks of r.m.s. fluctuating velocities have been well captured.

As discussed earlier in §4.3, calculation of wall shear stress for a steady channel flow is not possible in the present setup as a universal calibration of the CTA system cannot be obtained. There are, however, various indirect methods to calculate the wall shear stress from velocity measurement. Accurate estimations can be made by curve-fitting the mean velocity in viscous region of the flow, to calculate friction velocity ( $u_\tau$ ) and hence the wall shear stress. The velocity in this region is given by the expression,

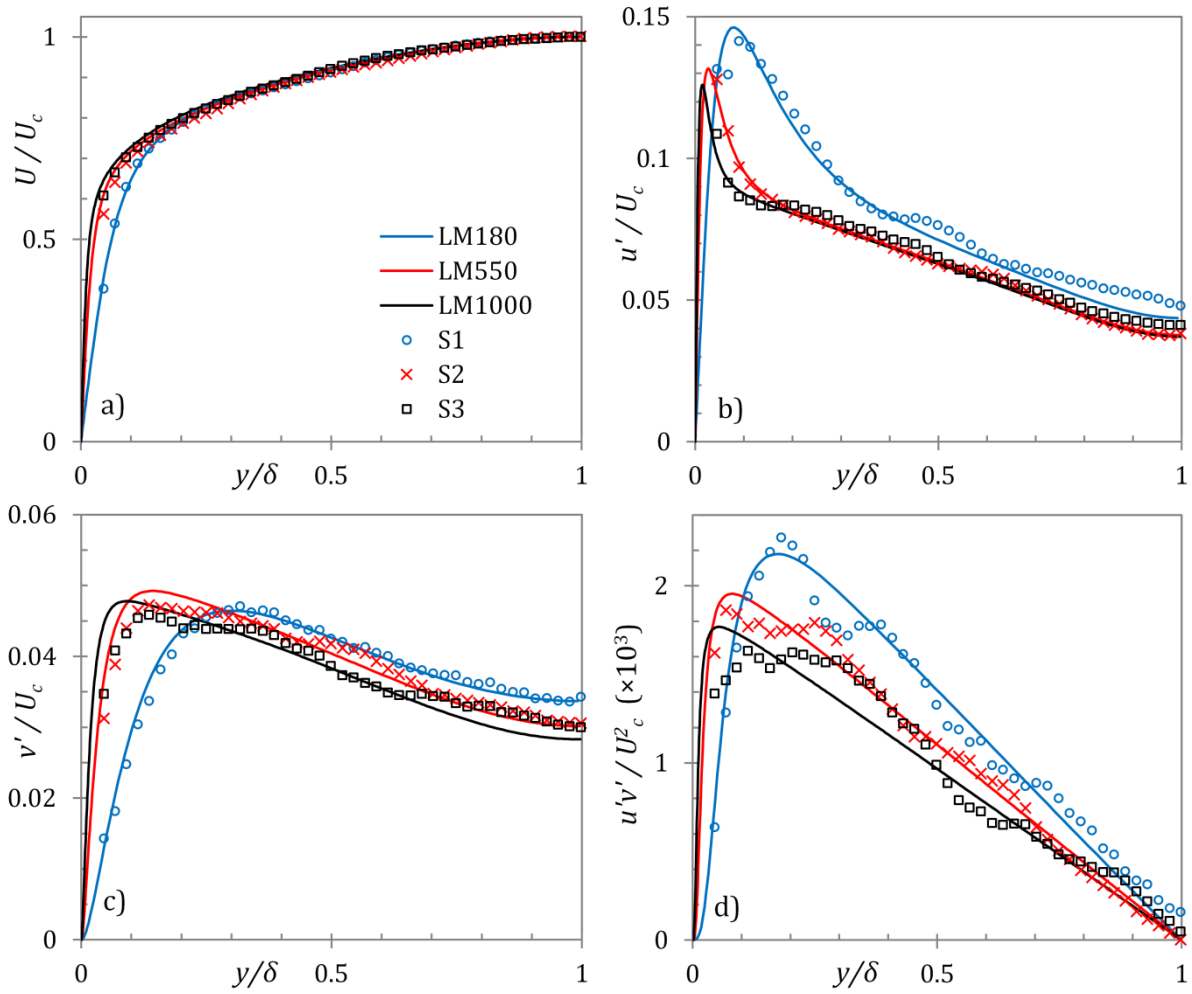


Figure 4.10 Comparison of outer-scaled present experimental data with DNS data of Lee & Moser [158] for steady channel flows at  $Re_b = 2800, 9800$  and  $20100$ .

$$\frac{\bar{U}}{u_\tau} = \frac{y u_\tau}{\nu} \quad \text{for } y^+ \leq 5 \quad (4.8)$$

Polynomial curve-fitting of the mean velocity in the buffer region can also be used to determine the friction velocity. Such polynomial expressions are presented by Spalding [171], Musker [172] and Durst *et al.* [173]. However, these methods require precise velocity measurements in the wall region. As discussed in §4.2, accurate PIV measurements very close to the wall cannot be made due to large velocity gradients in this region.

Alternative methods to determine the friction velocity from measurements away from the wall include curve-fitting the mean velocity in the logarithmic region of the flow. In this region the mean velocity is represented by the following expression due to von Kármán [174],

$$\frac{\bar{U}}{u_\tau} = \frac{1}{\kappa} \ln\left(\frac{y u_\tau}{\nu}\right) + C \quad \text{for } y^+ > 30 \quad (4.9)$$

where  $\kappa$  is the von Kármán constant and  $C$  is the empirical constant. Well accepted values of these constants for channel flows are 0.41 and 5.17, respectively. Linear extrapolation of Reynolds stress ( $\langle u'v' \rangle$ ) in the core of the flow towards the wall can also be used to determine the square of friction velocity. The above two methods are used to evaluate the Reynolds number based on friction velocity for S1-S3. Table 4.2 compares these predictions with the DNS data of Lee & Moser [158]. Also shown in the table are the predictions from interpolated of steady channel flow DNS data obtained using *CHAPSim* [7-9].

Case	Lee & Moser [158]	<i>CHAPSim</i> interpolation	Log-law eq. (4.9)	$\langle u'v' \rangle$ curve
S1	182.1	179.3	190.9	175.4
S2	543.5	524.2	514.2	499.3
S3	1000.5	1031.7	1028.6	978.1

Table 4.2  $Re_\tau$  obtained for LES simulations using different sub-grid models.

Figure 4.11 presents the comparison of statistical profiles of the above steady channel flows using inner-scaling (where  $u_\tau$  is obtained from log-law) with the DNS data of Lee & Moser [158].

It is clear that the friction velocity obtained from the log-law scales the flow fairly well. Although, the present experimental data for flow S3 deviates away from DNS at  $y^+ < 100$ , whereas the same in S1 occurs at  $y^+ < 10$ . But this is expected because as described in §4.2, as Reynolds number of the flow is increased, the scaled wall-normal distance ( $y^+$ ) for valid PIV velocity measurements increases.

It can be seen in Table 4.2, that the trend of friction velocity prediction obtained using the DNS code *CHAPSim* can roughly predict that obtained from log-law. Hence, given a flow rate the prediction from interpolation of *CHAPSim* data is used for the *dynamic calibration* of the CTA in the present investigations.

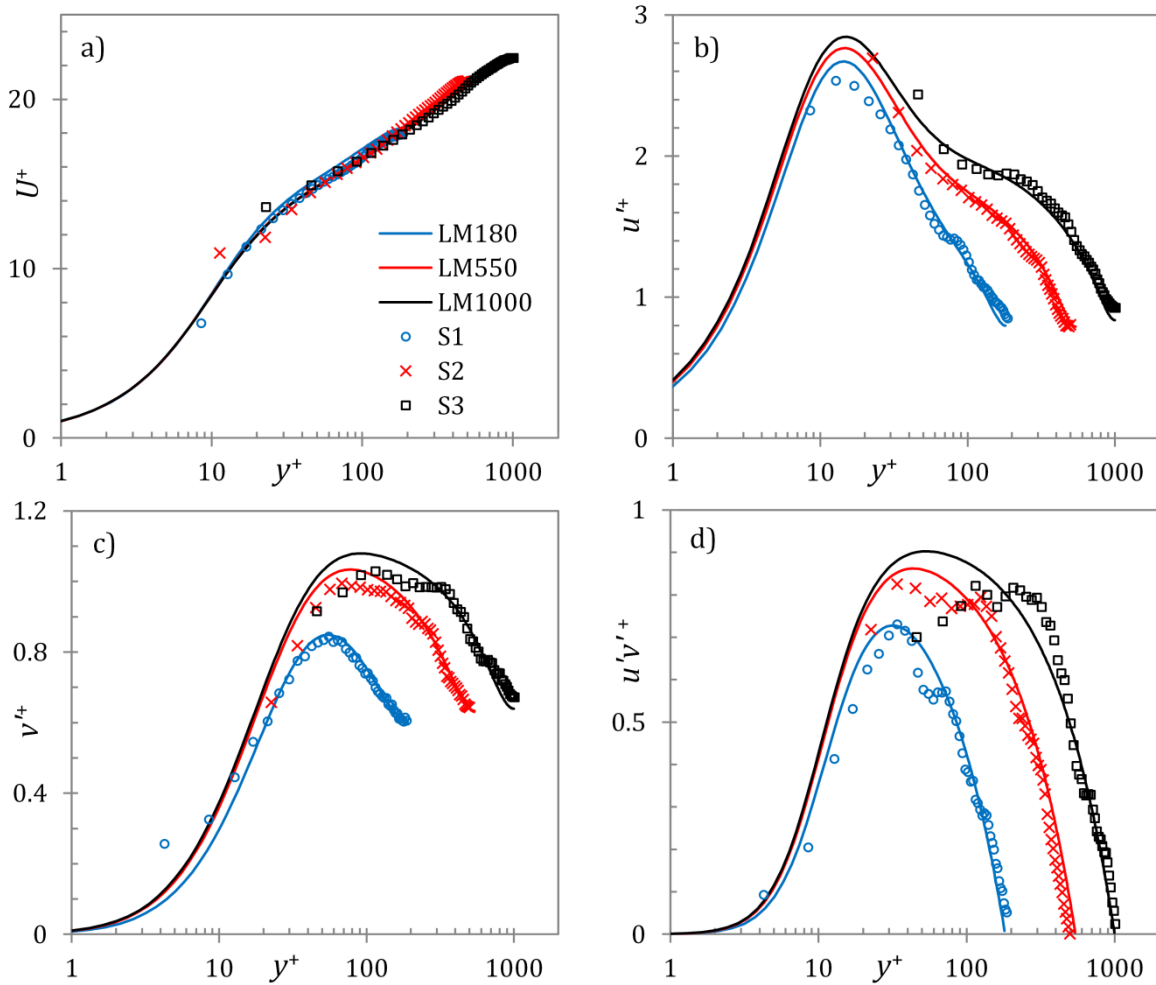


Figure 4.11 Comparison of inner-scaled present experimental data with DNS data of Lee & Moser [158] for steady channel flows at  $Re_b = 2800, 9800$  and  $20100$ .

### 4.5.2 Unsteady Flow Comparison

The transient response of an unsteady flow case is compared with the data of Gorji [60] for repeatability check. In the present unsteady flow case (E1), the flow is accelerated from  $Re_b = 2800$  to  $7400$  by sudden opening of the valve. The flow acceleration time (based on 80% of change in flow) for the case E1 is 1.8 seconds. Figure 4.12 presents a comparison for the transient development of the mean and fluctuating components against the flow case S29-76 of Gorji [60]. In case S29-76, the flow is reported to accelerate from  $Re_b = 2900$  to  $7600$  in 1.35 seconds.

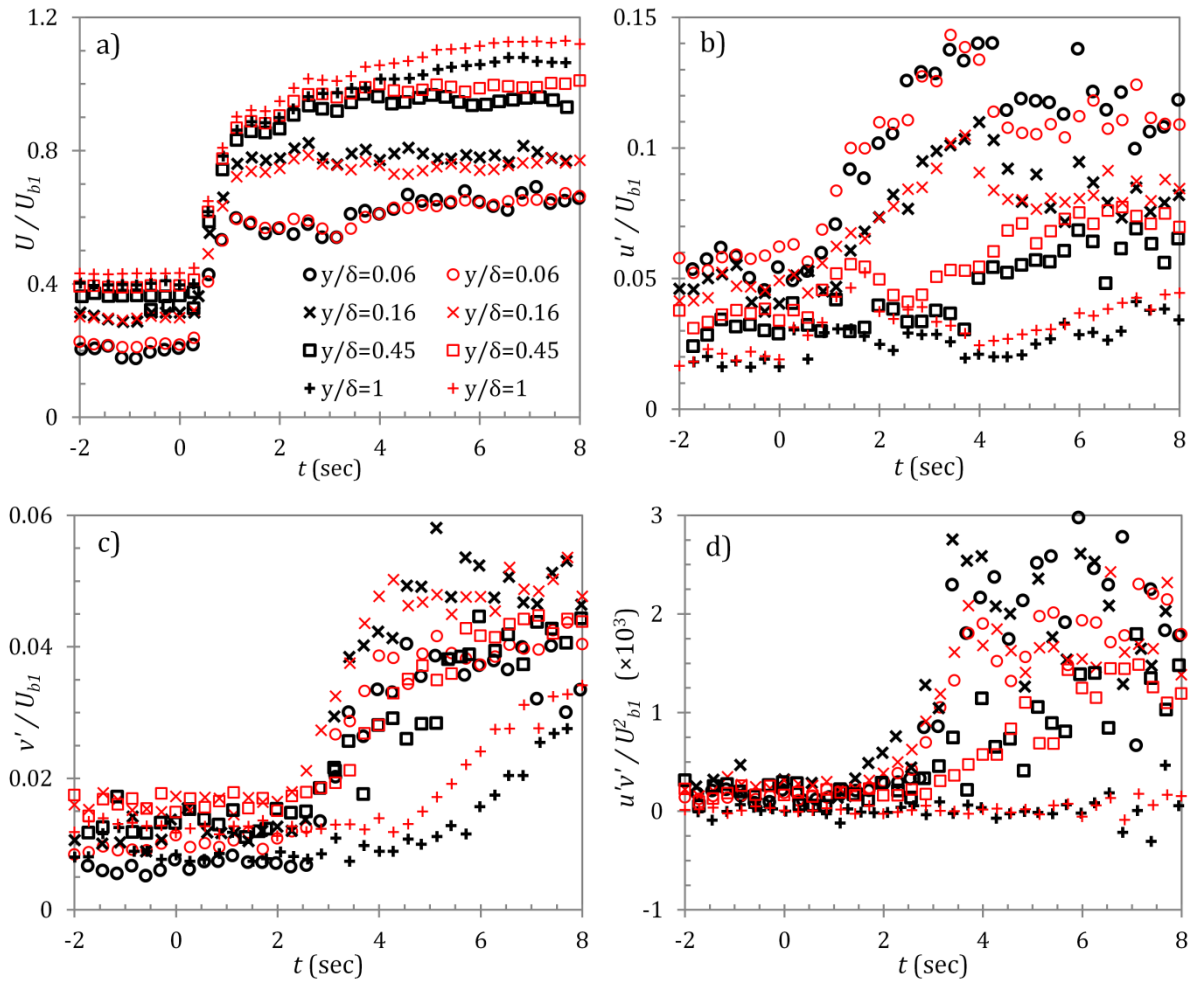


Figure 4.12 Comparison of present unsteady flow case E1 with flow case S29-76 of Gorji [60].

Symbols: Black ( $\circ$ ,  $\times$ ,  $\square$ ,  $+$ ) S29-76; Red ( $\circ$ ,  $\times$ ,  $\square$ ,  $+$ ) E1.

It is seen that the present data closely follows that of S29-76. Slight variations in magnitude and time-scale of responses between E1 and S29-76 may be attributed to the difference in initial and final Reynolds numbers and the flow acceleration time. The similar responses of E1 and S29-76 also provide evidence of reproducibility of unsteady flow using the channel flow loop facility.

Further validation of the present experimental unsteady flow against numerical data is presented in Chapter 6 where three flow cases are compared against the reproduced DNS and LES simulations.

### 4.5.3 Uncertainty in Experimental Data

Experimental uncertainty concerns the error between the measured and the true values, and can be estimated by the *accuracy* and *precision* of the experimental data. The former is a measure of how close the measured values are to the true value, while the latter concerns how two or more measurements agree with each other. In the present experimental investigation, quantification of the accuracy is infeasible as the true values are not known. Nevertheless, present data is compared to benchmark DNS data and other experimental data (as above). Precision of the present experimental data can be measured by calculating the *repeatability* of the flow, defined by the standard deviation of the measured data from multiple readings.

Figure 4.13 presents the repeatability of the bulk velocity ( $U_b$ ) determined using integration of PIV velocity profile data at different Reynolds number flows. Figure 4.13(a) presents the repeatability calculated from 100 image-pairs captured during a 50-second period of steady flow and represents the precision of the PIV measurements technique. It is seen that the values are within 5% for all steady flows. Figure 4.13(b) presents the repeatability calculated from the time-averaged values of 60 separate realizations of the steady flow and represents the precision of the valve in reproducing the same flow. It is seen that the repeatability of almost all steady flows is better than 2%, with better valve performance at higher flow rates.

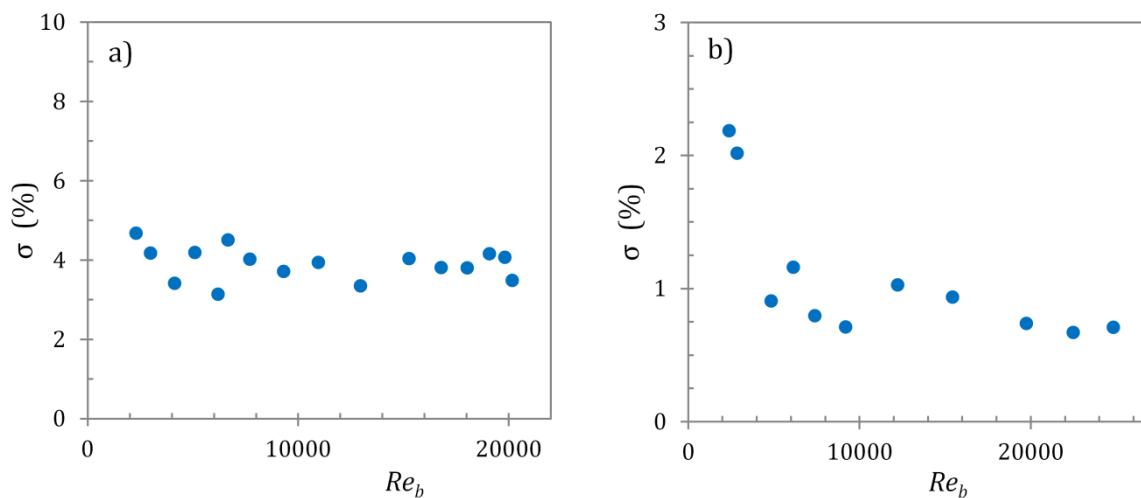


Figure 4.13 Repeatability ( $\sigma$ ) of the bulk velocity of steady flows at different Reynolds numbers for a) single, and b) multiple realizations.

Similarly, precision of the hotfilm measurements can be measured by computing the repeatability of the CTA output. Figure 4.14(a) presents the repeatability of the CTA output for steady flows at different Reynolds numbers, measured from a 100 Hz signal for durations of 60 seconds each. This represents the precision of the measurement technique. It is seen that all values are better than 1%, with higher precision at higher Reynolds numbers. Figure 4.14(b) presents the repeatability calculated from the time-averaged outputs of 10 different realizations of the steady flow and, thus, presents the precision of the CTA in reproducing the output for the same steady flow. The figure shows a poor repeatability for multiple realizations with values ranging from 10%-20%. This is attributed to a drift in the CTA calibration (also shown in Figure 4.9). Thus, as described previously, a universal calibration is not employed herein. A dynamic calibration technique is used instead, which uses separate calibration constants for each repeated realization.

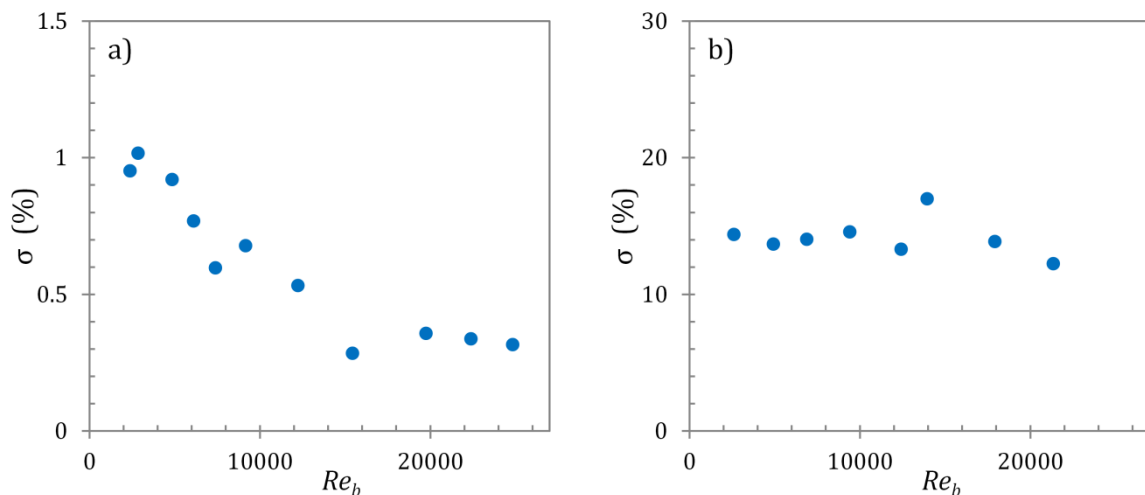


Figure 4.14 Repeatability ( $\sigma$ ) of the CTA output for steady flows at different Reynolds numbers for a) single, and b) multiple realizations.

## Chapter 5

# Large-Eddy Simulation of Step-Accelerating Flows

---

This chapter presents a numerical study of the response of turbulence in high-Reynolds number ratio step-like accelerating channel flows. He & Seddighi [7, 8] and Seddighi *et al.* [59] reported detailed DNS studies of the transitional response of step-like accelerating flows. The Reynolds number ratio of their study ranged from 1.1 to 4.5 (or *initial turbulence intensity* from 15.3% down to 3.8%). The purpose of the present study is to extend the range of Reynolds number ratio using Large-Eddy Simulations (LES) and to investigate its effect on the overall transition process, correlations of the transitional Reynolds numbers and the response of the turbulent quantities.

In §5.1, the simulation cases investigated in the present study are introduced. The behaviour of the instantaneous flow and the trend of flow structures are discussed in §5.2. In §5.3, the correlations of the present transitional Reynolds numbers and their accuracy are discussed. The response of the mean and r.m.s. fluctuating velocities is presented in §5.4. Finally, a summary of investigations undertaken herein is presented in §5.5.

## 5.1 Present Simulation Cases

Simulations are performed for spatially fully-developed turbulent channel flow subjected to a step-like linear acceleration using the in-house LES computational code *CHAPSim\_LES*. As discussed previously in §3.3, the computational code is developed for the purpose of this study, by integration of subgrid-scale models into the DNS code *CHAPSim* [7-9]. For the present investigations, the WALE model of Nicoud & Ducros [152] is used for the calculation of subgrid-scale (SGS) viscosity. Validation of the code and the SGS model is presented in §3.5.

The simulation parameters for the cases studied are presented in Table 5.1. Also presented in the table are the DNS cases of He & Seddighi [7, 8] (referred to as HS13 and HS15, respectively) for comparison. The first two cases, U1 and U2, reproducing the DNS cases of HS13 and HS15, are used to validate the present LES results (validation presented in §3.5.3). Further four cases are designed with increasing final Reynolds numbers. The *Re*-ratio for the present flow cases increases from 6.5 for case U3 to 19.3 for case U6; and thereby, decreases the *initial turbulence intensity* (defined in §5.3) from 2.6% for case U3 down to 0.9% for case U6.

Case	$Re_0$	$Re_1$	$\frac{Re_1}{Re_0}$	$Tu_0$	Grid	$L_x/\delta$	$L_z/\delta$	$\Delta x^{+1}$	$\Delta z^{+1}$	$\Delta y_c^{+1}$
HS13	2825	7404	2.6	0.065	$512 \times 200 \times 200$	12.8	3.5	11	7	7
HS15	2800	12600	4.5	0.038	$1024 \times 240 \times 480$	18	5	12	7	10
U1	2825	7400	2.6	0.065	$192 \times 128 \times 160$	12.8	3.5	28	9	13
U2	2825	12600	4.5	0.038	$450 \times 200 \times 300$	18	5	26	11	13
U3	2825	18500	6.5	0.026	$1200 \times 360 \times 540$	24	5	19	9	10
U4	2825	25000	8.8	0.019	$2400 \times 360 \times 360$	48	3	24	10	13
U5	2825	35000	12.4	0.014	$2400 \times 360 \times 360$	48	3	32	13	18
U6	2333	45000	19.3	0.009	$2400 \times 360 \times 360$	72	3	60	17	22

Table 5.1. Present accelerating flow cases with the DNS cases of He & Seddighi [7, 8] for comparison.

The spatial resolution provided in the table is in the wall units of the final flow. Multiple realizations are performed for each case, each starting from a different initial flow field. The spatial resolution of the cases U3-U5 resembles that of the LES validation cases, U1 and U2. However, due to limited computational resources, the resolution of the case U6 is restricted to lower values. It is expected that the basic physical phenomena and the trend of transition is captured despite the lower spatial resolution. In this chapter, the discussion is primarily focussed on the comparison between cases U3 and U6 to illustrate the effect of high  $Re$ -ratio. However, some quantitative features of other flow cases are also presented to facilitate the discussion.

Cases U3-U6 are repeated with different domain lengths to ensure that there is a minimal effect of the domain length on the physical process. This has been demonstrated later in §5.3. Case U3 is repeated with a domain length of  $18\delta$ ; cases U4 and U5 each with lengths  $18\delta$  and  $24\delta$ ; and case U6 with  $18\delta$ ,  $24\delta$  and  $48\delta$ . Table 5.2 presents the parameters employed for the additional simulations using the different domain lengths.

Case	Grid	$L_x/\delta$	$L_z/\delta$	$\Delta x^{+1}$	$\Delta z^{+1}$	$\Delta y_c^{+1}$
U3	$648 \times 300 \times 450$	18	5	26	10	12
U4	$900 \times 360 \times 540$	18	5	24	11	13
	$1200 \times 360 \times 540$	24	5	24	11	13
U5	$900 \times 360 \times 540$	18	5	32	15	18
	$1200 \times 360 \times 540$	24	5	32	15	18
U6	$900 \times 360 \times 540$	18	5	41	19	22
	$1200 \times 360 \times 540$	24	5	41	19	23
	$2400 \times 360 \times 360$	48	3	41	17	22

Table 5.2. Simulation parameters for additional simulations of cases U3-U6.

## 5.2 Instantaneous Flow Response

The flow structures at several time instants during the transient period for cases U3 and U6 are presented in Figure 5.1 using the iso-surface plots of  $u'/U_{b0}$  and  $\lambda_2/(U_{b0}/\delta)^2$ . Here, the blue and green iso-surfaces are the positive and negative streamwise velocity fluctuations,  $u'$  ( $= u - \bar{u}$ ); and red iso-surfaces are vortical structures represented by  $\lambda_2$ , where  $\lambda_2$  is the second largest eigenvalue of the symmetric tensor  $S^2 + \Omega^2$ ,  $S$  and  $\Omega$  are the symmetric and anti-symmetric velocity gradient tensor  $\nabla u$ . Figure 5.1(a) shows instantaneous plots in the entire domain size ( $24\delta \times 5\delta$  in X-Z direction) for case U3. However, due to space constraints, only one-third of the domain length of case U6 ( $24\delta \times 3\delta$  in X-Z directions) is presented in Figure 5.1(b). Also presented in the insets are the developments of the friction coefficient for the corresponding wall for a single realization of case U3 and U6. The symbols indicate the time instants for which the instantaneous plots are shown. The critical times of onset and completion of transition are clearly identifiable from the development of the friction coefficient (He & Seddighi [7]). The time of minimum friction coefficient approximately corresponds to the appearance of first turbulent spots and, hence, the onset of transition; while the time of first peak corresponds to a complete coverage of wall with newly generated turbulence and, hence, the completion time.

It is seen that the response of the transient flow is essentially the same as that described in He & Seddighi [7, 8] – a three stage response resembling the bypass transition of boundary layer flows. In the initial flow (at  $t^{+0} = 0$ ), patches of high- and low-speed fluctuating velocities and vortical structures are seen, representative of a typical turbulent flow. In the early period of the transient (at  $t^{+0} \sim 20$ ), elongated streaks are formed, represented by alternating tubular structures of iso-surfaces of positive and negative  $u'/U_{b0}$ . These structures are similar to those found in the pre-transition regions of the boundary layer flow (Jacobs & Durbin [64]; Matsubara & Alfredsson [84]). The number of vortical structures is also seen to reduce during this stage. Further at  $t^{+0} \sim 40$ , it is seen that the streak structures are further stretched and become

stronger. It is noted that in the higher Reynolds number-ratio case, the streaks appear stronger and longer; and the vortical structures appear to reduce by a greater extent – a trend also reported in He & Seddighi [8]. New vortical structures start to appear at  $t^{+0} \sim 65$ , representing burst of turbulent spots which signify the onset of transition. Afterwards, these turbulent spots grow with time to occupy more wall surface and eventually cover the entire domain when the transition is seen to have completed. It is again observed that the number of the initial turbulent spots at the start of transition seem to be more scarce for case U6 and some of the streaks extend for longer portions of the domain. Thus, the present domain lengths are sufficiently increased to reduce any effect of the domain size in the higher Reynolds-number ratio cases. This is further demonstrated later in the next section.

In order to visualise the instability and breakdown occurring in the low-speed streak, the site of the initial turbulent spot for case U3 is traced back in time with a sliding window (of size  $38 \times 18$  in the X-Z direction) which follows the event in the domain during the late pre-transition and early transitional period. Visualisations of 3D iso-surface structures inside this window are presented in Figure 5.2 at several time instants during this period. It is seen that for the most part of the pre-transition period the pictured low-speed streak undergoes elongation and enhancement. At about halfway during pre-transition period, the streak begins to develop an instability, similar to the sinuous instability of boundary-layer transitional flows (Brandt *et al.* [75, 78, 175]; Schlatter *et al.* [76]). This type of instability is reported to be driven by the spanwise inflections of the mean flow and is characterised by antisymmetric spanwise oscillations of the low-speed streak (Swearingen & Blackwelder [70]). In the late pre-transitional period (about  $t^{+0} = 57.3$ ), the streak appears to break down accompanying the generation of some vortical structures. Afterwards, bursts of turbulent structures appear surrounding the streak site, which continue to grow in size and soon outgrow the size of the window.

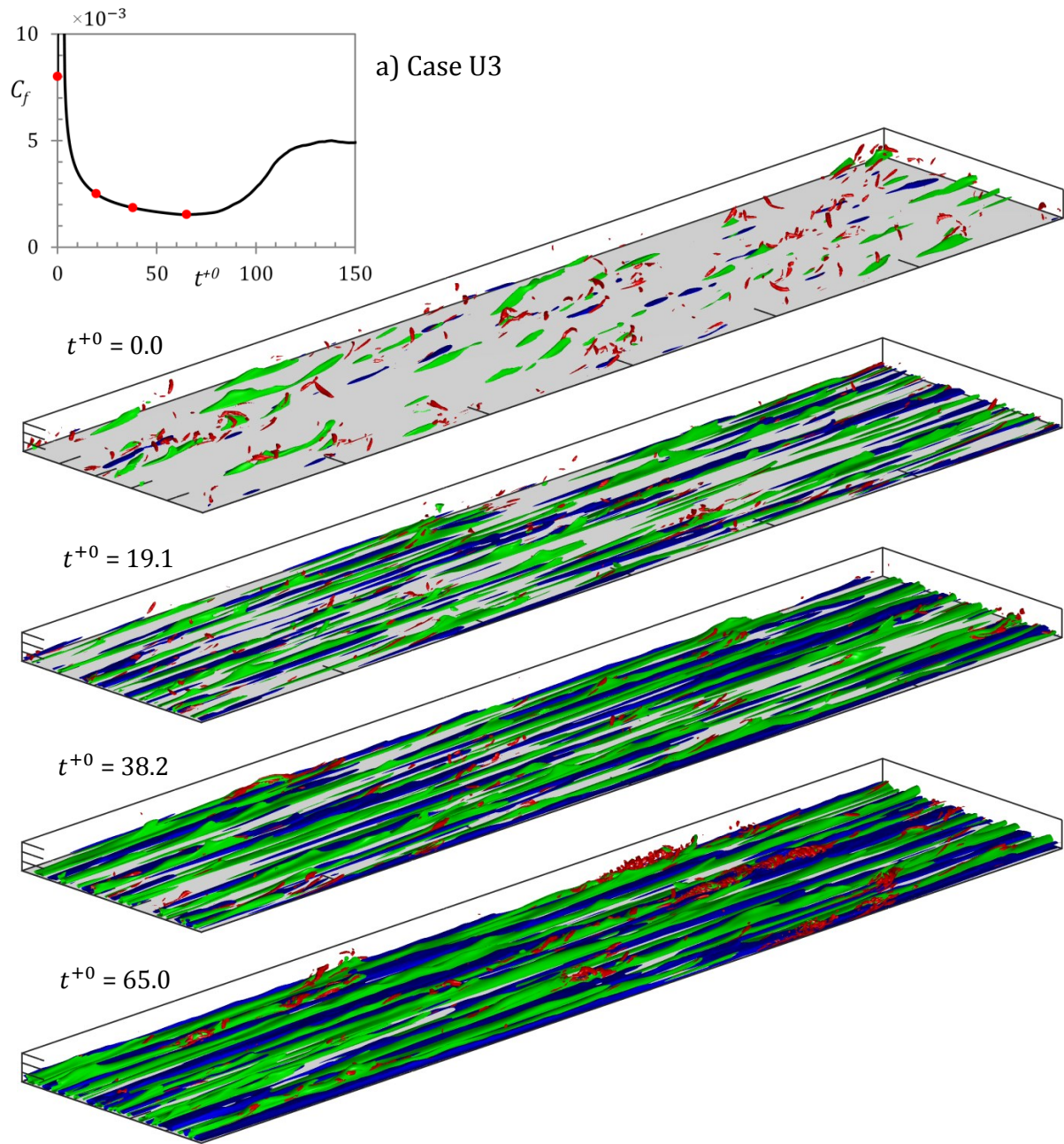
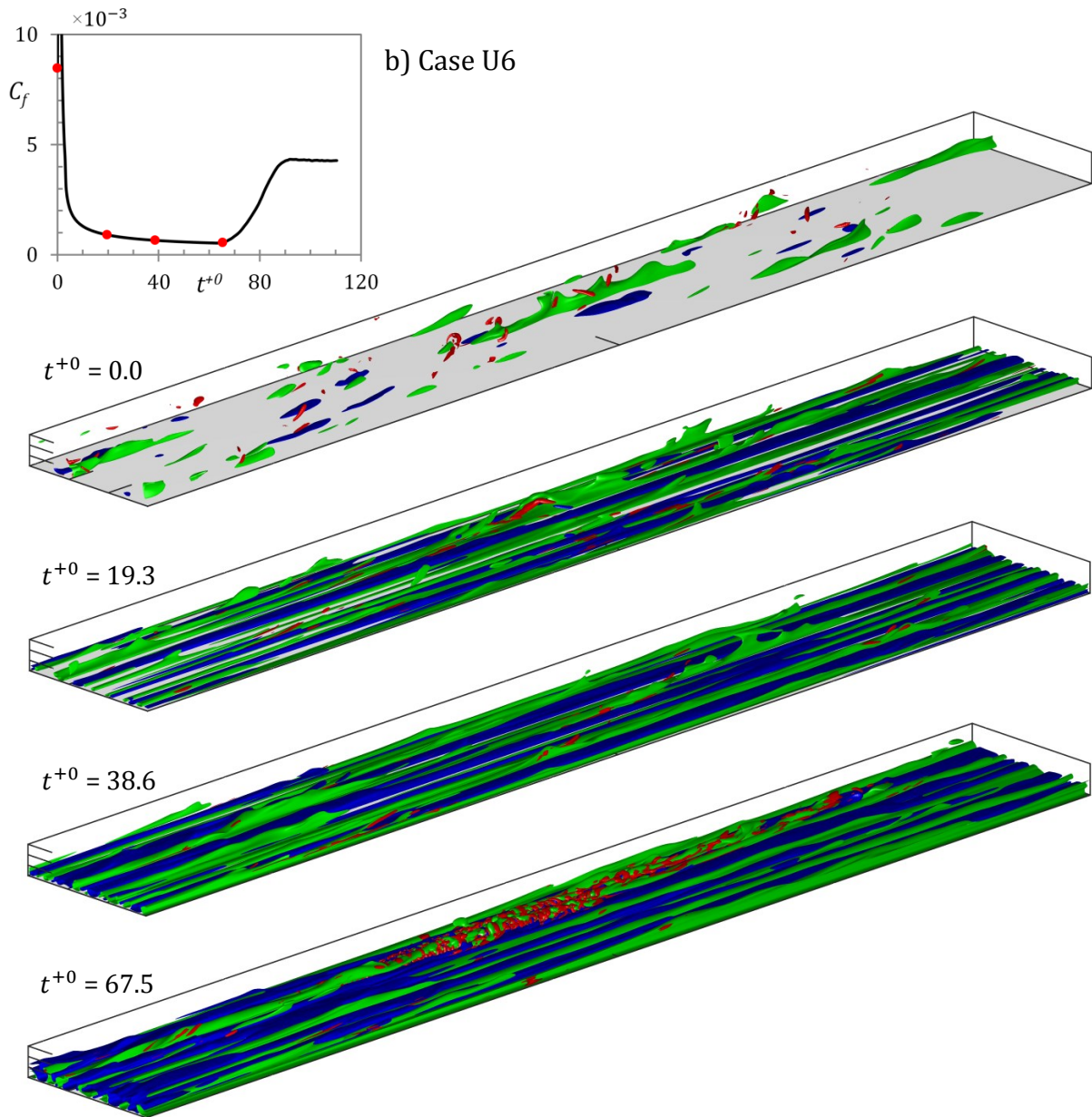


Figure 5.1. Three dimensional isosurfaces for cases (a) U3 and (b) U6. Streak structures are shown in blue/green with  $u'/U_{b0} = \pm 0.35$  and vortical structures are shown in red with  $\lambda_2/(U_{b0}/\delta)^2 = -5$ .



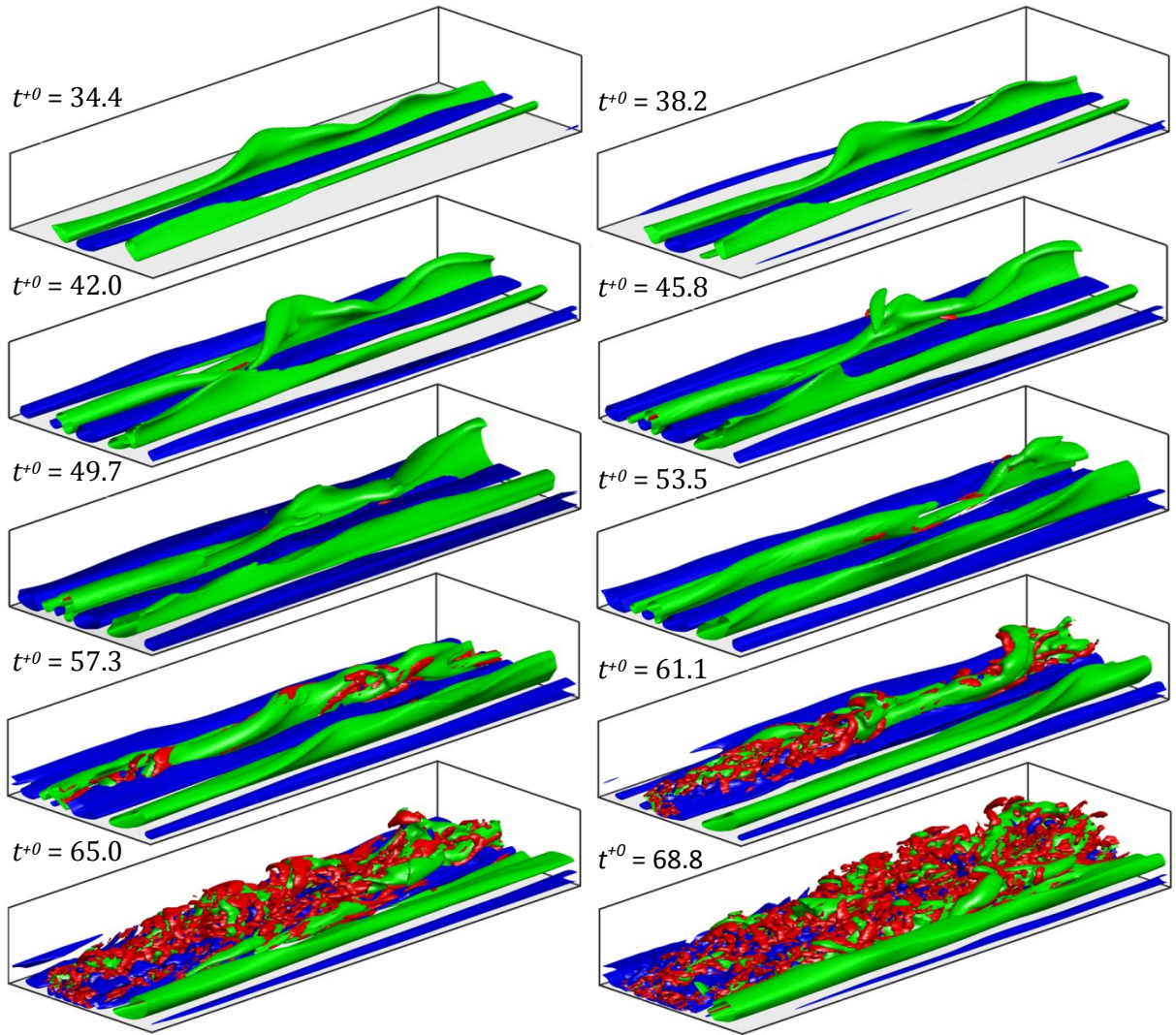


Figure 5.2. Visualization of streak instability and breakdown in case U3 using a sliding window. 3D iso-surface streak structures are shown in blue/green with  $u'/U_{b0} = \pm 0.65$ , and vortical structures are shown in red with  $\lambda_2/(U_{b0}/\delta)^2 = -80$ .

Overall, it is seen that the features of the transition process become more striking in case U6 than that in U3. Quantitative information about streaks can be obtained by the correlations of the streamwise velocity ( $R_{11}$ ). Correlations in the streamwise direction provide a measure of the length of the streaks, whereas those in the spanwise direction provides indication of the strength and the spacing between streaks. Figure 5.3 presents these correlations for case U3 (a,b) and U6 (c,d) in the streamwise (a,c) and spanwise directions (b,d). It can be seen from the initial flows (at  $t^+ = 0$ ) of both cases that the length of the streaks (given by the streamwise correlations) is about 800 wall units (based on the initial flow) and the location of minimum spanwise correlations is 50 wall units, implying that the spacing of streaks is about 100 wall

units. This is representative of a typical turbulent flow. After the start of the transient, these streaks are stretched in the streamwise direction. It is seen that until the end of the pre-transitional period (at  $t^{+0} = 70 - 80$ ), the streaks are stretched to a maximum of 1200 wall units in case U3, whereas to 3000 wall units in case U6. During this time, the spacing between the streaks is reduced to about 75 wall units in case U3, and to 56 wall units in case U6. The minimum value of the spanwise correlations provides an indication of the strength of the streaks. It is clearly seen that this value is lower for case U6 in comparison to that in U3, implying that the streaks are likely to be stronger in U6. Thus, the streaks in the pre-transitional stage of case U6 are much longer, stronger and more densely packed than those in case U3.

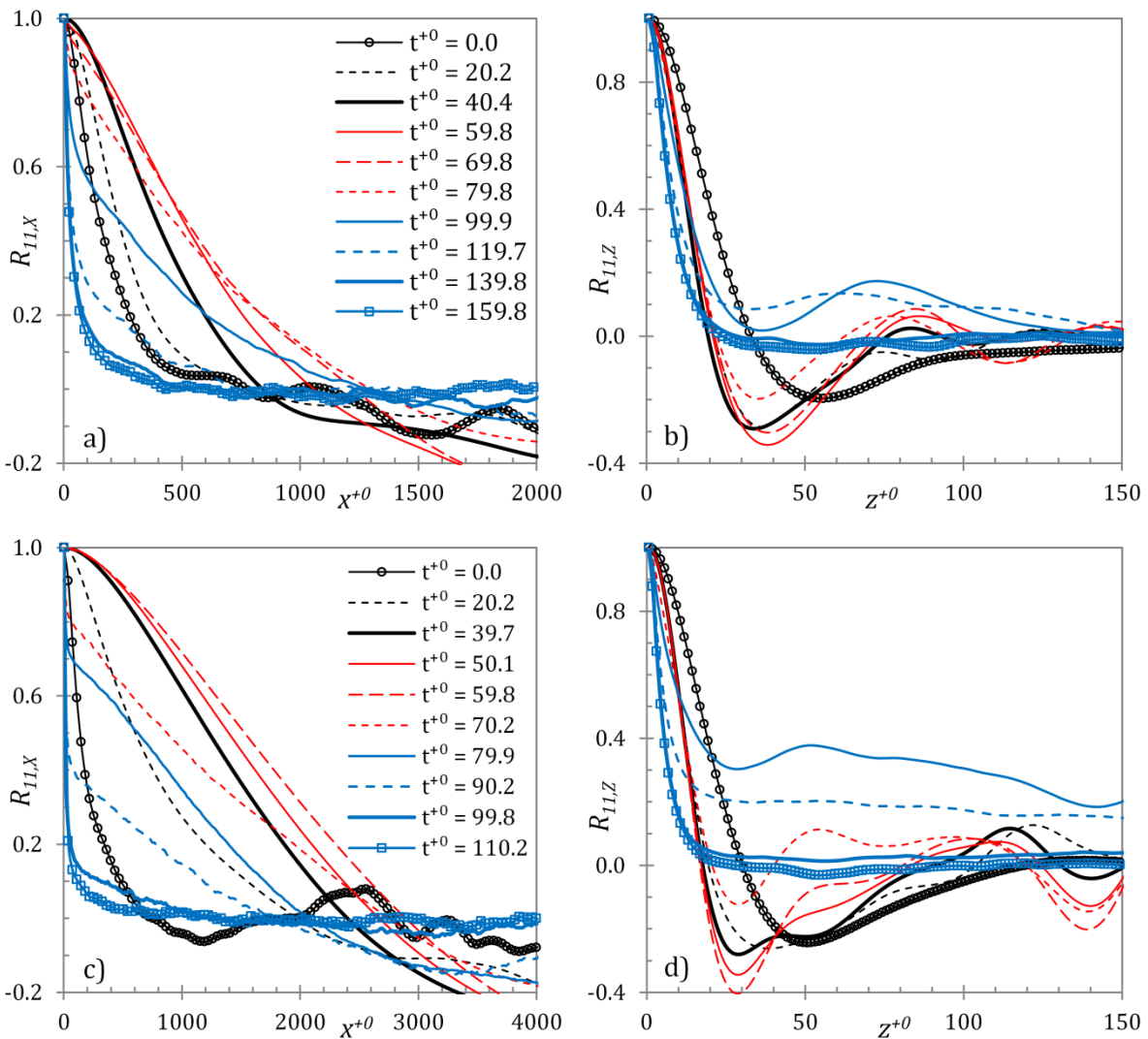


Figure 5.3. Streamwise velocity autocorrelations at several time instants during the transient for case U3 (a, b) and U6 (c, d) in the streamwise (a, c) and spanwise directions (b, d) at  $y^{+0} = 10$ .

The near wall vortical structures were visualised by the  $\lambda_2$ -criterion in Figures 5.1-5.2 earlier. The same criterion can also be used to get some quantitative information about these structures. Jeong & Hussain [176] noted that  $\lambda_2$  is positive everywhere outside a vortex core and can assume magnitudes comparable to the vortical  $-\lambda_2$  values. Jeong *et al.* [177] showed that due to significant cancellation of negative and positive regions of  $\lambda_2$  in the buffer region, a spatial mean  $\langle \lambda_2 \rangle$  was an ineffective indicator of the vortical events. It was reported that the r.m.s. fluctuation of  $\lambda_2$ ,  $\lambda'_{2,rms}$ , shows a peak value at  $y^+ \sim 20$ , indicating prominence of vortical structures in the buffer region. Hence, the maximum value of  $\lambda'_{2,rms}$  can be used to compare the relative strength of these structures in the flow. Figure 5.4 shows the variation of  $(\lambda'_{2,rms})_{max}$  during the transient for the cases U3 and U6. Here,  $(\lambda'_{2,rms})_{max}$  is normalised by the initial bulk velocity,  $U_{b0}$ , and channel half-height,  $\delta$ . It can be seen that in the early period of the transient, the value of  $(\lambda'_{2,rms})_{max}$  increases abruptly during the excursion of the flow acceleration (till  $t^{+0} \sim 3$ ). This is attributed to the straining of near-wall velocity due to the imposed flow acceleration resulting in distortion of the pre-existing vortical structures and, hence, high fluctuations of  $\lambda_2$ . After the acceleration, the values are seen to gradually reduce, which signifies the breakdown of equilibrium between the near-wall turbulent structures and the mean flow. The formation of a high shear boundary layer due to the imposed acceleration causes the high-frequency disturbances to damp and shelters the small structures from the free-stream turbulence. This phenomenon of disruption of the near-wall turbulence is referred to as the *shear sheltering* (Hunt & Durbin [178]). Later in the late pre-transition stage,  $(\lambda'_{2,rms})_{max}$  begins to increase gradually as the new structures begin to form. At the onset of transition, this value increases rapidly due to burst of turbulent spots and generation of new turbulent structures in the flow. The rate of increase of  $(\lambda'_{2,rms})_{max}$  can be used to indicate the strength of turbulence generation. It is clearly seen that the rate is higher for case U6, implying a stronger rate of turbulence generation in comparison to case U3.

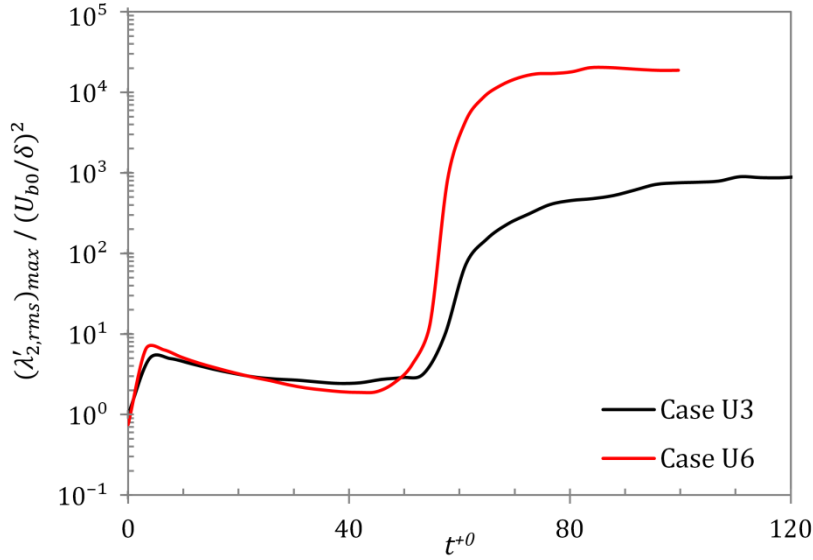


Figure 5.4. Time development of  $(\lambda'_{2,rms})_{max}/(U_{b0}/\delta)^2$  for cases U3 and U6.

This trend is similar to that observed in He & Seddighi [8]. Therein, the higher  $Re$ -ratio cases showed a distinct and clear transition process, but the transition of the lowest-ratio case was indiscernible from the instantaneous visualisations. Here, it is seen that as the  $Re$ -ratio is increased further (larger than those in He & Seddighi [8]), the features of the transition appear to be more striking and prominent. The streaks in the pre-transitional stage are longer and stronger, and are more densely packed, and after the onset of transition the generation of turbulence is stronger.

### 5.3 Correlations of Flow Transition

It has previously been shown by He & Seddighi [8] that the initial turbulence intensity, equivalent to the free-stream turbulence intensity of boundary layer flows, is of significant importance in transient flow transition. The initial turbulence intensity was described as the ratio of the peak turbulence of the initial flow the velocity of the final flow. Thus, the definition of turbulence intensity reads,

$$Tu_0 = \frac{(u'_{rms,0})_{max}}{U_{b1}} \quad (5.1)$$

Noting that the maximum turbulence intensity was a function of Reynolds number,  $(u'_{rms})_{max}/U_b \propto (Re)^{-0.1}$ , the definition of (5.1) can be re-formulated as [8],

$$Tu_0 \approx 0.375 \frac{U_{b0}}{U_{b1}} (Re_{b0})^{-0.1} \quad (5.2)$$

He & Seddighi [8] introduced another concept of equivalent Reynolds number for unsteady flows, which corresponds to the Reynolds number  $Re_x (= xU_\infty/\nu$ , where  $x$  is the distance from the leading edge, and  $U_\infty$  is the free-stream velocity) of boundary layer flows. Noting that the final bulk velocity is the characteristic convective velocity in the step-like unsteady flows, the equivalent characteristic length was re-defined as  $x = tU_{b1}$ . Hence, the equivalent Reynolds number for unsteady flows reads,

$$Re_t = \frac{tU_{b1}^2}{\nu} \quad (5.3)$$

It was demonstrated by He & Seddighi [8] that although these two Reynolds numbers cannot be quantitatively compared,  $Re_t$  has the same significance in the unsteady flow transition as  $Re_x$  has in boundary layer transition. The critical Reynolds number for boundary layer transitional flows shows a strong dependence on turbulence intensity. He & Seddighi [7] noted that the time of minimum friction coefficient corresponds to the time of the generation of initial turbulent spots, and hence the onset of transition. Thus, a critical time of onset of transition ( $t_{cr}$ ) can be obtained from the friction coefficient development and used to calculate an equivalent critical Reynolds number,  $Re_{t,cr} = t_{cr}U_{b1}^2/\nu$ , where  $U_{b1}$  is the bulk velocity of the final flow. The equivalent critical Reynolds number was shown to have a striking correlation with the initial turbulence intensity. The reported DNS flow cases were shown to be represented by the relation,

$$Re_{t,cr} = 1340 Tu_0^{-1.71} \quad (5.4)$$

Figure 5.5 shows the relation between the equivalent critical Reynolds number and the initial turbulence intensity for the present high  $Re$ -ratio LES cases and the DNS cases of He & Seddighi

[8] for comparison. The present data follows the equation (5.4) established from the higher turbulence intensity cases. However, the lower turbulent intensity cases, namely cases U5 and U6, are seen to diverge from this relation, with transition occurring at higher  $Re_t$  values. The low grid resolution for the higher  $Re$ -ratio cases may be a possible reason for this divergence. Alternatively, there could potentially be a slightly different physical process at play for these low- $Tu_0$  cases.

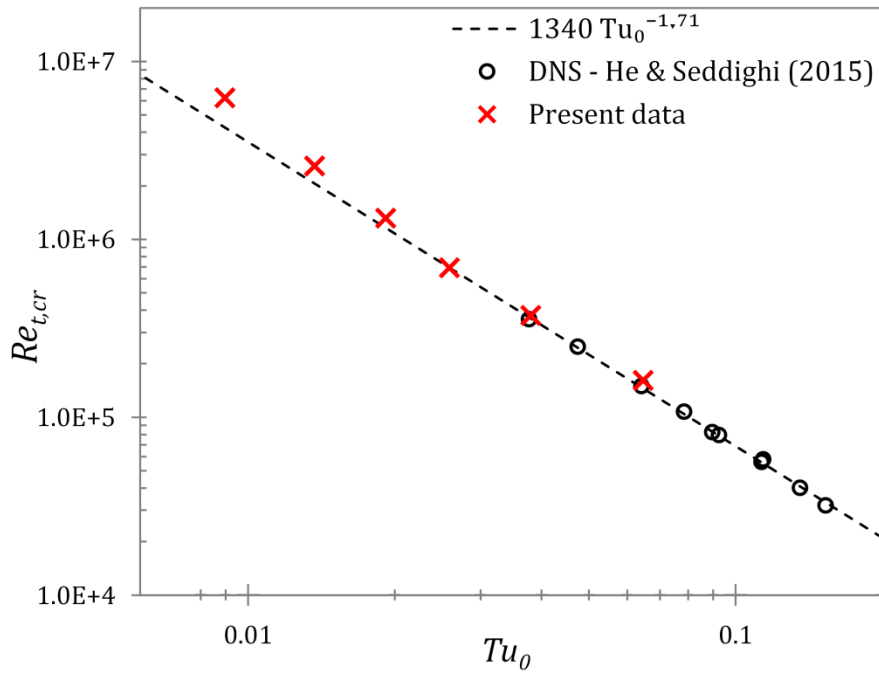


Figure 5.5. Dependence of equivalent critical Reynolds number on initial turbulence intensity.

The transition period is another important feature of transient flow transition, shown to be equivalent to the transition length of boundary layer flows [8]. The transition length of boundary layer flows is defined as the difference between the initial and final states of a transitional flow, that is as,

$$\Delta Re_{x,cr} = Re_{x,\gamma_2} - Re_{x,\gamma_1} \quad (5.5)$$

where  $\gamma$  is the level of intermittency,  $\gamma = 1$  resembling a fully turbulent flow and  $\gamma = 0$  resembling a laminar state. Researchers have used different values for the intermittency levels,  $\gamma_1$  and  $\gamma_2$ , to define the transition length. Notably, Narasimha *et al.* [86] used intermittency

levels  $\gamma_1 = 0.1$  and  $\gamma_2 = 0.9$ ; while Fransson *et al.* [85] used  $\gamma_1 = 0.25$  and  $\gamma_2 = 0.75$ . The transition length for boundary layer flows has been shown to be strongly correlated with  $Re_{x,\gamma=0.5}$ , which represents the flow at the halfway of transition process. Narasimha *et al.* [86] suggested the following power-law relationship between the two,

$$\Delta Re_{x,cr} = 9 Re_{x,\gamma=0.5}^{0.75} \quad (5.6)$$

More recently, Fransson *et al.* [85] proposed an alternative linear relation between the two,

$$\Delta Re_{x,cr} = 3.9 \times 10^4 + 0.33 Re_{x,\gamma=0.5} \quad (5.7)$$

In unsteady flow transition, friction coefficient development can also be used to determine the time of completion of the transition process ( $t_{turb}$ ). He & Seddighi [7] noted that time of recovery of friction coefficient corresponds to the time where the entire wall surface is covered by newly generated turbulence. Thus, by assuming that the transition is complete when the friction coefficient reaches its first peak, a transition period can be obtained as  $\Delta t_{cr} = t_{turb} - t_{cr}$ . The relation between the equivalent transition period Reynolds number ( $\Delta Re_{t,cr} = \Delta t_{cr} U_{b1}^2 / \nu$ ) and the critical Reynolds number is presented in Figure 5.6. Also shown in the figure for comparison are the boundary layer transition correlations; and the data for DNS cases of He & Seddighi [8]. In order to make appropriate comparisons,  $Re_{x,\gamma=0.5}$  of boundary layer flows, which represents halfway of transitional length, have been replaced by  $Re_{x,cr} + 0.5\Delta Re_{x,cr}$ .

It is seen that, similar to the findings of He & Seddighi [8], the present data is reasonably well predicted by the boundary layer correlations if a factor of 0.5 is applied to the present  $\Delta Re_{t,cr}$ . However, the present data seem to suggest a power-relation between  $\Delta Re_{t,cr}$  and  $Re_{t,cr}$ , similar to that of Narasimha *et al.* [86]. A best-fit curve to the present data gives the relation,  $\Delta Re_{t,cr} = 9.63 Re_{t,cr}^{0.82}$  (also plotted in the figure).

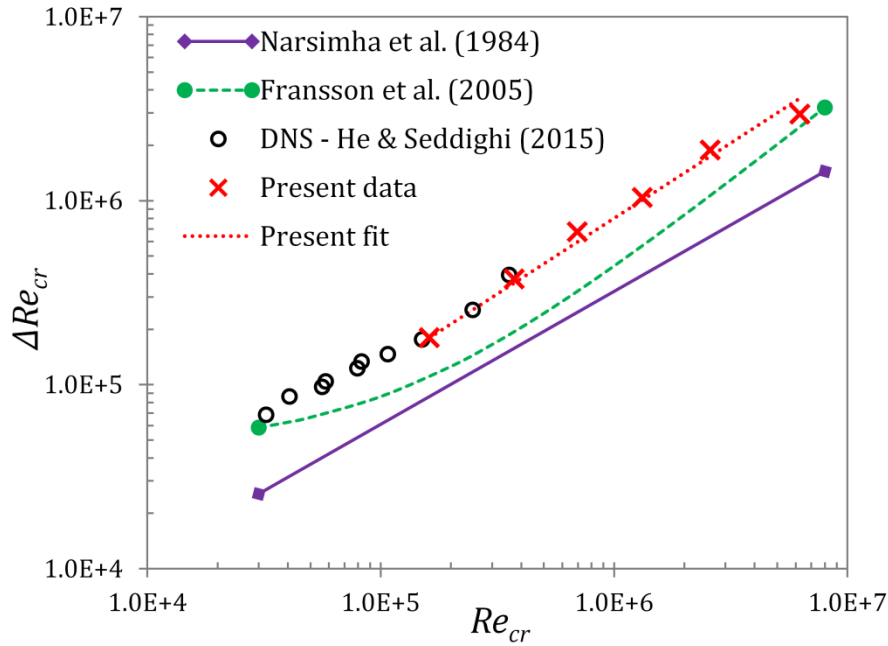


Figure 5.6. Relationship between the transition period Reynolds number critical Reynolds number.

### 5.3.1 Uncertainty in the Predictions of the Transitional Reynolds Numbers

The generation of turbulent spots is to some extent dependent on the initial flow structures. Due to this, the time and spatial position at which the generation of turbulent spots occurs can vary with different initial flow fields for any particular run of a transient flow. Thus, multiple realizations have been performed for each flow case, each starting from a different initial flow field to arrive at an average critical and transition period Reynolds numbers. It is observed that there are large deviations in prediction of the critical Reynolds number for different realizations, and for the top and bottom walls of a single realization for the present cases. Friction coefficient histories for both walls of different realizations for cases U3-U6 are presented in Figure 5.7. It is seen that the deviations in the prediction of the critical time are larger for the higher  $Re$ -ratio case. The deviations of the critical Reynolds number for the present cases are found to be linearly proportional to the average value. As shown in Figure 5.8, the r.m.s. of fluctuation of the critical Reynolds numbers is roughly 10% of the average value.

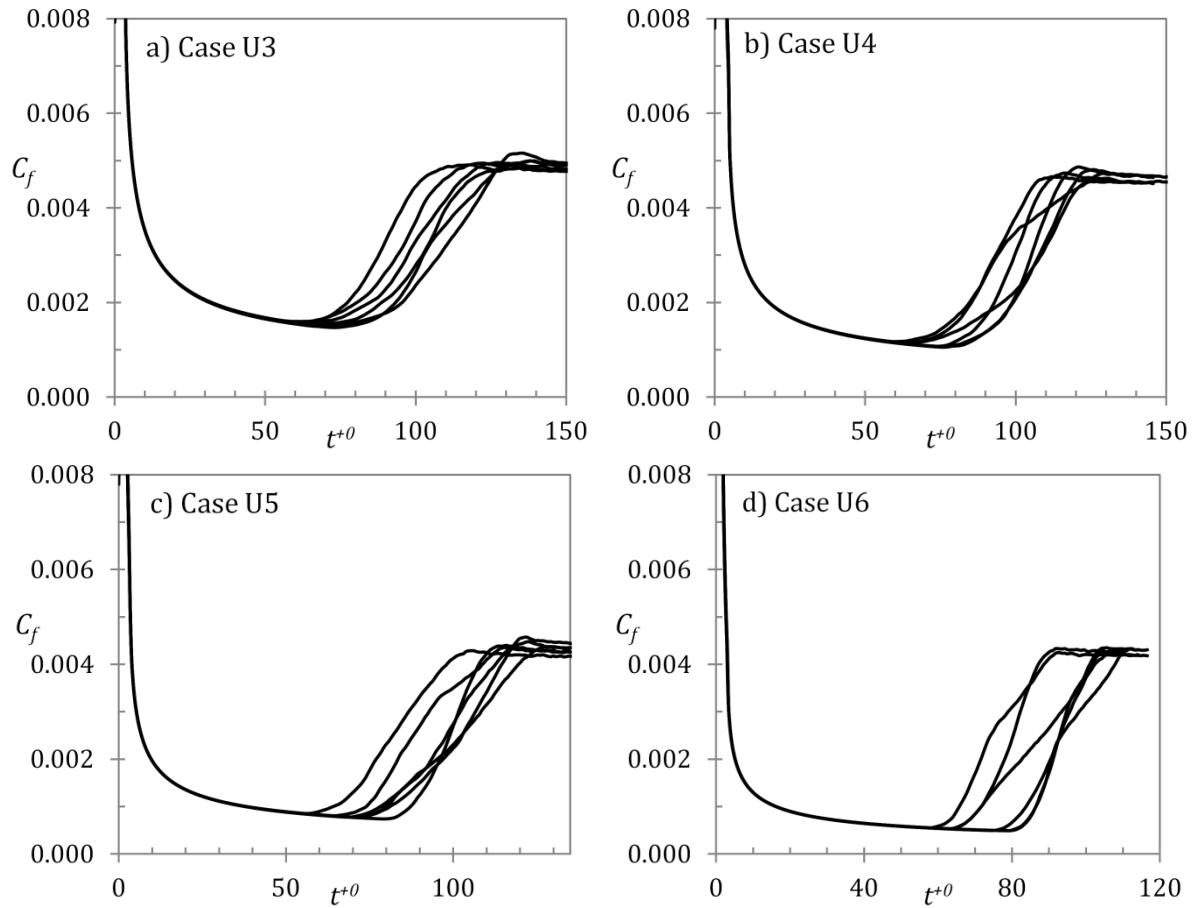


Figure 5.7. Deviations in friction coefficient development for multiple realizations for flow cases U3-U6.

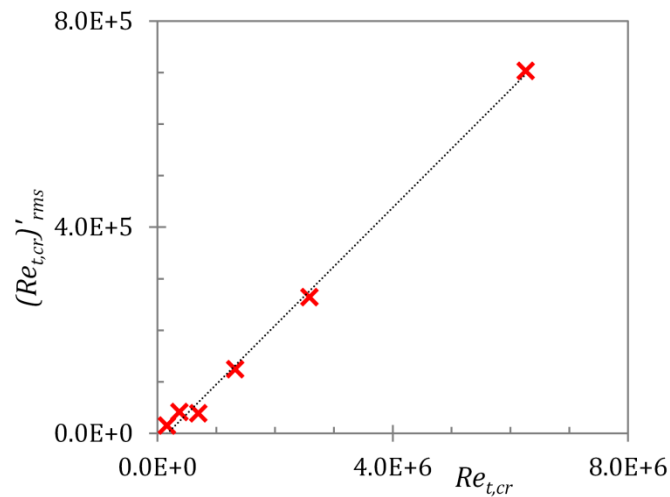


Figure 5.8. Deviations observed in the equivalent critical Reynolds number.

The present higher  $Re$ -ratio cases (namely, case U3-U6) are also simulated with different domain lengths to see its effect on the onset of transition and the deviations observed in its predicted critical time. Case U3 was performed with two different domain lengths – 18 $\delta$  and

24 $\delta$ ; cases U4 and U5 each with three lengths – 18 $\delta$ , 24 $\delta$  and 48 $\delta$ ; whereas, case U6 with four different lengths – 18 $\delta$ , 24 $\delta$ , 48 $\delta$  and 72 $\delta$ . The simulation parameters for these simulations are presented in Tables 5.1-5.2. It should be noted that the spatial resolution for different domain lengths of each case was kept roughly the same so that an appropriate comparison can be made. Figure 5.9 presents the friction coefficient histories for both walls of every realization for cases U3 and U6.

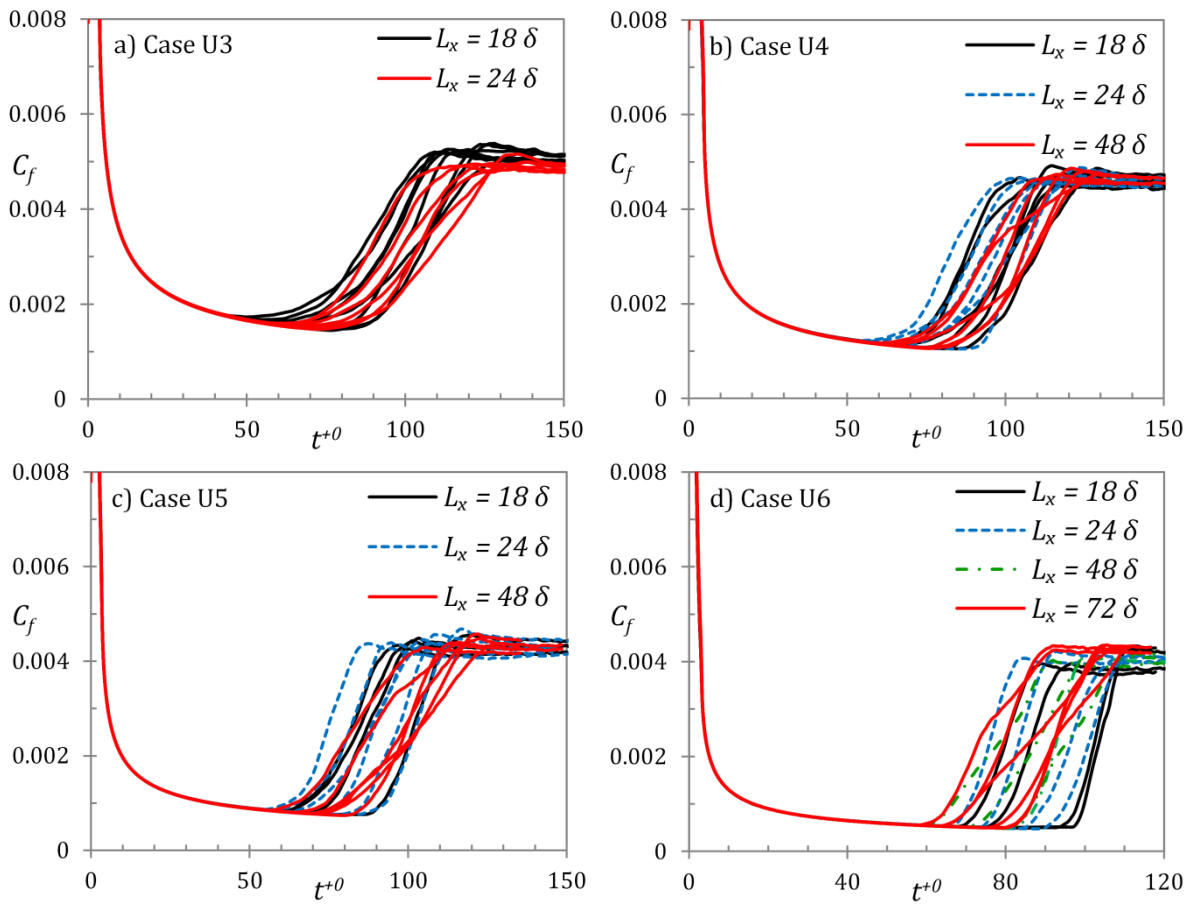


Figure 5.9. Friction coefficient developments using different domain lengths for cases U3-U6.

It is observed that as the domain length is increased, the spread of deviations of  $Re_{t,cr}$  for multiple realizations is slightly decreased. For case U6, the spread of deviations for the two larger domain lengths is almost identical. Hence, it can be deduced that the effect of domain lengths is very small for the two larger domains. The average critical Reynolds numbers, their

r.m.s. deviations and their relationship with average transition period Reynolds number, for different domain lengths of cases U3-U6 are presented in Figures 5.10(a), (b) and (c), respectively. It is clearly seen that for case U6, as the domain length is increased the critical Reynolds number is slightly decreased. This is expected as with an increase in domain size, a larger section of flow field is simulated posing a higher probability of breakdown of stable flow structures in the pre-transitional stage. This effect is only significant for cases where the initial spots are sparse, which occurs in high  $Re$ -ratio flows. The percentage change in  $Re_{t,cr}$  due to increase in domain length for the largest lengths in each case is less than 5%. It is seen the deviations in prediction of critical Reynolds number,  $(Re_{t,cr})'_{rms}$ , also decreases with increase in domain length, signifying better suitability of the larger domains over the smaller ones. For the largest-domain simulation of each flow case,  $(Re_{t,cr})'_{rms}$  is roughly 10% of  $Re_{t,cr}$ . However, it is noted that the  $(Re_{t,cr})'_{rms}$  value for case 'U6 –  $L_x=18\delta$ ', as seen in Figure 5.10(b), is much higher ( $\sim 15\%$  of  $Re_{t,cr}$ ) in comparison to that of the other cases. This can be attributed to the insufficiency of the domain length ( $18\delta$ ) for that particular flow case. The transitional period Reynolds number,  $\Delta Re_{t,cr}$ , is seen to increase with the increase of domain length. But this is expected, as larger domains take a longer time period to be covered with newly generated turbulence.

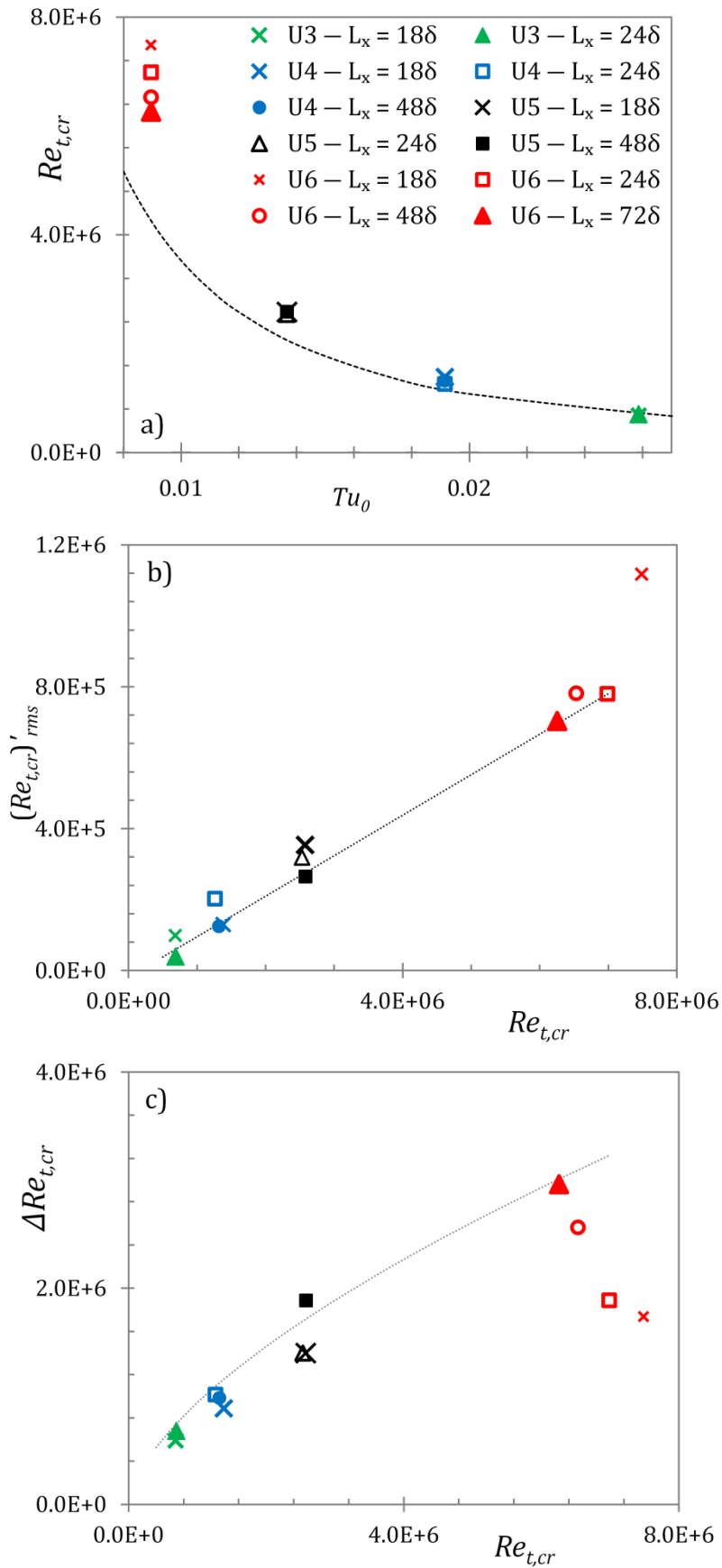


Figure 5.10. Effect of domain length on a) critical Reynolds number, b) r.m.s. fluctuation of critical Reynolds number, and c) transition period Reynolds number.

## 5.4 Ensemble-Averaged Flow Response

As discussed previously, multiple realizations were performed for each flow case, each starting from a different initial flow field. In order to carry out statistical calculation, a spatial-averaging for each wall in the homogenous ( $X$ - $Z$ ) directions is performed in combination with ensemble-averaging over both walls of each realization. This section provides a brief discussion on the response of the ensemble-averaged mean and turbulence quantities.

### 5.4.1 Boundary layer development

Before proceeding to the discussion of the high  $Re$ -ratio effect in the response of turbulence, the feature of time-developing boundary layer in unsteady flows (He & Seddighi [7, 8]) is revisited for the present high  $Re$ -ratio cases. Immediately following the commencement of the transient, a thin layer of boundary layer of high shear is formed adjacent to the wall which progressively develops into the flow. This time-developing boundary layer was shown to be similar to the time-developing laminar boundary layer until the onset of transition. In order to investigate the degree of change in the velocity profiles, He & Seddighi [7, 8] studied the development of the 'time-developing boundary layer' using the perturbation velocity profiles at several time instants. The perturbation velocity reads,

$$\bar{u}^\wedge(y^{+0}, t^{+0}) = \frac{\bar{u}(y^{+0}, t^{+0}) - \bar{u}(y^{+0}, 0)}{\bar{u}_c(t^{+0}) - \bar{u}_c(0)}, \quad (5.8)$$

where,  $\bar{u}(y^{+0}, t^{+0})$  is the local mean velocity at time  $t^{+0}$  at a distance  $y^{+0}$  from the wall and  $\bar{u}_c$  is the centreline velocity. The perturbation velocity represents a dimensionless measure of the change in velocity, where the initial flow is subtracted from the transient flow and then normalised with the resulting value at the centre. It was shown that the development of the perturbation velocity profiles for the unsteady flows can be represented by the laminar boundary layer development given by the solution to Stokes' first problem (Schlichting & Gersten [179]):

$$U(\eta) = 1 - \text{erf}(\eta) \quad (5.9)$$

where the similarity variable,  $\eta = y/2\sqrt{tv}$ ; and the error function,  $\text{erf}(\eta) = 2/\sqrt{\pi} \int_0^\eta e^{-\xi^2} d\xi$ . Figure 5.11 presents the development of the near-wall perturbation velocity profiles for the present cases during the early part of the transient in comparison with the Stokes' solution recast in terms of  $y^{+0}$  and  $t^{+0}$ . It is seen that for the entire pre-transition period ( $t^{+0} < 80$ ), the profiles of all the flow cases collapse on top of each other. For the early part of this period (say,  $t^{+0} \leq 50$ ), the development is closely represented by the Stokes' solution. The close agreement between the present unsteady flow profiles and the Stokes' solution show that unsteady flow resemble a laminar boundary layer during this period. Later, as the flow undergoes transition, the profiles are seen to rapidly deviate from the Stokes' solution and diverge from each other. It is clearly seen that the high *Re*-ratio cases develop more rapidly, implying a faster evolution of mean flow in higher *Re*-ratio cases.

To characterise the time-development of the transient flows, He & Seddighi [8] introduced a friction coefficient of the perturbation flow,

$$C_{f,du} = \frac{\tau_{w,du}}{\frac{1}{2} \rho (U_{b1} - U_{b0})^2} \quad (5.10)$$

where  $\tau_{w,du} = \mu\{\partial[\bar{u}(y, t^{+0}) - \bar{u}(y, 0)]/\partial y\}|_{y=0} = \tau_w - \tau_{w,0}$  is the wall shear stress of the perturbation flow and  $\tau_w$  and  $\tau_{w,0}$  are the values of wall shear stress of the flow at times  $t^{+0}$  and 0, respectively. Now, the friction coefficient for the solution of the Stokes' first problem [179] given by,

$$C_{f,Stokes} = \frac{2}{\sqrt{\pi}} \frac{1}{\sqrt{\frac{(U_{b1} - U_{b0})^2 t}{\nu}}} \quad (5.11)$$

where the theoretical wall shear stress of the solution of the Stokes' first problem is  $\tau_{w,Stokes} = \mu(U_{b1} - U_{b0})/\sqrt{\pi vt}$ . As the perturbation velocity profiles and Stokes' solution overlap each other at any  $t^{+0}$ , friction coefficient modified as below also overlap each other,

$$C'_{f,du} = C_{f,du} \frac{(U_{b1} - U_{b0})}{u_{\tau 0}} = \frac{\tau_{w,du}}{\frac{1}{2} \rho (U_{b1} - U_{b0}) u_{\tau 0}} \quad (5.12)$$

He & Seddighi [8] showed that the modified friction coefficient of the step-accelerating cases was only slightly elevated from the Stokes' solution, and can be represented by the following expression,

$$C'_{f,du} = \frac{2}{\sqrt{\pi}} \frac{1}{(t^{+0})^{0.47}} \quad (5.13)$$

The above expression recast in terms of  $C_{f,du}$  is only a slight modification of the Stokes' solution,

$$C_{f,du} = \frac{2}{\sqrt{\pi}} \frac{(t^{+0})^{0.03}}{\sqrt{\frac{(U_{b1} - U_{b0})^2 t}{\nu}}} = C_{f,Stokes} (t^{+0})^{0.03} \quad (5.14)$$

Figure 5.12 presents the development of the perturbation friction coefficient for the present cases compared to the Stokes' solution and equation (5.13). It is seen that there is a slight deviation in the early response ( $t^{+0} < 10$ ) of the friction coefficient. This is attributed to the difference in the acceleration period for the present cases. After this period, however, the present data for all the cases collapses onto a single curve, which is represented by the modification of the Stokes' solution. Thus, equation (5.13) can be used to predict the initial response of the wall friction for step-like accelerating flows. At the onset of transition in the flow, the friction coefficient deviates from this curve. It is seen from the figure that for the high  $Re$ -ratio unsteady flow cases, the timing of onset of transition in initial wall units remains roughly the same. Hence,  $t^{+0}$  proves to be a good measure of the stage of flow development. For cases U3-U6, the average critical time obtained from multiple realizations is in the close range,  $65 < t_{cr}^{+0} < 70$ . This, however, slightly deviates away from the low  $Re$ -ratio accelerating flows of He & Seddighi [8], in which critical time for all cases was in the range,  $80 < t_{cr}^{+0} < 110$ .

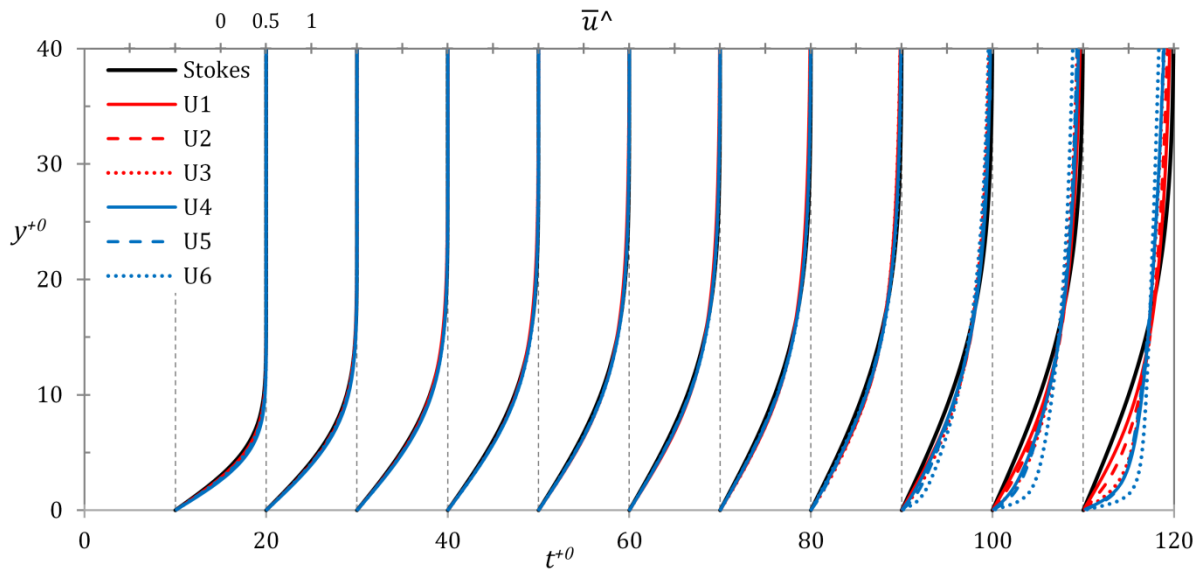


Figure 5.11. Development of the perturbation velocity profiles for the present cases during the pre-transition period compared with the Stokes' solution.

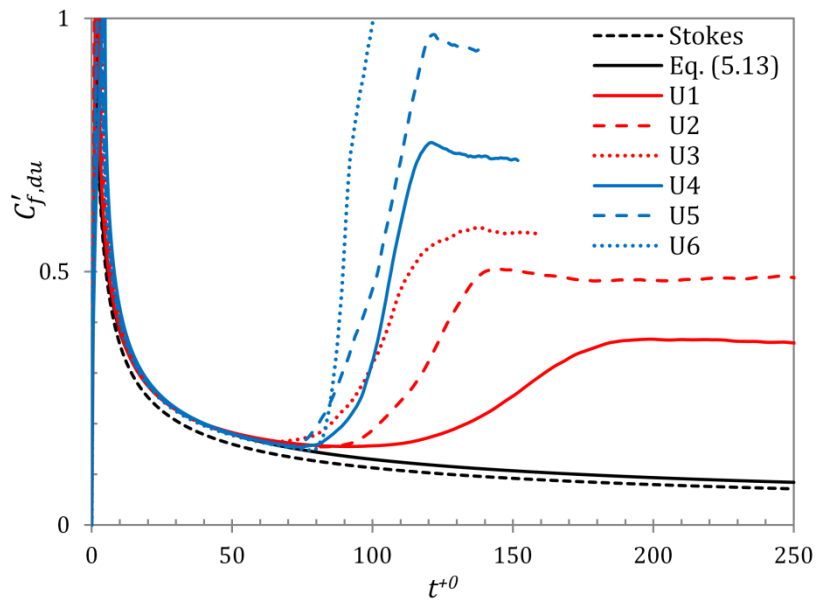


Figure 5.12. Development of the perturbation friction coefficient ( $C'_{f,du}$ ).

### 5.4.2 Response of r.m.s. fluctuating velocities

Figure 5.13 presents the development of the r.m.s. fluctuating velocity profiles for cases U3 (a)-(c) and U6 (d)-(f). While the critical time for both cases presented in the figure is approximately  $t^{+0} = 65$ , the completion times for U3 and U6 are roughly  $t^{+0} = 120$  and 85, respectively. It can be seen that following the start of the transient,  $u'_{rms}$  progressively increases in the wall region and maintains this trend until the onset of transition. This is attributed to the elongation and enhancement of the streak structures in the flow. The absence of generation of new turbulence is evident by the delayed response of the transverse components. During this period  $v'_{rms}$  and  $w'_{rms}$  reduce slightly from the initial values and remain largely unchanged for most of the pre-transition period. At the onset of transition, the transverse components finally respond owing to the newly generated turbulence, increasing rapidly and monotonically to peak values, showing a slight overshoot towards the end of the transient. During the transitional period,  $u'_{rms}$  further increases rapidly in the near wall region. It is interesting to note that case U6 clearly shows the formation of two peaks of  $u'_{rms}$  during this period ( $t^{+0} = 67 - 85$ ), however, case U3 shows a single peak. Similar double-peaks are also observed in cases U4 and U5 (not shown in the figure). The first peak, very close to the wall, is formed rapidly during the transitional period, increasing from very low initial values; whereas, the second peak, farther away from the wall, is only slightly higher than that at the point of onset of transition. At the end of the transitional period,  $u'_{rms}$  reduces and approaches its final steady value. The feature of two peaks during the transitional period is only shown by the streamwise component. This feature is very similar to the experimental results of Greenblatt & Moss [45].

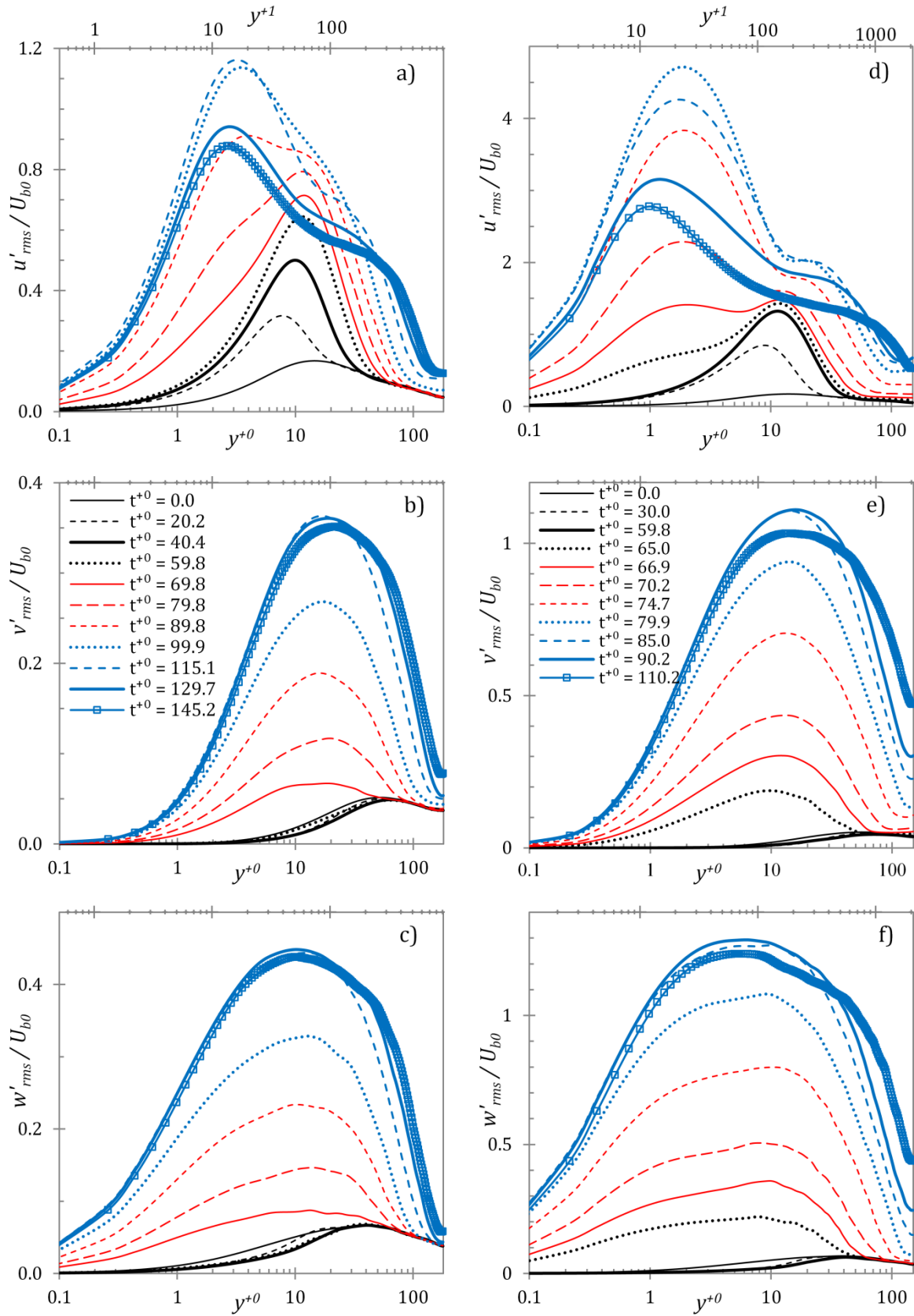


Figure 5.13. R.M.S. Fluctuating velocity profiles at several time instants during the transient for cases U3 (a)-(c) and U6 (d)-(f). Profiles of  $u'/U_{b0}$  (a, d);  $v'/U_{b0}$  (b, e);  $w'/U_{b0}$  (c, f).

To further analyse the origin and location of the two peaks in the present cases, the *conditional sampling* technique of Jeong *et al.* [177] and Talha [53] is used. Here, the r.m.s. fluctuation of  $\lambda_2$ ,  $\lambda'_{2,rms}$ , is used to distinguish the ‘active areas’ of turbulent generation from the ‘inactive areas’. It should be noted that this technique is performed to separate the active areas of turbulent generation in the  $x$ - $z$  domain, rather than in the wall-normal direction. The criterion is based on the comparison of a local r.m.s. fluctuation of  $\lambda_2$  with a *base* value. The base value chosen here is the  $\lambda'_{2,rms}$  of the entire  $x$ - $z$  plane at the critical time of onset of transition. Similar to that used by Jeong *et al.* [177], a window of size  $(\Delta x^+, \Delta z^+) = (120, 50)$  is used to determine the local r.m.s. fluctuation. The r.m.s. fluctuation,  $\lambda'_{2,rms}$ , is computed in the  $x$ - $z$  direction and, thus, is a function of  $y$ . The values are then summed in the wall-normal direction within 50 wall units and compared with each other. The criterion for determining active area reads,

$$\sum_{j=1}^{N_y^*} \lambda'_{2,loc,rms} \geq 0.1 \sum_{j=1}^{N_y^*} \lambda'_{2,p-cr,rms} \quad (5.15)$$

where  $\lambda'_{2,loc,rms}$  is the local r.m.s. value inside the window,  $\lambda'_{2,p-cr,rms}$  is the r.m.s. value of the entire  $x$ - $z$  plane at the onset of transition, and  $N_y^*$  is the number of control volumes in near wall region of  $y^+ < 50$ . The constant, 0.1, in equation (5.15) is an arbitrary value recommended by Talha [53]. It should be noted that the wall units are based on the average friction velocity of all active areas in the domain. Hence, the determination of the window size is an iterative process. Number of iterations was kept such that the change in active area determination for successive iterations was less than 0.1%. It is seen in Figure 5.4 that the value of  $(\lambda'_{2,rms})_{max}$  at the onset of transition reaches close to the fully turbulent value. Thus, the above criterion equation distinguishes the areas of *newly* generated turbulence in the transitional period. For any time before the onset of transition or after the completion of transition, the criterion gives 0% or 100% (of  $x$ - $z$  domain), respectively, as active areas of turbulence generation.

The above scheme is used to distinguish the active areas of turbulent generation for all the present cases. At the beginning of the transient, the entire wall surface is classified as inactive

region. At the onset of transition, the active region emerges at the location of the turbulent spot burst. During the transitional period, the active area grows in size and eventually covers the entire wall surface at the end of transitional period. To validate the above criterion, the instantaneous flow for case U3 during transitional period (at  $t^{+0} = 89.8$ ) is presented in Figure 5.14. The instantaneous 3D iso-structures of  $u'$  and  $\lambda_2$  are presented in Figures 5.14(a) & (b), respectively. Figure 5.14(c) shows the instantaneous contours of  $u'$  at  $y^{+0} = 5$ , and Figure 5.14(d) shows the approximation of the active wall surface determined using equation (5.15). It is clearly seen that the present scheme is suitable to capture the active areas of turbulent production during the transition. Although the edges of active regions are not perfectly accurate, the resulting mismatched contributions to the active/inactive areas are negligible.

Conditionally-averaged turbulent statistics for the active and inactive areas thus obtained are used to investigate the turbulent intensity contributions from each region. First, the statistics for case U6 at  $t^{+0} = 67.5$  are presented where the double peak first seems to emerge. For comparison, the statistics for case U3 are also presented at  $t^{+0} = 84.1$ , where the turbulent fluctuations seems to be at a similar stage of flow development (ref. Figure 5.13). At this instant, the active region constitutes 4.7% and 15.9% of the wall surface for cases U6 and U3, respectively. Figures 5.15(a) & (b) present the conditionally-averaged velocity profiles for the active ( $\bar{u}_a$ ) and inactive ( $\bar{u}_i$ ) regions, for cases U6 and U3, respectively, along with the domain-averaged velocity profile,  $\bar{u}_d$ . It can be seen that the profiles of the two regions are very different in both cases. The inactive region profile resembles that of the pre-transition period, exhibiting a plug-like response to the acceleration, with profile flat in the core. The active region profile, however, has developed farther away from the wall and the near-wall shear resembles that of the final steady flow.

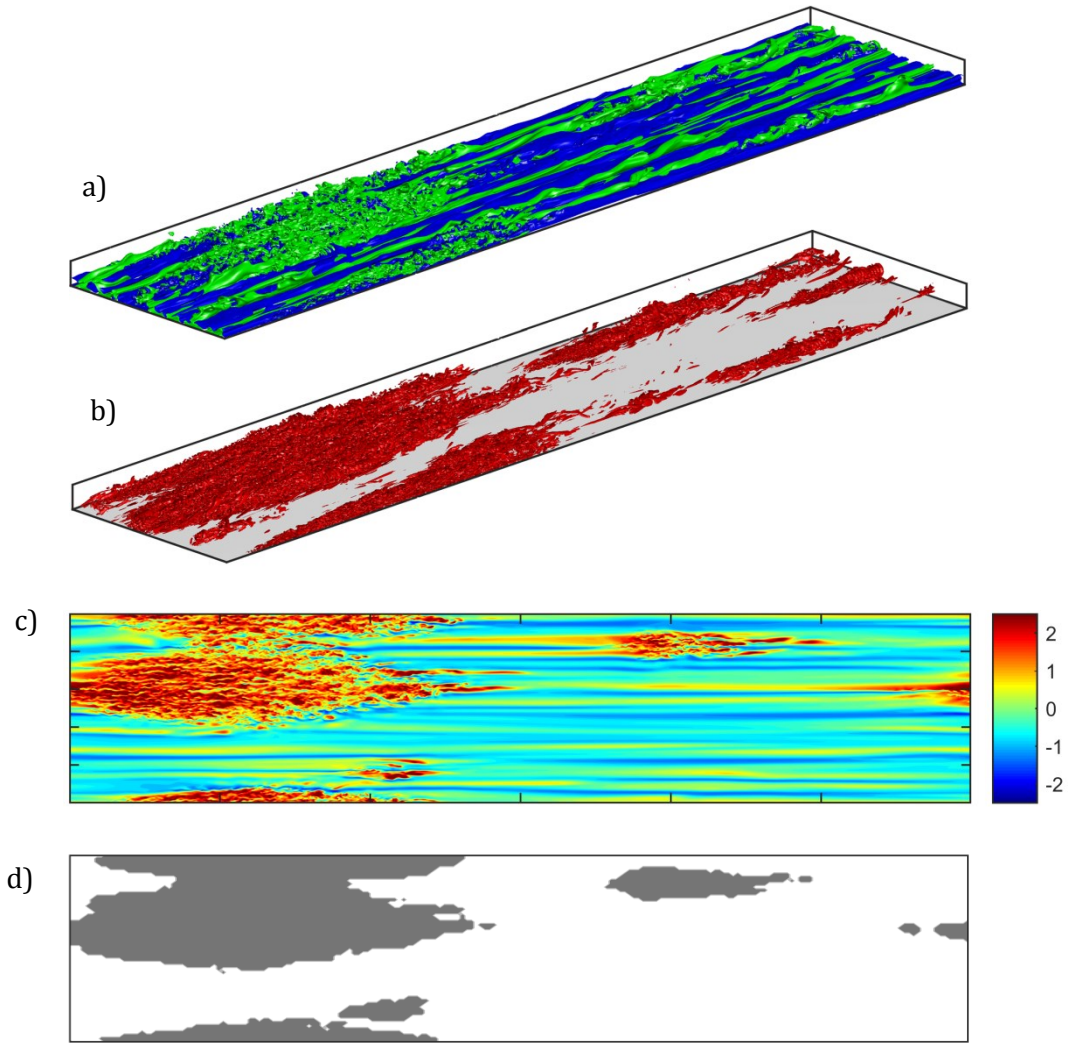


Figure 5.14. Instantaneous flow for case U3 at  $t^{+0} = 89.8$  (a) is-surface structures of  $u'/U_{b0} = \pm 0.35$ ; (b) iso-surface structures of  $\lambda_2/(U_{b0}/\delta)^2 = -5$ ; (c) contours of streamwise fluctuation velocity  $u'/U_{b0}$  at  $y^{+0} = 5$ ; (d) active region of turbulence production (shown in grey) determined using equation (5.15).

The conditionally-averaged streamwise fluctuation energy profiles at these times for cases U6 and U3 are presented in Figures 5.16(a) & (b), respectively. Herein, the fluctuation energy ( $u'_{rms}^2$ ) from active and inactive regions contribute to the domain-averaged profile. It is clear from Figure 5.16(a) that the double peaks in the streamwise fluctuations of case U6 is the combined effect of two separate peaks from two separate regions of the flow i.e. the active and inactive regions. The near-wall peak originates from the active region whereas that the peak further away from the wall originates from the inactive region. On the other hand, the two separate peaks from the two regions of case U3, in Figure 5.16(b), are seen to constitute to a

single peak in the domain-averaged profile. Although, the domain-averaged peak shows a tendency of a second peak at the location of active region peak at  $y^{+0} \sim 4$ , its close proximity to the inactive region peak results in masking the effect of the two peaks. The active region peak (located at  $y^{+0} \sim 1.2$  or  $y^{+1} \sim 15$  for case U6; and at  $y^{+0} \sim 3.3$  or  $y^{+1} \sim 16$  for case U3) is attributed to the burst of new turbulent structures in the active region with its  $y$ -location consistent with that of the final steady flow, whereas, the inactive region peak (located at  $y^{+0} \sim 12$  for both cases) is the contribution of the elongated streaks in the inactive region.

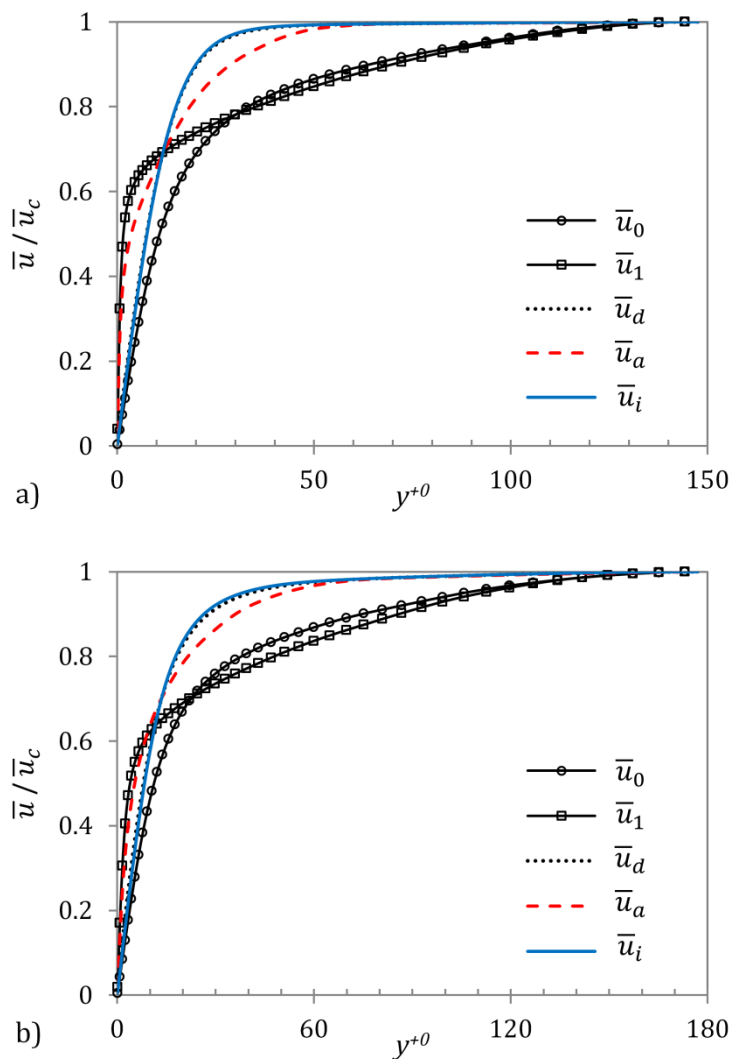


Figure 5.15. Conditionally-averaged mean velocity profiles of the active ( $\bar{u}_a$ ) and inactive ( $\bar{u}_i$ ) regions, along with domain-averaged ( $\bar{u}_d$ ) for a) case U6 at  $t^{+0} = 67.5$ , and b) case U3 at  $t^{+0} = 84.1$ . Also shown are the initial ( $\bar{u}_0$ ) and final ( $\bar{u}_1$ ) steady flow profiles, for comparison.

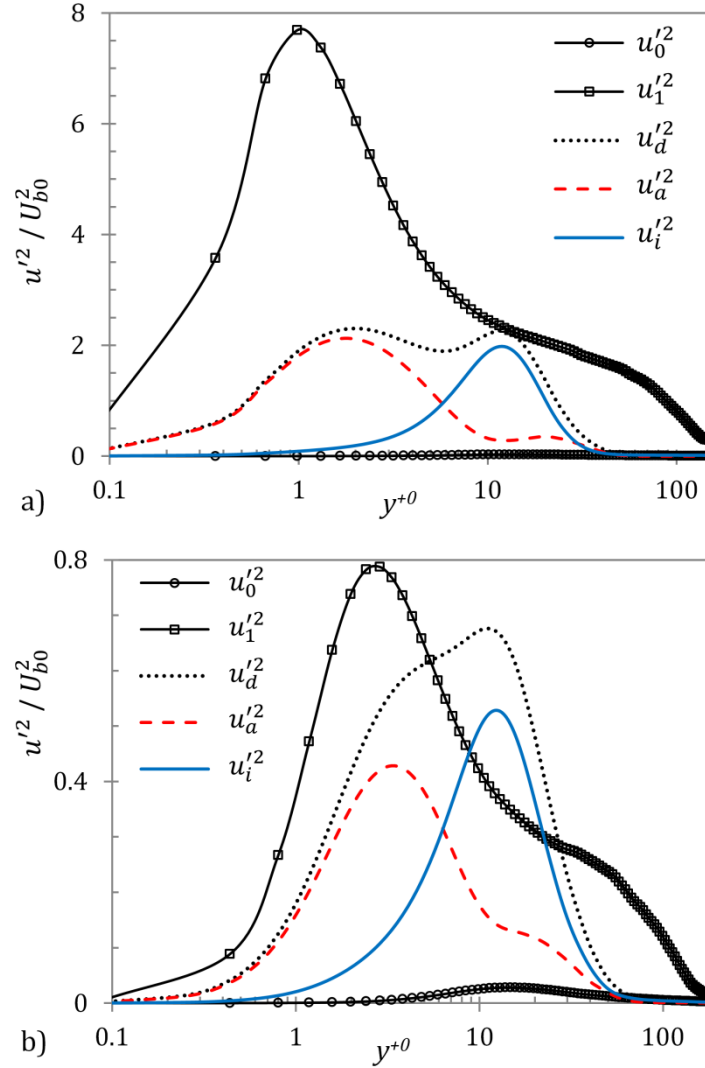


Figure 5.16. Conditionally-averaged streamwise fluctuation energy profiles of the active ( $u_a'^2$ ) and inactive ( $u_i'^2$ ) regions, along with domain-averaged ( $u_d'^2$ ) for a) case U6 at  $t^{+0} = 67.5$ , and b) case U3 at  $t^{+0} = 84.1$ . Also shown are the domain-averaged initial ( $u_0'^2$ ) and final ( $u_1'^2$ ) steady flow profiles, for comparison.

It should be noted that the active area profiles,  $u_a'^2$ , in Figure 5.16 too have a local second peak further away from the wall (around  $y^{+0} \sim 20$ ). This is merely a numerical feature due to the method employed in the calculation, where the fluctuation is calculated with respect to the domain-averaged mean profile i.e.  $u_a'^2 = \langle (u_a - \bar{u}_d)^2 \rangle$  and  $u_i'^2 = \langle (u_i - \bar{u}_d)^2 \rangle$ , where  $\langle \rangle$  denotes a spatial average in the homogeneous ( $x$ - $z$ ) plane. This, however, is not an appropriate representation of the conditionally-averaged fluctuation energy because the domain-averaged profile varies from the conditionally-averaged profiles of the active and inactive regions (as

seen in Figure 5.15). To further support this statement, conditionally-averaged r.m.s. fluctuation profiles within these two regions are presented separately in Figures 5.17(a) & (b), for cases U6 and U3, respectively. Here, the velocity fluctuation is calculated with respect to the conditionally-averaged mean flow, i.e.  $u'_{a,rms} = (u_a - \bar{u}_a)_{rms}$  and  $u'_{i,rms} = (u_i - \bar{u}_i)_{rms}$ . It is clear that the active region profile, here, shows a single peak consistent with the final steady profile.

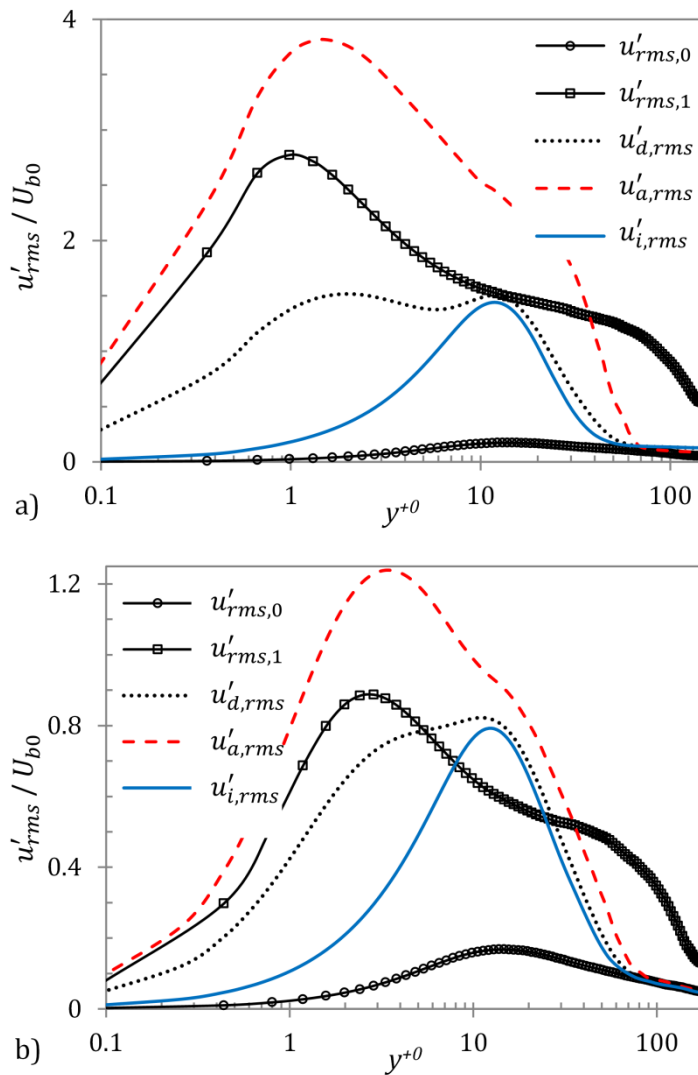


Figure 5.17. Conditionally-averaged streamwise fluctuation velocity profiles of the active ( $u'_{a,rms}$ ) and inactive ( $u'_{i,rms}$ ) regions, along with domain-averaged ( $u'_{d,rms}$ ) for a) case U6 at  $t^{+0} = 67.5$ , and b) case U3 at  $t^{+0} = 84.1$ . Also shown are the domain-averaged initial ( $u'_{rms,0}$ ) and final ( $u'_{rms,1}$ ) steady flow profiles, for comparison.

Now, the development of these conditionally-averaged r.m.s. fluctuation profiles during the transient is presented in Figures 5.18 and 5.19, for cases U6 and U3, respectively. It is seen that the inactive region profiles increase monotonically from the beginning of the transient until the end of the transitional period. For both cases, the peak of the profile originates at  $y^{+0} \sim 5$  and moves further away from the wall during the transient, reaching  $y^{+0} \sim 12$  until the end of the transitional period. On the other hand, the active region profile is generated at the point of onset of transition which thereafter reduced gradually during the transitional period. The peak of this profile originates at the onset of transition at  $y^{+0} \sim 1.2$  for case U6 and at  $y^{+0} \sim 3.6$  for case U3; and only moves slightly towards the wall during the transitional period and the post-transition period until it settles to the final steady value at  $y^{+0} \sim 1$  ( $y^{+1} \sim 14$ ) for case U6 and at  $y^{+0} \sim 2.5$  ( $y^{+1} \sim 13$ ) for case U3.

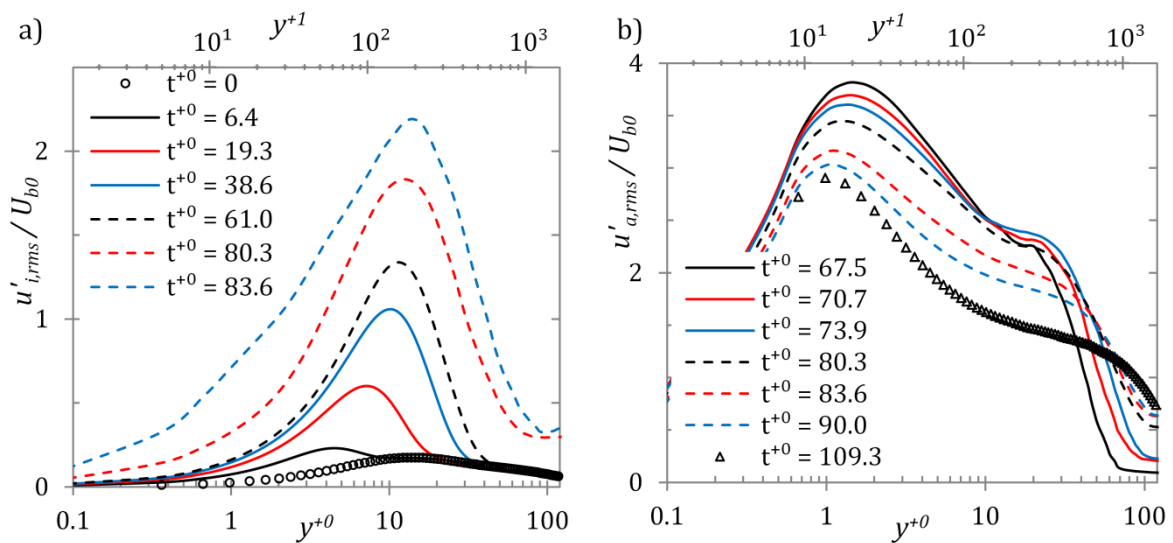


Figure 5.18. R.M.S streamwise fluctuating velocity profiles at several time instants during the transient for (a) inactive and (b) active regions for case U6.

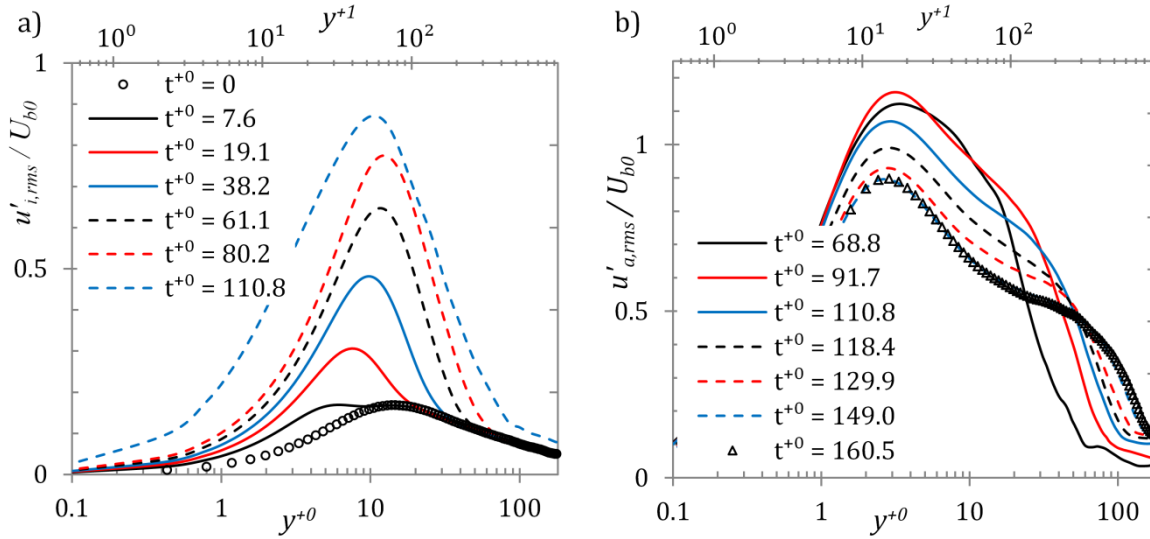


Figure 5.19. R.M.S streamwise fluctuating velocity profiles at several time instants during the transient for (a) inactive and (b) active regions for case U3.

The maximum streamwise energy growth,  $u'_{rms,max}{}^2 (= \max_y \{u'_{rms}\}^2)$ , of the two different regions for cases U6 and U3 are presented in Figures 5.20(a) & (b), respectively. The domain-averaged energy,  $(u'_{a,rms})^2$ , similar to that in DNS cases of He & Seddighi [8], exhibits an initial delay following the start of the transient which is attributed to an early receptivity stage (Fransson *et al.* [85]). During the pre-transitional period, the energy increases linearly with time until the onset of transition. At this point, the energy increases rapidly owing to the burst of 'new' turbulence, overshooting the final steady value and reaching a peak around the end of the transitional period and thereafter reducing to reach the final steady value. It is seen that the energy growth in the inactive region,  $(u'_{i,rms})^2$ , grows linearly even after the onset of transition and continues to do so until the end of the transitional period. This is expected as the burst of turbulence generation occurs only in the active region, while the inactive region is dominated by the stable streaky structures which continue to develop further. Energy in the active region  $(u'_{a,rms})^2$ , on the other hand, is generated at the onset of transition at a value much higher than the final steady value which gradually reduces until the end of the transitional period and reaches the final steady value. It is worth noting that the sharp increase and the high peak observed in the maximum domain-averaged energy during the transitional period is only a

numerical feature arising due to the method of statistical calculation. The domain-averaged term comprises of the turbulent fluctuations from the both active and inactive regions calculated with respect to the domain-averaged mean velocity, resulting in high values of fluctuations. A more suitable representation of the fluctuation energy during the transitional period is a weighted-average of the fluctuation energy,  $(u'_{rms})^2_w = \alpha \cdot (u'_{a,rms})^2 + (1 - \alpha) \cdot (u'_{i,rms})^2$ , where  $\alpha$  is the *active fraction* of wall surface (also plotted in Figure 5.20). It is clear that the average energy of the streamwise fluctuations show only a slight overshoot during the transitional period. The overshoot is attributed to the increasingly dominant effect of the active region during this period, while the slight decrease towards the end of the transitional period is attributed to the redistribution of streamwise energy to transverse components.

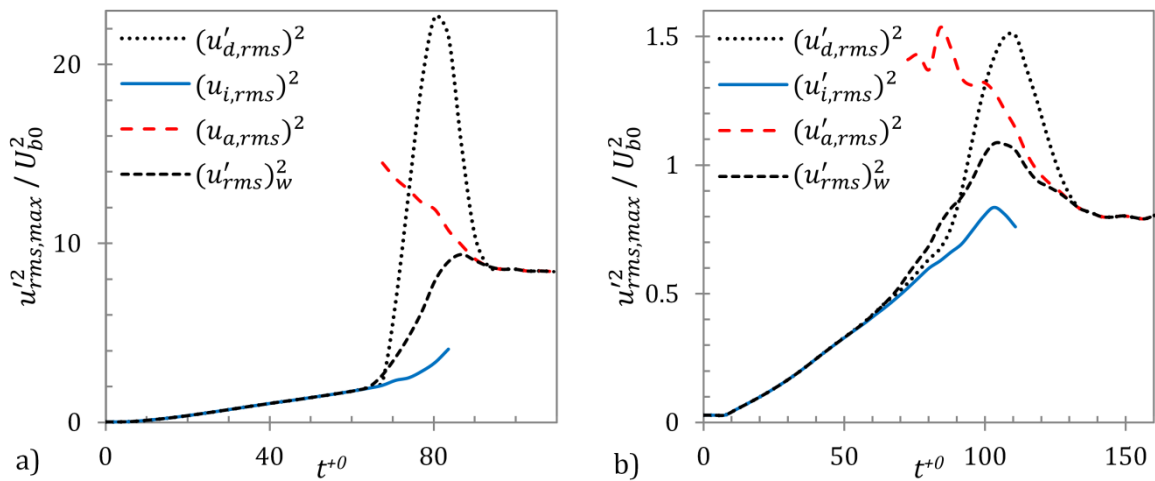


Figure 5.20. Conditionally-averaged maximum energy growth for a) case U6, and b) case U3.

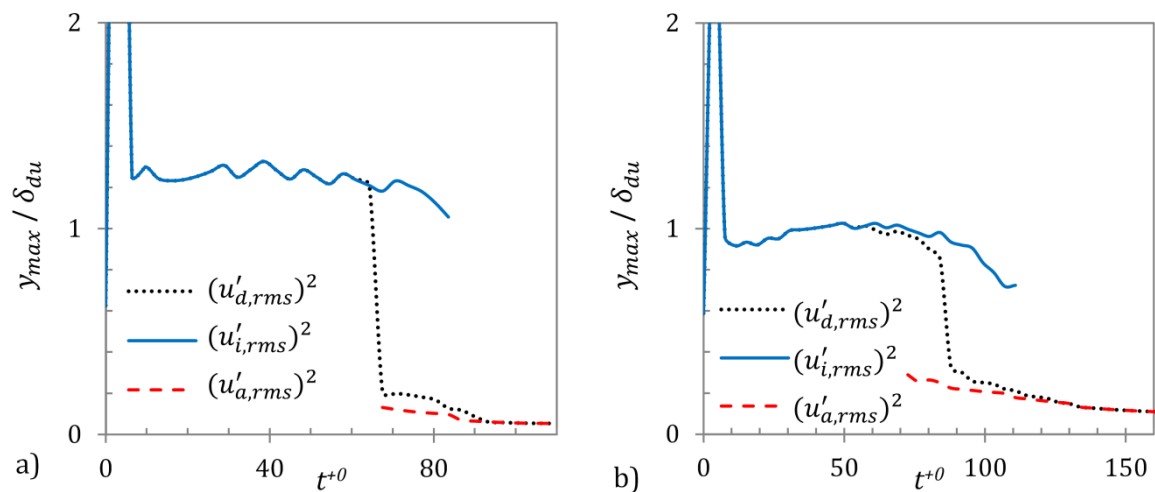


Figure 5.21. Peak location of the conditionally-averaged energy for a) case U6, and b) case U3.

The  $y$ -location of the maximum streamwise energy, normalised by the displacement thickness of the velocity field ( $\delta_u$ ), is shown in Figures 5.21(a) and (b) for cases U6 and U3, respectively. It should be noted that conditionally-averaged peak energy location is normalised by  $\delta_u$  of respective conditionally-averaged profile. Immediately after the commencement of the transient, a sharp increase is seen in the  $y/\delta_u$  location of the peak in the inactive region. This is attributed to the initial perturbation very close to the wall during the imposition of flow acceleration, resulting in a very small boundary layer thickness. Further, the peak location is seen to remain largely similar when normalised with  $\delta_u$ . For most of the pre-transition period, the peak remains at  $\sim 1.25\delta_u$  for case U6 and at  $\sim \delta_u$  for case U3. This signifies that the streamwise energy grows with the growth of the time-developing boundary layer and is scaled with the boundary layer rather than the inner scaling, which is atypical of turbulent flows. This is the well-accepted feature of bypass transitional flows, although the peak location therein has been shown to scale at  $\sim 1.3\delta_u$  (Andersson *et al.* [83]). The inactive region peak maintains its location even after the onset of transition showing only a slight decrease towards the end of the transitional period. The active region peak appears at the onset of transition at a location much closer to the wall, typical of turbulent flows. As the flow in the active region develops and becomes fully turbulent, the boundary layer thickness (and hence the displacement thickness,  $\delta_u$ ) increases. Thus, from the point of onset of transition until the end of the transient, the  $y$ -location of the peak normalised with  $\delta_u$  decreases. As expected, the peak location now scales with inner scaling, remaining at  $y^{+1} \sim 14$  during this period (ref. Figures 5.18-5.19). During the pre-transitional period, the entire wall surface is in the inactive region, thus the domain-averaged peak follows the same trend as that in the inactive region. At the onset of transition, the active region peak, which appears much closer to the wall, has a much higher value than that in the inactive region. At this point, the domain-averaged peak is dominated by the active region energy, following the location of the active region peak.

The maximum streamwise fluctuations and the  $y$ -location of the peaks for other cases are presented in Figures 5.22(a) & (b), respectively. From the point of onset of transition until the

end of transitional region, both active and inactive regions co-exist and exhibit separate developments of their respective streamwise energies. Although, this feature of separate developments exists in all the present cases (U1-U6), the feature of double peaks is clearly visible only in high  $Re$ -ratio cases (cases U4-U6). For these cases, there is a large difference between the peak energy of the active region and that in the inactive region at the onset of transition. Thus, even though the active region covers only a small fraction of the wall surface, the domain-averaged energy shows a dominant contribution from the active region in the near-wall region. The difference between the wall normal locations of the peak energies for the two regions also plays a role in enhancing the difference between the two separate contributions. The domain-averaged profile, thus, shows two peaks (like that in Figure 5.17a). The peak closer to the wall is attributed to the turbulent spots generated at the onset of transition, whereas, the one further away from the wall is attributed to the elongated streaks. In the late transitional period, most of the wall surface is covered with the new turbulence, thus reducing the area of the inactive region. This results in a decreasing contribution of the inactive region, until the inactive region energy is completely masked by the active region energy. At the end of the transitional period, the entire wall is classified as the active region with only a single peak in the entire domain. Thus, from the late-transitional period until the end of the transient, the domain-averaged profile shows only a single peak (i.e. the peak associated with the generation of 'new' turbulence in the active region).

At the onset of turbulence for low  $Re$ -ratio cases (cases U1-U3), the difference between the maximum fluctuations of the active and inactive regions is very small. The resulting active region contribution to the domain-averaged value in the near-wall region is also reduced, compared to that of the inactive region. Thus, the combined effect in the domain-averaged value for these cases shows only a single peak during the transitional period – the peak corresponding to the inactive region; while the active region peak is masked by the inactive region fluctuations. Later in the transitional period, when the active region grows in size, its contribution becomes comparable to that of the inactive region. However, due to close

proximity of the two peaks, the domain-averaged profile appears as a single peak. Again, in the late transitional period, the contribution of the inactive region becomes increasingly less and is masked by that of the active region. Thus, these cases show a single peak in the streamwise fluctuation during the entire transient period.

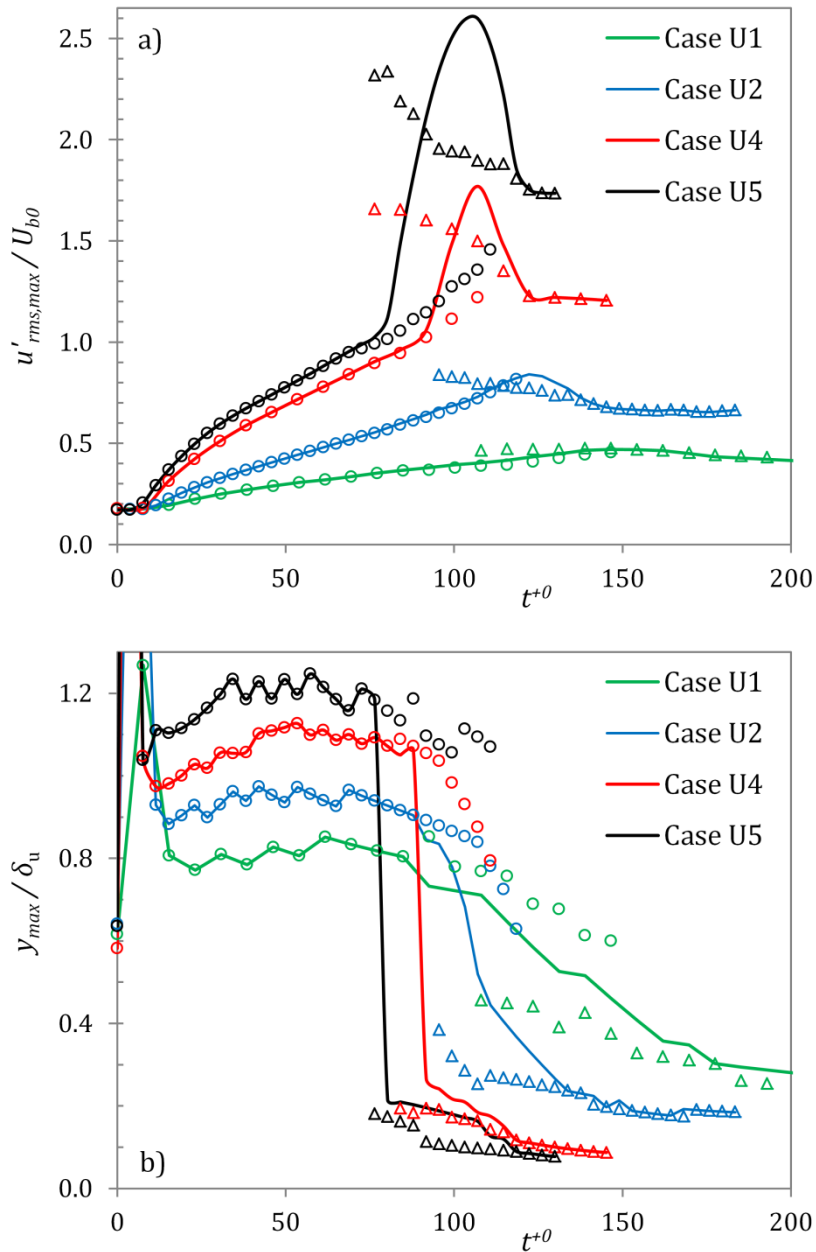


Figure 5.22. Domain- and conditionally-averaged a) maximum streamwise fluctuations, and b) the  $y$ -location of their peaks, for cases U1, U2, U4 and U5. (Symbols: Line – domain-averaged;  $\circ$  – inactive region;  $\Delta$  – active region; Colours: green – U1; blue – U2; red – U4; black – U5).

The two peaks shown by the streamwise component during the transient of high  $Re$ -ratio cases is very similar to the experimental results of Greenblatt & Moss [45]. However, in their case the peaks farther from the wall was formed at  $y^{+0} = 300$ , which persisted until the end of the unsteady flow period. Due to limitations in their near-wall velocity data, the full magnitude and location of the near-wall peak was not captured. Although the present results do show two peaks, a direct comparison of these two peaks with the two peaks of Greenblatt & Moss [45] may not be appropriate due to the large differences in the initial and final Reynolds numbers. It is possible that their peak farther from the wall (at  $y^{+0} = 300$ ) is a high Reynolds number effect.

## 5.5 Summary

Similar to the findings of He & Seddighi [7, 8], the present cases with higher  $Re$ -ratios also show a three stage response resembling that of the bypass transition in boundary layer flows. However, the features of transition become more striking when the  $Re$ -ratio increases – the elongated streaks in the pre-transitional period become increasingly longer and stronger, and the turbulent spots generated at the initial stage at the onset of transition become increasingly sparse.

For the lower turbulence intensity cases, the critical Reynolds number of transition is seen to diverge from the DNS trend of He & Seddighi [8]. The transition period Reynolds number was shown to have a power-relationship with the critical Reynolds number,  $\Delta Re_{t,cr} = 9.63 Re_{t,cr}^{0.82}$ . It was observed that there are large deviations of the critical Reynolds number for different realizations of each case. For the present cases, these deviations increase linearly with the mean value. It is observed that the length of the domain needs to be sufficiently large to accurately capture the transition time when the  $Re$ -ratio is high. The present cases are performed using different domain lengths to verify the adequacy of the domain lengths.

---

The higher  $Re$ -ratio cases exhibit double peaks in the transient response of streamwise fluctuations profiles shortly after the onset of transition. A conditional sampling technique, based on a  $\lambda_2$ -criterion, is used to classify the wall surface into active and inactive regions of turbulence generation. Conditionally-averaged turbulent statistics, thus obtained, are used to show that the fluctuation energies in the two regions undergo separate developments during the transitional period. For the high  $Re$ -ratio cases, the two peaks in the domain-averaged fluctuation profiles originate from the separate contributions of the active and inactive regions. The peak close to the wall is attributed to the generation of 'new' turbulence in the active region; whereas the peak further away from the wall is attributed to the elongated streaks in the inactive region. In the low  $Re$ -ratio cases, the peaks of the two regions are masked by each other during the entire transient, resulting in a single peak in the domain-averaged profile.

## Chapter 6

# Experimental Investigation of Ramp-Accelerating Flows

---

An experimental study has been carried out in a channel flow-loop facility to investigate the transitional behaviour of turbulence in response to ramp-up flow conditions. The flow rate is accelerated from a lower Reynolds number turbulent flow to a higher one. The acceleration is generated by sudden opening of the pneumatic control valve. Particle image velocimetry (PIV) and Constant-Temperature Anemometry (CTA) are used to measure the response of turbulence to the flow. The flow facility and data processing techniques have been detailed earlier in Chapter 4. DNS and LES simulations have also been carried out to reproduce certain experimental flow cases and cross-validate the findings.

In §6.1, the details of the experimental flow cases (and the reproduced simulation cases) investigated herein are introduced. The ensemble-averaged turbulent statistics and the instantaneous flow fields are then discussed to describe flow transition phenomena in §6.2 and §6.3, respectively. The correlations between the initial turbulence intensity, critical and transitional Reynolds number are presented in §6.4. Finally, §6.5 presents a summary of the experimental study undertaken here.

## 6.1 Present Experimental Cases

In the present investigation, the final Reynolds number of the accelerating flow is varied to produce a range of ‘initial turbulence intensity’. The flow acceleration occurs in response to the sudden opening of the valve. Therefore, the time period of flow acceleration depends on the final flow and the operational curve of the control valve (Figure 4.3). Figure 6.1 presents the variation of bulk Reynolds numbers obtained from integral of PIV velocity profile data for the present cases. The flow parameters of these cases are presented in Table 6.1. The bulk Reynolds number is defined as  $Re_b = U_b \delta / \nu$ , where  $U_b$  is the bulk velocity and  $\delta$  is the channel half-height. The ramp period,  $\Delta t$ , is defined as the time taken for the initial bulk flow to reach 80% of the final flow. During this period, the variation of the flow is approximately linear. Afterwards, the flowrate approaches the final flow rate asymptotically.

As discussed earlier in §4.1, the PIV measurements are carried out in two configurations. The first configuration (v-PIV) is used to measure wall-normal turbulent statistics. This method has been employed for all the cases. However, the second configuration (p-PIV), capturing instantaneous flow fields parallel to the wall, is employed for only two of the present cases, namely, E1 and E2. The wall-normal measurements are taken at a quarter-span of the channel ( $3.5\delta$  from the edge), as it provides a better resolution [60]. Both v-PIV and p-PIV are carried out at the bottom wall of the channel to avoid flow of any occasional air bubbles during the transient.

Along with PIV, CTA is employed for all cases to measure wall friction response during the flow transient. As described earlier in §4.3, a dynamic calibration procedure is employed herein to measure the transient response of the wall friction. For each unsteady run, the initial and final flows are maintained for a long time to ensure a statistically steady flow is achieved. The CTA signals at these known flow rates are then used for calibration for that particular run using DNS.

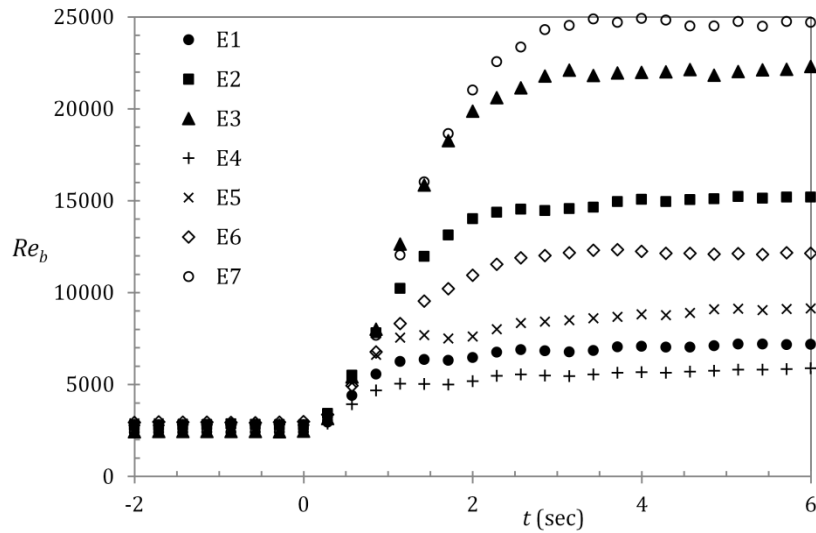


Figure 6.1 Variation of bulk Reynolds number obtained from integration of PIV data for the present experimental cases.

Case	$Re_b$	$U_b$ (m/s)	$\Delta t$ (sec)	Simulation	Measurements
E1	2800 – 7400	0.11 – 0.28	1.8	DNS, LES	v-PIV, p-PIV
E2	2800 – 15500	0.11 – 0.64	1.9	LES	v-PIV, p-PIV
E3	2400 – 22500	0.10 – 0.91	2.1	LES	v-PIV
E4	2800 – 6000	0.11 – 0.25	1.4	-	v-PIV
E5	2800 – 9200	0.11 – 0.36	1.8	-	v-PIV
E6	2800 – 12000	0.11 – 0.57	1.8	-	v-PIV
E7	2400 – 25000	0.09 – 0.93	2.1	-	v-PIV

Table 6.1. Variation of Reynolds number for the present experimental cases.

Simulations are also performed to reproduce the experimental flow cases. The flow rate history extracted from the PIV data is used to specify the ramp accelerations in the simulations. *CHAPSim* [7-9] and *CHAPSim\_LES* (as described in §3.3) are used to perform DNS and LES, respectively, reproducing the experimental case E1. While two other cases with higher final Reynolds numbers, namely E2 and E3, are reproduced only using LES by *CHAPSim\_LES*. Hereafter, the reproduced DNS and LES cases of E1 are termed E1D and E1L, respectively. The reproduced LES cases of E2 and E3 are termed as E2L and E3L. Table 6.2 presents the

parameters employed in these simulations. Figure 6.2 presents the variation of bulk velocity for the reproduced simulation cases compared to their respective experimental cases.

	Case	Domain	Grid	$\Delta x^{+1}$	$\Delta z^{+1}$	$\Delta y_c^{+1}$	
E1	DNS	E1D	$18 \delta \times 2 \delta \times 5 \delta$	$1024 \times 240 \times 480$	7	4	7
	LES	E1L	$18 \delta \times 2 \delta \times 5 \delta$	$300 \times 150 \times 180$	26	12	9
E2	LES	E2L	$18 \delta \times 2 \delta \times 5 \delta$	$648 \times 300 \times 450$	22	9	11
E3	LES	E3L	$24 \delta \times 2 \delta \times 5 \delta$	$1200 \times 360 \times 540$	22	10	12

Table 6.2. Simulation parameters used to reproduce the experimental flow cases.

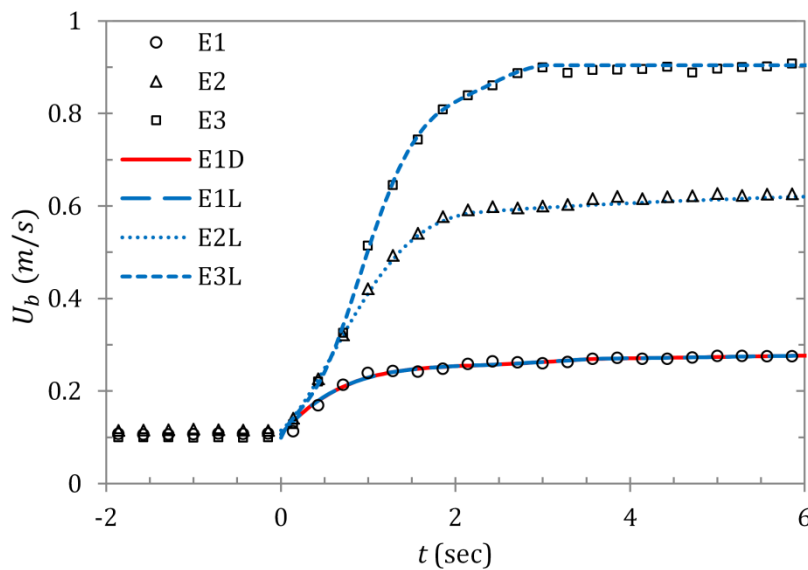


Figure 6.2. Variation of bulk velocity for the cases E1-E3 and their reproduced simulation cases.

In this chapter, the discussion is mainly focussed on the experimental cases E1-E3 along with their respective reproduced simulation cases. However, some basic quantitative features of other experimental cases (E4-E7) are presented to facilitate the discussion. The developments of friction coefficient and turbulence quantities for cases E4-E7 are indexed in Appendix A.

## 6.2 Ensemble-Averaged Flow Response

The transient response of the flow is investigated with the aid of ensemble-averaged flow statistics in this section. The response of the streamwise and wall-normal velocities was captured by v-PIV configuration. The FOV for this configuration was about  $35 \text{ mm} \times 35 \text{ mm}$

(equivalent to  $1.4\delta \times 1.4\delta$ ), while the final IA size for processing such images was set to 32 pixels  $\times$  32 pixels. For the purpose of ensemble-averaging, each experimental flow case is repeated 60 times. The averaging was then performed both in streamwise direction within FOV and over repeated runs, as previously described in §4.4. CTA, with a dynamic calibration method, has been used to measure the response of wall friction. Ensemble-averaging over repeated runs is then performed on the response of wall friction. Three realizations of each simulation case was performed, each starting from a different initial flow field. Spatial- and ensemble-averaging of flow statistics was performed for both walls of each realization for each simulation case.

### 6.2.1 Response of friction coefficient and wall shear stress

Figure 6.3 presents the response of the friction coefficient during the transient for experimental cases, E1-E3, along with their reproduced simulation cases, E1D and E1L-E3L. The numerical data is seen to show a trend consistent with the experimental data. The results of the low *Re*-ratio cases E1D and E1L agree well with the experimental data of case E1. Overall, the results of the higher *Re*-ratio cases E2L and E3L also agree well in magnitude with their respective experimental cases, E2 and E3, during the transient period. However, there appears to be a slight delay in the recovery of the friction coefficient curve. But this delay is insignificant. Hence, the numerical data is shown to represent the experimental data reasonably accurately.

As described in He & Seddighi [7, 8], the initial response of sharp increase of friction coefficient is attributed to the plug-like response of the flow, with the formation of a thin layer of high shear near the wall. Further in the pre-transitional period, this thin boundary layer develops into the flow causing the friction coefficient to decrease, reaching a minimum at roughly  $t = 2.46, 2.05$  and  $2.10$  seconds for cases E1, E2 and E3, respectively. At the onset of transition, the generation of new turbulence structures causes the friction coefficient to increase rapidly. The friction coefficient for cases E1, E2 and E3 reach the final steady state at about  $t = 4.65, 3.30$  and  $3.50$  seconds, respectively.

The wall shear stress response for cases E1-E3 is presented in Figure 6.4, along with their reproduced simulation cases. Also shown in the plots is the trend of *pseudo-steady* values representing the variation of wall shear stress in steady flows at corresponding Reynolds numbers during the transient. The trends of numerical and experimental data agree well with each other. However, the difference in magnitude of experimental and numerical data is more apparent here than shown in friction coefficient. The difference is larger for higher *Re*-ratio ramps. The most likely reason for the mismatch can be the mismatch in the flow rate, which will show strongly in wall shear stress but may be partly cancelled in friction coefficient. Other reasons may include the unsuitability of the present dynamic calibration technique of hotfilms, or alternatively, a drift in the calibration constants themselves during the transient period.

The transient response of the wall shear stress displays more detailed flow characteristics during the pre-transitional period. After the commencement of the acceleration, the wall shear stress sharply overshoots the pseudo-steady values, which is attributed to the formation of a thin, high-shear boundary layer. As this boundary layer extends into the flow with time, the rate of the increase of wall shear stress reduces. Further in time, the absence of turbulence becomes increasingly important. The combination of the decreasing viscous stresses and low turbulence causes the wall shear stress to undershoot the pseudo-steady values and undergo a period of reduction. At the onset of transition, the wall shear stress increases rapidly approaching the pseudo-steady values. This is consistent with the trend previously reported in He *et al.* [48, 50, 51] and Seddighi *et al.* [57, 59].

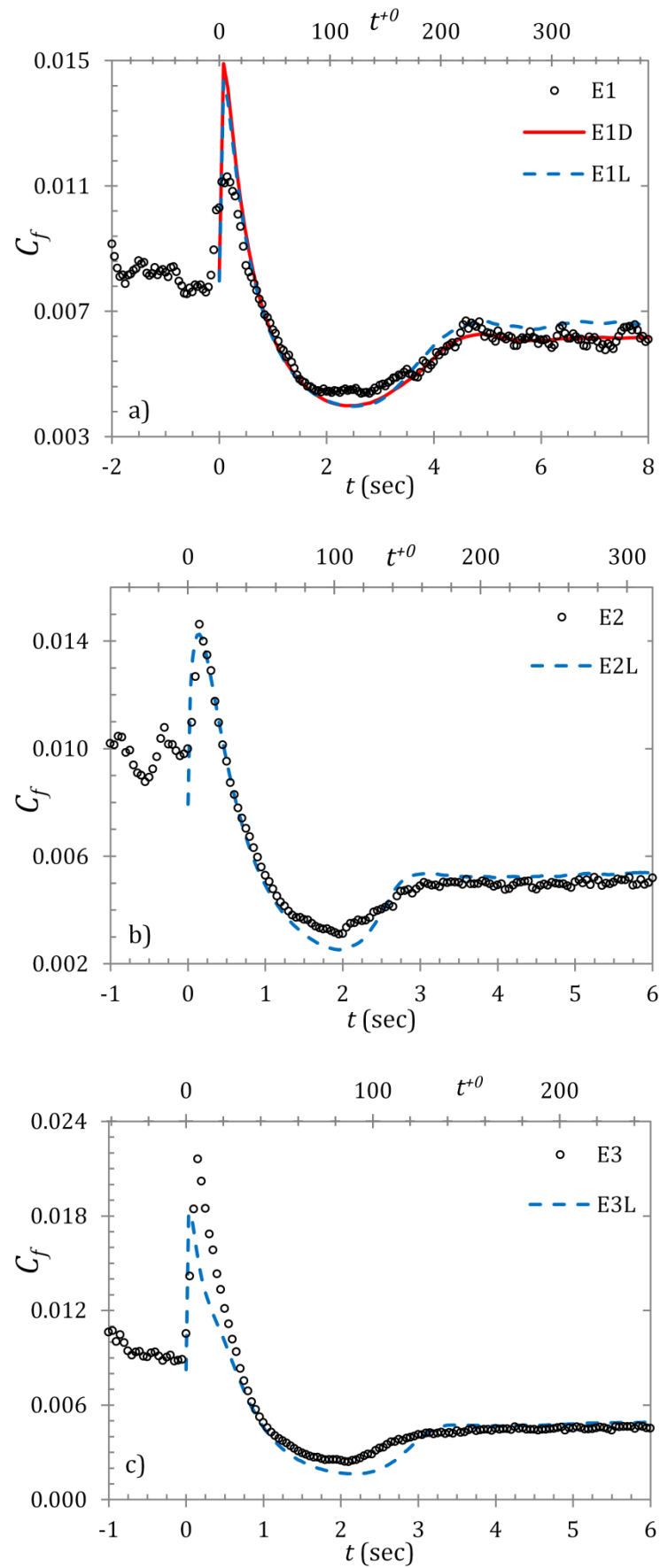


Figure 6.3. Response of the friction coefficient during the transient for cases a) E1, b) E2, and c) E3.

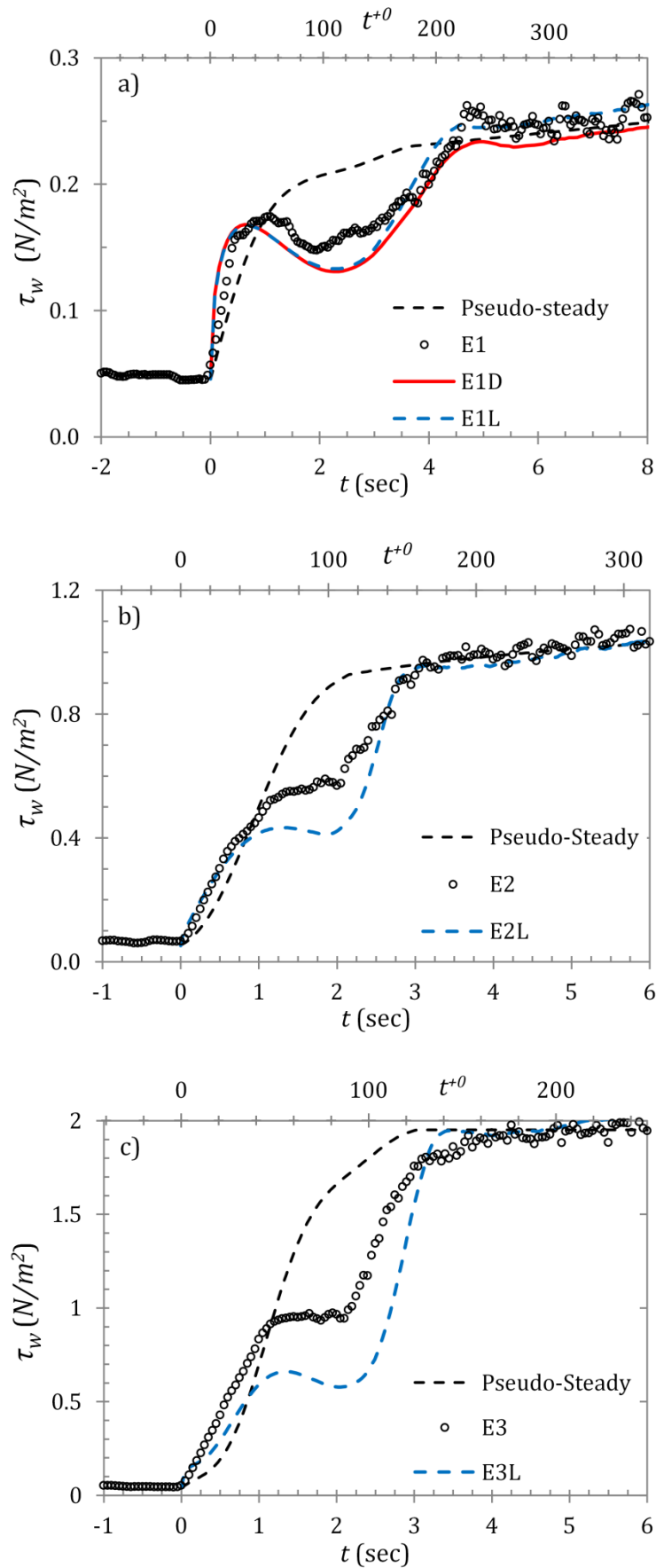


Figure 6.4. Response of the wall shear stress during the transient for cases a) E1, b) E2, and c) E3.

As previously discussed, the response of the friction coefficient for accelerating turbulent flows is seen to be similar to that in boundary layer bypass transition, and can be used to determine the timing of the transition phenomena. The initial turbulent spots are first observed at the time of minimum friction coefficient and can be regarded as the critical time of onset of transition in the flow. Similarly, the completion of transition process can be assumed to be the point where the entire wall surface is covered with the newly generated turbulence, which corresponds to the time of recovery of the friction coefficient. Using the time-history of friction coefficient, the critical time of transition ( $t_{cr}$ ) and time of fully-turbulent flow ( $t_{turb}$ ) are obtained for each case. Table 6.3 presents these times for the present experimental cases, while Table 6.4 presents those for the reproduced simulation cases. He & Seddighi [8] suggested that time in the initial wall units ( $t^{+0} = tu_{\tau_0}^2/\nu$ ) is a useful quantity to characterise the time of onset of transition. For their DNS step-like flow acceleration cases, this time was found to be in the range  $80 < t^{+0} < 110$ , whereas for the ramp-like experimental flow cases of Gorji [60], the range was  $80 < t^{+0} < 130$ . It should be noted that Gorji [60] used the near-wall turbulent statistics ( $u'_{rms}$  and  $v'_{rms}$ ), instead of friction coefficient, to estimate these values. Nevertheless, the present cases show a range similar to that of Gorji [60].

Case	$t_{cr}$ (sec)	$t_{turb}$ (sec)	$t_{cr}^{+0}$	$t_{turb}^{+0}$
E1	2.46	4.65	119.3	225.5
E2	2.05	3.30	108.4	174.5
E3	2.10	3.50	87.0	145.0
E4	2.47	4.65	127.3	239.6
E5	2.15	4.35	110.7	224.0
E6	2.05	3.65	133.7	238.0
E7	2.60	3.85	96.9	143.4

Table 6.3. Critical and completion times of transition for different cases determined using the measured friction coefficient development.

Case	$t_{cr}$ (sec)	$t_{turb}$ (sec)	$t_{cr}^{+0}$	$t_{turb}^{+0}$
E1D	2.42	4.76	117.4	230.9
E1L	2.43	4.55	117.9	220.8
E2L	1.95	3.08	102.9	162.6
E3L	2.19	3.43	90.5	141.7

Table 6.4. Critical and completion times of transition for the reproduced simulation cases determined using the friction coefficient developments of the simulations.

### 6.2.2 Boundary layer development

As discussed earlier, the transient behaviour of flow after a step change in flow rate shows a three-stage response – namely, the pre-transition, transition and fully turbulent – which bears strong similarity to the three regions of the boundary layer bypass transition. He & Seddighi [7, 8] showed that after the start of the transient, a thin layer of boundary layer of high shear is formed adjacent to the wall which progressively develops into the flow. In order to quantify the boundary layer development, He & Seddighi [7] defined the time-developing boundary layer, given by the perturbation velocity,

$$\bar{u}^{\wedge}(y^{+0}, t^{+0}) = \frac{\bar{u}(y^{+0}, t^{+0}) - \bar{u}(y^{+0}, 0)}{\bar{u}_c(t^{+0}) - \bar{u}_c(0)}, \quad (6.1)$$

where,  $\bar{u}(y^{+0}, t^{+0})$  is the local mean velocity at time  $t^{+0}$  at a distance  $y^{+0}$  from the wall and  $\bar{u}_c$  is the centreline velocity. It was shown that the perturbation velocity profiles of all step-like accelerating flow cases collapsed on top of each other in the pre-transition period and were closely represented by the solution of Stokes' first problem during this period. The same has been demonstrated for the higher Reynolds number ratio step-accelerating flows cases in §5.4.

Now, the Stokes' first problem is concerned with a sudden movement of a solid boundary, which is why it can be used to represent the response of a step-like change in the flow. As discussed in Seddighi *et al.* [59], the boundary layer development in a slower accelerating changing flow is an integral consequence of continuous changes in the flow. Hence, the time-development for such

cases can be better represented by the extension of the Stokes' solution to time-varying velocity. If the time-varying velocity is considered as a *multi-step function* with small steps, the entire solution consists of superposition of elementary solutions for each velocity step (Schlichting & Gersten [179]). The velocity at any time,  $t$ , is given by,

$$u(y, t) = \int_0^t dU_b \operatorname{erfc}\left(\frac{y}{2\sqrt{\nu(t-\tau)}}\right) \quad (6.2)$$

where *erfc* is the complimentary error function; and the time-varying velocity function  $U_b(t)$  is represented by small steps of velocity  $dU_b$  over a small time step  $d\tau$ . The present ramp-type accelerating flow is divided into small finite steps and the integral of the laminar boundary-layer development over time is determined using equation (6.2). Figure 6.5 presents the comparison between the development of laminar boundary-layer velocity profiles and the perturbation velocity profiles for cases E1-E3 and their respective simulation cases. It is seen that the experimental and numerical data shows a good agreement between each other for the early part of pre-transition period ( $t^{+0} < 40$ ). Later in the pre-transition period, the experimental data is seen to diverge from the numerical data in the near-wall region ( $y^{+0} < 15$ ). Unlike for the wall friction measurements, the differences between the experiment and numerical velocity profiles are smaller for higher *Re*-ratio ramp flows. After the onset of transition, the differences appear to be reducing. For  $t^{+0} > 130$ , the experimental and numerical are again seen to agree well with each other. The differences in the early part of the transient may be partly attributed to 'poor' PIV measurements in the high velocity gradient region near the wall.

Considering the numerical velocity profile data, it is clear from Figure 6.5 that the response of the present ramp flow accelerations collapses well with the laminar solution up to  $t^{+0} = 100$ . After roughly  $t^{+0} = 100$ , as the flow undergoes transition, the profiles of the present cases are seen to start diverging from those of laminar boundary layer. The near-wall profiles for cases with larger flow acceleration (E2L and E3L) are seen to diverge more rapidly than that of E1D and E1L. This is consistent with the findings of He & Seddighi [8] and Gorji [60].

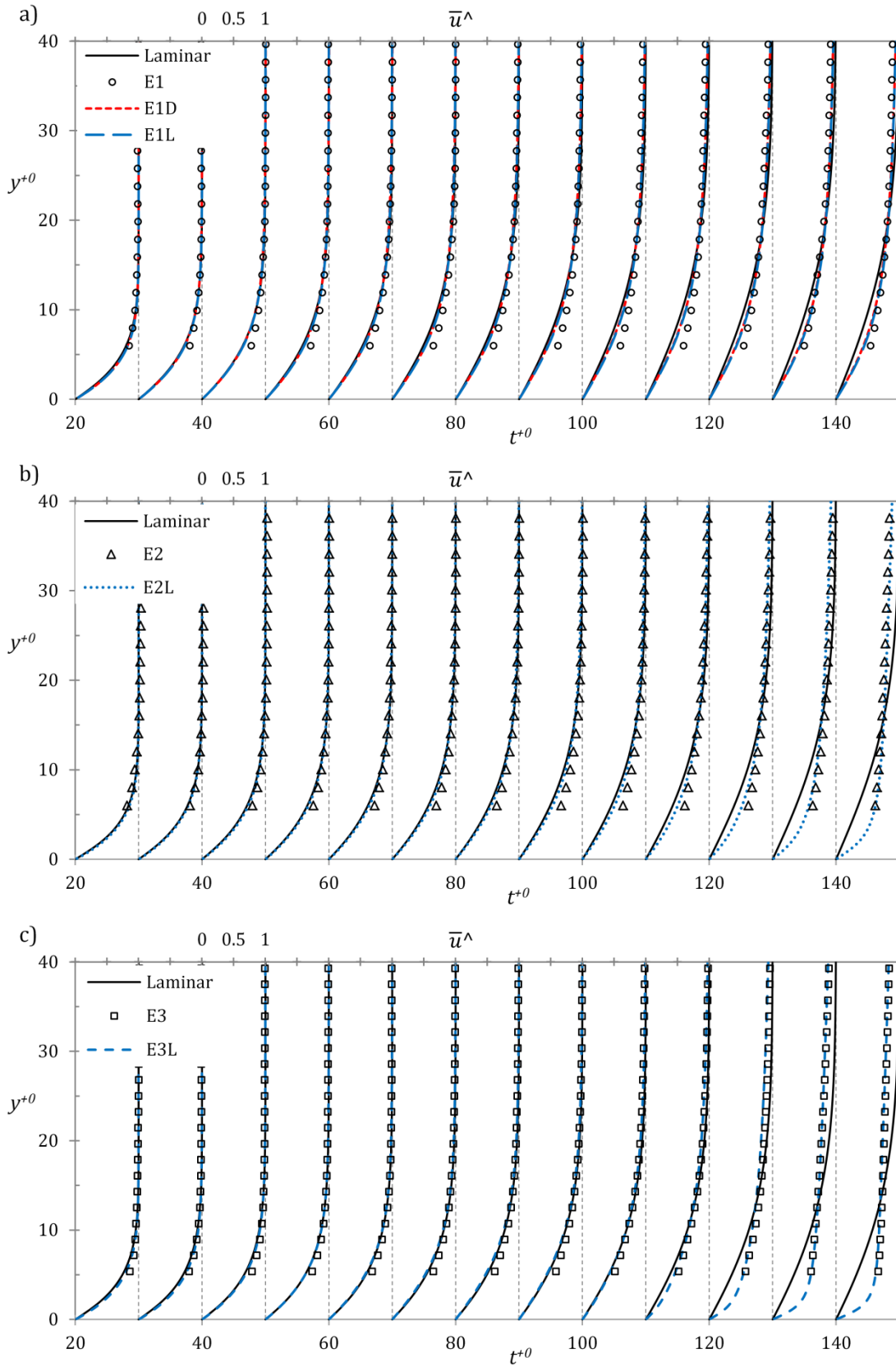


Figure 6.5. Development of the perturbation velocity profiles ( $\bar{u}^\wedge$ ) compared with the laminar boundary-layer development for time varying perturbation for cases a) E1, b) E2, and c) E3.

Now, in step-like accelerating flow cases, the bulk velocity changes to that of the final flow ( $U_{b1}$ ) immediately following the commencement of the transient. Thus, the friction coefficient, as in equation (5.12), is normalised by final change in velocity, ( $U_{b1} - U_{b0}$ ). However, for a slower ramp-type flow, the bulk velocity changes continuously during a long period of the transient. Hence, the modified friction coefficient for these cases is normalised with the intermediate change in velocity to take this into consideration,

$$C''_{f,du} = \frac{\tau_{w,du}}{\frac{1}{2}\rho \{U_b(t) - U_{b0}\} u_{\tau 0}} \quad (6.3)$$

Now, the laminar solution, equation (6.2), can also be used to determine the friction coefficient of the laminar boundary-layer. The laminar wall shear stress of the time-varying perturbation, obtained by differentiating equation (6.2), reads

$$\tau_{w,lam} = \rho \int_0^t dU_b \sqrt{\frac{\nu}{\pi(t-\tau)}} \quad (6.4)$$

Figure 6.6(a) presents the development of the modified friction coefficient for cases E1-E3 and the reproduced simulation cases. Figures 6.6(b)-(d) present the comparison of modified friction coefficients of the present cases with that of the laminar solution, obtained from equation (6.4). As discussed earlier, the experimental and numerical data agree reasonably well for the lowest *Re*-ratio case, E1. For cases E2 and E3, the larger differences between experiment and numerical are likely to be due to hotfilm calibration. Thus, the numerical data from the reproduced simulation cases are considered better representatives of the wall friction.

It is seen that the modified friction coefficient of the reproduced simulation cases is slightly elevated from that of the laminar solution ( $C''_{lam}$ ), but can be represented during the pre-transition period by a slight correction (which is also used in §5.4 for the step-change flow) to the laminar solution as below,

$$C''_{f,du} = C''_{lam} (t^{+0})^{0.03} \quad (6.5)$$

It can be deduced that, similar to that in step-like acceleration, the time-developing boundary layer of ramp-type flow acceleration during the pre-transition period bears strong resemblance to laminar boundary layer. The early response of the wall friction for ramp-type accelerating flows can be determined using equations (6.4)-(6.5).

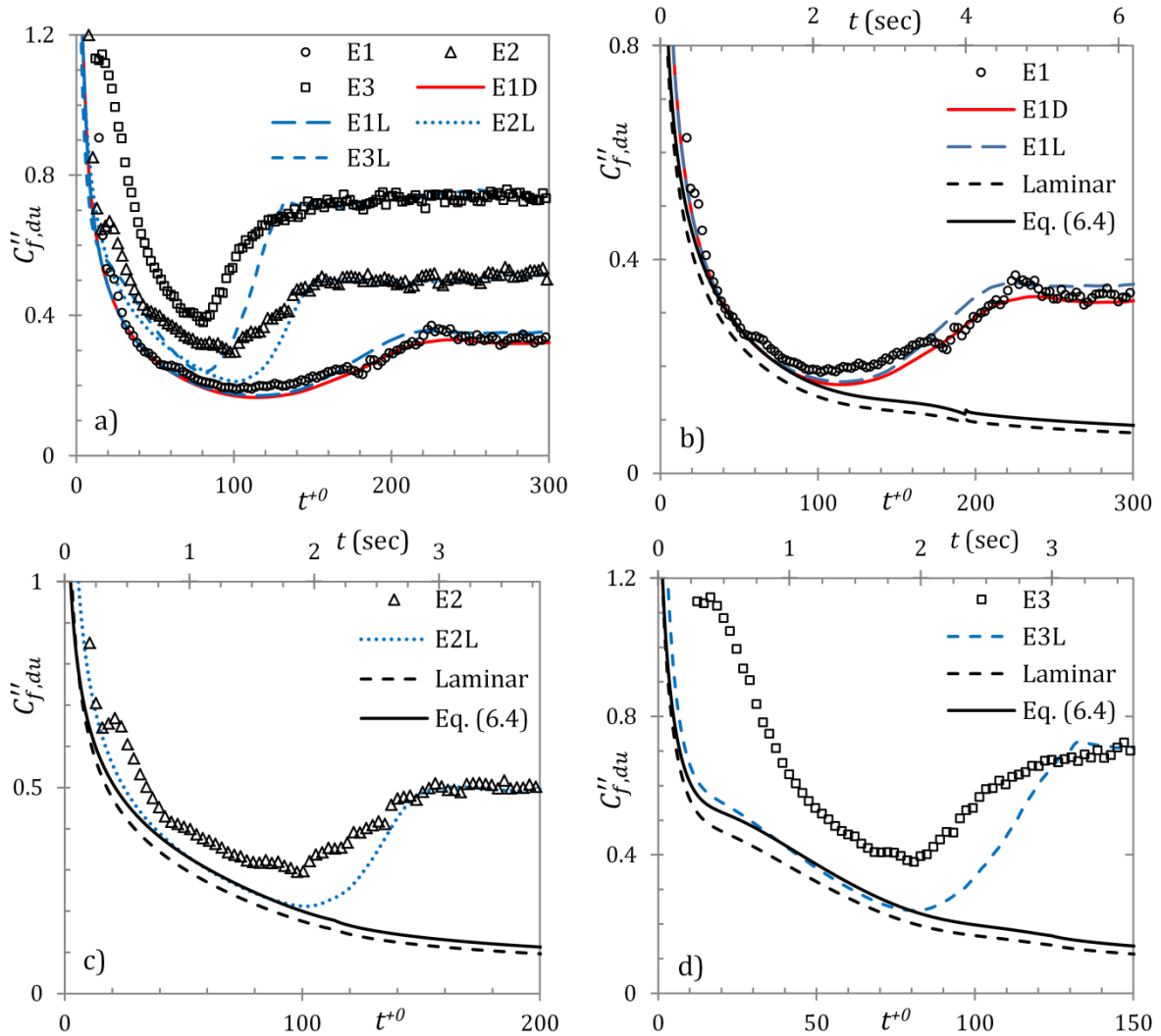


Figure 6.6. Development of the modified friction coefficient for cases E1-E3 and their respective reproduced simulation cases, along with the laminar boundary-layer solution for time-varying velocity.

He & Seddighi [7] re-defined the displacement thickness ( $\delta_{du}$ ), the momentum thickness ( $\theta_{du}$ ), and the shape factor ( $H$ ) for perturbation boundary layer of unsteady internal flows as,

$$\delta_{du}(t^{+0}) = \int_0^1 (1 - \bar{u}^\wedge(y/\delta, t^{+0})) d(y/\delta) \tag{6.6}$$

$$\theta_{du}(t^{+0}) = \int_0^1 \bar{u}^\wedge(y/\delta, t^{+0}) (1 - \bar{u}^\wedge(y/\delta, t^{+0})) d(y/\delta) \quad (6.7)$$

$$H(t^{+0}) = \delta_{du}(t^{+0}) / \theta_{du}(t^{+0}) \quad (6.8)$$

Figure 6.7 presents the development of the momentum-thickness Reynolds number ( $Re_\theta = \theta \bar{u}_c / \nu$ ) and the shape factor for the cases E1, E1D and E1L in comparison with those of the step-like acceleration of He & Seddighi [7] (HS13, having similar initial and final Reynolds numbers). Also presented in the figure for comparison are the boundary layer bypass transitional flow cases T3A and T3B of Roach & Brierley [180]. For comparing the spatial development of boundary layer flow with temporal development of unsteady internal flow, He & Seddighi [7] re-defined the streamwise distance ( $x$ ) of boundary layer as  $x = U_{conv}t$  (where  $U_{conv}$  is the convective velocity). By curve-fitting the early response of transient channel flow with the Blasius solution, this velocity was determined as  $U_{conv} = 0.74U_{b1}$ .

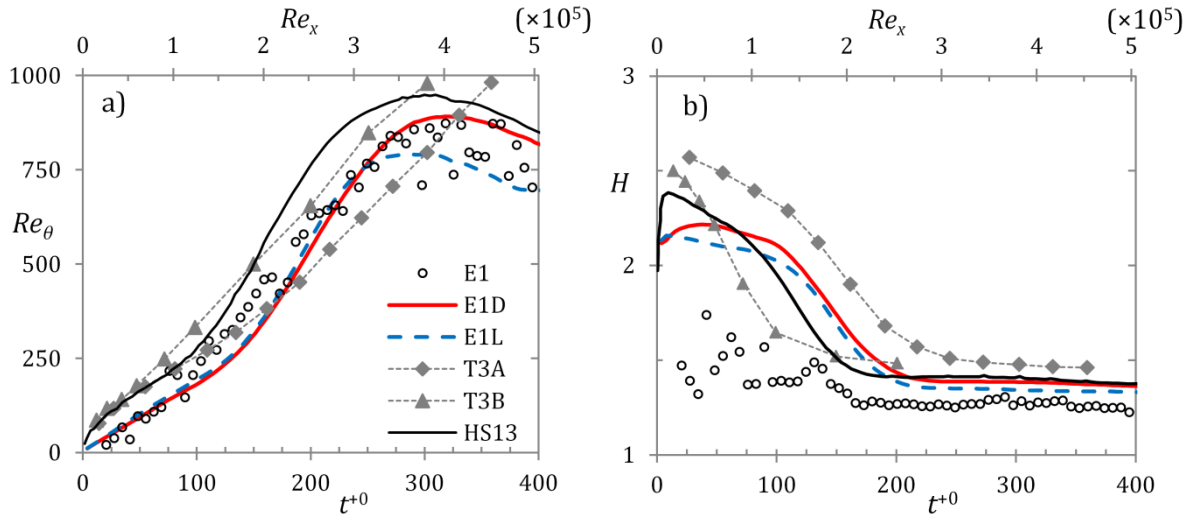


Figure 6.7. Development of the a) momentum thickness Reynolds number ( $Re_\theta$ ), and b) shape factor ( $H$ ) for case E1, E1D and E1L compared with that of step-acceleration case (HS13) of He & Seddighi [7], and bypass transitional flow cases (T3A and T3B) of Roach & Brierley [180].

It is seen that the numerical data shows a good agreement with the experimental data for the development of momentum thickness Reynolds number. However, poor PIV measurements in the wall region seem to affect the accuracy of the displacement thickness. The numerical data of

E1D and E1L are assumed to be a better representative of the flow development than the experimental data of E1.

The early development of the momentum thickness of cases E1D and E1L is qualitatively similar to that of HS13, which is a characteristic of laminar flow. However, the rate of the development here is slightly slower. In HS13, the transition occurs at  $t^{+0} \sim 90$ , at which point the value of  $Re_{\theta}$  is  $\sim 250$ . The transition is delayed in the present case, occurring at  $t^{+0} \sim 120$  when  $Re_{\theta} \sim 225$ . It can be deduced that both the rate of the development and the magnitude of the changes of the present case are lower than those in the step-like acceleration of HS13. A similar trend is also shown in the development of the shape factor for the present case. For case HS13, the value of  $H$  reaches nearly 2.4 in the early part of the transient ( $t^{+0} \sim 10$ ) indicating a ‘laminarizing’ effect of the flow acceleration. However, the same in the present case reaches a maximum of 2.2 at  $t^{+0} \sim 40$  and reduces relatively gradually thereafter. At the point of onset of transition, the value of  $H$  is  $\sim 2$ , matching that of HS13. The momentum-thickness Reynolds number and shape factor of the present cases E1-E3 and their reproduced simulation cases are compared with each other in Figure 6.8.

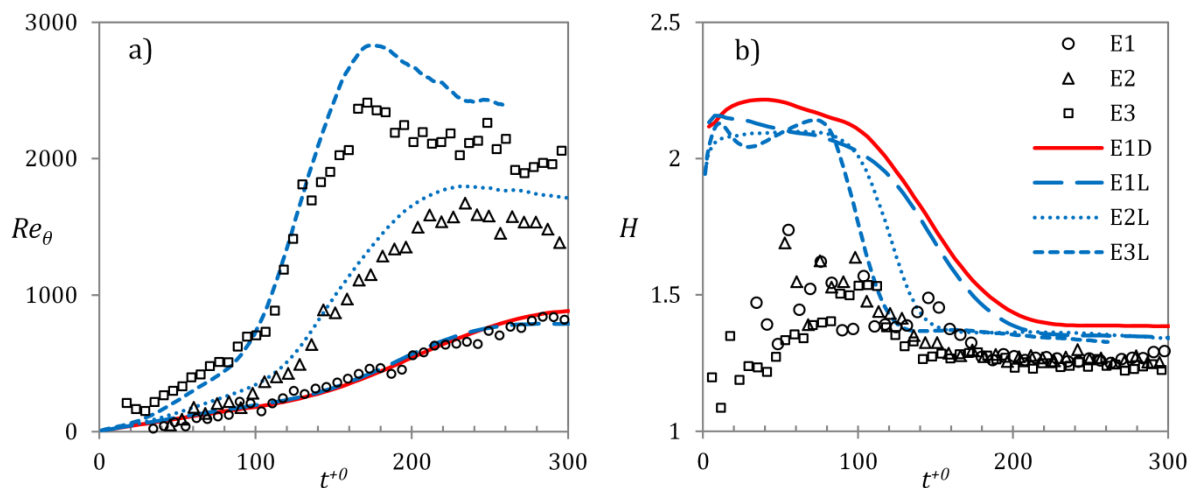


Figure 6.8. Development of the a) momentum thickness Reynolds number ( $Re_{\theta}$ ), and b) shape factor ( $H$ ) for case E1, E2, E3 and their respective reproduced simulation cases.

### 6.2.3 Response of mean and r.m.s. fluctuating velocities

In this section, the transient behaviours of mean and r.m.s. fluctuating velocities are investigated. The initial and final velocities and the corresponding Reynolds numbers for these cases are presented in Table 6.1. As discussed earlier, the increase in flow is achieved by sudden opening of the control valve; however, the time taken to achieve the higher flowrate is a characteristic of the flow-loop system.

The transient development of the statistical quantities at different wall normal locations for case E1 is presented in Figure 6.9. Also presented in the figure are the simulation cases E1D and E1L. The wall normal locations  $y/\delta = 0.07, 0.2, 0.45$  and  $1$  correspond to  $y^{+0} = 11.9, 35.6, 80.1$  and  $178$ . It should be noted that all subplots share the same legend, shown in subplots (a) and (c). The times of onset and completion of transition for case E1, as obtained from friction coefficient development, are 2.45 and 4.65 seconds, respectively.

For PIV measurements, it is seen that a small jump of  $u'_{rms}$  in the core of the flow is recorded immediately after the start of the transient. This is attributed to the finite repeatability of sudden opening of the control valve. Gorji [60] used both PIV and LDV measurements to demonstrate that a *controlled* flow opening does not suffer from this shortcoming. The *ideal* response of the streamwise component can be seen in the response of E1D and E1L, where the streamwise component remains unchanged in the core region during this time. Barring the anomalous behaviour of  $u'_{rms}$  experimental data in the core region, it is clear that there is a good agreement between experiment and simulations. The timing and magnitude of the responses of both mean and turbulent quantities are well represented by the simulations.

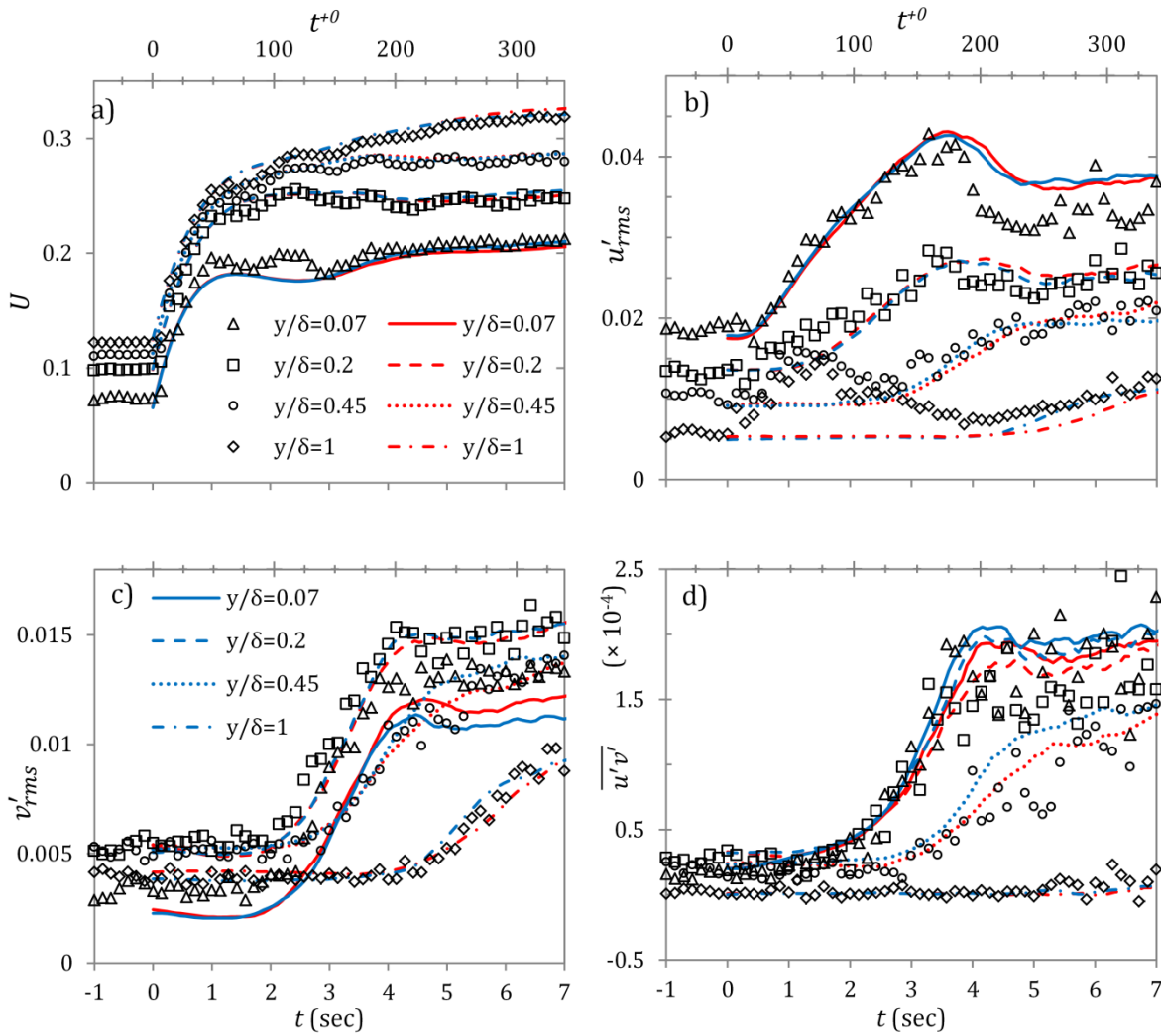


Figure 6.9. Transient development of mean, fluctuating and Reynolds stress components for case E1, E1D and E1L. Symbols denote the experimental data of E1; red and blue lines represent the numerical data of E1D and E1L, respectively. All quantities are in absolute units:  $m/s$  for (a)-(c); and  $m^2/s^2$  for (d). All subplots share the same legend, which is split into subplots (a) and (c).

The mean velocity at all locations is seen to respond immediately at the start of the transient representing a plug-like response of the mean flow. The r.m.s. fluctuating velocities show a different behaviour from that of the mean flow. The streamwise component,  $u'_{rms}$ , responds immediately after the start of the transient only in the near-wall locations, while it undergoes a delay in the core of the flow. On the other hand, the transverse component,  $v'_{rms}$ , and Reynolds stress,  $\overline{u'v'}$ , remain unchanged at all locations during the pre-transition period. The early response of the streamwise component in the wall region is attributed to the elongation and enhancement of the streaky structures. During the pre-transitional period,  $u'_{rms}$  in the near-wall

region undergoes a significant increase, approaching or even overshooting the final steady value. This, however, is not a measure of the increase of ‘conventional’ turbulence activity. The absence of change in the transverse components can be seen as evidence of absence of the generation of new turbulence during this period. As discussed by He & Seddighi [7, 8], these flow features correspond to the buffeted laminar region of the boundary layer bypass transition.

The wall-normal component and the Reynolds stress begin responding in the near-wall region at the onset of transition, representing the generation of ‘new’ turbulent structures in the flow. During the transitional period, these increase monotonically reaching the final steady values with only a slight overshoot over the final steady values. During this period, the streamwise component in this region reaches a peak and decreases slightly afterwards to reach the final steady value. This decrease in the near-wall region is attributed to the breakdown of streaks and generation of turbulent spots, resulting in redistribution of energy to the transverse components.

In the core region, the response of  $u'_{rms}$ ,  $v'_{rms}$  and  $\overline{u'v'}$  show a similar trend of a delayed response, with increasing delays at increasing distance from the wall. This is consistent with the well-accepted feature of unsteady flows and has been attributed to a diffusion mechanism due to propagation of turbulence from the wall to the core of the flow (He & Jackson [44]).

The transient development of the mean, fluctuating and Reynolds shear stress components for cases E2 and E3 are presented in Figure 6.10 and Figure 6.11, respectively. Also shown in the figures are their reproduced LES simulation cases E2L and E3L, respectively. The trends of mean and turbulence behaviour in these cases are similar to that observed in E1. It is again seen that the reproduced simulation cases show a consistent response of mean flow and turbulence in comparison to the experimental data. However, the numerical data of E3L shows a slightly earlier response in the wall-normal component in the near-wall region.

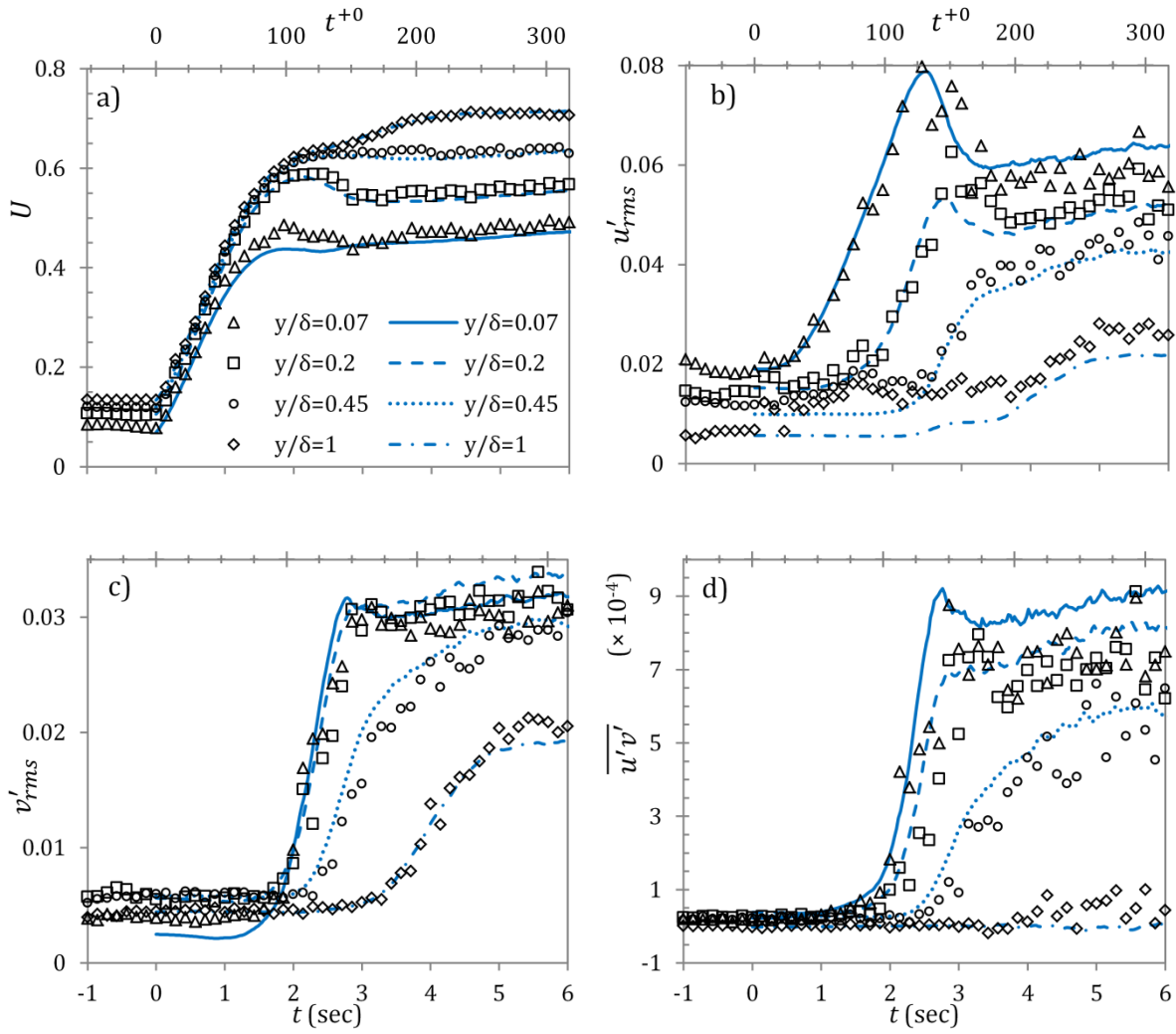


Figure 6.10. Transient development of mean, fluctuating and Reynolds stress components for case E2 and E2L. Symbols denote the experimental data of E2; blue lines represent the numerical data of E2L. All quantities are in absolute units:  $m/s$  for (a)-(c); and  $m^2/s^2$  for (d). All subplots share the same legend.

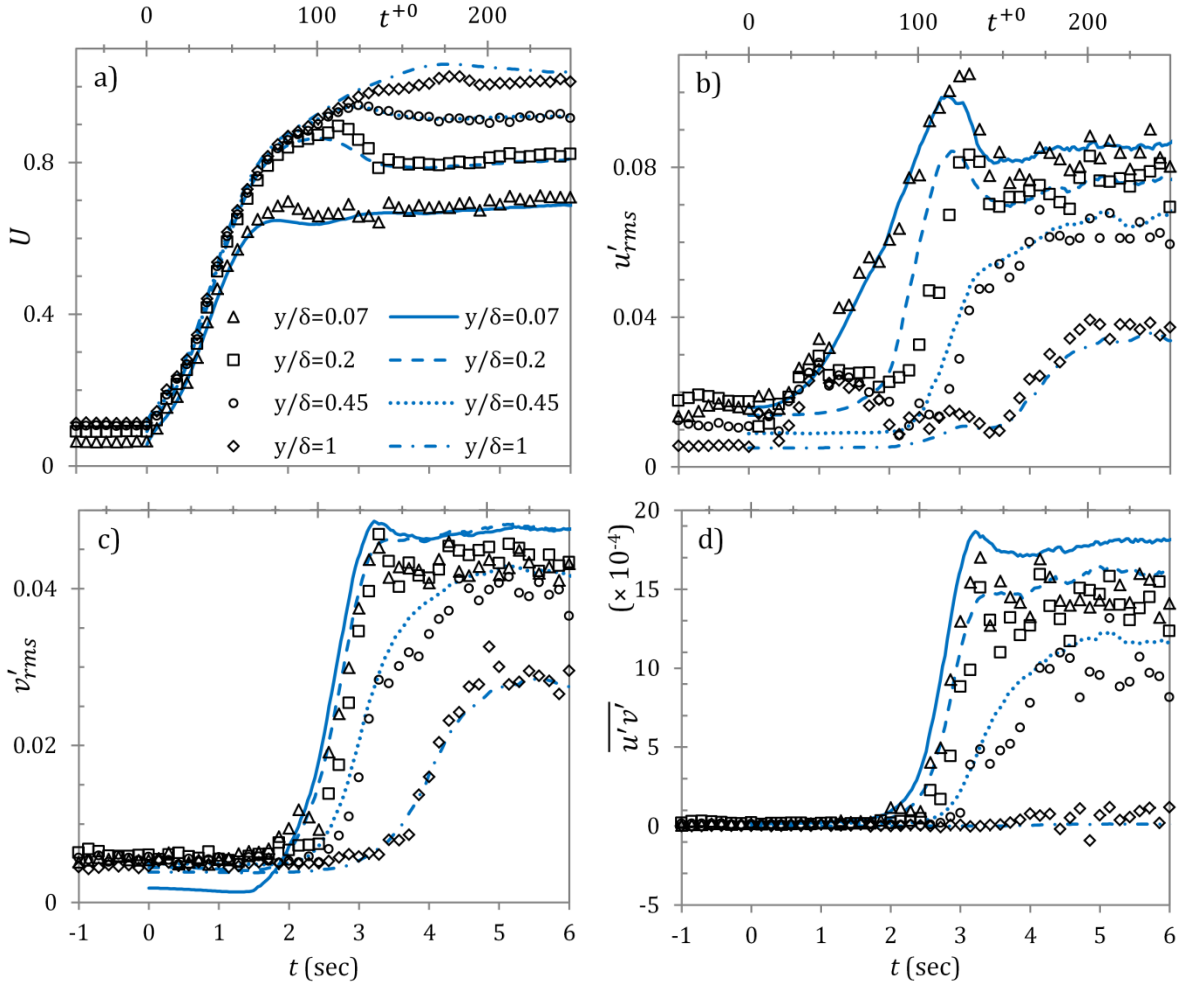


Figure 6.11. Transient development of mean, fluctuating and Reynolds stress components for case E3 and E3L. Symbols denote the experimental data of E3; blue lines represent the numerical data of E3L. All quantities are in absolute units:  $m/s$  for (a)-(c); and  $m^2/s^2$  for (d). All subplots share the same legend.

In order to make appropriate comparisons between the behaviours of turbulence in cases E1-E3, the change in turbulent quantities is scaled corresponding to the flow acceleration in each case. The scaled r.m.s. fluctuating velocity is defined as,

$$u'_{rms}^{\wedge}(y^{+0}, t^{+0}) = \frac{u'_{rms}(y^{+0}, t^{+0}) - u'_{rms}(y^{+0}, 0)}{U_{b1} - U_{b0}} \quad (6.9)$$

$$v'_{rms}^{\wedge}(y^{+0}, t^{+0}) = \frac{v'_{rms}(y^{+0}, t^{+0}) - v'_{rms}(y^{+0}, 0)}{U_{b1} - U_{b0}} \quad (6.10)$$

The development of the scaled r.m.s. velocity profiles for the present cases are shown in Figure 6.12. The reproduced simulation cases are shown to clearly follow their respective experimental cases, except  $v'_{rms}^{\wedge}$  in E3L which is seen to develop more rapidly than that in E3. This early response of E3L is also seen in Figure 6.11.

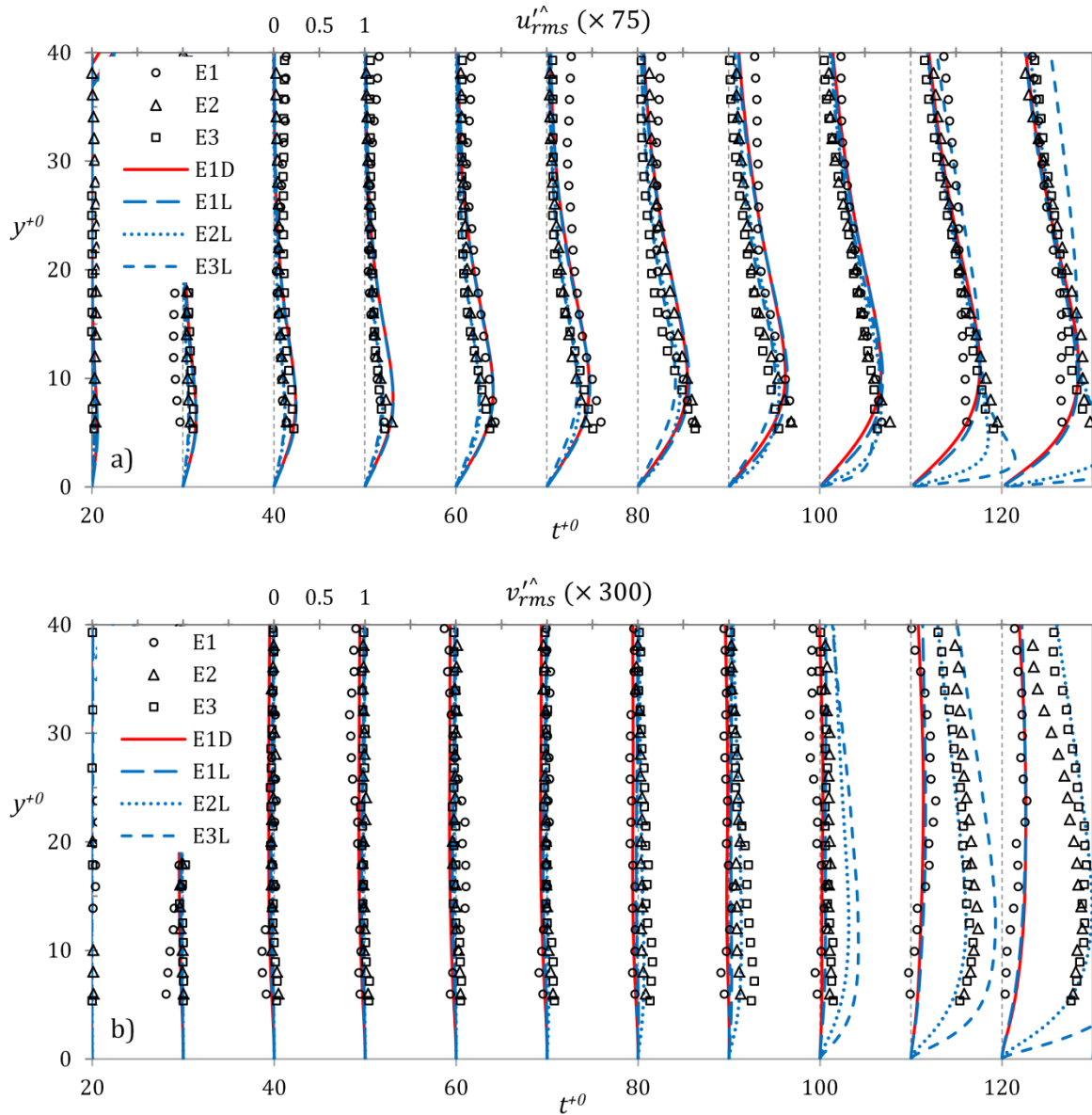


Figure 6.12. Development of the scaled r.m.s. velocity profiles at several time instants in the pre-transition period for a) streamwise component ( $\hat{u}'_{rms}$ ), and b) wall-normal component ( $\hat{v}'_{rms}$ ). The profiles are shifted by an amount proportional to time ( $t^{+\theta}$ ).

The profiles of all cases are shown to collapse with each other during the pre-transitional period. The streamwise component shows a steady increase following the start of the transient, which is attributed to the elongation and enhancement of streaks. The collapse of  $\hat{u}'_{rms}$  profiles for all present cases during this period is evidence for the enhancement of streaks (or the increase in streamwise energy) being proportional to the magnitude of flow acceleration. The wall normal component remains largely unchanged during this period, indicating the absence of

'conventional' turbulence. After the onset of transition, the profiles of  $\hat{v}_{rms}'$  increase rapidly due to the generation of new turbulence; while the profiles of  $\hat{u}_{rms}'$  also diverge from each other during this time. The near-wall velocities, more apparent in the reproduced simulation cases, are seen to evolve more rapidly for cases with a larger flow acceleration. This is consistent with the findings of He & Seddighi [8] and Gorji [60].

### 6.3 Instantaneous Flow Response

This section is devoted to discussing the instantaneous behaviour of the flow. The instantaneous streamwise and spanwise velocities for cases E1 and E2 were captured by the p-PIV configuration. As described earlier in §4.2, this configuration requires the camera to be placed on top of the test section, while the laser is fired from the side. The field-of-view (FOV) for this configuration was about  $75 \text{ mm} \times 75 \text{ mm}$  (equivalent to  $3\delta \times 3\delta$ ), while the interrogation area (IA) size for processing these images was set to  $64 \text{ pixels} \times 64 \text{ pixels}$ .

The instantaneous streamwise fluctuation contours at several time instants during the transient are presented in Figure 6.13 and Figure 6.14 for cases E1 and E2, respectively. The instantaneous fluctuations are obtained from subtraction of the mean velocity, averaged in both streamwise and spanwise directions of the FOV, from the instantaneous velocity ( $u' = u - \bar{u}$ ). The measurement plane is 2 mm above the bottom wall of the channel, equivalent to  $y/\delta = 0.08$  or  $y^{+0} \sim 14$ . Also presented alongside in the figures are the contours obtained from the reproduced simulations at similar time instants; Figures 6.13 (b) and (c) present the reproduced DNS and LES cases of E1 – namely E1D and E1L, respectively, and Figure 6.14(b) presents case E2L. It should be noted that the domain size used to show the contours of the simulation cases in these figures have been clipped to match the FOV of the PIV experimental results of E1 and E2. The original domain size of these simulation cases, as showed in Table 6.2, is  $18\delta \times 5\delta$  in the X-Z direction. However, in order to make appropriate comparison with the experimental results, only a section of the domain –  $3\delta \times 3\delta$  – is shown here.

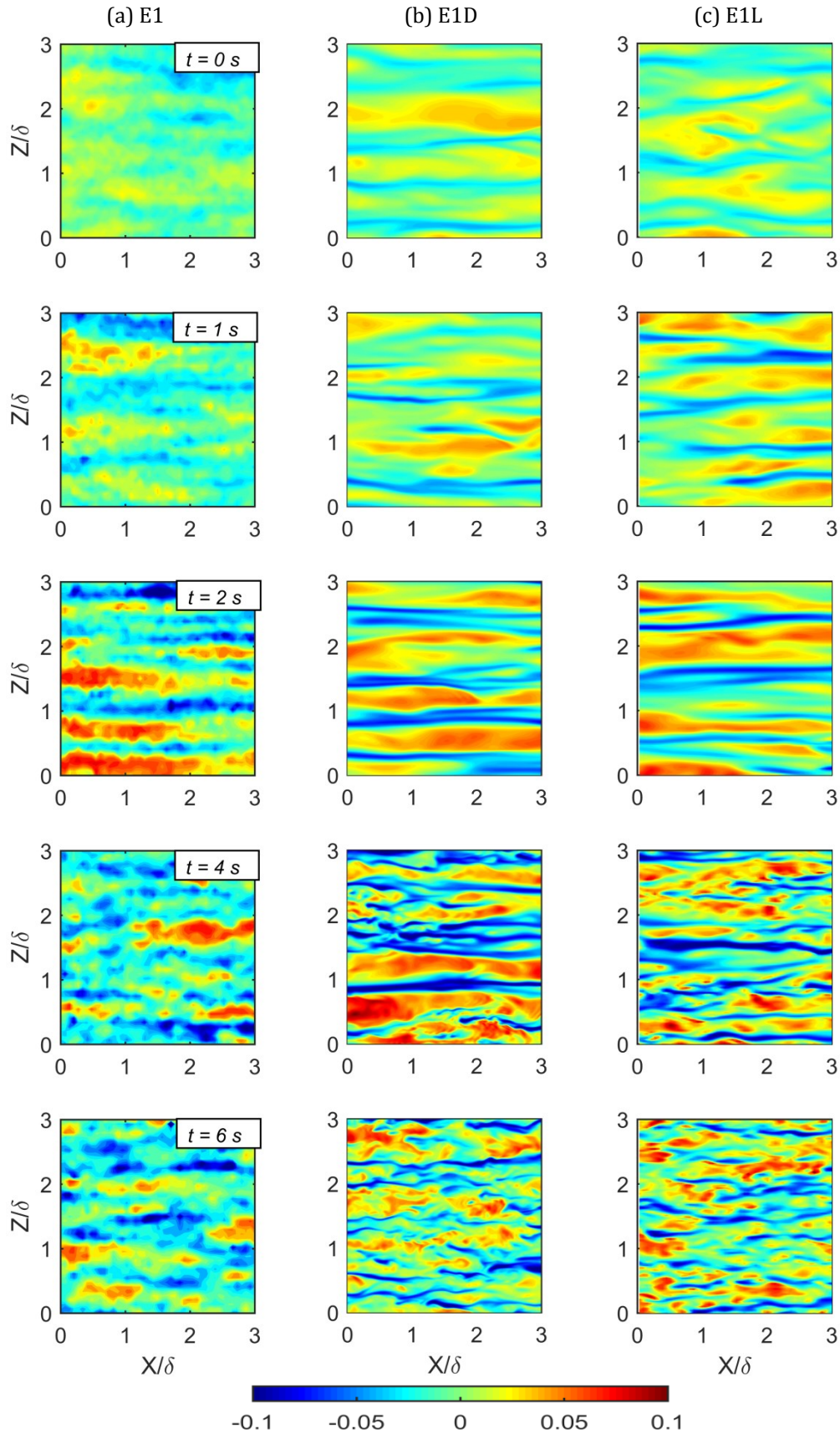


Figure 6.13 Contour plots of streamwise velocity fluctuations,  $u'$  (m/s), at several instants during the transient at wall distance of  $y = 2$  mm for cases a) E1, b) E1D, and c) E1L.

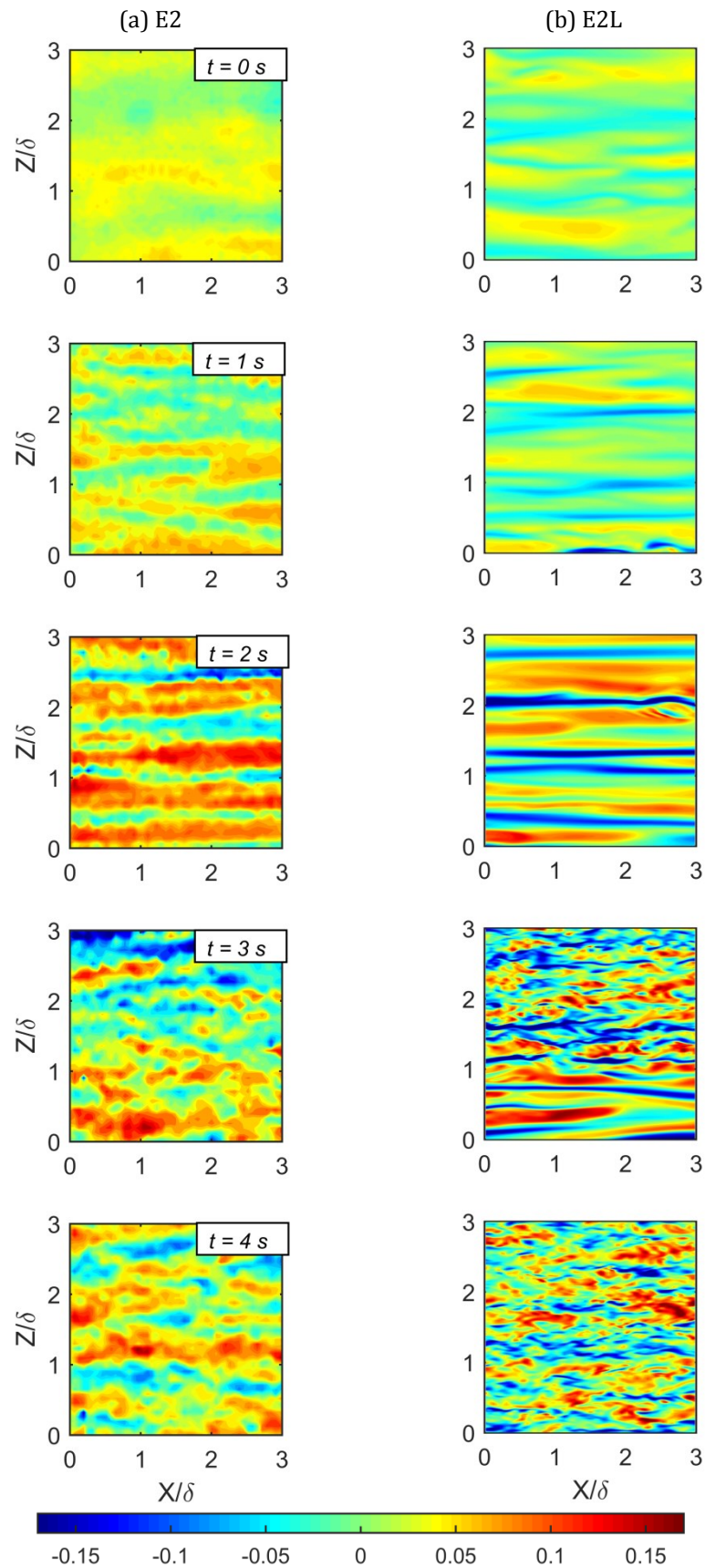


Figure 6.14 Contour plots of streamwise velocity fluctuations,  $u'$  (m/s), at several instants during the transient at wall distance of  $y = 2$  mm for cases a) E2, and b) E2L.

Figure 6.13 shows a remarkable comparison for the elongation, enhancement and breakdown of streaks between the experimental case (E1) and the numerical cases (E1D and E1L). On the other hand, there are slight differences between the timing and magnitude of streak development of experimental case, E2, and the reproduced simulation case, E2L, as seen in Figure 6.14. As the formation and instability of streaks are dependent of the initial flow structures in the fully developed flow before the commencement of the acceleration, slight changes are expected. However, as shown in §6.2, the ensemble-averaged behaviours of the turbulent statistics for E2 and E2L are similar. It is clear that the simulation cases are able to accurately reproduce the flow structures captured by p-PIV measurements.

Considering the experimental contours (Figure 6.13(a) and Figure 6.14(a)), it is seen that the initial flow (at  $t = 0$  sec) has finite streak structures of streamwise fluctuations, which is typical of a fully-developed turbulent flow. After the commencement of the acceleration, the streaky structures are seen to elongate and become stronger in magnitude. The formation and enhancement of these structures are evident in the Figure 6.13(a) and Figure 6.14(a) at  $t = 1$  and 2 seconds, which denote the pre-transitional period (ref. Table 6.3). Further in the transitional period, these streaks are seen to break up and isolated spots of turbulence bursts appear in the flow. This is shown in Figure 6.13 at  $t = 4$  seconds for case E1; and in Figure 6.14 at  $t = 3$  seconds for case E2. As time proceeds, these isolated spots grow in size and merge with each other. The transition is said to be complete when the entire wall surface is covered by this newly generated turbulence, represented by the final plots at  $t = 6$  and 4 seconds for cases E1 and E2, respectively. The flow structures described above are the same as those found in the DNS studies of step-like accelerating flows presented by He & Seddighi [7, 8], even though the present cases undergo a much slower flow acceleration. This is consistent with the observations of DNS study of Seddighi *et al.* [59] and experimental study of Gorji [60].

Quantitative information about the streaks can be obtained by the near-wall correlations of the streamwise velocity ( $R_{11}$ ). Due to technical difficulties, p-PIV measurements closer than 2 mm

of the bottom wall could not be made in the present investigation. Thus, a quantitative comparison of the correlations obtained from the reproduced simulations is presented herein. Figure 6.15 presents the correlations in the streamwise and spanwise directions for simulations E1D and E2L.

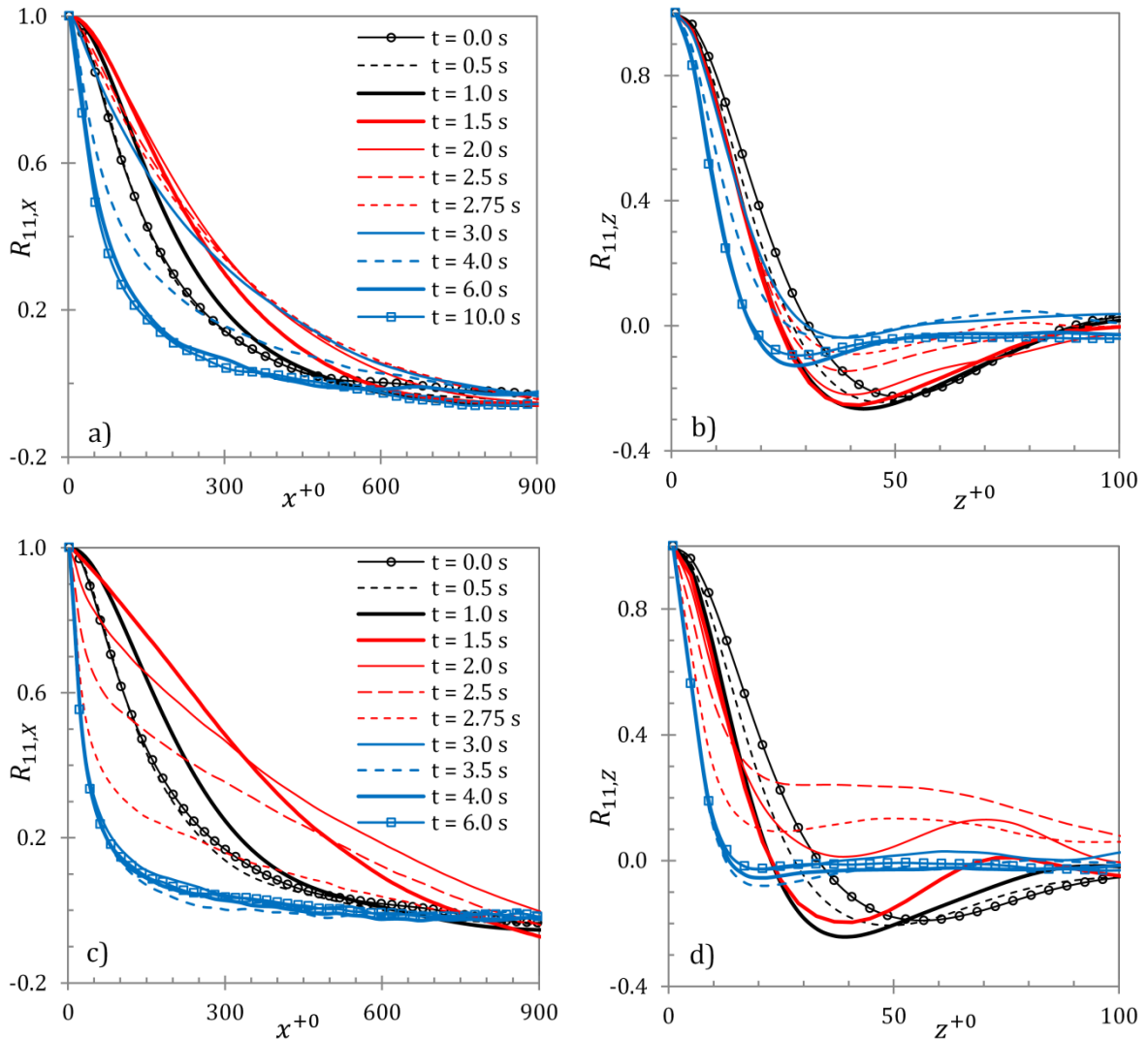


Figure 6.15. Streamwise velocity auto-correlations ( $R_{11}$ ) at several time instants for case E1D (a,b) and E2L (c,d) in the streamwise (a,c) and spanwise directions (b,d) at  $y^+ = 5$ . Subplots (a-b) share a legend; while (c-d) share a legend.

The streamwise correlations of E1D show that the averaged streaks have an initial length of 600 wall units, which get stretched up to roughly 760 wall units in the late pre-transition period. Thereafter, in the transitional period the correlations are seen to reduce and reach the final steady value of 500 wall units. These values can be directly compared to the step-like

acceleration case of He & Seddighi [7] – HS13, having similar initial and final Reynolds numbers. It was reported that in the pre-transition period of the case HS13, the streaks were stretched from 580 wall units to 900 wall units. It is clear that the elongation of streaks in the present case is much weaker in comparison. In contrast to the streamwise correlations, the development of spanwise correlations is similar for cases E1D and HS13. The location of minimum spanwise correlation represents half the streak spacing, whereas the minimum value of the correlation indicates the strength of the streaks. For E1D, the spacing of streaks in the initial flow was 100 wall units which gets reduced to about 80 in the pre-transition stage and further reduces to 60 during the transitional period, which are consistent with the values reported for case HS13. The difference of streak development between the present ramp-type case E1D and the step-like case of HS13 is consistent with the observation of Seddighi *et al.* [59].

The development of streaks is also quantitatively different in the cases E1D and E2L. In case E2L, the streaks are much longer and are more densely packed in comparison to those in E1D. For case E2L, the initial streaks of length of 700 wall units are stretched to about 900 wall units in the pre-transition period, while the spacing between the streaks is reduced from 100 to roughly 75 wall units. This accentuated behaviour for the higher acceleration case is consistent with that of the step-like cases reported in the previous chapter.

## 6.4 Correlations of Flow Transition

As discussed previously, He & Seddighi [8] showed that the onset of transition in accelerating flows can be correlated with the initial turbulence intensity, in a similar manner as the critical Reynolds number ( $Re_{x,cr}$ ) of boundary layer flows is correlated with the free-stream turbulence (FST) intensity. The same has been shown for high  $Re$ -ratio step-like accelerating flow cases in Chapter 5. The initial turbulence intensity,  $Tu_0$  defined in equation (5.2), can be described as the peak turbulence, which remains unchanged from that of the initial flow immediately after the acceleration, existing in the bulk of the final flow velocity. He & Seddighi [8] also defined an

equivalent Reynolds number,  $Re_t$  defined in equation (5.3), which corresponds to the Reynolds number,  $Re_x$ , of a boundary layer flow. It was demonstrated by He & Seddighi [8], that  $Re_t$  has the same significance in unsteady flow transition as  $Re_x$  has in boundary layer transition.

For step-like acceleration flow cases of the DNS study of He & Seddighi [8] and the high  $Re$ -ratio acceleration study in the previous chapter, the bulk velocity changes to that of the final flow almost immediately following the acceleration. Hence, it can be assumed that the final bulk velocity ( $U_{b1}$ ) is the characteristic convective velocity during the entire transition process. However, in the present experimental cases, the acceleration is much slower i.e. the velocity is continuously increasing during the transient and the transition occurs within the ramp period itself. Hence, the final bulk velocity cannot be used as the characteristic convective velocity. In order to correlate the onset of transition, herein, the convective velocity is assumed to be the bulk velocity at the onset of transition,  $U_b(t_{cr})$ . The turbulence intensity in the ramp-like unsteady flow is redefined as,

$$Tu_0 = \frac{(u'_{rms,0})_{max}}{U_b(t_{cr})} \approx 0.375 \frac{U_{b0}}{U_b(t_{cr})} (Re_{b0})^{-0.1} \quad (6.11)$$

In a step-like flow acceleration, the equivalent Reynolds number was defined using the analogy of distance travelled by fluid particle ( $x = tU_{b1}$ ). For the present slowly developing cases, this distance is given by  $x(t) = \int_0^t U_b(t) dt$ . The equivalent Reynolds number is, thus, redefined as,

$$Re_t(t) = \frac{x(t) U_b(t)}{\nu} = \frac{U_b(t)}{\nu} \int_0^t U_b(t) dt \quad (6.12)$$

As discussed earlier, the critical time of onset of transition ( $t_{cr}$ ) and completion of transition ( $t_{turb}$ ) can be obtained from the development of the friction coefficient. He & Seddighi [7, 8] noted that the time of minimum value of the friction coefficient corresponds to the generation of new turbulent spots, and hence the onset of transition. The time of first peak of friction coefficient, after its recovery, corresponds to the completion of transition. These times obtained for the present cases are presented in Tables 6.3-6.4.

The equivalent critical Reynolds number and the transition period Reynolds number for ramp-type unsteady flows are defined as,

$$Re_{t,cr} = \frac{U_b(t_{cr})}{\nu} \int_0^{t_{cr}} U_b(t) dt \quad (6.13)$$

$$\Delta Re_{t,cr} = \frac{U_b(t_{turb})}{\nu} \int_{t_{cr}}^{t_{turb}} U_b(t) dt \quad (6.14)$$

Figure 6.16 presents the relation between the equivalent critical Reynolds number ( $Re_{t,cr}$ ) and the corresponding initial turbulence intensity,  $Tu_0$  for the present experimental cases (E1-E7) and the simulations cases (E1D; E1L-E3L). Also shown in the figure is the relation presented by He & Seddighi [8] and the high  $Re$ -ratio LES cases of Chapter 5 (U1-U6), for comparison.

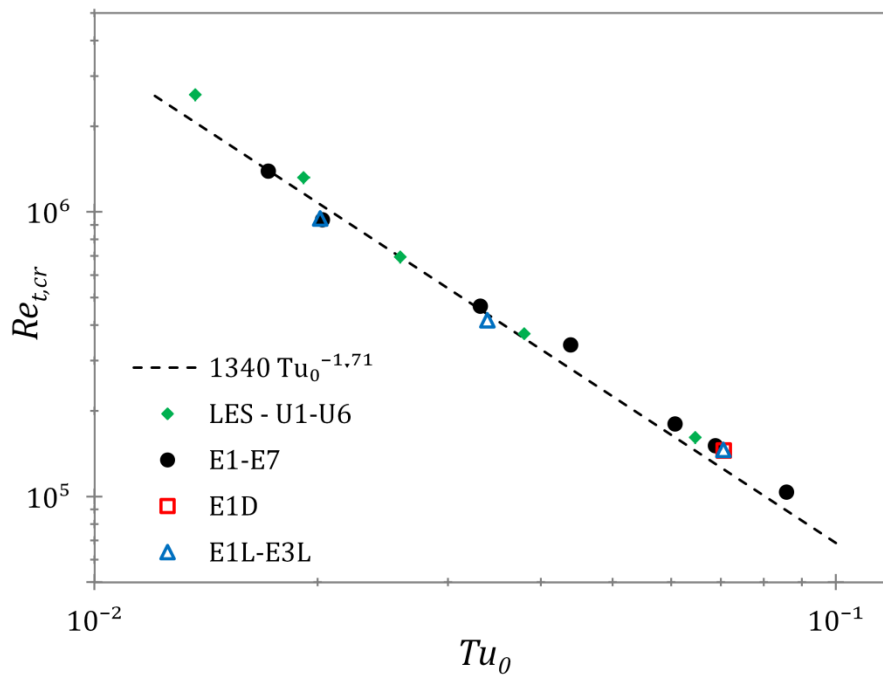


Figure 6.16. Dependence of equivalent critical Reynolds number on initial turbulence intensity for the present cases E1-E7 and their reproduced simulation cases.

The present data is seen to follow a trend similar to that of He & Seddighi [8]. A best-fit curve to the present experimental data gives a relation,  $Re_{t,cr} = 1910 Tu_0^{-1.62}$ . Although the equivalent length-scale ( $x$ ) has been modified for the present ramp accelerations, the choice of characteristic velocity used for normalisation –  $U_{b1}$  for step-like cases,  $U_b(t_{turb})$  and  $U_b(t_{cr})$

for the present cases — is still arbitrary. However, the relation of He & Seddighi [8] can be used for rough estimation of the onset of transition in ramp-like flow accelerations, using the modified definitions, equations (6.11) and (6.13).

The transitional period has been shown to be another important parameter for unsteady flow transition [8]. For boundary layer bypass transition flows, several empirical relations have been presented in the past, correlating the transitional length Reynolds number with the critical Reynolds number, notably the power-relation of Narasimha *et al.* [86], and the linear-relation of Fransson *et al.* [85]. He & Seddighi [8] correlated the same for unsteady flows. It was shown that the data for unsteady flow cases can be reasonably predicted by boundary layer correlations if a factor of 0.5 is applied. In Chapter 5, it is shown that high *Re*-ratio accelerating cases follow a similar trend.

For the present ramp-type flow accelerations, the dependence of the transitional period Reynolds number on critical Reynolds number is presented in Figure 6.17, making use of the modified definitions. The figure also shows the numerical results of He & Seddighi [8] and the high *Re*-ratio LES cases (U1-U6) of Chapter 5.

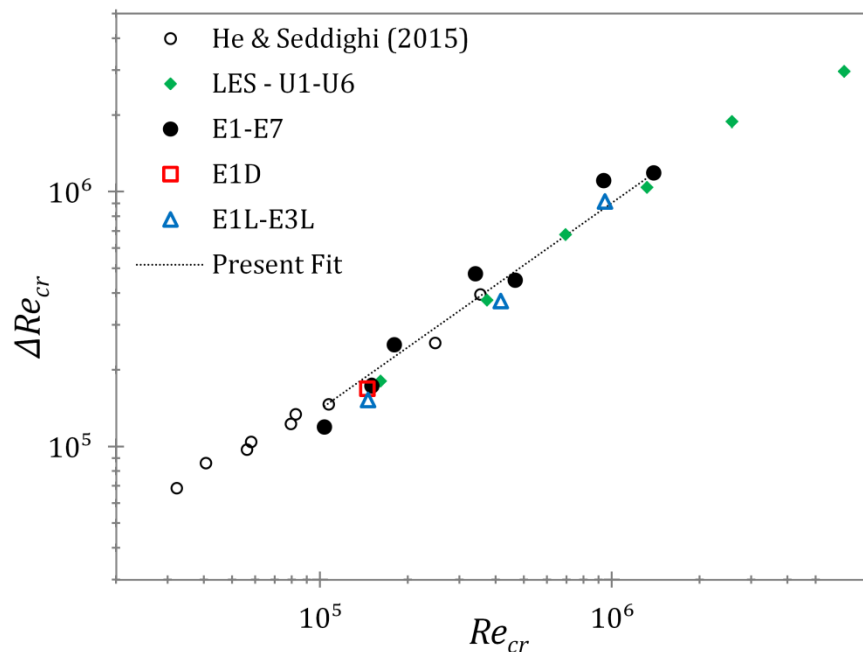


Figure 6.17. Relationship between transition period Reynolds number and critical Reynolds number for the present experimental cases E1-E7 and their reproduced simulation cases.

It is seen that the present experimental data is reasonably consistent with the trend of numerical results of He & Seddighi [8]. Similar to the step-like flow accelerations the present data can be estimated by the boundary layer correlations if a factor of 0.5 is applied. The trend of the present experimental data, similar to the step-like accelerations of Chapter 5, suggests a power correlation between  $\Delta Re_{t,cr}$  and  $Re_{t,cr}$ . A best-fit curve gives the relation,  $\Delta Re_{t,cr} = 12.5 Re_{t,cr}^{0.81}$ .

## 6.5 Summary

Ramp-type flow excursions with varying Reynolds number-ratio are carried out in the flow facility, and are then reproduced in simulation using DNS and LES. The numerical data is shown to be in good agreement with the experimental data. The time of minimum friction coefficient and its recovery period predicted using simulations agree well with those obtained from the wall friction hotfilm measurements. For low  $Re$ -ratio ramps, the measured friction is well represented by the numerical data; however, there are some, but still small inconsistencies in experiment and simulation for high  $Re$ -ratio ramps, which is largely due to the hotfilm calibration. The responses of mean and turbulence quantities obtained from simulations are shown to closely follow the PIV measurements. However, in the near-wall region, the PIV measurements in the high-velocity gradient region are poor and are not able to provide reliable data for comparison. A small jump in the streamwise fluctuations far from the wall is captured in the PIV measurements immediately following the commencement of the acceleration. This, however, is attributed to the finite repeatability of the control valve. The simulations are shown not to suffer from this shortcoming and, thus, are considered better representative of an *ideal* response.

It is shown that the ramp-type accelerating flows respond in fundamentally the same transition process as seen in simulations of step-like flow accelerations. The flow is shown to respond in three stages – namely, the pre-transition, transition and fully turbulent stage due to He &

Seddighi [7] – which resemble the three regions of bypass transition of boundary layer flows. In comparison to step-like flow acceleration, the onset of transition in ramp-type flow acceleration is delayed, with a slower rate of flow development and reduced changes in the flow – which is consistent with the findings of the DNS study of Seddighi *et al.* [59]. The time-development of the mean flow to a step-like flow acceleration has previously been shown to bear resemblance to that of the laminar boundary layer given by the solution to Stokes' first problem. Herein, the Stokes' solution is modified for multi-step increase of bulk velocity to account for the slower flow acceleration. It is shown that during the entire pre-transition period, the time-developing perturbation velocity and wall friction for the ramp-like acceleration is represented accurately by the laminar solution.

The definitions of the equivalent critical Reynolds number ( $Re_{t,cr}$ ) and the turbulence intensity ( $Tu_0$ ) have been modified in the present study to account for the time-varying bulk velocity of the present ramp-type accelerations. Using the modified definitions, the relationship for the present data is found to be  $Re_{t,cr} = 1910 Tu_{0,cr}^{-1.62}$ , reasonably consistent with the power-relation given for step-like unsteady flows. Similar to critical Reynolds number, the definition of equivalent transition period Reynolds number ( $\Delta Re_{t,cr}$ ) is also modified to account for the ramp-type acceleration. The transition period Reynolds number is shown to have a power-relation with the critical Reynolds number,  $\Delta Re_{t,cr} = 12.5 Re_{t,cr}^{0.81}$ .

## Chapter 7

# Direct Numerical Simulation of Decelerating Flows

---

This chapter reports a numerical investigation studying the response of turbulence in a decelerating flow using Direct Numerical Simulations (DNS). The deceleration rate of the base flow case investigated herein is higher than those reported in previous studies such as He & Jackson [44], Ariyaratne *et al.* [49], Seddighi *et al.* [57] and Talha [53]. The response of turbulence to the step-like flow deceleration is compared to that in step-like accelerating flows. The deceleration rate of the flow case is also varied from step-like to ramp-type to study the effect of different deceleration rates on the dynamics of turbulence.

The simulation cases investigated herein are introduced in §7.1. In §7.2, the transient behaviour of wall friction, mean and fluctuating velocities, Reynolds stress budget, turbulence spectra and velocity auto-correlations in response to flow deceleration is discussed. The instantaneous flow response is presented in §7.3. Finally, a brief summary of investigations undertaken herein is presented in §7.4.

## 7.1 Present Simulation Cases

Simulations are performed for spatially fully-developed turbulent channel flow subjected to a linear deceleration using the in-house DNS code *CHAPSim* [9]. Although the code has previously been validated in several studies in the literature [7, 9, 57], a validation with benchmark data is presented in §3.5 for the sake of completeness herein.

In the present DNS study, the simulations are performed in a domain of size  $12.8\delta \times 2\delta \times 3.5\delta$ , in the streamwise ( $x$ ), wall-normal ( $y$ ) and spanwise ( $z$ ) directions, respectively (where  $\delta$  is the channel half-height). Fully-developed turbulent flow at  $Re_b = 4200$  ( $Re_\tau \sim 250$ ) is subjected to a linear temporal deceleration to a final steady state of  $Re_b = 2825$  ( $Re_\tau \sim 180$ ). Table 7.1 lists the simulation parameters for the steady flow condition at the initial and final flows.

Case	$Re$	$Re_\tau$	$\Delta x^+$	$\Delta z^+$	$\Delta y_{min}^+$	$\Delta y_{max}^+$	$L_x^+$	$L_z^+$
Initial Flow	4200	252.7	6.30	4.41	0.43	3.95	3226	882
Final Flow	2825	178.9	4.45	3.12	0.31	2.85	2278	623

Table 7.1. Simulation parameters based on initial and final flow conditions.

Cases	Ramp rate <sup>1</sup>	$\Delta t^{+0}$	$\gamma$
D1	1	0.56	$-580.0 \times 10^{-3}$
D2	1/5	2.8	$-116.0 \times 10^{-3}$
D3	1/15	8.4	$-38.7 \times 10^{-3}$
D4	1/50	28	$-11.6 \times 10^{-3}$
D5	1/100	56	$-58.0 \times 10^{-3}$
D6	1/250	140	$-2.32 \times 10^{-3}$
D7	1/500	280	$-1.16 \times 10^{-3}$

Table 7.2. Decelerating flow cases investigated in the present study.

<sup>1</sup> Ramp rates shown relative to the base case, D1

The deceleration flow cases are detailed in Table 7.2. The base case (D1) is subjected to the same ramp rate magnitude as the accelerating case ‘S14’ of He & Seddighi [8] (step-like accelerating flow from  $Re_b = 2800$  to  $Re_b = 4200$ ). Six other cases (D2-D7) are performed with ramp rates 5, 15, 50, 100, 250 and 500 times slower than that of the base case, respectively. The choice of the flow is aimed to cover a range of transient flow characteristics, from a step-like change in case D1 to a ramp-type change in case D7, as will be presented below. Ariyaratne *et al.* [49] represented the deceleration rate with dimensionless parameter  $\gamma$ ,

$$\gamma = \frac{\nu}{u_{\tau 0}^2} \left( \frac{1}{U_{b0}} \frac{dU_b}{dt} \right), \quad (7.1)$$

where  $u_{\tau 0}$  is the friction velocity for the initial steady flow and  $U_{b0}$  is the initial bulk velocity. The ratio  $\nu/u_{\tau 0}^2$  represents the time-scale of turbulence production, and the ratio  $U_{b0}/(dU_b/dt)$  represents the time-scale of the inertia. The value of this parameter for the present decelerating cases is shown in Table 7.2.

## 7.2 Ensemble-Averaged Flow Response

For the purpose of ensemble-averaging, six realizations of each flow case are performed. For each realization, the initial flow fields are taken from different time instants of the same steady flow simulation, separated by  $t^{+0} \sim 500$ . As discussed previously in §3.4, the statistical quantities are averaged over the homogeneous wall-normal plane and over repeated realizations. In this section the behaviour of ensemble-averaged mean and turbulent quantities in response to flow deceleration is discussed.

### 7.2.1 Response of friction coefficient

Figure 7.1 shows the responses of the friction coefficient for the seven cases presented here. For the sake of clarity, the main figure shows the entire post-transient response, while the inset shows the early response of the four faster deceleration cases (D1-D4). The horizontal (dashed)

reference lines represent the initial and final steady state friction coefficients. The early response of sharp decrease is attributed to the dominant effect played by inertia at the beginning of the transient, as previously discussed in Ariyaratne *et al.* [49] and Seddighi *et al.* [57]. The flow responds in a plug-flow-like manner, with very little or no change in the turbulent statistics and in the shape of the velocity profile except for the velocity gradient very close to the wall which decreases sharply. The minimum value of the friction coefficient becomes more negative with increase of the deceleration rate, a trend also reported by Ariyaratne *et al.* [49]. This is expected as the inertial effect is proportional to the imposed deceleration rate. For Cases D1-D4, wall shear stress reaches negative values, indicating a flow separation at the wall. The point where there is a sudden change in gradient corresponds to the time when the imposed flow deceleration ends.

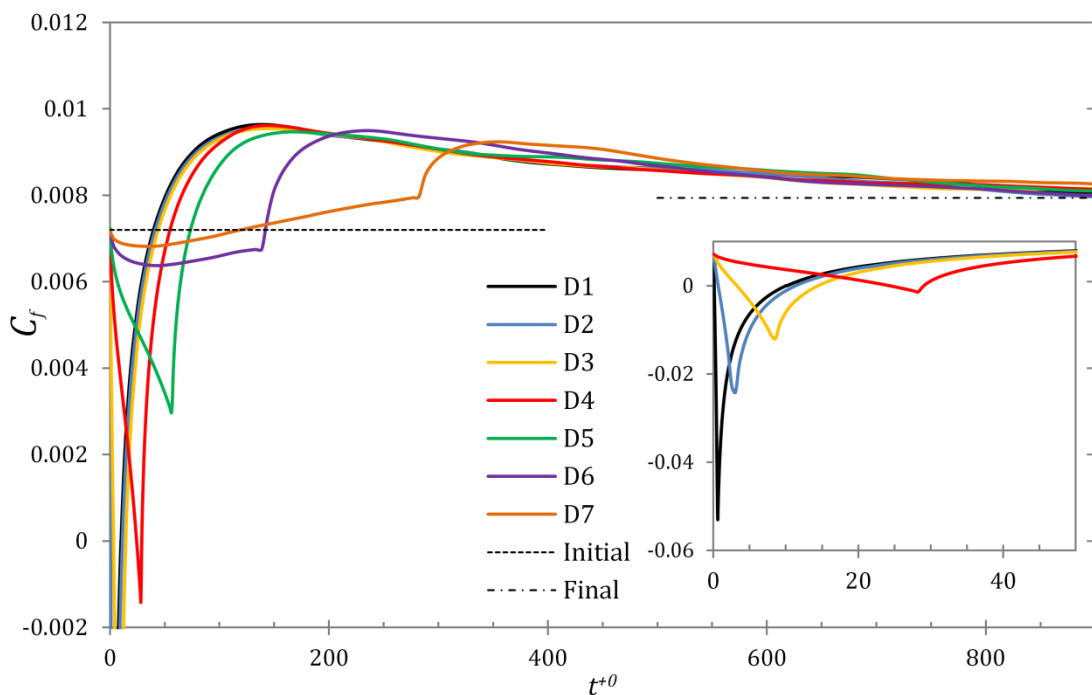


Figure 7.1. Transient response of friction coefficient (Inset shows the cases S1-S4 in a different scale).

At the end of the deceleration period, the plug-flow response of the mean flow leaves a large ‘perturbation’ in the near-wall region, while the shape of velocity far from the wall remains the same as that of the initial flow. This perturbation grows into the flow with time, leading to a sharp increase in wall shear stress and, hence, the friction coefficient. Thereafter, the friction

coefficient reaches a maximum and then gradually settles to the final value. In the subsequent section, it will be shown that this perturbation bears strong similarity to the accelerating flow perturbation.

### 7.2.2 Boundary layer development

Figure 7.2 shows the ensemble-averaged velocity profiles at several time instants. For convenience, only four of the present seven cases have been shown in the figure. The main figures show the profile for the channel half-height, whereas the inset shows the near-wall profiles for each case. For each figure, the legend entry with circle symbol represents the time instant when the deceleration has ended. It is clear that the early response of the flow is plug-like with no change in the shape of the velocity profile, except for the near-wall region. For the fast ‘step-like’ cases (Figures 7.2a & b), the flow at the wall undergoes separation followed by reversal. For the ramp-like case D7 (Figure 7.2d), the near-wall profile is hardly distorted at all, but attains the shape corresponding to the final steady-state at the end of the deceleration period, although the profile in the core of the flow still retains the shape of the initial flow profile. After the deceleration period ends, the profile begins to gradually adjust to the new flow conditions.

In order to investigate the time-developing boundary layer of the unsteady flow, He & Seddighi [7] defined a perturbing velocity,  $\bar{u}^+(y^{+0}, t^{+0})$  in equation (5.8), representing a dimensionless measure of the change in mean velocity. Similar perturbation velocity has also been calculated for the present decelerating flow cases. The profiles of  $\bar{u}^+$  at various  $t^{+0}$  for the base case (D1) are presented in Figure 7.3 along with the accelerating cases ‘S14’ and ‘S03’ of He & Seddighi [8]. Case ‘S14’ accelerates from  $Re_b = 2800$  to 4200 in  $\Delta t^{+0} \sim 0.5$ ; while ‘S03’ accelerates from  $Re_b = 4200$  to 7400 in  $\Delta t^{+0} \sim 1.8$ . Also shown in the figure for comparison is the solution of Stokes’ first problem, given by equation (5.9), recast in terms of  $y^{+0}$  and  $t^{+0}$ .

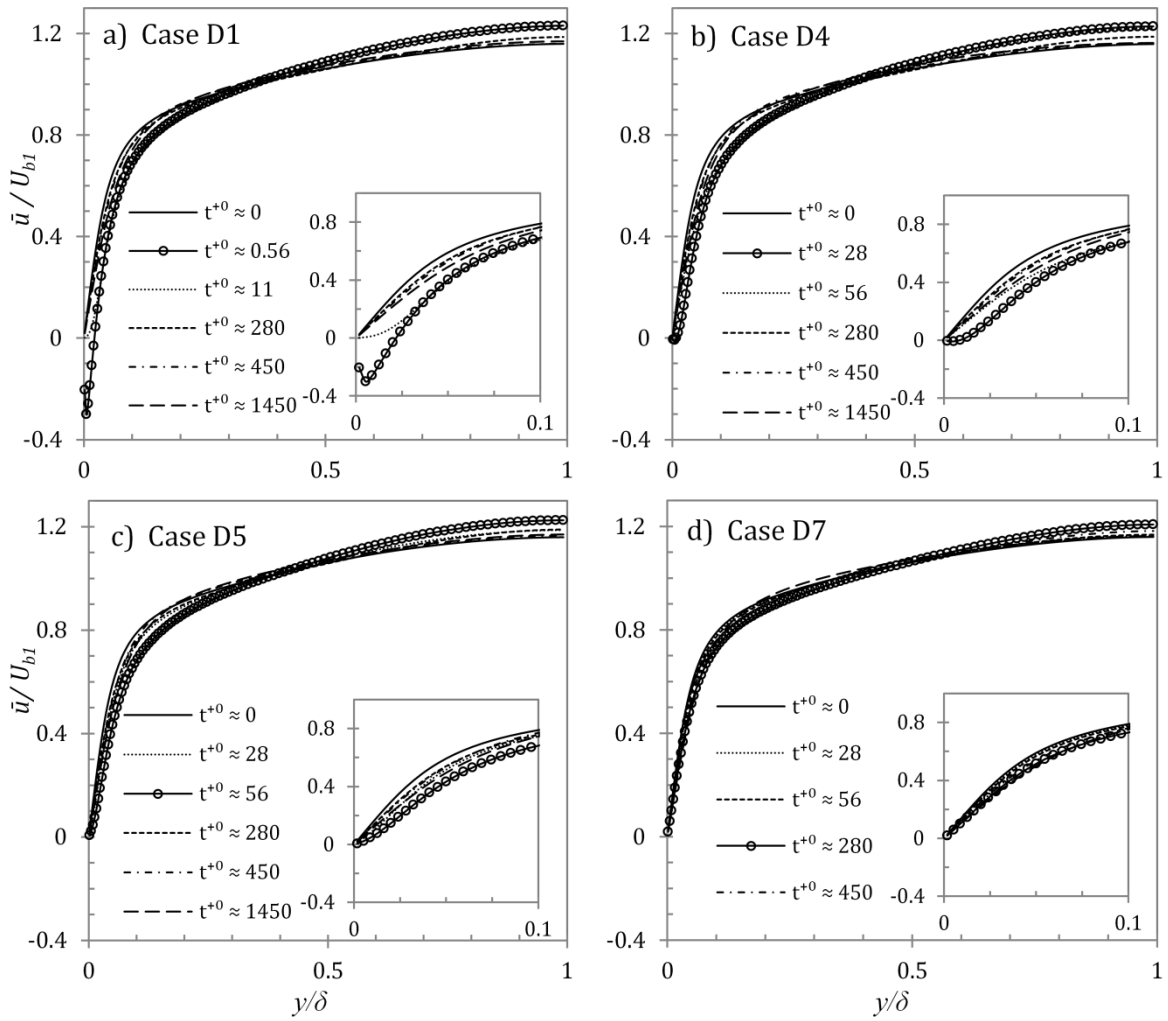


Figure 7.2. Mean velocity profiles of cases D1, D4, D5 and D7 at several time instants (Legend entry with symbols represent end of deceleration period).

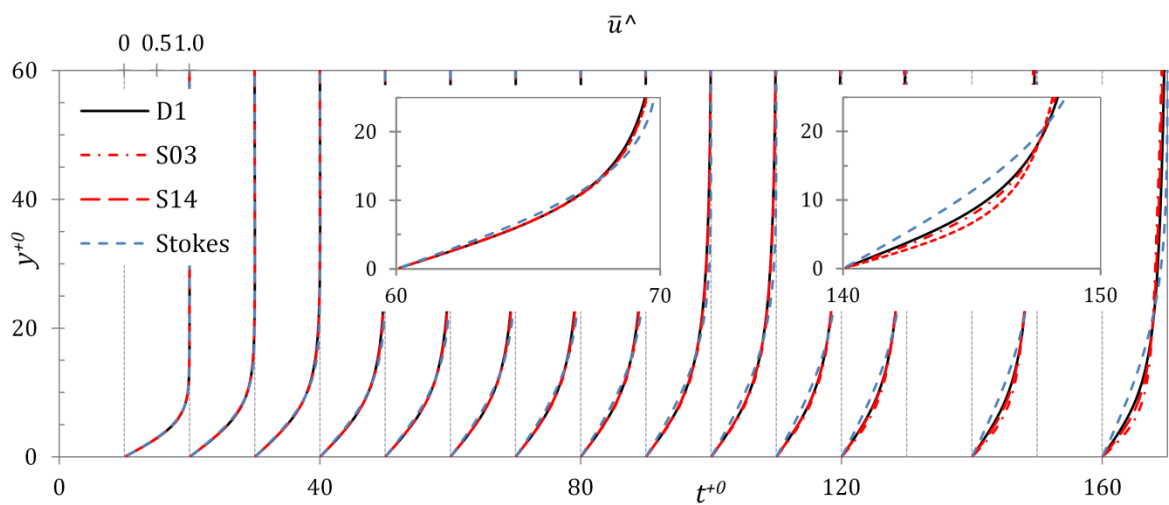


Figure 7.3. Development of the perturbation velocity profiles at several time instants for the present base case D1, the cases ‘S14’ and ‘S03’ of He & Seddighi [8] and the Stokes’ solution. (The profiles are shifted at an amount proportional to the time).

As discussed earlier, the early perturbation is only in the near-wall region due to the plug-like response to the imposed deceleration. This perturbation which starts at the wall then gradually develops into the core region and can be regarded as a time-developing boundary layer originated at the start of the deceleration. This boundary layer development is seen to have strong similarities to that in accelerating flows of He & Seddighi [8]. It is clearly seen in Figure 7.3 that the perturbation velocity profiles of case D1 collapse on top of the accelerating cases 'S03' and 'S14' for  $t^{+0} < 140$ , implying that the time-developing boundary layer of the present case grows at a rate that is the same as that in the accelerating flows. In early stages ( $t^{+0} < 60$ ), these velocity profiles closely resemble those of the Stokes' solution. Later,  $60 < t^{+0} < 140$ , the accelerating and decelerating flow profiles deviate from the Stokes' solution, but they are still in close agreement with each other. Further  $t^{+0} > 140$ , the decelerating flow profiles diverge from that of accelerating flows. It is noted that unlike in the accelerating flows, the perturbation in the decelerating flow is opposite to the flow but this does not cause any difference in the boundary layer development.

To characterise the time-development of step-accelerating flows in pre-transitional stage, He & Seddighi [8] introduced a modified friction coefficient of the perturbation flow,  $C'_{f,du}$  in equation (5.12). It was shown that this friction coefficient was represented by a slight modification of the Stokes' solution, equation (5.14). The similarly modified friction coefficient of equation (5.12) has also been calculated for the present step-like deceleration case, D1. Figure 7.4 compares this modified friction coefficient with that of the step-like accelerating cases 'S03' and 'S14' [8]. Also presented in the figure is the friction coefficient for the solution of the Stokes' first problem and equation (5.13). It is clearly seen that the response of the perturbation friction coefficient of the present step-deceleration case collapses with that of the accelerating flows for  $t^{+0} < 100$ , implying similar initial responses in accelerating and decelerating flows. Thus, similar to that in step-accelerating flow cases, the initial response ( $t^{+0} < 60$ ) of wall shear stress for the step-like deceleration case can be calculated from equation (5.13).

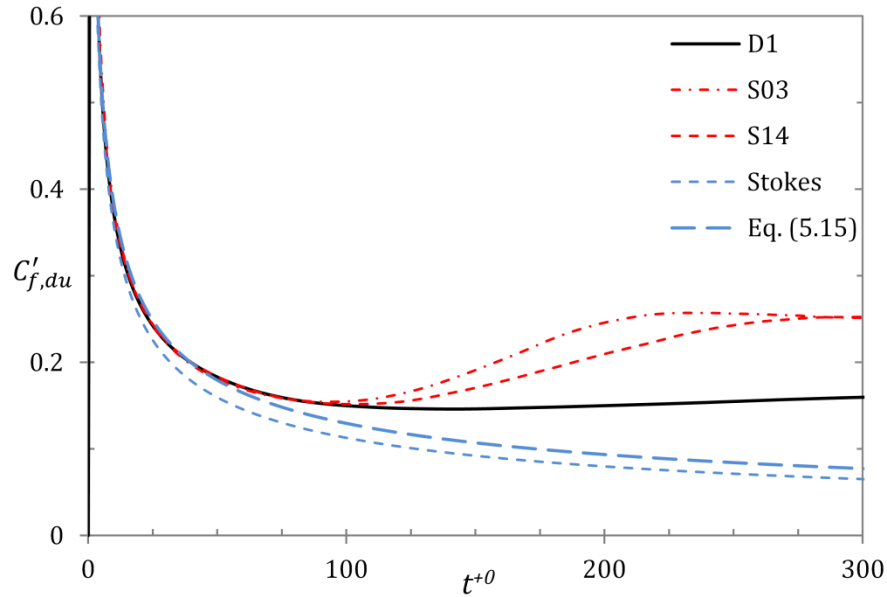


Figure 7.4. Development of the modified friction coefficient ( $C'_{f,du}$ ) for the base case (D1), and the accelerating cases 'S14' and 'S03' of He & Seddighi [8].

A comparison of perturbation velocity profiles for the different decelerating flow cases is presented in Figure 7.5. For clarity, cases D2 and D3 have not been plotted in the figure, but it is of little consequence as it will be shown that these profiles are very similar to those of case D1, except very early in the transient. It can be seen that at  $t^{+0} \sim 50$ , profiles of cases D5-D7 approximately overlap with each other. However, the near-wall profiles of D1 and D4 are seen to be different, implying faster development in these cases due to the stronger plug-like response of the higher deceleration rates imposed on the flow. Apart from this difference, the profiles can be seen flat in the core region i.e. the flow structure remains unchanged from the initial flow. Later in the transient, the profiles for case D5 begin to deviate from those of cases D6 and D7. At  $t^{+0} \sim 100 - 150$ , the profiles of cases D6-D7 are seen to overlap each other, but not with others. D1, D4 and D5 seem to have undergone more changes than these two. Further at  $t^{+0} \sim 200$ , D7 has undergone very little change, whereas D6 has developed even further. Profiles for the cases D1, D4 and D5 overlap at this time. It can be deduced that profiles for the cases D2 and D3 will also overlap with them, as they are at an intermediate level of deceleration rate. The boundary layer development of the slower deceleration cases appear to be delayed in comparison to that of the base case. After sufficient time has passed, all cases reach a final

steady state. At  $t^{+0} \sim 700$ , profiles for all cases are seen overlapping with each other corresponding to the final bulk velocity.

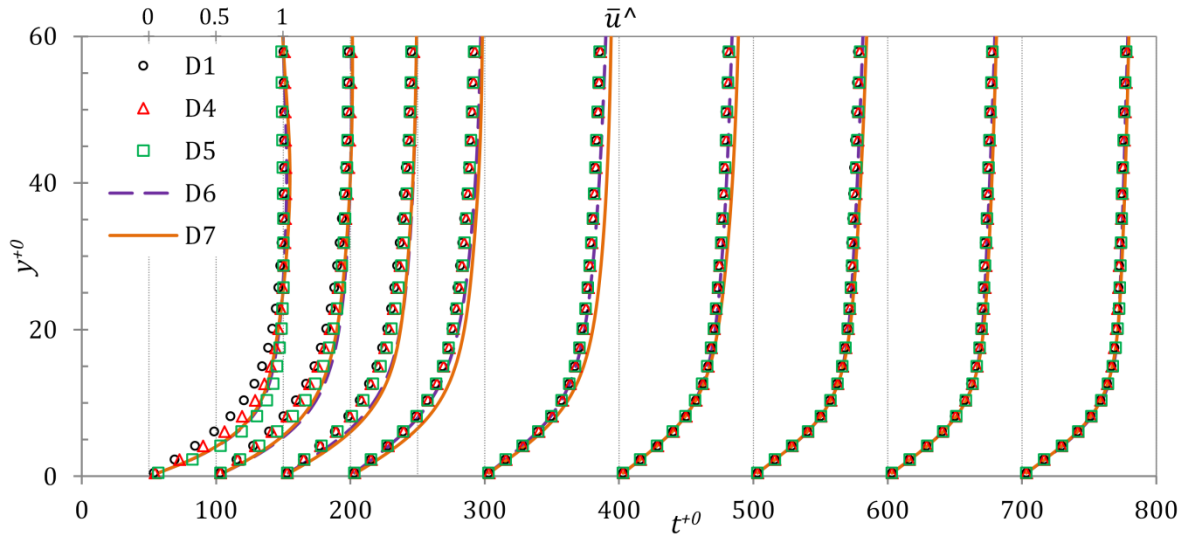


Figure 7.5. Development of the perturbation velocity profiles at several time instants for selected decelerating cases (The profiles are shifted at an amount proportional to the time).

The rate of development of the boundary layer for the present cases is elucidated by comparing their friction coefficients. As discussed in §6.2, modified friction coefficient of ramp-like flows is normalised by the intermediate change in velocity, and is given by  $C''_{f,du}$  in equation (6.3). Figure 7.6 presents the development of this modified friction coefficient for the present decelerating cases. Also presented in the figure is the modified friction coefficient of the ramp-like accelerating case ‘RAMP’ of Seddighi *et al.* [59], which accelerates from  $Re_b = 2800$  to 7400 in  $\Delta t^{+0} \sim 375$  (the critical time of onset of transition for this case is  $t^{+0} \sim 205$ ). It is seen that the friction coefficients for the slower decelerating cases collapse on a single curve during the deceleration periods. As the definition of this modified friction coefficient takes the intermediate change in velocity into account, the development of this modified friction coefficient is not affected by the magnitude of the deceleration and can be represented by a single curve. Early part of this curve ( $t^{+0} < 110$ ) is well represented by the equation,

$$C''_{f,du} = \frac{3.41}{\sqrt{\pi}} \frac{1}{(t^{+0})^{0.45}} \quad (7.2)$$

After the end of the deceleration period, a new perturbation occurs in the near-wall region growing into the flow leading to a sudden increase in the wall shear stress and, hence, a sudden decrease in the perturbation wall shear stress ( $\tau_{w,du}$ ). Thus, the modified friction coefficient,  $C''_{f,du}$ , shows an abrupt decrease. Afterwards, the modified friction coefficient reaches a minimum and gradually relaxes towards the final value. It is interesting to note that the linearly accelerating case, RAMP, also follows the same curve, equation (7.2), for early part of the pre-transition period. It is clear that both accelerating and decelerating flows have a similar initial response and the modified friction coefficient for both flows can be represented by a single curve.

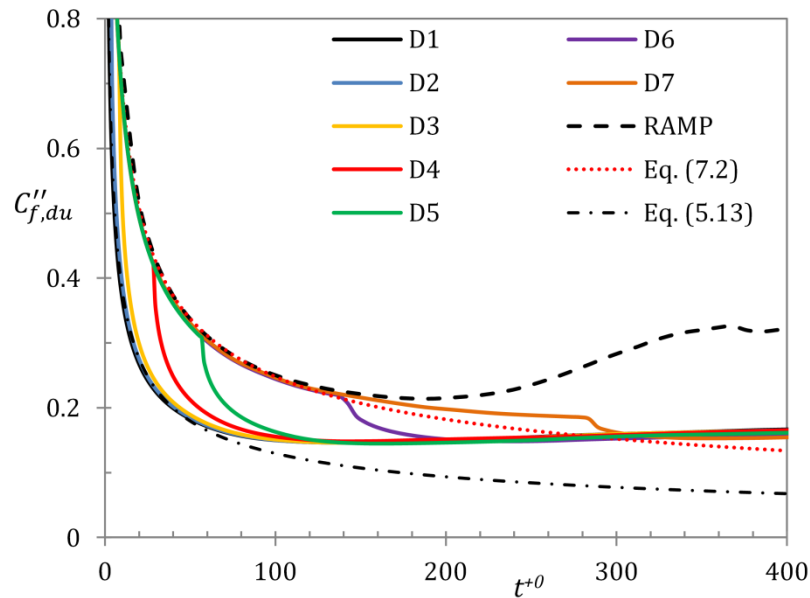


Figure 7.6. Development of the modified friction coefficient for present decelerating cases, along with the linearly accelerating case (RAMP) of Seddighi *et al.* [59].

As discussed previously in §6.2, the time-development of the ramp-like flows can be better represented by the extension of the Stokes' solution to time-varying velocity, equation (6.2). The present ramp flow decelerations are divided into small finite steps and the integral of laminar boundary-layer development for time-varying perturbation is determined. Figure 7.7 presents the comparison between the perturbation velocity profiles of cases D4 and D7 with the laminar boundary layer profiles for their respective time-varying perturbation. It is clear that the laminar solution of the time-varying velocity represents the slower ramp-type decelerating

cases during the early part of the transient accurately. Similar to that in the base case D1, the profiles of case D4 are closely represented by the laminar solution until  $t^{+0} \sim 60$ ; however, case D7 closely follows the laminar solution till  $t^{+0} \sim 120$ . After this period, the profiles of the present deceleration cases diverge from the laminar solution, developing farther from the wall at a faster rate than the laminar solution.

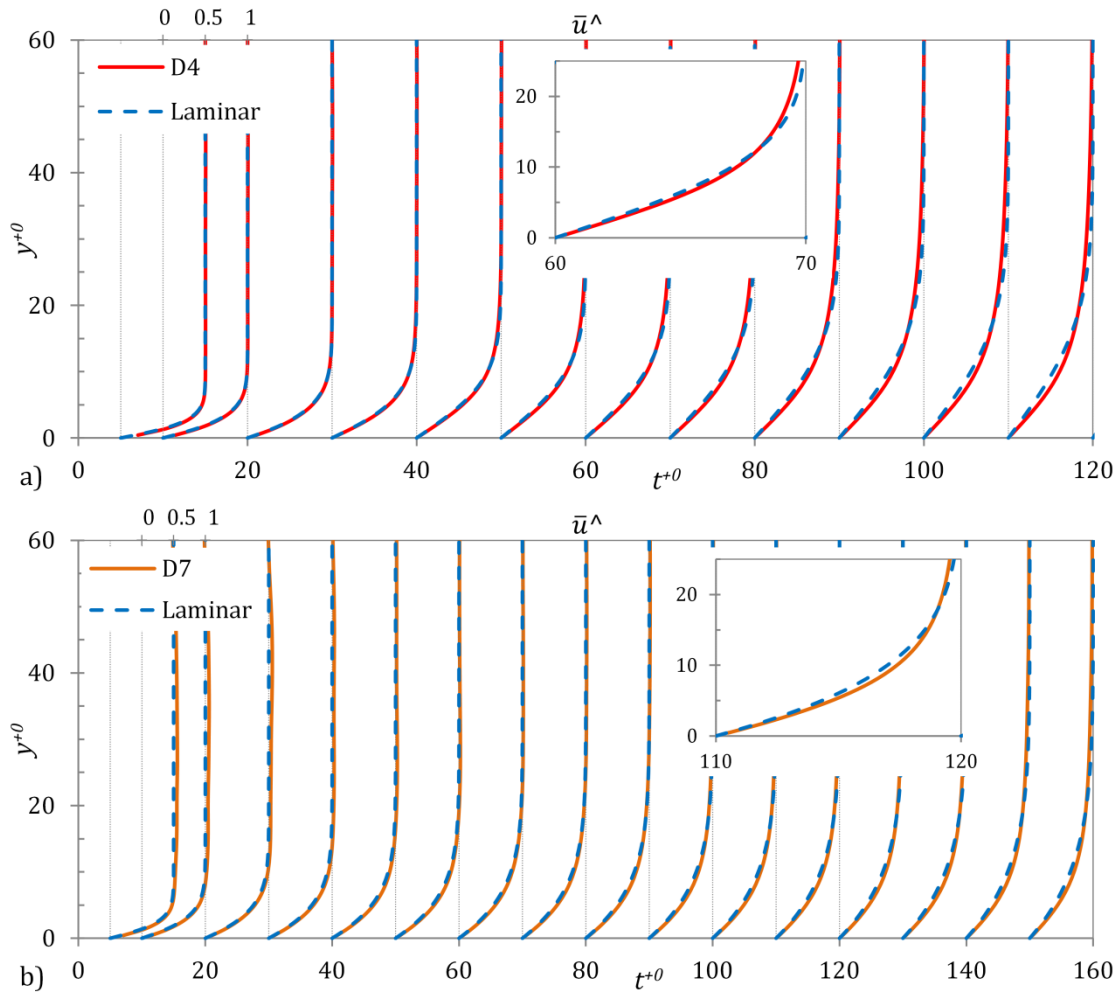


Figure 7.7. Development of the perturbation velocity profiles at several time instants for (a) case D4, and (b) case D7, along with the laminar boundary layer solution.

Similar to ramp-type accelerating flows, the development of the modified friction coefficient for the present ramp-type decelerations can also be compared with the laminar boundary-layer solution. Figure 7.8 presents the modified friction coefficient, given by equation (6.3), for the cases D4 and D7 along with that of the laminar boundary-layer solution for the time-varying

perturbation, determined using equation (6.4). It is seen that similar to that of ramp-type accelerating flows, the modified friction coefficient of the present decelerating flows, is slightly elevated from the laminar solution and can be represented by a slight correction –  $C''_{lam} (t^{+0})^{0.03}$ .

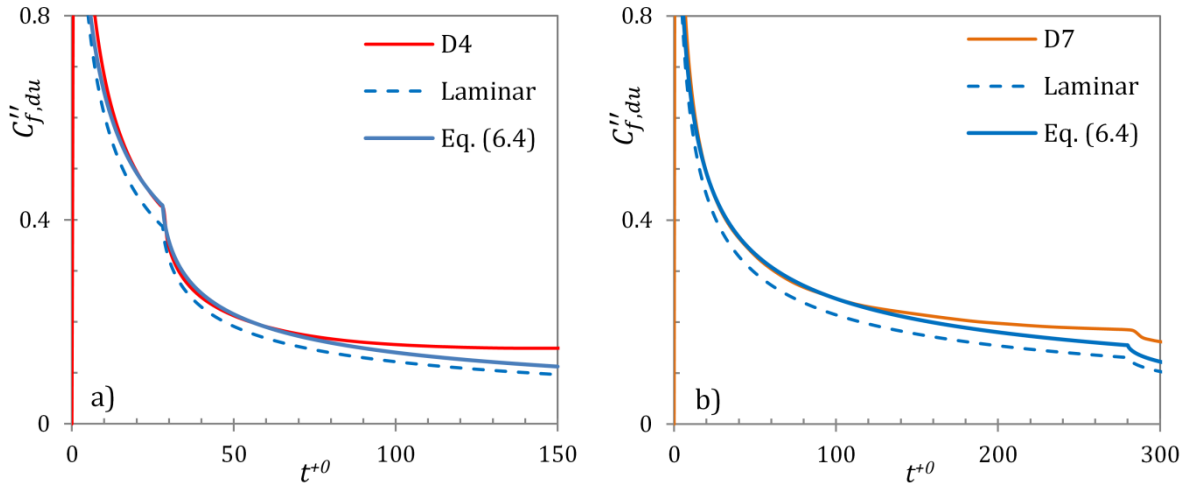


Figure 7.8. Development of the modified friction coefficient for cases a) D4, and b) D7, along with the laminar boundary-layer solution for time-varying velocity.

The similarity between the boundary-layer development of the present ramp-type decelerating cases and that of the laminar flow is seen again here. The ‘corrected’ laminar solution, equation (6.5), closely represents cases D4 and D7 until  $t^{+0} \sim 60$  and  $t^{+0} \sim 110$ , respectively. Intermediate flow deceleration cases D5 and D6 (not shown in the figure) follow the laminar solution until  $t^{+0} \sim 60$  and  $t^{+0} \sim 100$ , respectively.

The rate of the development of the decelerating flows is seen to be similar to that of the accelerating flows. The early response of the wall shear stress for the near-step decelerations, like that in step-accelerating flows, can be calculated using equation (5.13); while that in ramp-type decelerating flow can be calculated using equations (6.4)-(6.5). Moreover, the development of the modified friction coefficient, expressed as in equation (6.3), is not affected by the rate of flow deceleration. During the deceleration periods, the modified friction coefficient of all cases collapse onto a single curve.

It has been previously shown that the response of the time-developing boundary layer in accelerating flows diverges from the laminar solution after the flow undergoes a transition process. Having shown that the boundary layer development in decelerating flows too exhibits a laminar-like initial response, it is conceivable that the decelerating flows may too undergo a transition process after this initial period. This is further discussed later with the aid of turbulence statistics and instantaneous flow response.

Another interesting feature to note is the difference between the behaviours of the various ramp-down cases. The rapidly decelerating cases D1-D5, despite having different rates of deceleration, follow the laminar solution up to similar times in the transient ( $t^{+0} \sim 60$ ). The slower cases, D6-D7, however, follow the laminar solution for longer periods of time ( $t^{+0} \sim 100 - 110$ ). This critical time in the more rapidly decelerating cases (D1-D5) is not affected by the change of the deceleration rate; while that in the slower cases is affected by the slower deceleration rate. Thus, the present decelerating cases may be divided into two groups. This is elaborated later with the aid of statistics and instantaneous flow response.

### 7.2.3 Turbulence decay

Figure 7.9 shows the development of the maximum values of r.m.s fluctuations for the streamwise, wall-normal and spanwise velocities of the decelerating cases. The subplots (a) and (b) show the early behaviour until  $t^{+0} = 500$ ; whereas the overall behaviour during the transient is shown in subplot (c) using a different scale. It is seen in Figure 7.9(a) that there is a momentary increase in the streamwise component for all cases. In cases D1-D5, this increase lasts till  $t^{+0} \sim 10$ , and thereafter decay occurs at a similar rate in all these cases. Despite the large differences in ramp rates (D5 is 100 times slower than D1), the decays in these cases are almost identical. In cases D6 and D7, the streamwise component increases slightly till  $t^{+0} \sim 45$  and  $t^{+0} \sim 70$ , respectively, and thereafter decays at a rate slower than in D1-D5, with D7 decaying slower than D6. D1-D5 reach the final steady state at  $t^{+0} \sim 200$ , whereas D6 and D7 reach at  $t^{+0} \sim 270$  and  $t^{+0} \sim 400$ , respectively. The wall-normal and spanwise components

remain unchanged till  $t^{+0} \sim 70$  in cases D1-D5, whereas till  $t^{+0} \sim 120$  in cases D6-D7. After this initial delay, both wall-normal and spanwise components decay at similar rates reaching the final steady state at around  $t^{+0} \sim 1000$ . It is interesting to note that the period of little or no change in the transverse components is very similar to the period during which the modified friction coefficient follows the laminar solution.

The decay of turbulence here seems to show a two-stage development – a small period when there is little change, followed by a period of fast relaxation. This trend is the same as that for the history of the wall shear stress reported by Chung [56], Seddighi *et al.* [57] and Talha [53], however the delays in the present study are much smaller. The momentary increase of streamwise component is discussed further in the next section.

The delayed and slower response of the wall-normal and spanwise components is explained by the fact that the source of these components is through redistribution of the streamwise component. This feature can be more clearly observed in Figure 7.10 showing the total turbulent kinetic energy and its individual contributions from streamwise, wall-normal and spanwise components relative to their initial values. It can be seen that the total turbulent kinetic energy along with its streamwise component decrease almost instantly with the start of the deceleration, owing to a drop in generation of turbulence. However, there is a marked increase in the transverse components. This is indicative of an increase in re-distribution of energy from streamwise component to transverse components.

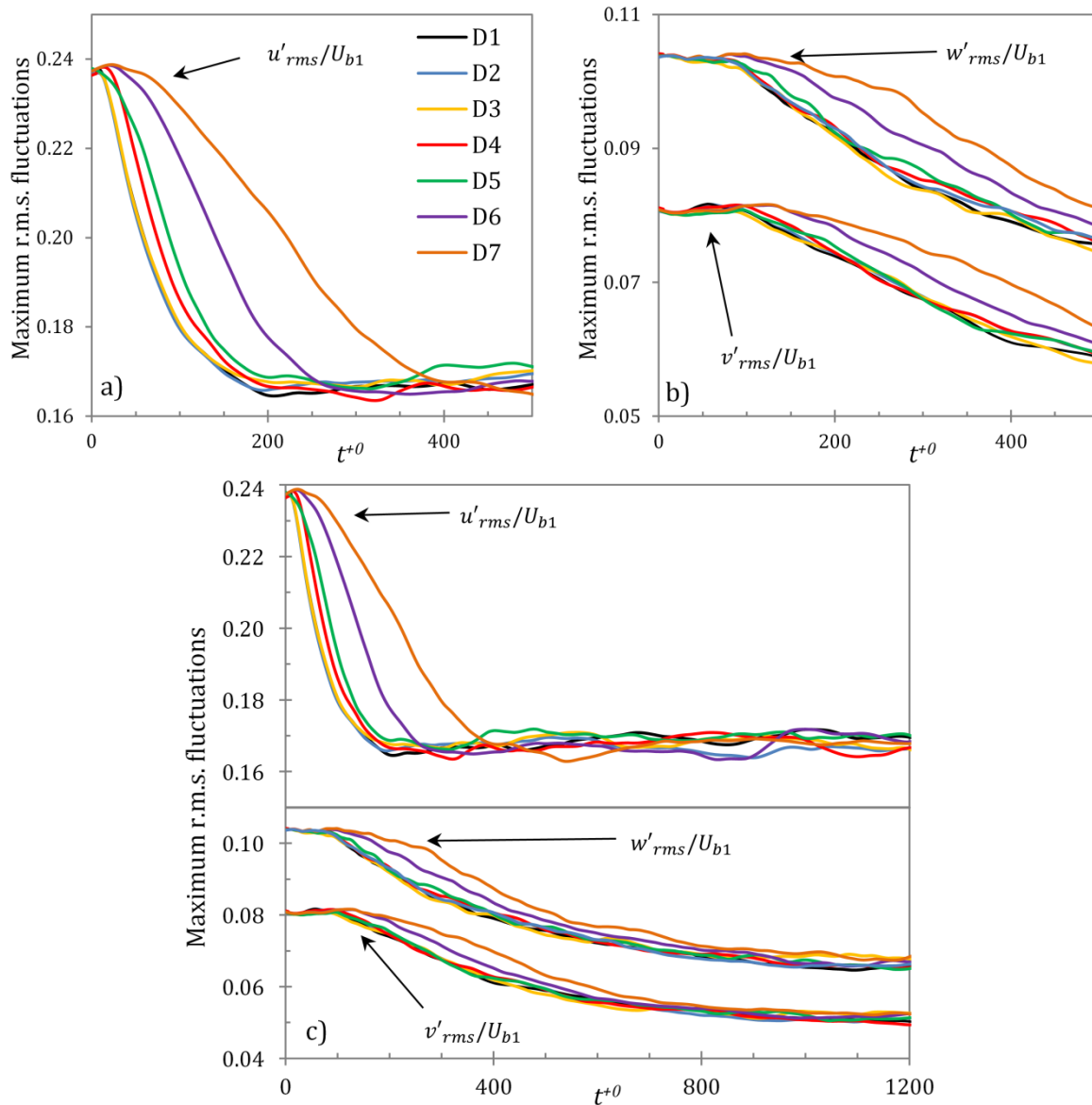


Figure 7.9. Development of maximum r.m.s. fluctuating velocities for a) streamwise component; b) wall-normal and spanwise components. c) All three components shown in different scale.

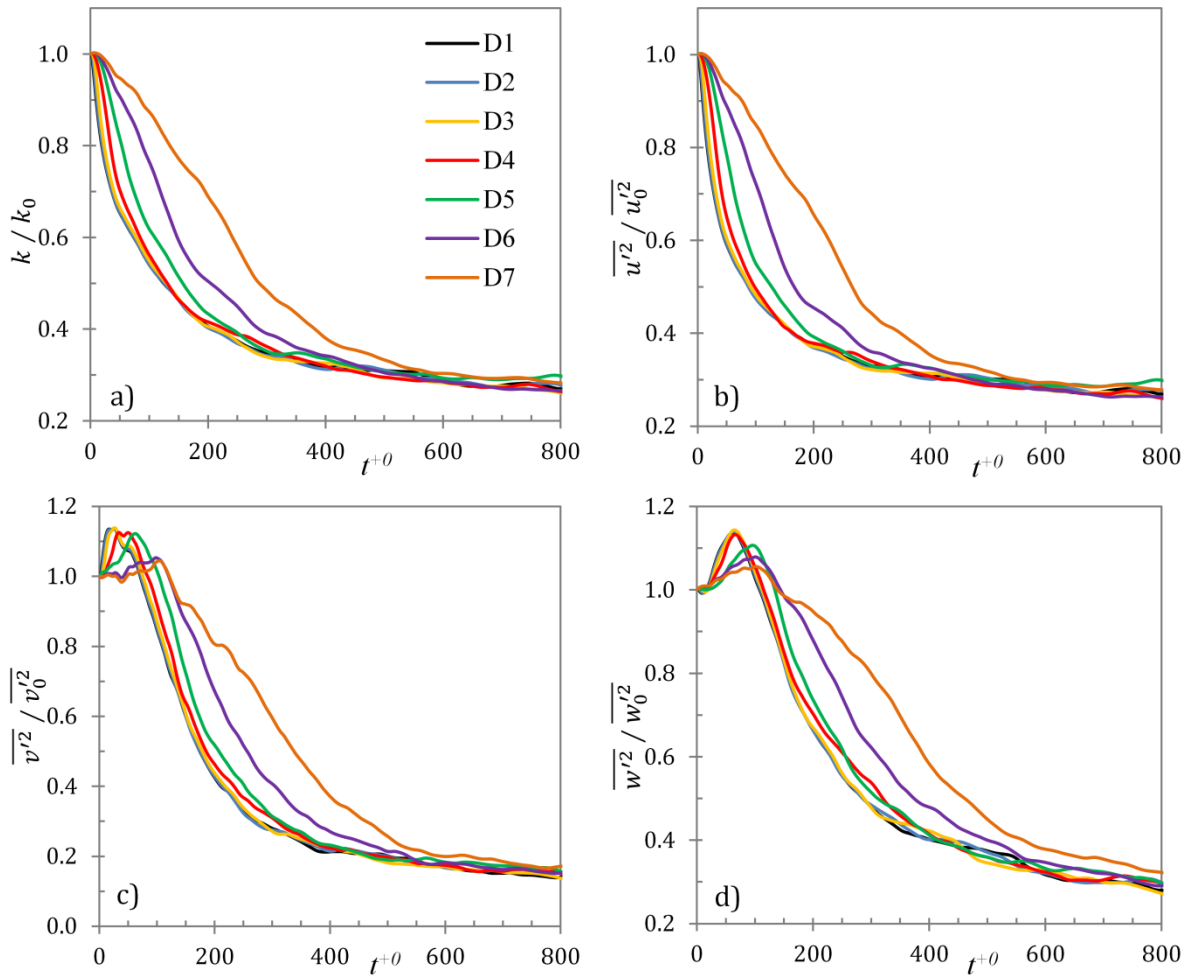


Figure 7.10. Development of a) turbulent kinetic energy; b) streamwise, c) wall-normal and d) spanwise fluctuating velocities at wall-normal location of  $y^{+0} = 5$ .

To further support this explanation, the integrated budgets terms of streamwise velocity fluctuations are presented in Figure 7.11. The production and dissipation terms,  $P_{11}$  and  $\varepsilon_{11}$ , drop immediately after the deceleration begins. However, the pressure-strain term ( $\Pi_{11}$ ), which is responsible for re-distribution of the energy, maintains its value for a period and then decays. The period of no or little change in the pressure-strain component is  $t^{+0} \sim 60$  for cases D1-D5, whereas for slower deceleration cases, D6-D7, this period is  $t^{+0} \sim 100$ . This delay is consistent with the time of delay in response of transverse components (Figure 7.9).

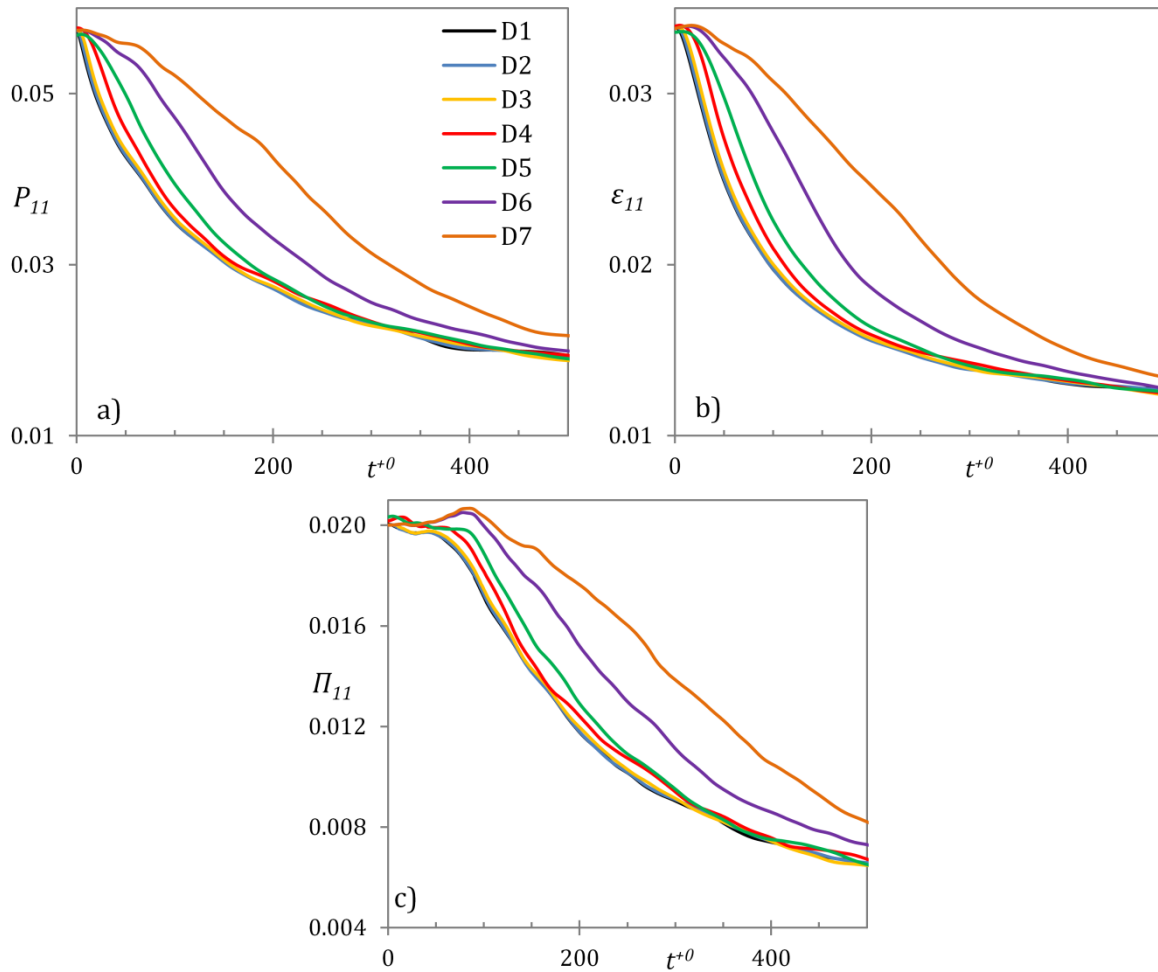


Figure 7.11. Development of the budget terms of  $u'^2$  integrated over channel half-height, normalised with  $u^4_{\tau_0}/\nu\delta$  – a) production, b) dissipation, and c) pressure-strain terms.

In accelerating flows, the streamwise fluctuations respond to the transient immediately, however its immediate increase is attributed to the formation of elongated streaks. The response of the ‘conventional’ turbulence is represented by the delayed response of the transverse components. In decelerating flows, the immediate response of the streamwise component can be attributed to the drop in turbulence production and the suppression of the streak structures. The delayed response of the transverse components may be considered as the response of ‘real’ turbulence. This time delay in the response of the real turbulence is consistent with the critical time until which the perturbation flow follows the laminar solution. Thus, decelerating flows may also be considered to have a transitional response, with an initial period characterised by little or no change in ‘real’ turbulence (or equivalently the period during which

the laminar solution represents the flow perturbation); followed by a response of transverse components and the perturbation flow diverging from the laminar solution.

It is seen again that cases D1-D5, despite having different deceleration rates behave similarly, whereas cases D6 and D7, with a further decrease in deceleration rates behave quantitatively differently. This is similar to the dichotomous behaviour seen in boundary layer development. The behaviour of turbulence decay can, thus, be classified into two groups – D1-D5 which undergo a decay at similar rates in non-dimensional form; and D6-D7 which undergo decay at slower rates. D1 undergoes a deceleration hundred times faster than D5, and yet the behaviour of turbulence dynamics in both decelerations is similar. The decay of turbulence intensities and budget terms, here, is not affected by the change in the deceleration rate. It can be deduced that a time-scale of turbulence response exists. If the time-scale of the imposed deceleration is smaller than this time-scale, the change in the deceleration rate has no effect on the turbulence. However, if the deceleration time-scale becomes larger than the turbulence time-scale (slower decelerations like D6-D7), the decay of turbulence is affected by the slower deceleration rate itself. A measure of this time-scale of turbulence response can be estimated from the critical time until which the perturbation flow of the base case (or an ideal step change) is seen to follow the laminar solution. This critical period is shown to be roughly  $t^{+0} \sim 60$ . The deceleration periods for the first group (D1-D5) are smaller than the critical time, while that for the second group (D6-D7) are larger.

#### **7.2.4 Turbulence spectra intensity and velocity auto-correlations**

Figures 7.12 and 7.13 show the pre-multiplied wavenumber spectra of the streamwise velocity at  $y^{+0} = 5$  for cases D1 and D7 in the streamwise and spanwise directions, respectively. The main plots in Figure 7.12 show the spectra of high wavenumbers ( $k_x^{+0} > 0.05$ ) in a log-log scale, whereas low wavenumbers ( $k_x^{+0} < 0.05$ ) are shown in the inset in a semi-log scale. It is seen that at the start of the transient for case D1, there is a small increase of energy in the high- and mid-range wavenumbers for a short period, while there is an immediate decrease of energy in

the low wavenumber region. This implies that the energy of the smaller structures increases almost immediately following the start of the transient while the energy of large structures starts to decrease. This early increase in energy in high wavenumber region can be attributed to a sudden burst of turbulence caused by the imposed deceleration (and hence, the adverse pressure gradient) leading to instability in the flow. This is in agreement with the predictions of Maruyama *et al.* [43], and can also be seen in the development of turbulent intensities in Figure 7.9. The early response of turbulence, similar to that in accelerating flow, is in the high wavenumber region (or energy of smaller structures). However, this “enhancement” behaviour is in contrast of the “sheltering” effect observed in the accelerating case of He & Seddighi [8], in which the high frequency wavenumbers are damped during the very early stage of the transient flow. Similar behaviour of early increase in high and mid-range wavenumber regions is also shown in cases D2-D5 (not shown in the figure). For slower deceleration cases D6-D7, however, the first response is found to be only in the high wavenumbers. It can be seen in Figure 7.12(b), that the early response of the deceleration for D7 is the increase in energy in the high wavenumbers. This increase in the energy lasts only till  $t^{+0} \sim 50$  in D1 and  $t^{+0} \sim 100$  in D7. While, the energy in the low wavenumber region shows little or no change until this period, it reduces thereafter. The energy in the low wavenumber region reaches the corresponding value of the final state at  $t^{+0} \sim 600$  for D1 and  $t^{+0} \sim 800$  for D7. The energy of the high and mid-range wavenumber structures also exhibiting reduction after the initial increase, reaches the final state at  $t^{+0} \sim 800$  and 1200 for D1 and D7, respectively. The slower decay of energy in D7 is in agreement with the observation in the decay of turbulent intensities and their budgets terms (Figures 7.9-7.11).

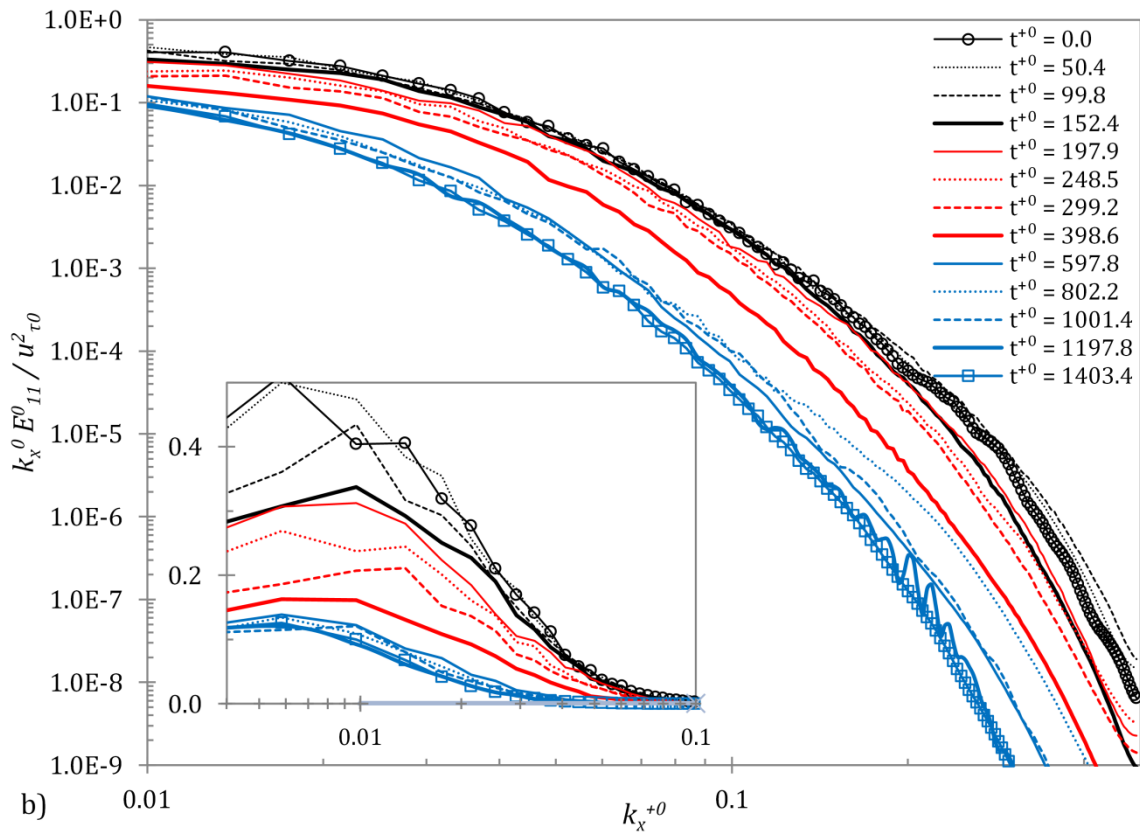
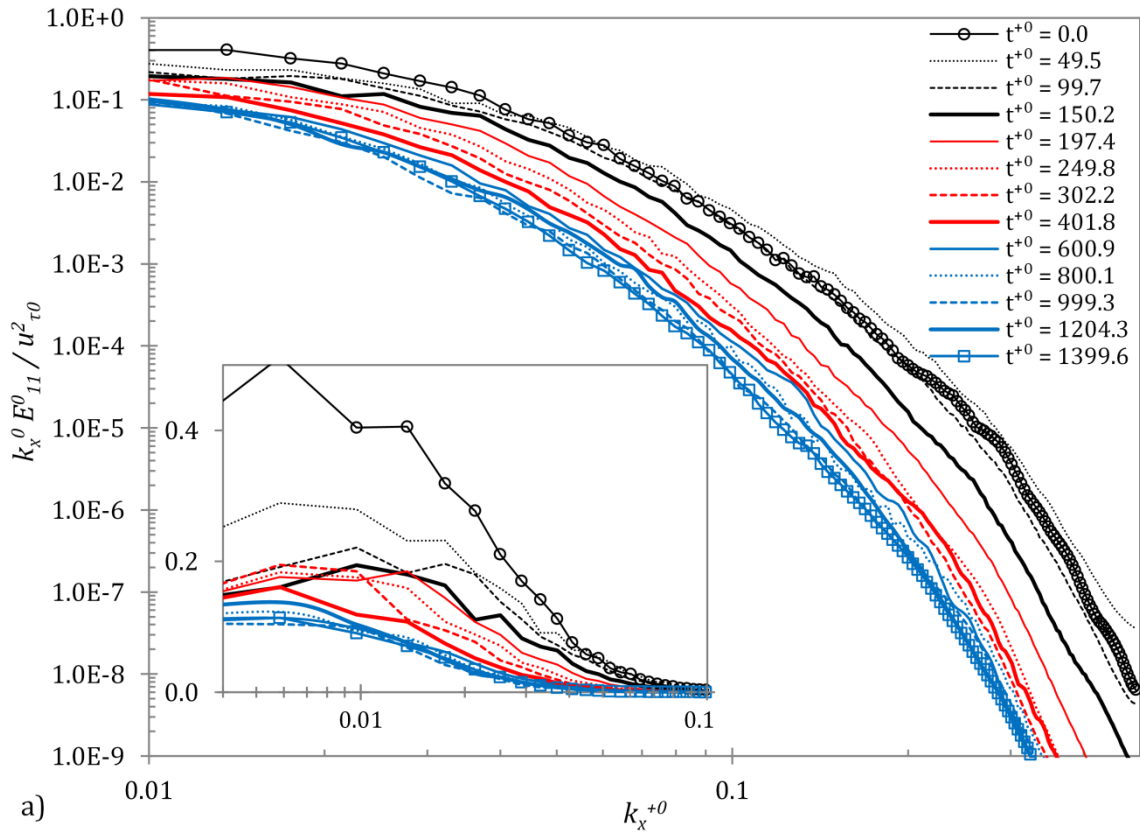


Figure 7.12. Development of the pre-multiplied streamwise wavenumber spectra of the streamwise velocity at  $y^{+0} = 5$  for cases a) D1, and b) D7.

It is seen that in decelerating flows, the reduction in energy happens first in the low wavenumber region (or large structures) and reaches the final steady value earlier, whereas in high wavenumber region the steady state is delayed. This is expected because the reduction in the mean flow is expected to first suppress the pre-existing large vortical and streaky structures causing a reduction in their energy. This is in contrast to the response in accelerating flows where the energy responds in both high- and low-wavenumber regions simultaneously. In accelerating flows, the high-wavenumber region shows an initial response of significant decrease in energy due to the sheltering effect. In contrast, the energy in the high-wavenumber region of decelerating flows increases due to the instability caused by adverse pressure gradient leading to momentary burst of turbulence in the flow.

The spanwise wavenumber spectra presented in Figures 7.13(a) & (b) for cases D1 and D7, respectively, show a similar behaviour of delayed and slower decay of energy in case D7 in comparison that in case D1. It is seen that the energy in high-wavenumbers for case D1 decreases immediately following the start of the transient; however, there is a delay in the same for case D7. Similar to that in streamwise spectra, the energy reduction happens in the high-wavenumber region first. For cases D1 and D7, the energy in the high-wavenumber region reaches the final value at  $t^{+0} \sim 200$  and  $t^{+0} \sim 400$ , respectively, while that in the low-wavenumber region reaches the final value at  $t^{+0} \sim 400$  and  $t^{+0} \sim 600$ , respectively.

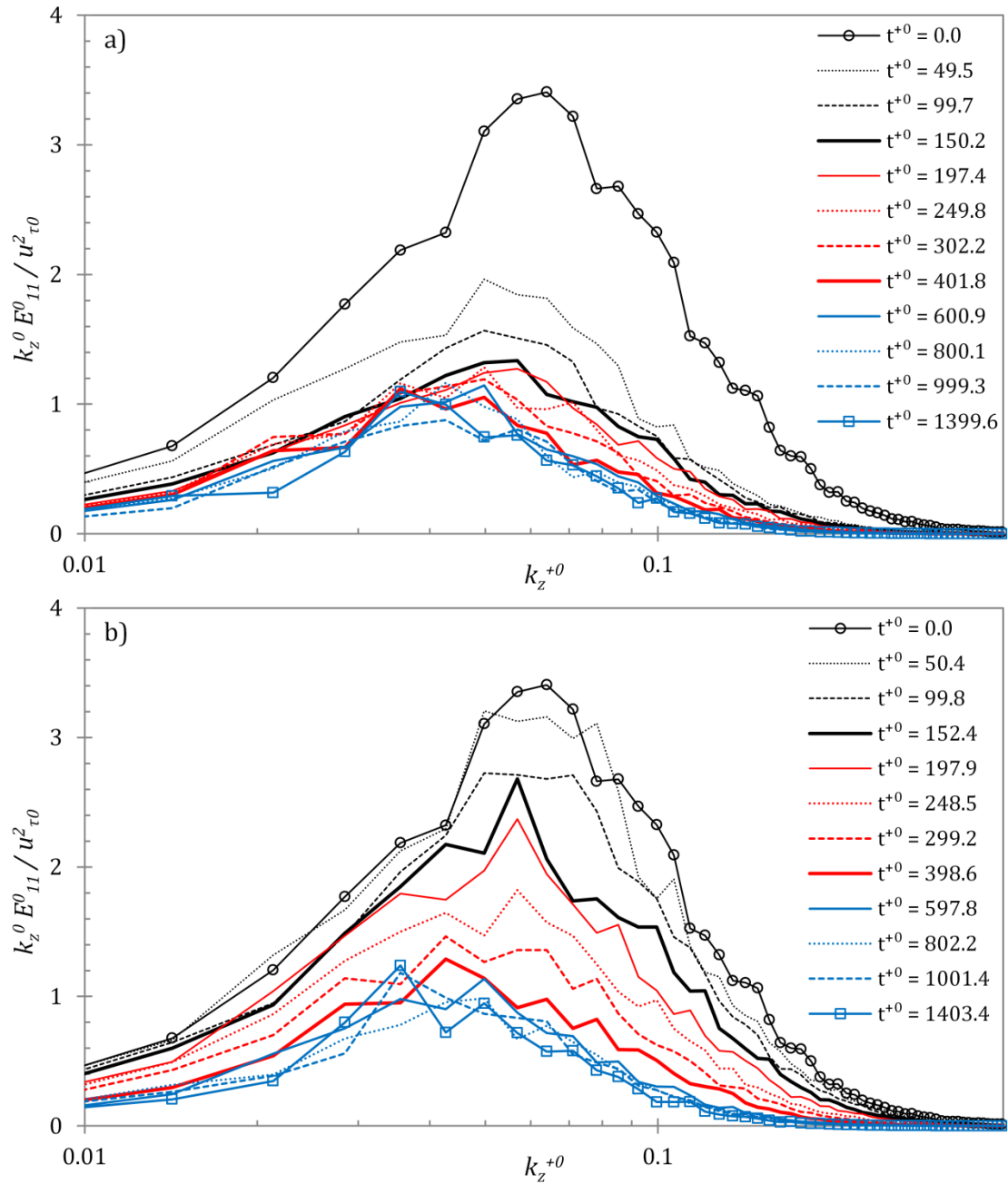


Figure 7.13. Development of the pre-multiplied spanwise wavenumber spectra of the streamwise velocity at  $y^{+0} = 5$  for cases a) D1, and b) D7.

Quantitative information about the flow structures can be obtained from the two-point auto-correlation of the streamwise fluctuation velocity. The correlation in the streamwise direction ( $R_{11,x}$ ) provides a measure of the length of the streaks whereas that in the spanwise direction ( $R_{11,z}$ ) measures the strength and the spacing between the streaks. Figure 7.14 presents these correlations for cases D1 (a, b) and D7 (c, d) at a wall height of  $y^{+0} = 5$ . It is seen in the figure that the streamwise correlations for D1 decrease shortly after the start of the transient implying

a decrease in length of the streaks. This decrease lasts for only  $t^{+0} \sim 100$ , after which the correlations start to increase. However, the streamwise correlations for D7 do not appear to show any change immediately following the start of the transient. The length of the streaks appear to remain the same until  $t^{+0} \sim 400$ , after which the correlations start to increase. It is interesting to note that this response time would be similar to that of D1 ( $t^{+0} \sim 100$ ) if the deceleration period ( $\Delta t^{+0} \sim 280$ ) is removed from the transient of D7. The correlations reach the final steady value at  $t^{+0} \sim 600$  and  $t^{+0} \sim 1200$  for cases D1 and D7, respectively. The spanwise correlations for case D1 and D7 are presented in Figures 7.14(b) & (d), respectively. It is seen that for case D1, the location of the minimum correlation increases immediately after the start of the transient, implying a widening of spaces between the streaks. The minimum value, however, remains the same until  $t^{+0} \sim 200$ , implying that the relative strength of the streaks remains unchanged during this time. Thereafter, the minimum value decreases further and reaches the final value at  $t^{+0} \sim 600$ . For case D7, the spanwise correlations are seen to respond after a delay. They remain unchanged till about  $t^{+0} \sim 100$ , after the minimum location begins to increase without any change in the minimum value. At  $t^{+0} \sim 300$ , the minimum value of the correlation begins to decrease reaching the final value at about  $t^{+0} \sim 1200$ . The delayed and slower response of case D7 is in agreement with the above observations of turbulence spectra intensity, turbulent intensities and their budget terms.

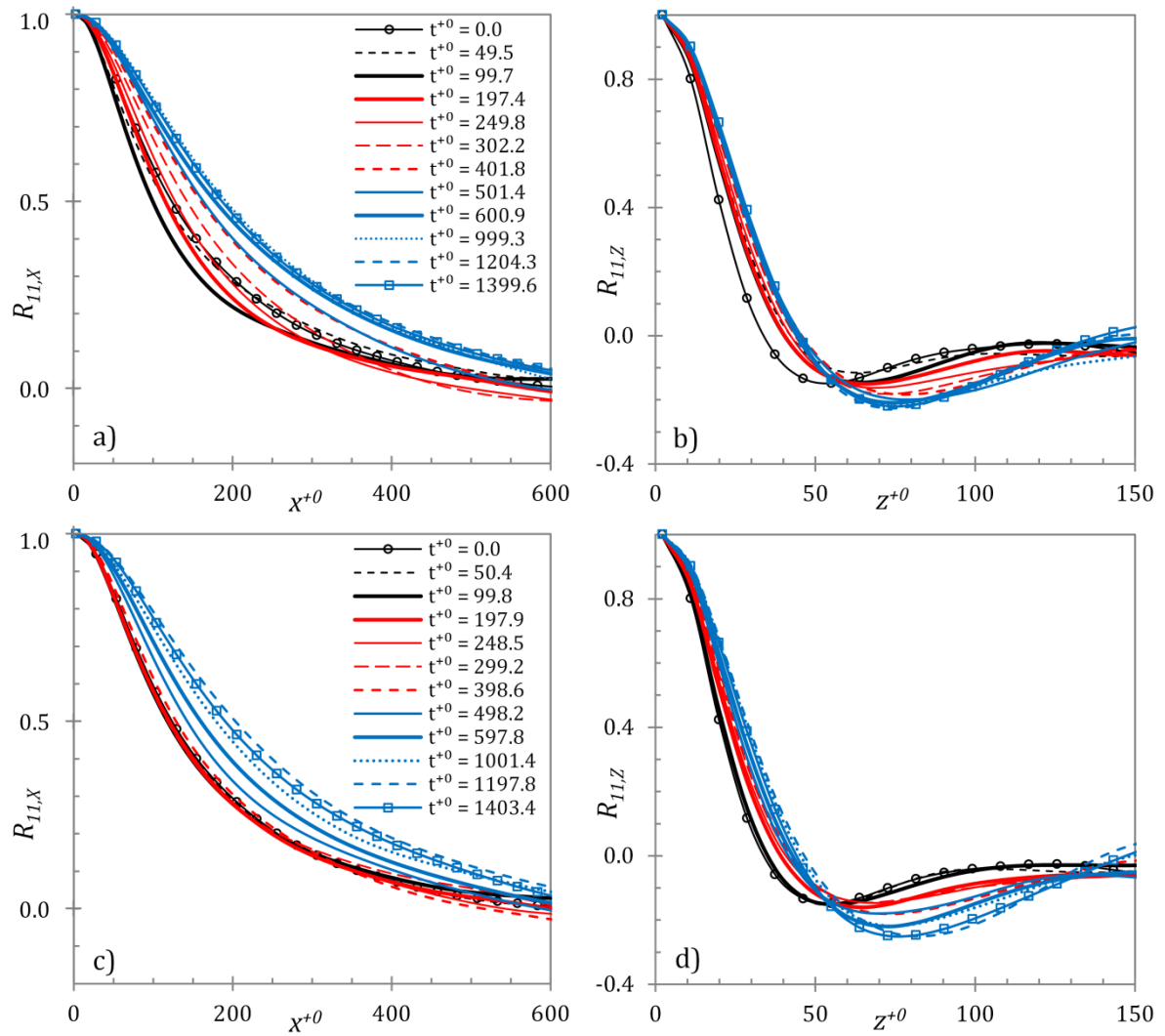


Figure 7.14. Development profiles of the two-point auto-correlation of the streamwise velocity in the streamwise (a, c) and spanwise (b, d) directions at  $y^+0 = 5$  for cases D1 (a, b) and D7 (c, d).

### 7.3 Instantaneous Flow Response

The flow structure at several time instants during the transient for selected cases are presented in Figure 7.15 using 3D iso-surface plots of  $u'/U_{b1}$  and  $\lambda_2/(U_{b1}/\delta)^2$ . Here,  $u'$  is the instantaneous streamwise fluctuating velocity and  $\lambda_2$  is the second largest eigenvalue of the symmetric tensor  $S^2 + \Omega^2$  where  $S$  and  $\Omega$  are the symmetric and anti-symmetric parts of the velocity gradient tensor. The first two cases (D1 and D4) presented in the figure belong to the first group of cases, as discussed above, which show similar decay of turbulence despite having different deceleration rates, whereas the third case is slowest deceleration (D7) showing a slower decay of turbulence.

The deceleration in cases D1, D4 and D7 end at times  $t^{+0} \sim 0.56$ ,  $t^{+0} \sim 28$  and  $t^{+0} \sim 280$ , respectively. The second plot ( $t^{+0} \sim 50$ ) represents a time instant after the deceleration period for the cases D1 and D4; and during the deceleration for D7. At this time instant, it can be seen that for cases D1 and D4, the streak structures are reduced slightly. This can be attributed to the direct suppression of streamwise component due to the imposed deceleration. However, there are no visible changes in the vortical structures implying that the deceleration itself has little or no effect on the turbulent structures already present in the flow. The immediate response in streak structures and the delay in response of turbulence structures is in agreement with the turbulent statistics presented above. For case D7, there are no visible changes in both the streak and vortical structures. Further at time  $t^{+0} \sim 150$ , both vortical and streak structures show a marked decrease in the cases D1 and D4, whereas those for case D7 have decreased only slightly. This longer delay in response of turbulence for D7 is also seen in turbulent statistics above.

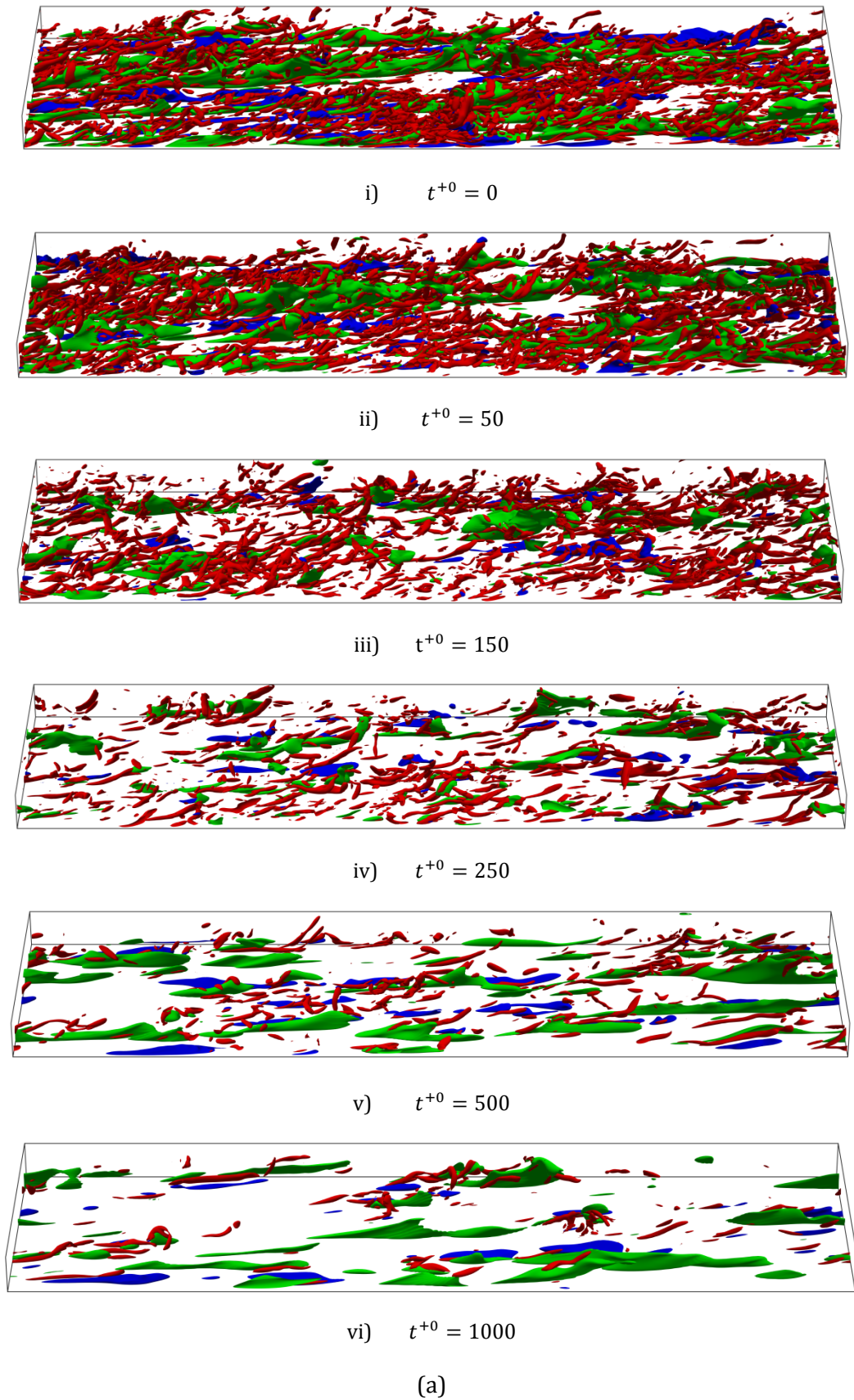
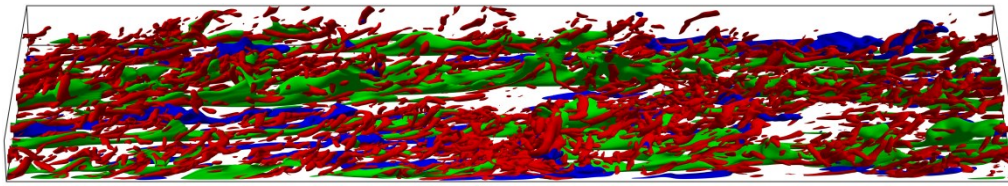
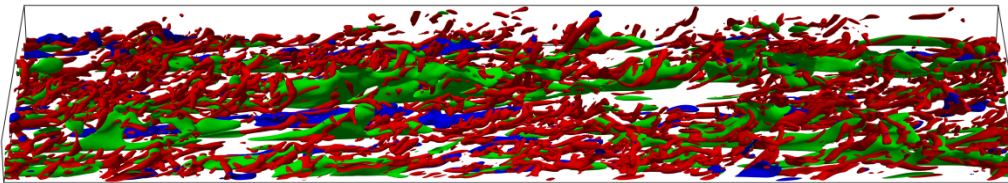


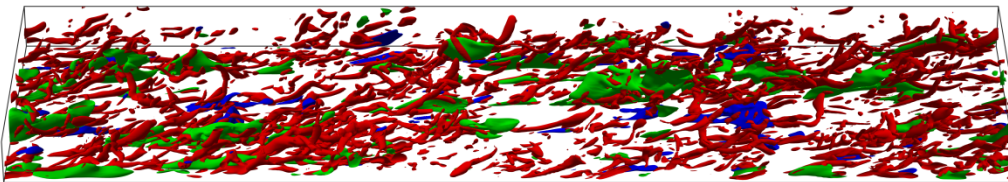
Figure 7.15. Flow structures in 3D iso-surface plots in cases a) D1, b) D4, and c) D7. Streaks are shown in blue/green with  $u'/U_{b1} = \pm 0.3$ , and vortical structures are shown in red with  $\lambda_2/(U_{b1}/\delta)^2 = -5$ .



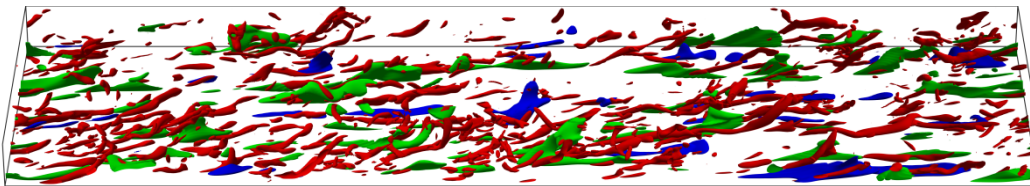
i)  $t^{+0} = 0$



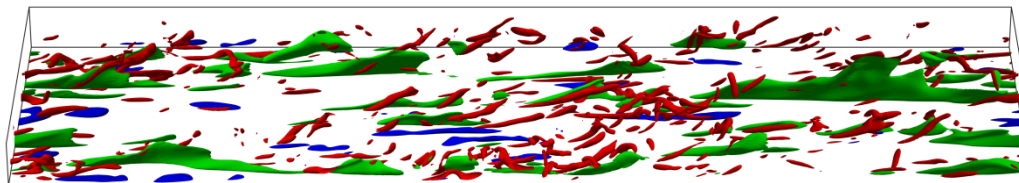
ii)  $t^{+0} = 50$



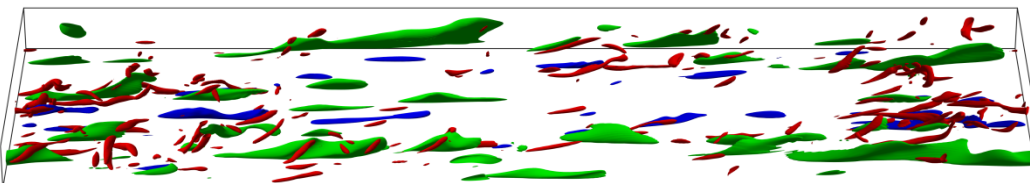
iii)  $t^{+0} = 150$



iv)  $t^{+0} = 250$

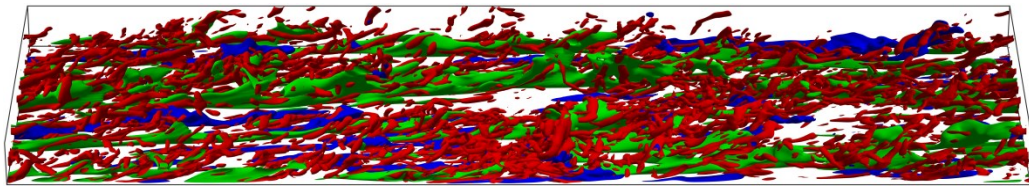


v)  $t^{+0} = 500$

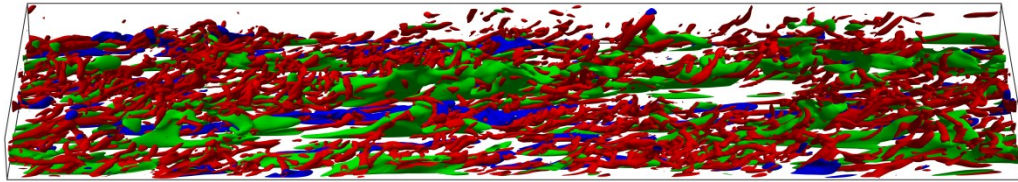


vi)  $t^{+0} = 1000$

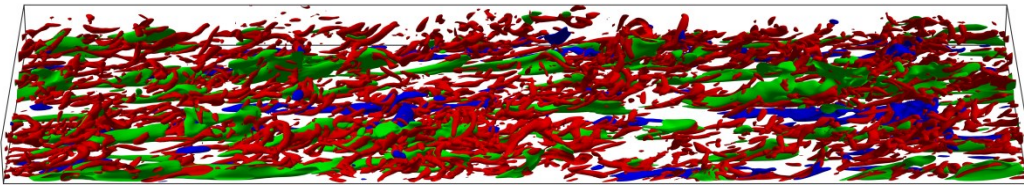
(b)



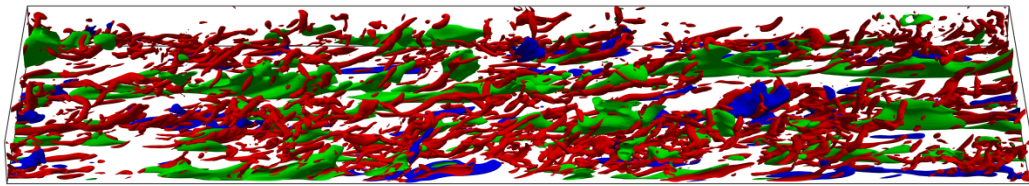
i)  $t^{+0} = 0$



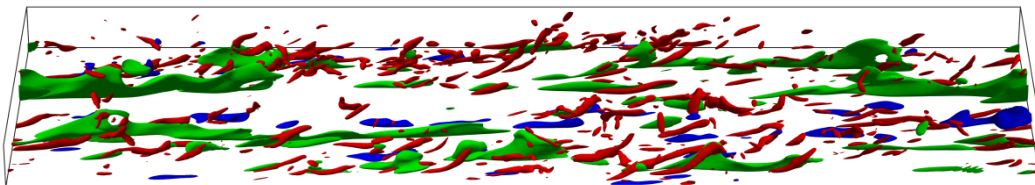
ii)  $t^{+0} = 50$



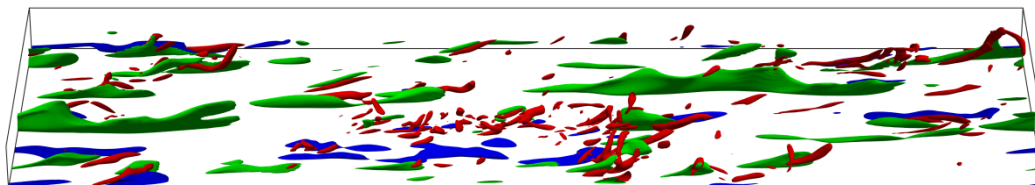
iii)  $t^{+0} = 150$



iv)  $t^{+0} = 250$



v)  $t^{+0} = 500$



vi)  $t^{+0} = 1000$

(c)

As discussed previously in §5.2, the maximum value of r.m.s. fluctuation of  $\lambda_2$ ,  $(\lambda'_{2,rms})_{max}$ , can be used to compare the relative strength of these structures in the flow. Figure 7.16 presents the development of  $(\lambda'_{2,rms})_{max}$  during the transient for the cases D1, D4 and D7. Here,  $(\lambda'_{2,rms})_{max}$  is normalised with the final bulk velocity,  $U_{b1}$ , and the channel half-height,  $\delta$ . The delayed and slower decay of vortical structures in case D7, as discussed above, is clearly visible in the figure. Due to the longer delay in D7, the value of  $(\lambda'_{2,rms})_{max}$  at time  $t^{+0} \sim 150$  is comparable to the value of  $(\lambda'_{2,rms})_{max}$  in the cases D1 and D4 at time  $t^{+0} \sim 50$ . Hence, it can be assumed that the cases D1 and D4 at  $t^{+0} \sim 50$  are at a similar stage of flow development as case D7 at  $t^{+0} \sim 150$ . Henceforth, after a time period of 100 wall units in the transient (i.e. at time  $t^{+0} \sim 150$  for cases D1 and D4; and at time  $t^{+0} \sim 250$  for case D7), there is a notable reduction the  $(\lambda'_{2,rms})_{max}$  value in cases D1 and D4; whereas for the case D7, the reduction is comparatively smaller, implying that the decay of turbulence structures in case D7 is slower than that in D1 and D4.

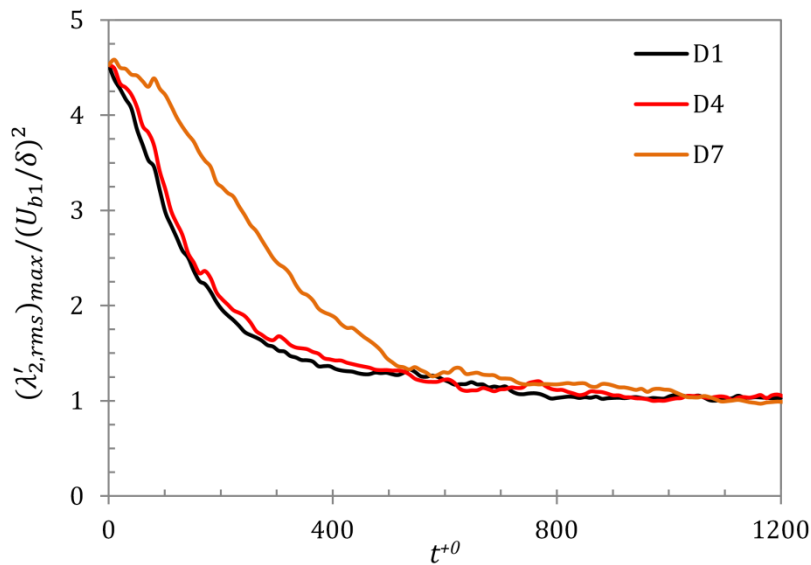


Figure 7.16. Development of  $(\lambda'_{2,rms})_{max} / (U_{b1} / \delta)^2$  for cases D1, D4 and D7 during the transient.

It is seen that at similar times during the transient, cases D1 and D4 show similar turbulent structures. Both intensity and number of vortical structures and high-/low-speed streaks are similar in these two cases, implying that turbulence decay is similar and that different deceleration rates imposed on the flow do not affect the evolution of turbulence in these cases. On the other hand, the number of vortical and streak structures for D7 are clearly seen to be

more in comparison to the other two cases at equivalent times. This again substantiates the existence of a time-scale regulating the decay of turbulence.

Overall, it is seen that the evolution of turbulent structures, shown in Figure 7.15, appears to be a gradual process. For both the near-step and ramp-like cases, the structures do not appear to undergo any rapid changes during the transient. In accelerating flow studies of He & Seddighi [8] and Seddighi *et al.* [59], it was shown that low  $Re$ -ratio and ramp-like accelerations undergo the same process of transition as seen in step-like, high  $Re$ -ratio cases, even though the phenomenon was not clearly visible from the evolution of turbulent structures. Here too, even though the flow structures do not exhibit a clear transition process in decelerating flows, the laminar-like initial behaviour of perturbation flow and delayed response of transverse components indicate existence of such a process.

## 7.4 Summary

Similar to accelerating flows, a time-developing boundary layer is generated in decelerating flows which grows into the flow at a rate similar to that in the accelerating flows. It bears a strong resemblance to the time-developing laminar boundary layer. The initial development of the near-wall perturbation velocity and hence, the perturbation wall friction of the decelerating flows can be estimated from the same laminar solution that is obtained for the accelerating flow.

An early increase in the streamwise fluctuation velocity is shown to immediately follow the commencement of the deceleration, which is attributed instability in the flow due to the imposed adverse pressure gradient. Shortly thereafter, the streamwise component decreases owing to a reduction in the turbulent production and suppression of the streak structures. The delayed response of the transverse components, attributed to the re-distribution of streamwise fluctuation energy to other two components, can be regarded as the response of 'real' turbulence. This delay in response is consistent with the critical time until which the

perturbation flow follows the laminar solution. The development of instantaneous flow shows that a rapid change in the deceleration does not affect the turbulent structures already present in the flow in the faster transients. However, the decay of the vortical and streaky structures appears to be a gradual process with no rapid changes during the transient, unlike that seen in step-accelerating flows. Nevertheless, the initial response to flow deceleration is characterised by little or no change in 'real' turbulence and the laminar solution represents the flow perturbation which is followed by the response of transverse components and perturbation flow diverging from the laminar solution, clearly indicating the existence of a transition-like process. The transition mechanism and the timings of the different transitional stages are unclear possibly due to the masking effect by the existing flow structures at the beginning of the transient or due to the step down size chosen herein.

The decelerating flow cases are divided in two groups on the basis of an intrinsic time-scale of the turbulence response. A measure of this time-scale can be estimated from the critical time until which the perturbation flow of an ideal step-change is seen to follow the laminar solution. This critical period is shown to be roughly  $t^{+0} \sim 60$  for the present deceleration. It is shown that if the deceleration period is smaller than the critical time-scale (like those in cases D1-D5), the different deceleration rates do not affect the flow development; the rate of turbulence decay is found to be similar. If, however, the deceleration period is larger (like that in case D6-D7), the rate of decay of turbulence is influenced by the deceleration rate itself.

## Chapter 8

# Low-Reynolds Number Modelling – Launder-Sharma $k$ - $\varepsilon$ Model

---

The low-Reynolds number  $k$ - $\varepsilon$  model due to Launder & Sharma [10], although initially proposed for swirling flows, has been reported to predict several types of turbulent flows reasonably well. However, some researchers have reported poor and inconsistent performance of this model in comparison to other formulations. This chapter presents an evaluation of the performance of this model, and its sensitivity to different interpretations of the mathematical formulation. A brief introduction to low-Reynolds number modelling is presented in §8.1. In §8.2, the Launder-Sharma model is introduced, along with a review of its performance reported in the literature. The performance of the model in comparison to other commercial and in-house codes is presented in §8.3. The sensitivity of model performance to different interpretations is shown in §8.4. The model performance in predicting wall shear stress response of unsteady channel flow is then compared to the numerical and experimental results of the previous chapters in §8.5. Finally, §8.6 presents a summary of the investigation.

### 8.1 Low-Reynolds Number Modelling

A challenge to turbulence modelling is that the direct application of the no-slip wall boundary condition to the model yields unsatisfactory results in the prediction of the flow near the wall.

This is due to the presence of a very thin layer adjoining the wall where the eddy viscosity of the flow changes rapidly with distance from the wall, and its effect on the transport processes cannot be computed by an arithmetic- or harmonic-mean across this region. To overcome this shortcoming, a wall-function method is used by Launder and Spalding [181]. This approach bridges the viscous sublayer by employing empirical formulae in the region providing the boundary conditions to the mean-flow and turbulence equations. This circumvents the need to resolve the viscous sublayer with a fine mesh and solve the transport equations right up to the wall. The first grid node for this approach needs to lie outside the viscous sublayer. A typical requirement is  $y_1^+ > 20$ . An alternative to the wall-function method is the low-Reynolds number (LRN hereafter) approach, where the transport equations are solved right up to the wall using a LRN model, which is developed to account for the near-wall phenomena. Jones and Launder proposed a LRN formulation in the 1972 paper [107], which was tested for shear flows in their 1973 paper [182]. The most widely used version of this model is the Launder–Sharma model [10] which uses the optimised model constants of Launder and Spalding [181].

## 8.2 Launder-Sharma Model

The Launder–Sharma LRN model [10], as a modified version of the standard  $k$ - $\varepsilon$  model is one of the earliest and most widely used models for resolving the near-wall flow behaviour. The LS model differs from the standard model by the inclusion of damping functions in order to account for the viscous and wall effects. The model formulated for an unsteady axi-symmetric flow reads,

Constitution equations:

$$-\overline{\rho u'v'} = \mu_t \frac{\partial u}{\partial r}, \quad \mu_t = \rho C_\mu f_\mu \frac{k^2}{\varepsilon} \quad (8.1)$$

Turbulent kinetic energy equation:

$$\rho \frac{\partial k}{\partial t} + \rho \frac{\partial(Uk)}{\partial x} + \frac{1}{r} \rho \frac{\partial(rVk)}{\partial r} = \frac{\partial}{\partial x} \left[ \left( \mu + \frac{\mu_t}{\sigma_k} \right) \frac{\partial k}{\partial x} \right] + \frac{1}{r} \frac{\partial}{\partial r} \left[ r \left( \mu + \frac{\mu_t}{\sigma_k} \right) \frac{\partial k}{\partial r} \right] + P_k - \rho \varepsilon \quad (8.2)$$

Turbulent energy dissipation equation:

$$\rho \frac{\partial \tilde{\varepsilon}}{\partial t} + \rho \frac{\partial (U \tilde{\varepsilon})}{\partial x} + \frac{1}{r} \rho \frac{\partial (rV \tilde{\varepsilon})}{\partial r} = \frac{\partial}{\partial x} \left[ \left( \mu + \frac{\mu_t}{\sigma_\varepsilon} \right) \frac{\partial \tilde{\varepsilon}}{\partial x} \right] + \frac{1}{r} \frac{\partial}{\partial r} \left[ r \left( \mu + \frac{\mu_t}{\sigma_\varepsilon} \right) \frac{\partial \tilde{\varepsilon}}{\partial r} \right] + C_1 f_1 \frac{\tilde{\varepsilon}}{k} P_k - C_2 f_2 \rho \frac{\tilde{\varepsilon}^2}{k} + E_\varepsilon \quad (8.3)$$

where  $\tilde{\varepsilon} = (\varepsilon - D_\varepsilon)$ . The empirical constants,  $C_1$ ,  $C_2$ ,  $C_\mu$ ,  $\sigma_k$  and  $\sigma_\varepsilon$  have the same value as in the standard  $k$ - $\varepsilon$  model (i.e. 1.44, 1.92, 0.09, 1.0 and 1.3, respectively).

The third term on the right hand side of equation (8.2),  $P_k$ , represents the production of kinetic energy and is defined as:

$$P_k = \mu_t S^2 \quad (8.4)$$

where  $S$  is the strain-rate magnitude. For an axi-symmetric coordinate system, the strain-rate magnitude is defined as:

$$S = \sqrt{2S_{ij}S_{ij}} = \sqrt{\left[ 2 \left\{ \left( \frac{\partial U}{\partial x} \right)^2 + \left( \frac{\partial V}{\partial r} \right)^2 + \left( \frac{V}{r} \right)^2 \right\} + \left( \frac{\partial U}{\partial r} + \frac{\partial V}{\partial x} \right)^2 \right]} \quad (8.5)$$

The damping functions in the above equations are defined as:

$$D_\varepsilon = 2 \frac{\mu}{\rho} \left[ \left( \frac{\partial \sqrt{k}}{\partial r} \right)^2 + \left( \frac{\partial \sqrt{k}}{\partial x} \right)^2 \right]$$

$$E_\varepsilon = 2 \frac{\mu \mu_t}{\rho} \left[ \left( \frac{\partial S}{\partial r} \right)^2 + \left( \frac{\partial S}{\partial x} \right)^2 \right] \quad (8.6)$$

$$f_1 = 1.0, \quad f_2 = 1 - 0.3 \exp(-Re_t^2), \quad f_\mu = \exp \left[ \frac{-3.4}{(1 + Re_t/50)^2} \right]$$

In the above equations,  $Re_t$  represents the local turbulent Reynolds number and is defined using the local values of kinetic energy,  $k$ , and its modified dissipation rate,  $\tilde{\varepsilon}$ :

$$Re_t = \frac{\rho k^2}{\mu \tilde{\varepsilon}} \quad (8.7)$$

The damping functions,  $f_1$ ,  $f_2$  and  $f_\mu$ , account for the near-wall effects and have the value unity far from the wall.

In the model,  $\tilde{\varepsilon}$  ( $= \varepsilon - D_\varepsilon$ ) is a modified dissipation rate of  $k$ ,  $\varepsilon$  is the originally-defined dissipation rate, and  $D_\varepsilon$  a damping term. The reason for solving the  $\tilde{\varepsilon}$  equation is purely computational as there are disadvantages in implementing the non-zero wall-boundary condition of  $\varepsilon$ . The transport equation of  $\tilde{\varepsilon}$  is solved with a boundary value of zero at the wall, and the correct form of  $\varepsilon$  is recovered through  $\varepsilon = (\tilde{\varepsilon} + D_\varepsilon)$  which is then used in the  $k$  transport equation. The value of  $D_\varepsilon$  is significant close to the wall but is negligible away from the wall. The final term in the dissipation equation,  $E_\varepsilon$ , has no physical significance. It is included to increase the predicted dissipation rate, and hence, to obtain realistic predictions of turbulent kinetic energy in the near-wall region. The definition of  $E_\varepsilon$  given in Launder & Sharma [10] was formulated for a special case, namely, swirling axi-symmetric flows. The formulation in the present study, equation (8.6), is an interpretation of that definition for an axi-symmetric flow, and will reduce to the original form for swirling flows.

Although the Launder-Sharma (LS hereafter) model was initially proposed for predicting swirling flows, it has been widely accepted a benchmark LRN  $k$ - $\varepsilon$  formulation and used for a variety of turbulent flows in the literature. Comparative studies of different LRN models were done by Patel *et al.* [115] for boundary layer flows and by Betts & Dafa'Allah [116] for natural convection cavity flows. Both studies reported that LS model was one of only four LRN models that were in good agreement with experimental data. Similar studies were presented for turbulent pipe flow by Hrenya *et al.* [117, 118] and Thakre & Joshi [119] in which the LS model performed reasonably well against DNS and experimental data. Cotton & Jackson [183] and Kim *et al.* [121] extended the study by testing its performance for mixed convection air flow in vertical pipes and concluded that the model was in agreement with experiments in buoyancy-aided flows. He *et al.* [184] reported similar conclusions for mixed convection heat transfer to supercritical fluids.

The model is further proved to be able to predict unsteady turbulence as well. Jackson *et al.* [185] reported that LS model is able to reproduce transient response to heat transfer in

turbulent pipe flow. Transient turbulence response has also been reported to be in good agreement with experiments by He and colleagues [48-50, 131] for accelerating/decelerating pipe flows; and by Cotton and colleagues [35-37, 39] for small-amplitude oscillating pipe flows.

In the above studies, the LS model had been implemented in '*in-house*' CFD codes, and had performed reasonably well in comparison with experimental and/or DNS data. However, recent reports using commercial CFD codes suggest otherwise. Wang & Majumdar [129] investigated the prediction of heat transfer for impingement jets using five LRN models available in the commercial CFD code ANSYS Fluent 6.1, and found that the LS model significantly overestimate the Nusselt number in the impinging region, performing worst among the models used. Similar results were reported by Du *et al.* [130] for heat transfer to supercritical CO<sub>2</sub> in vertical tubes, using the formulation available in ANSYS Fluent 6.2. Applicability of LRN models for flow past underwater hulls was investigated by Jagadeesh & Murali [128] with respect to surface pressure coefficient and pressure surface boundary layer. Four models implemented in ANSYS Fluent 6.1 were considered. Although all four models performed similarly, LS model showed most deviations from the experimental data.

A comparison of different CFD codes was discussed by Iaccarino [127], where the performance of LS model was investigated for a two-dimensional diffuser flow using three commercial codes – ANSYS Fluent 5.3, CD-Adapco StarCD 3.1 and ANSYS CFX 4.3. It was reported that even with the same computational grid and flow conditions, the three codes showed variations in velocity and turbulent kinetic energy profiles. A grid sensitivity analysis had also been performed to show that grid convergence had been reached in each code.

The difference in performance of the LS model discussed above is striking and is likely to be attributable to the way in which the model is implemented in the code. In the present study, an investigation is carried out to study the effect of different implementations and/or interpretations of the model on the performance of the model. Herein, the LS model is implemented in ANSYS Fluent 12.1 using user-defined functions (UDFs) and its performance is

compared with that of the LS implemented in *in-house* CFD codes as well as that of the LS model inbuilt in ANSYS Fluent. The sensitivity of different interpretations of the model formulation is also tested using the Fluent-UDF approach.

The LS model implemented in ANSYS Fluent 12.1 using UDFs is referred to as UDF-LS hereafter. The inbuilt viscous models in the CFD solver are turned off, and the turbulence parameters,  $k$  and  $\tilde{\epsilon}$  are solved as scalar quantities along with the momentum equations. The production and dissipation terms in these equations are added as 'scalar sources' to the transport equations, and the diffusivities of  $k$  and  $\tilde{\epsilon}$  are assigned accordingly. The eddy viscosity is computed from these scalar quantities and is added to the molecular viscosity for computing the effective viscosity of the momentum transport equations. The UDF code is detailed in Appendix B.

Apart from UDF-LS, two other implementations are also used. The first is the inbuilt low-Reynolds number LS model available in ANSYS Fluent 12.1 (referred to as Fluent-LS hereafter). The second model, referred to as TRANPIPE hereafter, is an *in-house* CFD code [131] developed using FORTRAN specifically for modelling turbulent pipe flows. The model implemented is the same as that in UDF-LS, namely following the definitions of the original paper [10]. This in-house code has been used and validated extensively over the years [48-50, 121, 131, 184, 185].

### 8.3 Model Performance of Different RANS Codes

The main objective of the study reported in this section is testing the sensitivity of the model performance to particular coding when the same version of the model (namely, the original [10]) is used. For this purpose, the UDF-LS and the TRANPIPE are used to reproduce and compare with some published simulations of the LS model. In addition, these simulations are compared with those using the inbuilt LS model in ANSYS Fluent 12.1.

Friction coefficients for steady pipe flow at four different Reynolds numbers are reported by Ismael & Cotton [35] using an in-house CFD code developed by the authors. These simulations

are reproduced using three codes: UDF-LS, Fluent-LS and TRANPIPE. The results are compared with those by Ismael & Cotton [35] as well as the Blasius prediction (i.e.  $f = 0.079Re_b^{-0.25}$ ). The friction coefficients for these simulations are presented in Figure 8.1. For all Reynolds numbers, the results of Ismael and Cotton [35] and those of TRANPIPE are indistinguishable whereas those of UDF-LS are slightly lower but still very close to them. In contrast, Fluent-LS is found to predict a significantly higher friction coefficient in comparison with the other three codes. The discrepancies are larger for higher Reynolds numbers. It can also be seen that the Blasius correlation agrees well with the prediction of the first three codes for the two high Reynolds number cases but is somewhat lower than model predictions for low Reynolds number cases. It should be noted that the Blasius correlation is known to be unreliable for low Reynolds number flows. These results are included here for the sake of completeness.

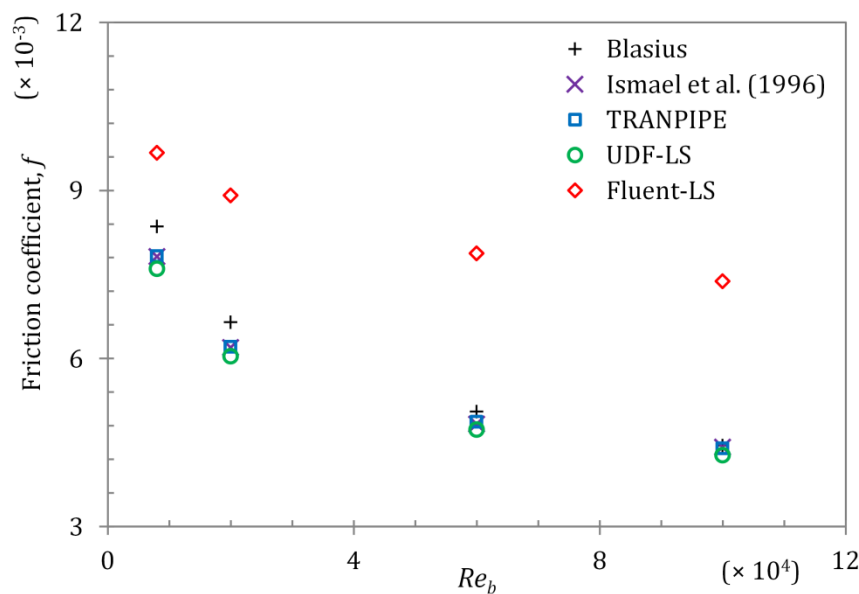


Figure 8.1 Comparison of friction coefficient predicted using different CFD codes for steady pipe flows.

Next, comparisons are made with DNS data with which detailed comparison on velocity profiles can be made. Four sets of turbulent pipe flow data were chosen to cover a range of Reynolds numbers:  $Re_b = 5300$  by Eggels *et al.* [186], 24590 and 60800 by Boersma [187] and 44000 by Wu & Moin [188]. Figures 8.2 (a)-(d) show the comparison of the logarithmic velocity profile of the flow at the various Reynolds numbers. Again the prediction of UDF-LS and TRANPIPE agree well with each other for all Reynolds numbers and are close to the DNS data. In contrast, Fluent-

LS's predictions are lower than the DNS data, with greater discrepancies at higher Reynolds numbers. A detailed inspection shows that the reason for this under-prediction of  $U^+$  ( $= U/u_\tau$ ) is the over-prediction of  $u_\tau$  ( $= \sqrt{\tau_w/\rho}$ ). When the velocity profiles in the dimensional form are compared, the Fluent-LS significantly over-predicts the near-wall velocity gradient, resulting in an over-prediction of  $\tau_w$  and  $u_\tau$ . This is consistent with the results shown in Figure 8.1 where the friction coefficient is over-predicted by Fluent-LS.

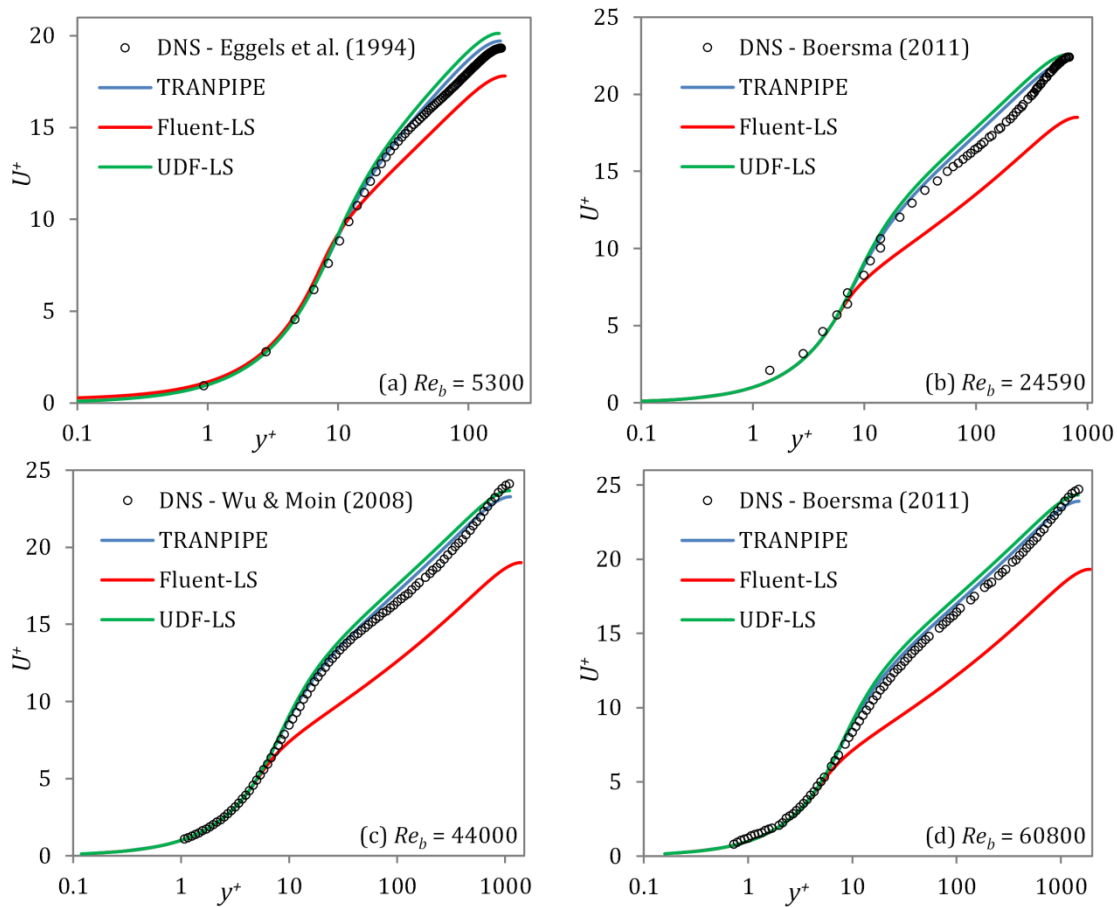


Figure 8.2 Comparison of mean velocity predicted using different CFD codes for steady pipe flows.

Figure 8.3 shows comparisons made with the experimental data of He [131] for an accelerating pipe flow with Reynolds number ramping from 7000 to 45000 in 5s. Predictions of Reynolds stress at four radial locations by TRANPIPE have previously been compared with the experimental data and predictions of Cotton *et al.* [36] in He *et al.* [48]. These are reproduced in Figures 8.3(a) & (b). In addition, the Fluent-LS and UDF-LS models are also used to simulate the same unsteady flow and results of which are shown in Figures 8.3(c) & (d), respectively.

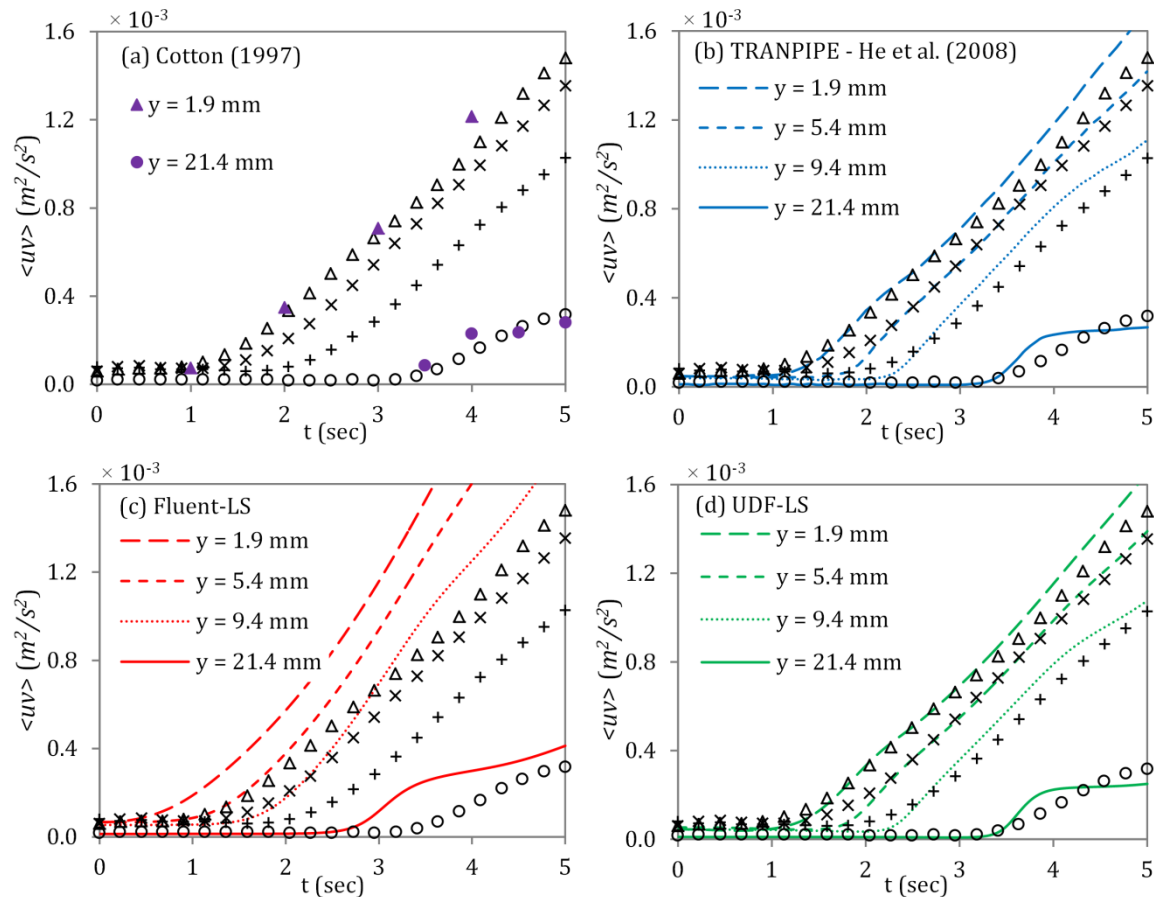


Figure 8.3 Reynolds stress predicted using different CFD codes compared with experimental data of He [131] for an unsteady pipe flows. Experimental data points:  $\Delta$   $y = 1.9$  mm;  $\times$   $y = 5.4$  mm;  $+$   $y = 9.4$  mm;  $o$   $y = 21.4$  mm.

It is seen that the prediction of UDF-LS of Reynolds stress distribution agrees very well with experimental data, which is consistent with the results of He *et al.* [49] and Cotton *et al.* [36]. As discussed previously, the Reynolds stress remains frozen initially and later starts to respond first near the wall, then away from the wall. This delay period is smaller near the wall and increases with the distance away from the wall. For the first and the last radial locations ( $y = 1.9$  mm and  $21.4$  mm), the UDF-LS predicts this delay to be  $\sim 1.2$  s and  $\sim 3.4$  s, respectively, which agree with the predictions of He *et al.* [49] and Cotton *et al.* [36]. The Fluent-LS, however, shows a faster response of turbulence across the radial locations, e.g.,  $\sim 0.4$  s and  $\sim 2.6$  s at  $y = 1.9$  mm and  $21.4$  mm, respectively.

Similar observations are made from the wall shear stress behaviour of the above transient flow, shown in Figure 8.4. Wall shear stress response predicted by all three codes show the same

characteristics of an initial overshoot followed by an undershoot and a recovery as discussed in He [131]. The TRANPIPE simulations of He *et al.* [48] and the UDF-LS results obtained in this study show similar values of the time-scales for the wall shear stress overshoot, undershoot and recovery. The Fluent-LS, however, predicts much lower values, i.e. much faster turbulence production in the near-wall region. This observation is consistent with that in Figure 8.3.

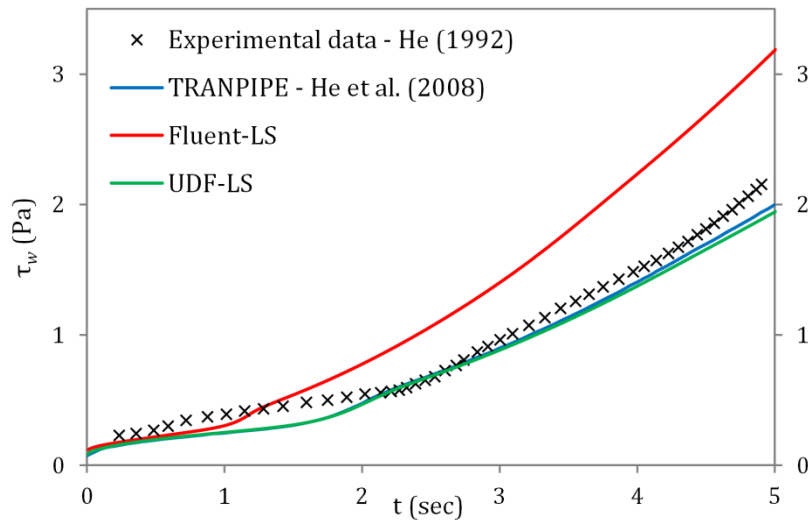


Figure 8.4 Comparison of wall shear stress predicted using different CFD codes with experimental data of He [131] for an unsteady pipe flow.

## 8.4 Model Sensitivity

The second part of the study concerns the interpretation of the LS model. As discussed earlier, an important feature of the LS model is that it uses a modified dissipation rate,  $\tilde{\varepsilon}$  ( $= \varepsilon - D_\varepsilon$ ). The difference between  $\varepsilon$  and  $\tilde{\varepsilon}$  is small as their values are effectively the same for most part of the flow, and are different only in the region very close to the wall. As  $\varepsilon$  is replaced by  $\tilde{\varepsilon}$  in the model only for numerical advantages, there is a question as which of these should be used in the definition of the eddy viscosity ( $\mu_t$ ) and the turbulent Reynolds number ( $Re_t$ ). The modified dissipation rate  $\tilde{\varepsilon}$  is used in the original paper [10] but theoretically speaking, the original  $\varepsilon$  should be used. Several test cases have been designed to study the effect of these different interpretations.

The base case, referred to as Case A, is one where the definitions of  $\mu_t$  and  $Re_t$  use the modified dissipation rate,  $\tilde{\varepsilon}$ , as given by the original paper, Launder & Sharma [10]. Table 8.1 lists the rest of the implemented cases used in the study. All cases are implemented in ANSYS Fluent 12.1 using user-defined functions (UDFs).

Cases	Eddy viscosity, $\mu_t$	Turbulent Reynolds Number, $Re_t$
UDF-LS (Case A)	$\rho C_\mu f_\mu \frac{k^2}{\tilde{\varepsilon}}$ ( <i>Original</i> )	$\frac{k^2}{\nu \tilde{\varepsilon}}$ ( <i>Original</i> )
Case B	$\rho C_\mu f_\mu \frac{k^2}{\tilde{\varepsilon} + D_\varepsilon}$	<i>Original</i>
Case C	<i>Original</i>	$\frac{k^2}{\nu(\tilde{\varepsilon} + D_\varepsilon)}$
Case D	$\rho C_\mu f_\mu \frac{k^2}{\tilde{\varepsilon} + D_\varepsilon}$	$\frac{k^2}{\nu(\tilde{\varepsilon} + D_\varepsilon)}$

Table 8.1 Launder-Sharma implementation cases in the present study

Three additional cases are considered to study the effects of using  $\varepsilon$  (instead of  $\tilde{\varepsilon}$ ) in  $\mu_t$  and  $Re_t$  as shown in Table 8.1. The values of wall shear stress of steady pipe flow at  $Re_b = 45000$  for the different implementations are shown in Figure 8.5. Transient wall shear stress responses of these different cases are shown in Figure 8.6 for the accelerating pipe flow ramping from  $Re_b = 7000$  to 45000 in 5 s.

It is observed that the use of different interpretations of the model has a significant impact on the prediction of the model. While Cases B to D under-predict the steady wall shear stress compared to UDF-LS (Case A), Fluent-LS over-predicts it. The prediction of the transient response of the wall shear stress shows the capability of the model in reproducing unsteady turbulence behaviours. Cases B to D show a much slower turbulent response to the imposed acceleration than that of the base case (UDF-LS). While the base case predicts that the wall shear stress starts to recover at  $\sim 1.8$  s, Cases B and C predict this delay to be  $\sim 4$  s and  $\sim 2.5$  s, respectively. Case D predicts the slowest response, where the response of the wall shear stress

does not reach the end of the delay period during the imposed acceleration period of 5 s. The Fluent-LS, on the other hand, predicts a much faster response with a delay of  $\sim 1.1$  s.

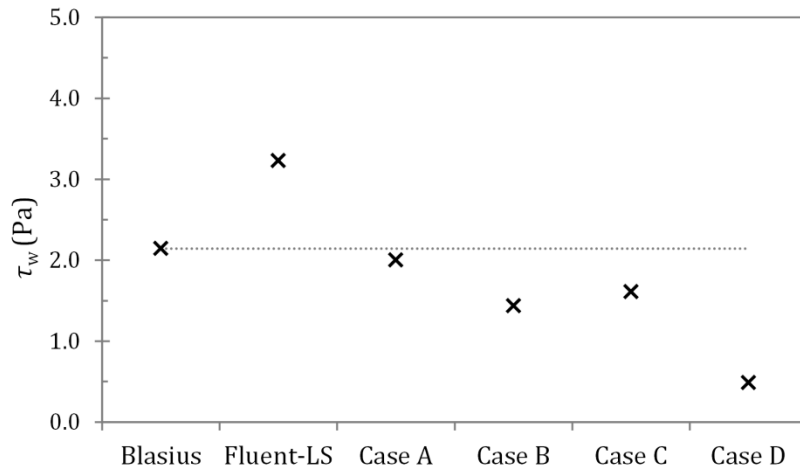


Figure 8.5 Comparison of different LS model interpretations for steady pipe flow at  $Re_b = 45000$

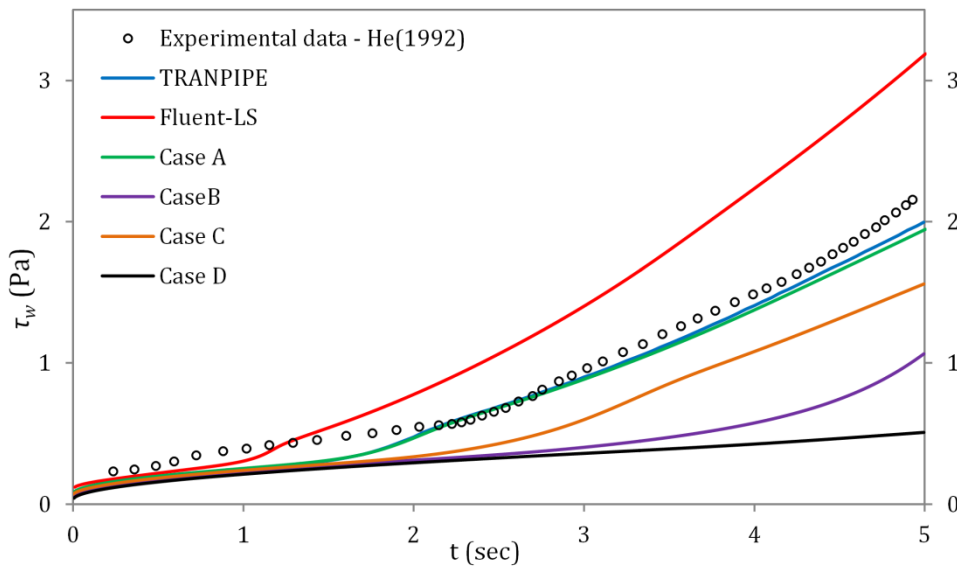


Figure 8.6 Comparison of different LS model interpretations for a 5 second ramp-up pipe flow.

These results show that, although  $\varepsilon$  and  $\tilde{\varepsilon}$  only differ in a very small region close to the wall, the choice of using either  $\varepsilon$  or  $\tilde{\varepsilon}$  in  $\mu_t$  and  $Re_t$  has a significant effect on the performance of the model in predicting both steady and unsteady flow behaviours. It is not surprising that the formulation using  $\tilde{\varepsilon}$  works better than that using  $\varepsilon$  because the model was tuned using the former. Although theoretically speaking  $\varepsilon$ , not  $\tilde{\varepsilon}$ , should be used, there is no real significance in

using either of them because of the empirical nature of the damping functions. The difference can be absorbed by modifying the damping functions. For example,  $\mu_t = \rho C_\mu f_\mu k^2 / \tilde{\varepsilon}$  can be recast as  $\mu_t = \rho C_\mu (f_\mu \varepsilon / \tilde{\varepsilon}) k^2 / \varepsilon$ , with a new damping function  $f'_\mu = (f_\mu \varepsilon / \tilde{\varepsilon})$ . This way,  $\varepsilon$  indeed appears in the definition of  $\mu_t$ .

## 8.5 Model Performance for Unsteady Channel Flow

The performance of the LS model in predicting wall stress response of accelerating and decelerating channel flows is now assessed using the numerical results of the Chapters 5-7. The two implementations, UDF-LS and Fluent-LS, have been used to reproduce four cases of unsteady channel flow, namely, the ramp acceleration case E2 of Chapter 6, the step-acceleration case of Chapter 5, the ramp- and step-deceleration cases D7 and D1, respectively, of Chapter 7.

Figures 8.7(a) & (b) present the predictions of the two implementations for accelerating cases, E2 and U3 along with the respective LES results from Chapters 6 and 5. It is shown that the early response of the rapid increase of wall shear stress is predicted reasonably accurately by both implementations. This however is expected as this behaviour is an inertial effect of the flow acceleration that is not strongly influenced by turbulence. Further in time, UDF-LS is shown to produce the same three-stage response of wall shear stress as that of LES results, however the time scales here are shorter in comparison. The time of onset of transition (time at which a sudden change in the response of  $\tau_w$  occurs) predicted by UDF-LS is roughly  $\sim 1.6$  s and  $\sim 0.95$  s, for cases E2 and U3, respectively, whereas that predicted by LES is  $\sim 2.0$  s and  $\sim 1.25$  s, respectively. The final steady value of the wall shear stress is also slightly under-predicted by UDF-LS, in comparison to LES results. On the other hand, Fluent-LS severely over-predicts the wall shear stress and under-predicts the time scales of its response. After the initial increase of wall shear stress, Fluent-LS fails to predict its reduction and the delay in its response. The three-

stage response is not apparent in either the ramp- or the step-accelerating case. The predicted response of wall shear stress by Fluent-LS for case E2 (Figure 8.7a) increases monotonically throughout the transient with values much higher than those predicted by UDF-LS and LES; whereas that for case U3 (Figure 8.7b) appears to oscillate after the initial increase, settling at a much higher value than LES and UDF-LS values. The anomalous behaviour of Fluent-LS is consistent with the observations in Figures 8.1 and 8.4.

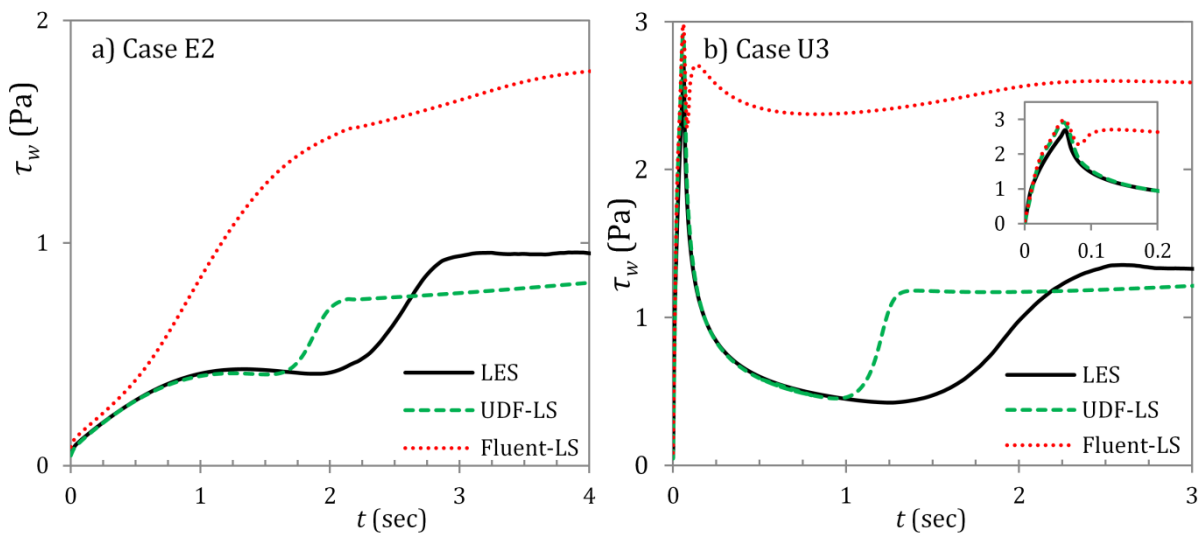


Figure 8.7 Comparison of prediction of wall shear stress response using UDF-LS and Fluent-LS implementations for a) ramp-accelerating case E2, and b) step-accelerating case U3. The inset in subplot (b) shows the early response using a different scale.

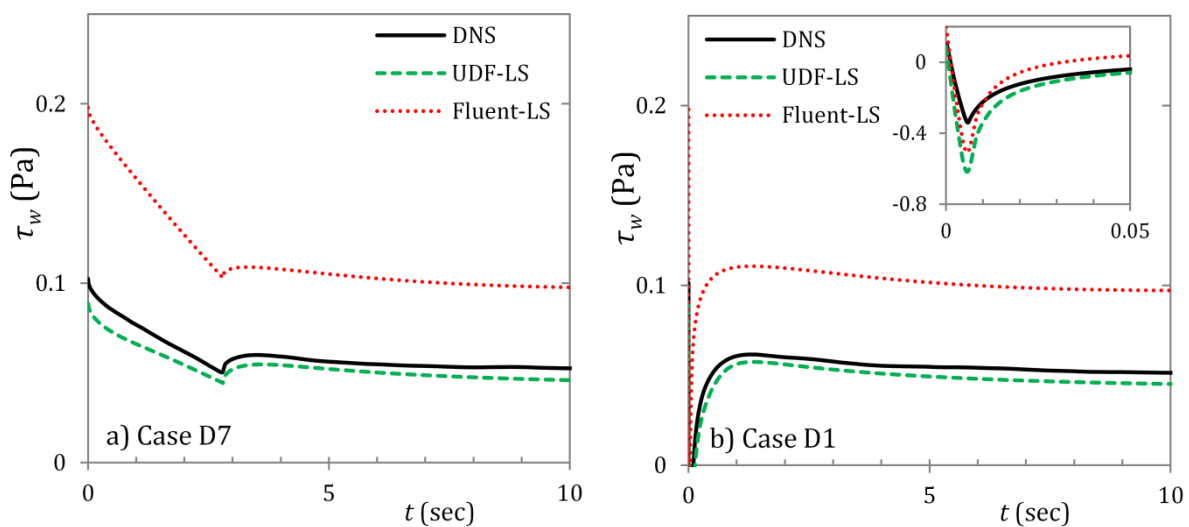


Figure 8.8 Comparison of prediction of wall shear stress response using UDF-LS and Fluent-LS implementations for a) ramp-decelerating case D7, and b) step-decelerating case D1. The inset in subplot (b) shows the early response using a different scale.

The response of wall shear stress predicted by the two implementations for decelerating cases, D7 and D1 are presented in Figures 8.8(a) & (b), respectively, along with DNS results from Chapter 7. Consistent with that in accelerating flows, UDF-LS slightly under-predicts the wall shear stress value while Fluent-LS severely over-predicts it. However, unlike that in accelerating flows, it is shown that UDF-LS and Fluent-LS predict the time scales of wall shear stress response pretty accurately compared to the DNS results for both ramp- and step-decelerations during the entire transient. After the initial rapid decrease of wall shear stress due to inertia, both the time of its recovery and time to reach the final steady value predicted by the two implementations are nearly equal. It appears that the shortcoming of Fluent-LS in predicting transient response of wall shear stress (as that seen in accelerating flows) is not explicit in decelerating flows. However, the over-prediction of the wall shear stress values by Fluent-LS in the steady flows is also seen in the transient response here, which makes Fluent-LS unsuitable for predicting decelerating flows as well.

## 8.6 Summary

It is shown that the presently implemented model (UDF-LS), using the formulation initially proposed in the original paper (Launder & Sharma [10]), agrees well with the predictions of the 'in-house' codes reported in the literature. They closely reproduce steady and unsteady pipe/channel flow experimental and DNS/LES data, confirming that the robustness and insensitivity of the model to the numerical methods/coding used as long as the model formulation is the same. The Fluent-LS model, however, compares rather badly with experimental and DNS data. This is likely to be associated with the formulation chosen to be used in the code rather than the numerical methods used as demonstrated through comparisons between the simulations of Fluent-LS and UDF-LS, which are based on the same numerical/coding framework.

---

It has previously been assumed that the choice  $\varepsilon$  or  $\tilde{\varepsilon}$ , for the calculation of  $\mu_t$  and  $Re_t$ , would have minor influence on results as they are the same everywhere in the flow field except for only a small region very close to the wall. However, the present results show that the choice has significant effect on the predictions of the model and that the formulation proposed in the original paper (i.e. using  $\tilde{\varepsilon}$ ) performs best when compared with experimental and DNS results.

# Chapter 9

## Conclusions

---

This chapter gathers the findings of the present investigations of the response of turbulence and wall friction to flow unsteadiness. Concluding remarks on the behaviour of mean flow and turbulence in accelerating and decelerating flows are presented herein. Subsequently, some remarks on low-Reynolds number modelling are also discussed. Finally, suggestions for potential future investigations are presented in the last section.

### 9.1 Accelerating Flows

Step-like accelerating flows with high  $Re$ -ratio have been investigated using Large Eddy Simulations (LES). It is shown that, similar to the low  $Re$ -ratio cases of He & Seddighi [7, 8], the present cases show a three stage response resembling the three regions of bypass transition in boundary layer flows. However, the features of transition become more striking when the  $Re$ -ratio increases – the elongated streaks in the pre-transitional period become increasingly longer, stronger and are more densely packed; and the turbulent spots generated at the initial stage at the onset of transition become increasingly sparse. Experimental investigations of ramp-like accelerating have been performed using Particle-Image Velocimetry (PIV) and

Constant-Temperature Anemometry (CTA). Consistent with the findings of Seddighi *et al.* [59], it is shown that despite some quantitative differences, the present cases respond in fundamentally the same process of three-stage transitional response. In comparison to step-like flow acceleration, the onset of transition is delayed, with a slower rate of flow development.

For high  $Re$ -ratio step-like cases, similar to that in low  $Re$ -ratio cases, the new boundary layer is formed instantly over the wall which develops into the flow with time. However, for the ramp-like cases, the boundary layer development can be described as an integral consequence of continuous changes in the flow. The development of the step-like cases is shown to be represented by the laminar solution to Stokes' first problem; while that of the ramp-like cases is shown to be represented by an extension of the laminar solution to a time-varying perturbation.

For the step-like cases with a turbulence intensity similar to or slightly higher than that in He & Seddighi [8], the transition is well predicted by the correlation of He & Seddighi [8], whereas the low-turbulence intensity cases are seen to diverge from this trend. It is shown that the ramp-like cases roughly follow the same correlation as that of He & Seddighi [8] based on modified definitions of turbulence intensity,  $Tu_0$ , and equivalent Reynolds number,  $Re_t$ , to account for slower acceleration and continuously changing bulk velocity. For both step- and ramp-like cases, the transition period Reynolds number is shown to have a power-relationship with the critical Reynolds number.

The high  $Re$ -ratio step-like cases are shown to have double peaks in the transient response of streamwise fluctuations profiles shortly after the onset of transition. A conditional sampling technique, based on a  $\lambda_2$ -criterion, is used to show that the two peaks in the domain-averaged fluctuation profiles originate from the separate contributions of the active and inactive regions of turbulence generation. The peak closer to the wall is attributed to the generation of 'new' turbulence in the active region; whereas the peak further away from the wall is attributed to the elongated streaks in the inactive region. Although separate developments of the two regions

exist in the low  $Re$ -ratio cases, the peaks of the two regions are masked by each other during the entire transient, resulting in a single peak in the domain-averaged profile.

## 9.2 Decelerating Flows

Direct Numerical Simulations (DNS) of decelerating flows, ranging from step-like to ramp-like, are performed. The early response of deceleration is plug-like – no change in the shape of the velocity profile, except close to the wall where the velocity gradient drops sharply. At high rates of deceleration, flow separation is observed at the wall, followed by reversal. Similar to accelerating flows, a time-developing boundary layer is generated in decelerating flows which grows into the flow at a rate similar to that in the accelerating flows. The perturbation velocity ( $\bar{u}^{\wedge}$ ) and modified friction coefficient ( $C_{f,du}''$ ) for both decelerating and accelerating flows exhibit the same initial response, bearing strong resemblance to the laminar boundary layer. The early development of the near-wall perturbation velocity and wall friction of the step-like flows can be estimated using the Stokes' solution for laminar flow; while that for ramp-like flows can be estimated using an extension of the laminar solution to time-varying perturbation.

An early increase in streamwise fluctuation velocity is shown to immediately follow the commencement of the deceleration, which is attributed to the instability in the flow due to the imposed adverse pressure gradient. The momentary initial increase is immediately followed by a decrease in the streamwise component attributed to the drop in turbulence production and suppression of the streak structures. The transverse components, on the other hand, are shown to respond after a delay and can be regarded as the response of 'real' turbulence.

The development of the instantaneous flow shows that a change in the deceleration rate does not affect the turbulent structures already present in the flow in the faster transients. The decay of the vortical and streaky structures appears to be a gradual process with no rapid changes during the transient. Unlike in step-accelerating flows, the turbulence in decelerating flows

appears to exhibit a gradual development. However, the initial response period is characterised by little or no change in real turbulence and the laminar solution represents the flow perturbation which is followed by the response of transverse components and perturbation flow diverging from the laminar solution, clearly indicating the existence of a transition-like process.

A time-scale of turbulence response is shown to exist which can be estimated from the critical time until which an ideal step-change deceleration follows the laminar solution. The transient decelerating flow cases are divided in two groups on the basis of this intrinsic time-scale. If the deceleration period is smaller than this critical time-scale, the different deceleration rates do not affect the flow development; the rate of turbulence decay is found to be similar. If, however, the deceleration period is larger, the rate of turbulence decay is influenced by the deceleration rate itself.

### 9.3 Launder-Sharma $k$ - $\varepsilon$ Model

An investigation is carried out to study the sensitivity of the Launder-Sharma low-Reynolds number turbulence model to methods of implementation in CFD codes. A user-defined function (UDF) is developed to implement the LS model to the commercial CFD code ANSYS Fluent. Its performance in predicting both steady and unsteady flows is compared with that of the inbuilt LS model in ANSYS Fluent and those implemented in several in-house codes previously reported in the literature. The UDFs developed is also used to study the effect of using  $\varepsilon$  or  $\tilde{\varepsilon}$  in the definition of  $\mu_t$  and  $Re_t$  in the coding.

It is shown that the presently implemented model (UDF-LS), using the formulation proposed in the original paper (Launder & Sharma [10]), agrees well with the predictions of the 'in-house' codes reported in the literature. They closely reproduce steady and unsteady pipe/channel flow

experimental and DNS/LES data, confirming the robustness of the model to the numerical methods/coding used as long as the model formulation is the same.

The ANSYS Fluent in-built LS model produces results that are significantly different from that of the LS implemented in Fluent using UDF in the present study and those of results published in the literature using 'in-house' codes. The Fluent-LS model predictions compare rather badly with experimental and DNS data. This is likely to be associated with the formulation chosen to be used in the code rather than the numerical methods used as demonstrated through comparisons between the simulations of Fluent-LS and UDF-LS, which are based on the same numerical/coding framework.

Theoretically speaking,  $\varepsilon$  rather than  $\tilde{\varepsilon}$  should be used in the calculation of  $\mu_t$  and  $Re_t$ , albeit the latter is used in the original paper. It has previously been assumed that this choice would have minor influence on results as they are the same everywhere in the flow field except for only a small region very close to the wall. However, the present results show that the choice has significant effect on the predictions of the model and that the formulation proposed in the original paper (i.e. using  $\tilde{\varepsilon}$ ) performs best when compared with experimental and DNS results.

## 9.4 Suggestions for Future Work

Some suggestions for potential future investigations are detailed below:

- i) The initial Reynolds number in the present numerical and experimental investigations of accelerating flows was deliberately kept low so as to increase the Reynolds number-ratio. Effort should be made to increasing these values so as to extend the range of correlations to predict transition.
- ii) Due to high computational resources, the initial turbulence intensity ( $Tu_0$ ) in the present numerical investigation could not be decreased below 0.9%. The response of turbulence dynamics in unsteady flows with  $Tu_0 \sim 0.1\%$  (similar to FST levels in TS-

wave transition) would be interesting to study. The experimental flow facility could potentially be remodelled to generate a much larger driving pressure gradient by increasing the height of the header tank, so as to reach lower  $Tu_0$  values.

- iii) The present experimental investigations lacked good visualisations of the response of near-wall turbulent structures using PIV. In future studies, better visualisation techniques could be implemented in the flow facility, such as hydrogen-bubble generation; dye injection, pressure- and shear-sensitive coating, etc.
- iv) The calibration of the hotfilm sensors posed a challenge in the present study; and subsequently resulted in inconsistent results in comparison to numerical data for high  $Re$ -ratio transient flows. In future studies, effort should be made to devise a more reliable calibration method to capture accurate wall shear stress response.
- v) In the present computational investigation of decelerating flows, the delay in response of turbulence can be estimated from the critical time until which a laminar solution represents the flow perturbation. However, the underlying transition mechanism is not identifiable from the flow structures. In future studies, effort should be made to vary the range of Reynolds numbers and  $Re$ -ratios in decelerating flows to better elucidate the transition process and, potentially, quantify the onset and completion of such a process.
- vi) In light of the new findings in accelerating and decelerating flows, future studies could potentially be devoted to turbulent periodic flows such as square or triangular waves to study the effect of unsteadiness on wall shear stress and its prediction using laminar solutions.

# References

- [1] S. S. Varghese and S. H. Frankel, "Numerical Modeling of Pulsatile Turbulent Flow in Stenotic Vessels," *Journal of Biomechanical Engineering*, vol. 125, p. 445, 2003.
- [2] S. S. Varghese, S. H. Frankel, and P. F. Fischer, "Modeling transition to turbulence in eccentric stenotic flows," *J Biomech Eng*, vol. 130, p. 014503, Feb 2008.
- [3] A. F. Colombo, P. Lee, and B. W. Karney, "A selective literature review of transient-based leak detection methods," *Journal of Hydro-environment Research*, vol. 2, pp. 212-227, 2009.
- [4] J. Dullhoste, G. Besançon, L. Torres, O. Begovich, and A. Navarro, "About friction modelling for observer-based leak estimation in pipelines," presented at the *50th IEEE Conference on Decision and Control and European Control Conference*, Orlando, USA, 2011.
- [5] R. M. C. So and C. G. Speziale, "A review of turbulent heat transfer modeling," *Annual Review of Heat Transfer*, vol. 10, pp. 177-219, 1999.
- [6] F. Roelofs, A. Shams, I. Otic, M. Böttcher, M. Duponcheel, Y. Bartosiewicz, *et al.*, "Status and perspective of turbulence heat transfer modelling for the industrial application of liquid metal flows," *Nuclear Engineering and Design*, vol. 290, pp. 99-106, 2015.
- [7] S. He and M. Seddighi, "Turbulence in transient channel flow," *Journal of Fluid Mechanics*, vol. 715, pp. 60-102, 2013.
- [8] S. He and M. Seddighi, "Transition of transient channel flow after a change in Reynolds number," *Journal of Fluid Mechanics*, vol. 764, pp. 395-427, 2015.
- [9] M. Seddighi, "Study of turbulence and wall shear stress in unsteady flow over smooth and rough wall surfaces," Ph.D., University of Aberdeen, 2011.
- [10] B. E. Launder and B. I. Sharma, "Application of the energy-dissipation model of turbulence to the calculation of flow near a spinning disc," *Letters in Heat and Mass Transfer*, vol. 1, pp. 131-138, 1974.
- [11] J. H. Gerrard, "An experimental investigation of pulsating turbulent water flow in a tube," *Journal of Fluid Mechanics*, vol. 46, pp. 43-64, 1971.
- [12] T. Mizushina, T. Maruyama, and Y. Shiozaki, "Pulsating turbulent flow in a tube," *Journal of Chemical Engineering of Japan*, vol. 6, pp. 487-494, 1973.
- [13] T. Mizushina, T. Maruyama, and H. Hirasawa, "Structure of the turbulence in pulsating pipe flows," *Journal of Chemical Engineering of Japan*, vol. 8, pp. 210-216, 1975.
- [14] B. R. Ramaprian and S. W. Tu, "Experimental study of oscillatory pipe flow at transitional Reynolds numbers," *Journal of Fluid Mechanics*, vol. 100, pp. 513-544, 1980.
- [15] B. R. Ramaprian and S. W. Tu, "Fully developed periodic turbulent pipe flow. Part 2 - The detailed structure of the flow," *Journal of Fluid Mechanics*, vol. 137, pp. 59-81, 1983.
- [16] S. W. Tu and B. R. Ramaprian, "Fully developed periodic turbulent pipe flow. Part 1 - Main experimental results and comparison with predictions," *Journal of Fluid Mechanics*, vol. 137, pp. 31-58, 1983.
- [17] M. Ohmi, S. Kyomen, and T. Usui, "Analysis of velocity distribution in pulsating turbulent pipe flow with time-dependent friction velocity," *Bulletin of JSME*, vol. 21, pp. 1137-1143, 1978.

- [18] F. S. Tardu, G. Binder, and R. F. Blackwelder, "Turbulent channel flow with large-amplitude velocity oscillations," *Journal of Fluid Mechanics*, vol. 267, pp. 109-151, 1994.
- [19] M. Iguchi, M. Ohmi, and S. Tanaka, "Experimental Study of turbulence in a pulsatile pipe flow," *Bulletin of JSME*, vol. 28, pp. 2915-2922, 1985.
- [20] F. S. Tardu and P. Vezin, "Response of the streaks, the active and passive eddies in an unsteady channel flow," *International Journal of Heat and Fluid Flow*, vol. 25, pp. 915-932, 2004.
- [21] F. S. Tardu and P. da Costa, "Experiments and modelling of an unsteady turbulent channel flow," *AIAA Journal*, vol. 43, pp. 140-148, 2005.
- [22] S. F. Tardu, "Spectral Characteristics of the Near-Wall Turbulence in an Unsteady Channel Flow," *Journal of Applied Mechanics*, vol. 74, pp. 172-175, 2007.
- [23] F. S. Tardu and R. Maestri, "Wall shear stress modulation in a turbulent flow subjected to imposed unsteadiness with adverse pressure gradient," *Fluid Dynamics Research*, vol. 42, p. 035510, 2010.
- [24] S. He and J. D. Jackson, "An experimental study of pulsating turbulent flow in a pipe," *European Journal of Mechanics, B/Fluids*, vol. 28, pp. 309-320, 2009.
- [25] M. Hino, M. Kashiwayanagi, A. Nakayama, and T. Hara, "Experiments on the turbulence statistics and the structure of a reciprocating oscillatory flow," *Journal of Fluid Mechanics*, vol. 131, pp. 363-400, 1983.
- [26] L. Shemer and E. Kit, "An experimental investigation of the quasisteady turbulent pulsating flow in a pipe," *Physics of Fluids*, vol. 27, pp. 72-76, 1984.
- [27] L. Shemer, I. Wygnanski, and E. Kit, "Pulsating flow in a pipe," *Journal of Fluid Mechanics*, vol. 153, pp. 313-337, 1985.
- [28] Z. Mao and T. J. Hanratty, "Studies of wall shear stress in a turbulent pulsatile pipe flow," *Journal of Fluid Mechanics*, vol. 170, pp. 545-564, 1986.
- [29] Z. Mao and T. J. Hanratty, "Wall shear rate in large amplitude unsteady reversing flow," *Experiments in Fluids*, vol. 12, pp. 342-350, 1992.
- [30] Z. Mao and T. J. Hanratty, "Influence of large amplitude oscillations on turbulent drag," *AIChE Journal*, vol. 40, pp. 1601-1610, 1994.
- [31] G. J. Brereton, W. C. Reynolds, and R. Jayaraman, "Response of a turbulent boundary layer to sinusoidal free-stream unsteadiness," *Journal of Fluid Mechanics*, vol. 221, pp. 131-159, 1990.
- [32] G. J. Brereton and W. C. Reynolds, "Dynamic Response of boundary layer turbulence to oscillatory shear," *Physics of Fluids A*, vol. 3, pp. 178-187, 1991.
- [33] A. Scotti and U. Piomelli, "Numerical simulation of pulsating turbulent channel flow," *Physics of Fluids*, vol. 13, pp. 1367-1384, 2001.
- [34] A. Scotti and U. Piomelli, "Turbulence models in pulsating flows," *AIAA Journal*, vol. 40, pp. 537-544, 2002.
- [35] J. O. Ismael and M. A. Cotton, "Calculations of wall shear stress in harmonically oscillated turbulent pipe flow using a low-Reynolds number  $k-\epsilon$  model," *Journal of Fluids Engineering*, vol. 118, pp. 189-194, 1996.
- [36] M. A. Cotton, A. W. Guy, and B. E. Launder, "Second-moment modelling of periodic and transient pipe flow," In *11th Symposium on Turbulent Shear Flows*, Grenoble, France, vol., pp. 14.6-14.11, 1997.

- [37] M. A. Cotton, T. J. Craft, A. W. Guy, and B. E. Launder, "On modelling periodic motion with turbulence closures," *Flow, Turbulence and Combustion*, vol. 67, pp. 143-158, 2001.
- [38] M. A. Cotton and A. W. Guy, "Analytical and Reynolds stress transport model results for periodically oscillated turbulent flows," *Journal of Hydraulic Research*, vol. 42, pp. 293-302, 2004.
- [39] M. A. Cotton, "Resonant responses in periodic turbulent flows: computations using a  $k-\epsilon$  eddy viscosity model," *Journal of Hydraulic Research*, vol. 45, pp. 54-61, 2007.
- [40] G. J. Brereton and R. R. Mankbadi, "Review of recent advances in the study of unsteady turbulent internal flows," *Applied Mechanical Reviews*, vol. 48, pp. 189-212, 1995.
- [41] M. Y. Gündoğdu and M. O. Çarpınlioğlu, "Pulsatile flow theory. Part 2: Turbulent flow regime," *JSME International Journal*, vol. 42, pp. 398-410, 1999.
- [42] M. Nabavi and K. Siddiqui, "A critical review on advanced velocity measurement techniques in pulsating flows," *Measurement Science and Technology*, vol. 21, p. 042002, 2010.
- [43] T. Maruyama, T. Kuribayashi, and T. Mizushima, "The structure of the turbulence in transient pipe flows," *Journal of Chemical Engineering of Japan*, vol. 9, pp. 431-439, 1976.
- [44] S. He and J. D. Jackson, "A study of turbulence under conditions of transient flow in a pipe," *Journal of Fluid Mechanics*, vol. 408, pp. 1-38, 2000.
- [45] D. Greenblatt and E. A. Moss, "Rapid temporal acceleration of a turbulent pipe flow," *Journal of Fluid Mechanics*, vol. 514, pp. 65-75, 2004.
- [46] E. B. Shuy, "Wall shear stress in accelerating and decelerating turbulent pipe flows," *Journal of Hydraulic Research*, vol. 34, pp. 173-183, 1996.
- [47] J. Kurokawa and M. Morikawa, "Accelerated and decelerated flows in a circular pipe," *Bulletin of JSME*, vol. 29, pp. 758-765, 1986.
- [48] S. He, C. Ariyaratne, and A. E. Vardy, "A computational study of wall friction and turbulence dynamics in accelerating pipe flows," *Computers and Fluids*, vol. 37, pp. 674-689, 2008.
- [49] C. Ariyaratne, S. He, and A. E. Vardy, "Wall friction and turbulence dynamics in decelerating pipe flows," *Journal of Hydraulic Research*, vol. 48, pp. 810-821, 2010.
- [50] S. He and C. Ariyaratne, "Wall shear stress in the early stage of unsteady turbulent pipe flow," *Journal of Hydraulic Engineering*, vol. 137, pp. 606-610, 2011.
- [51] S. He, C. Ariyaratne, and A. E. Vardy, "Wall shear stress in accelerating turbulent pipe flow," *Journal of Fluid Mechanics*, vol. 685, pp. 440-460, 2011.
- [52] G. N. Coleman, J. Kim, and P. R. Spalart, "Direct numerical simulation of a decelerated wall-bounded turbulent shear flow," *Journal of Fluid Mechanics*, vol. 495, pp. 1-18, 2003.
- [53] T. Talha, "A numerical investigation of three-dimensional unsteady turbulent channel flow subjected to temporal acceleration," Ph.D., University of Warwick, 2012.
- [54] P. A. Krogstad and P. E. Skåre, "Influence of a strong adverse pressure gradient on the turbulent structure in a boundary layer," *Physics of Fluids*, vol. 7, pp. 2014-2024, 1995.
- [55] Y. Nagano, T. Tsuji, and T. Houra, "Structure of turbulent boundary layer subjected to adverse pressure gradient," *International Journal of Heat and Fluid Flow*, vol. 19, pp. 563-572, 1998.
- [56] Y. M. Chung, "Unsteady turbulent flow with sudden pressure gradient changes," *International Journal For Numerical Methods in Fluids*, vol. 47, pp. 925-930, 2005.

- [57] M. Seddighi, S. He, P. Orlandi, and A. E. Vardy, "A comparative study of turbulence in ramp-up and ramp-down unsteady flows," *Flow, Turbulence and Combustion*, vol. 86, pp. 439-454, 2011.
- [58] S. Y. Jung and Y. M. Chung, "Large-eddy simulation of accelerated turbulent flow in a circular pipe," *International Journal of Heat and Fluid Flow*, vol. 33, pp. 1-8, 2012.
- [59] M. Seddighi, S. He, A. E. Vardy, and P. Orlandi, "Direct Numerical Simulation of an accelerating channel flow," *Flow, Turbulence and Combustion*, vol. 92, pp. 473-502, 2014.
- [60] S. Gorji, "A study of turbulence in transient channel flows," Ph.D., University of Sheffield, 2015.
- [61] O. Reynolds, "An experimental investigation of the circumstances which determine whether the motion of water shall be direct or sinuous, and of the law of resistance in parallel channels," *Philosophical Transactions of the Royal Society of London*, vol. 174, pp. 935-982, 1883.
- [62] L. Kleiser and T. A. Zang, "Numerical simulation of transition in wall-bounded shear flows," *Annual Review of Fluid Mechanics*, vol. 23, pp. 495-537, 1991.
- [63] M. V. Morkovin, "On the Many Faces of Transition," in *Viscous Drag Reduction*: Springer US, 1969, pp. 1-31.
- [64] R. G. Jacobs and P. A. Durbin, "Simulations of bypass transition," *Journal of Fluid Mechanics*, vol. 428, pp. 185-212, 2001.
- [65] J. M. Kendall, "Experimental study of disturbances produced in a pre-transitional laminar boundary layer by weak freestream turbulence," *AIAA Paper*, p. 1695, 1985.
- [66] T. Ellingsen and E. Palm, "Stability of linear flow," *Physics of Fluids*, vol. 18, pp. 487-488, 1975.
- [67] L. S. Hultgren and L. H. Gustavsson, "Algebraic growth of disturbances in a laminar boundary layer," *Physics of Fluids*, vol. 24, pp. 1000-1004, 1981.
- [68] M. T. Landahl, "A note on an algebraic instability of inviscid parallel shear flows," *Journal of Fluid Mechanics*, vol. 98, pp. 243-251, 1980.
- [69] P. H. Alfredsson and M. Matsubara, "Streaky structures in transition," in *Transitional Boundary Layers in Aeronautics*: Elsevier, 1996, pp. 373-386.
- [70] J. D. Swearingen and R. F. Blackwelder, "The growth and breakdown of streamwise vortices in the presence of a wall," *Journal of Fluid Mechanics*, vol. 182, pp. 255-290, 1987.
- [71] M. Asai, M. Minagawa, and M. Nishioka, "The instability and breakdown of a near-wall low-speed streak," *Journal of Fluid Mechanics*, vol. 455, pp. 289-314, 2002.
- [72] X. Yu and J. T. C. Liu, "On the mechanism of sinuous and varicose modes in three-dimensional viscous secondary instability of nonlinear Görtler rolls," *Physics of Fluids*, vol. 6, pp. 736-750, 1994.
- [73] F. Waleffe, "On a self-sustaining process in shear flows," *Physics of Fluids*, vol. 9, pp. 883-900, 1997.
- [74] P. A. Elofsson, M. Kawakami, and P. H. Alfredsson, "Experiments on the stability of streamwise streaks in plane Poiseuille flow," *Physics of Fluids*, vol. 11, pp. 915-930, 1999.
- [75] L. Brandt, P. Schlatter, and D. S. Henningson, "Transition in boundary layers subject to free-stream turbulence," *Journal of Fluid Mechanics*, vol. 517, pp. 167-198, 2004.
- [76] P. Schlatter, L. Brandt, H. C. D. Lange, and D. S. Henningson, "On streak breakdown in bypass transition," *Physics of Fluids*, vol. 20, pp. 101505-101505, 2008.

- [77] P. Andersson, L. Brandt, A. Bottaro, and D. S. Henningson, "On the breakdown of boundary layer streaks," *Journal of Fluid Mechanics*, vol. 428, pp. 29-60, 2001.
- [78] L. Brandt and D. S. Henningson, "Transition of streamwise streaks in zero-pressure-gradient boundary layers," *Journal of Fluid Mechanics*, vol. 472, pp. 229-261, 2002.
- [79] N. J. Vaughan and T. A. Zaki, "Stability of zero-pressure-gradient boundary layer distorted by unsteady Klebanoff streaks," *Journal of Fluid Mechanics*, vol. 681, pp. 116-153, 2011.
- [80] A. C. Mandal, L. Venkatakrishnan, and J. Dey, "A study on boundary-layer transition induced by free-stream turbulence," *Journal of Fluid Mechanics*, vol. 660, pp. 114-146, 2010.
- [81] D. Arnal, J. C. Juillen, and R. Michel, "Experimental analysis and computation of the onset and development of the boundary layer transition," *NASA Technical Memorandum*, 1978.
- [82] K. J. A. Westin, A. V. Boiko, B. G. B. Klingmann, V. V. Kozlov, and P. H. Alfredsson, "Experiments in a boundary layer subjected to free stream turbulence. Part 1 - Boundary layer structure and receptivity," *Journal of Fluid Mechanics*, vol. 281, pp. 193-218, 1994.
- [83] P. Andersson, M. Berggren, and D. S. Henningson, "Optimal disturbances and bypass transition in boundary layers," *Physics of Fluids*, vol. 11, pp. 134-150, 1999.
- [84] M. Matsubara and P. H. Alfredsson, "Disturbance growth in boundary layers subjected to free-stream turbulence," *Journal of Fluid Mechanics*, vol. 430, pp. 149-168, 2001.
- [85] J. H. M. Fransson, M. Matsubara, and P. H. Alfredsson, "Transition induced by free-stream turbulence," *Journal of Fluid Mechanics*, vol. 527, pp. 1-25, 2005.
- [86] R. Narasimha and M. A. B. S. C. Narayanan, "Turbulent spot growth in favourable pressure gradients," *AIAA Journal*, vol. 22, pp. 837-839, 1984.
- [87] U. Piomelli, W. H. Cabot, P. Moin, and S. Lee, "Subgrid-scale backscatter in turbulent and transitional flows," *Physics of Fluids A*, vol. 3, pp. 1766-1771, 1991.
- [88] F. Ducros, P. Comte, and M. Lesieur, "Large-eddy simulation of transition to turbulence in a boundary layer developing spatially over a flat plate," *Journal of Fluid Mechanics*, vol. 326, pp. 1-36, 1996.
- [89] P. Schlatter, S. Stolz, and L. Kleiser, "Applicability of LES models for prediction of transitional flow structures," presented at the *6th IUTAM Symposium on Laminar-Turbulent Transition*, Bangalore, 2004.
- [90] M. Germano, U. Piomelli, P. Moin, and W. H. Cabot, "A dynamic subgrid-scale eddy viscosity model," *Physics of Fluids A*, vol. 3, pp. 1760-1765, 1991.
- [91] D. K. Lilly, "A proposed modification of the Germano subgrid-scale closure method," *Physics of Fluids A*, vol. 4, pp. 633-635, 1992.
- [92] C. Meneveau, T. S. Lund, and W. H. Cabot, "A Lagrangian dynamic subgrid-scale model of turbulence," *Journal of Fluid Mechanics*, vol. 319, pp. 353-385, 1996.
- [93] X. Huai, R. D. Joslin, and U. Piomelli, "Large-Eddy Simulation of transition to turbulence in boundary layers," *Theoretical and Computational Fluid Dynamics*, vol. 9, pp. 149-163, 1997.
- [94] X. Huai, R. D. Joslin, and U. Piomelli, "Large-eddy simulation of boundary-layer transition on a swept wedge," *Journal of Fluid Mechanics*, vol. 381, pp. 357-380, 1999.
- [95] P. R. Voke and Z. Yang, "Numerical study of bypass transition," *Physics of Fluids*, vol. 7, pp. 2256-2264, 1995.

- [96] F. Péneau, H. C. Boisson, A. Kondjoyan, and N. Djilali, "Structure of a fat plate boundary layer subjected to free-stream turbulence," *International Journal of Computational Fluid Dynamics*, vol. 18, pp. 175-188, 2007.
- [97] Y. Zang, R. L. Street, and J. R. Koseff, "A dynamic mixed subgrid-scale model and its application to turbulent recirculating flows," *Physics of Fluids A: Fluid Dynamics*, vol. 5, p. 3186, 1993.
- [98] V. M. Calo, "Residual-based multiscale turbulence modelling - Finite volume simulations of bypass transition," Ph.D., Stanford University, 2004.
- [99] T. J. R. Hughes, V. M. Calo, and G. Scovazzi, "Variational and multiscale methods in turbulence," presented at the *11th International Congress of Theoretical and Applied Mechanics*, Dordrecht, 2004.
- [100] T. J. R. Hughes, L. Mazzei, and K. E. Jansen, "Large Eddy Simulations and the variational multiscale method," *Computing and Visualization in Science*, vol. 3, pp. 47-59, 2000.
- [101] P. Schlatter, "LES of transition and turbulence in wall-bounded shear flow," Ph.D., ETH Zurich.
- [102] P. Schlatter, S. Stolz, and L. Kleiser, "LES of transitional flows using the approximate deconvolution model," *International Journal of Heat and Fluid Flow*, vol. 25, pp. 549-558, 2004.
- [103] S. Stolz, N. A. Adams, and L. Kleiser, "An approximate deconvolution model for large-eddy simulation with application to incompressible wall-bounded flows," *Physics of Fluids*, vol. 13, pp. 997-1015, 2001.
- [104] L. Prandtl, *Journal of Applied Mathematics and Mechanics*, pp. 136-139, 1925.
- [105] L. Prandtl, *Akad. Wiss. Gottingen, Math-Phys. Kl.*, pp. 6-19, 1945.
- [106] P. R. Spalart and S. R. Allmaras, "A one-equation turbulence model for aerodynamic flows," *AIAA Paper*, vol. 92-0439, 1992.
- [107] W. P. Jones and B. E. Launder, "The prediction of laminarization with a two-equation model of turbulence," *International Journal of Heat and Mass Transfer*, vol. 15, pp. 301-314, 1972.
- [108] D. C. Wilcox, "Reassessment of the scale-determining equation for advanced turbulence models," *AIAA Journal*, vol. 26, pp. 1299-1310, 1988.
- [109] B. E. Launder, G. J. Reece, and W. Rodi, "Progress in the development of a Reynolds-stress turbulence closure," *Journal of Fluid Mechanics*, vol. 68, pp. 537-566, 1975.
- [110] C. G. Speziale, S. Sarkar, and T. B. Gatski, "Modelling the pressure-strain correlation of turbulence: an invariant dynamical systems approach," *Journal of Fluid Mechanics*, vol. 227, pp. 245-272, 1991.
- [111] P. A. Durbin, "Separated flow computations with the  $k-\epsilon-v^2$  model," *AIAA Journal*, vol. 33, pp. 659-664, 1995.
- [112] S. Parneix, P. A. Durbin, and M. Behnia, "Computation of 3D boundary layers using the V2F model," *Flow, Turbulence and Combustion*, vol. 60, 1998.
- [113] R. B. Langtry and F. R. Menter, "Correlation-based transition modeling for unstructured parallelized computational fluid dynamics codes," *AIAA Journal*, vol. 47, pp. 2894-2906, 2009.
- [114] A. Sarkar and R. M. C. So, "A critical evaluation of near-wall two-equation models against direct numerical simulation data," *International Journal of Heat and Fluid Flow*, vol. 18, pp. 197-208, 1997.

- [115] V. C. Patel, W. Rodi, and G. Scheuerer, "Turbulence models for near-wall and low Reynolds number flows - A review," *AIAA Journal*, vol. 23, pp. 1308-1319, 1985.
- [116] P. L. Betts and A. A. Dafa'Alla, "Turbulent buoyant air flow in a tall rectangular cavity," In *ASME Winter Annual Meeting*, vol. 60, 1986.
- [117] C. M. Hrenya, E. J. Bolio, D. Chakrabarti, and J. L. Sinclair, "Comparison of low Reynolds number  $k-\epsilon$  turbulence models in predicting fully developed pipe flow," *Chemical Engineering Science*, vol. 50, pp. 1923-1941, 1995.
- [118] C. Hrenya, S. Miller, T. Mallo, and J. Sinclair, "Comparison of low Reynolds number  $k-\epsilon$  turbulence models in predicting heat transfer rates for pipe flow," *International Journal of Heat and Mass Transfer*, vol. 41, pp. 1543-1547, 1998.
- [119] S. S. Thakre and J. B. Joshi, "CFD modeling of heat transfer in turbulent pipe flows," *AIChE Journal*, vol. 46, pp. 1798-1812, 2000.
- [120] S. S. Thakre and J. B. Joshi, "A low-Reynolds number  $k$ -epsilon modelling of turbulent pipe flow: flow pattern and energy balance," *The Canadian Journal of Chemical Engineering*, vol. 79, pp. 214-226, 2001.
- [121] W. S. Kim, S. He, and J. D. Jackson, "Assessment by comparison with DNS data of turbulence models used in simulations of mixed convection," *International Journal of Heat and Mass Transfer*, vol. 51, pp. 1293-1312, 2008.
- [122] Z. Yang and T. H. Shih, "New time scale based  $k$ -epsilon model for near-wall turbulence," *AIAA Journal*, vol. 31, pp. 1191-1198, 1993.
- [123] K. Y. Chien, "Predictions of channel and boundary-layer flows with a low-Reynolds number turbulence model," *AIAA Journal*, vol. 20, pp. 33-38, 1982.
- [124] H. K. Myong and N. Kasagi, "A new approach to the improvement of  $k$ -epsilon turbulence model for wall-bounded shear flows," *JSME International Journal*, vol. 33, pp. 63-72, 1990.
- [125] A. Khalegi, M. Pasandideh-Fard, M. Malek-Jafarian, and Y. M. Chung, "Assessment of common turbulence models under conditions of temporal acceleration in a pipe," *Journal of Applied Fluid Mechanics*, vol. 3, pp. 25-33, 2010.
- [126] S. Gorji, M. Seddighi, C. Ariyaratne, A. E. Vardy, T. O'Donoghue, D. Pokrajac, *et al.*, "A comparative study of turbulence models in a transient channel flow," *Computers & Fluids*, vol. 89, pp. 111-123, 2014.
- [127] G. Iaccarino, "Predictions of a turbulent separated flow using commercial CFD codes," *Journal of Fluids Engineering*, vol. 123, pp. 819-828, 2001.
- [128] P. Jagadeesh and K. Murali, "Application of low-Re turbulence models for flow simulations past underwater vehicle hull forms," *Journal of Naval Architecture and Marine Engineering*, vol. 1, pp. 41-54, 2005.
- [129] S. J. Wang and A. S. Mujumdar, "A comparative study of five low Reynolds number  $k-\epsilon$  models for impingement heat transfer," *Applied Thermal Engineering*, vol. 25, pp. 31-44, 2005.
- [130] Z. Du, W. Lin, and A. Gu, "Numerical investigation of cooling heat transfer to supercritical CO<sub>2</sub> in a horizontal circular tube," *The Journal of Supercritical Fluids*, vol. 55, pp. 116-121, 2010.
- [131] S. He, "On transient turbulent pipe flow," Ph.D., Department of Engineering, University of Manchester, 1992.
- [132] S. A. Orszag and G. S. Patterson, "Numerical simulation of three-dimensional homogeneous isotropic turbulence," *Physical Review Letters*, vol. 28, pp. 76-79, 1972.

- [133] J. Kim, P. Moin, and R. Moser, "Turbulence statistics in fully developed channel flow at low Reynolds number," *Journal of Fluid Mechanics*, vol. 177, pp. 133-166, 1987.
- [134] R. D. Moser and P. Moin, "Direct numerical simulation of curved turbulent channel flow," *NASA Technical Memorandum*, vol. 85, p. 11316, 1984.
- [135] J. W. Deardorff, "A numerical study of three-dimensional turbulent channel flow at large Reynolds numbers," *Journal of Fluid Mechanics*, vol. 41, pp. 453-480, 1970.
- [136] J. Smagorinsky, "General circulation experiments with the primitive equations," *Monthly Weather Review*, vol. 91, pp. 99-164, 1963.
- [137] J. Kim and P. Moin, "Application of a fractional-step method to incompressible Navier-Stokes equations," *Journal of Computational Physics*, vol. 59, pp. 308-323, 1985.
- [138] P. Orlandi, *Fluid flow phenomena: a numerical toolkit*: Kluwer Academic Publishers, 2000.
- [139] S. V. Patankar, *Numerical heat transfer and fluid flow*: Taylor & Francis, 1980.
- [140] F. H. Harlow and J. E. Welch, "Numerical calculation of time-dependent viscous incompressible flow of fluid with free surface," *Physics of Fluids*, vol. 8, pp. 2182-2189, 1965.
- [141] Y. Morinishi, T. S. Lund, O. V. Vasilyev, and P. Moin, "Fully conservative higher order finite difference schemes for incompressible flow," *Journal of Computational Physics*, vol. 143, pp. 90-124, 1998.
- [142] P. Moin and J. Kim, "Numerical investigation of turbulent channel flow," *Journal of Fluid Mechanics*, vol. 118, pp. 341-377, 1982.
- [143] H. Choi and P. Moin, "Effects of the computational time step on numerical solutions for turbulent flow," *Journal of Computational Physics*, vol. 113, pp. 1-4, 1994.
- [144] G. N. Coleman and R. D. Sandberg, "A primer on direct numerical simulation of turbulence - Methods, procedures and guidelines," *Technical Report AFM-09/01a*, University of Southampton, 2010.
- [145] P. Moin and M. K., "Direct Numerical Simulation: A tool in turbulence research," *Annual Review of Fluid Mechanics*, vol. 30, pp. 539-578, 1998.
- [146] N. N. Yanenko, *The method of fractional steps*: Springer, 1971.
- [147] R. M. Beam and R. F. Warming, "An implicit finite-difference algorithm for hyperbolic systems in conservation-law form," *Journal of Computational Physics*, vol. 22, pp. 87-110, 1976.
- [148] S. B. Pope, *Turbulent Flows*: Cambridge University Press, 2000.
- [149] "Fluent Release 16.2 Theory Guide," ANSYS Inc., 2015.
- [150] "Code\_Saturne v4.1.1 Theory Guide," EDF R&D, 2015.
- [151] "CFX-Solver Release 16.2 Theory Guide," ANSYS Inc., 2015.
- [152] F. Nicoud and F. Ducros, "Subgrid-scale stress modelling based on the square of the velocity gradient tensor," *Flow, Turbulence and Combustion*, vol. 62, pp. 183-200, 1999.
- [153] R. Moser, J. Kim, and N. N. Mansour, "DNS of turbulent channel flow up to  $Re_\tau=590$ ," *Physics of Fluids*, vol. 11, pp. 943-945, 1999.
- [154] B. J. Geurts and J. Fröhlich, "A framework for predicting accuracy limitations in large-eddy simulation," *Physics of Fluids*, vol. 14, pp. 41-44, 2002.

- [155] I. B. Celik, Z. N. Cehreli, and I. Yavuz, "Index of resolution quality for large eddy simulations," *Journal of Fluids Engineering*, vol. 127, pp. 949-958, 2005.
- [156] I. Celik, M. Klein, and J. Janicka, "Assessment measures for engineering LES applications," *Journal of Fluids Engineering*, vol. 131, p. 031102, 2009.
- [157] X. Zhang, T. Knopp, M. Valentino, R. Kessler, and G. Lube, "Investigation of resolution requirements for wall-modelled LES of attached and massively separated flows at high Reynolds numbers," in *New Results in Numerical and Experimental Fluid Mechanics VII*. vol. 112: Springer Berlin Heidelberg, 2010, pp. 167-174.
- [158] M. Lee and R. D. Moser, "Direct numerical simulation of turbulent channel flow up to  $Re_\tau \approx 5200$ ," *Journal of Fluid Mechanics*, vol. 774, pp. 395-415, 2015.
- [159] R. B. Dean, "Reynolds number dependence of skin friction and other bulk flow variables in two-dimensional rectangular duct flow," *Journal of Fluids Engineering*, vol. 100, pp. 215-223, 1978.
- [160] J. P. Monty, "Developments in smooth wall turbulent duct flows," Ph.D., University of Melbourne, 2005.
- [161] R. D. Keane and R. J. Adrian, "Optimization of particle image velocimeters. Part I: Double pulsed systems," *Measurement Science and Technology*, vol. 1, pp. 1202-1215, 1990.
- [162] R. D. Keane and R. J. Adrian, "Optimization of particle image velocimeters: Part II. Multiple pulsed systems," *Measurement Science and Technology*, vol. 2, pp. 963-974, 1991.
- [163] M. Raffel, C. E. Willert, S. T. Wereley, and J. Kompenhans, *Particle Image Velocimetry - a practical guide*: Springer, 2007.
- [164] R. D. Keane and R. J. Adrian, "Theory of cross-correlation analysis of PIV images," *Applied Scientific Research*, vol. 49, pp. 191-215, 1992.
- [165] A. Fage and V. M. Falkner, "On the relation between heat transfer and surface friction for laminar flow," *ARC R&M*, vol. 1408, 1931.
- [166] H. Ludwig, "Instrument for measuring the wall shearing stress of turbulent boundary layers," *NACA Technical Memorandum*, vol. 1284, 1950.
- [167] H. W. Liepmann and G. T. Skinner, "Shearing stress measurements by use of a heated element," *NACA Technical Note*, vol. 3268, 1954.
- [168] B. J. Bellhouse and D. L. Schultz, "Determination of mean and dynamic skin friction, separation and transition in low-speed flow with a thin-film heated element," *Journal of Fluid Mechanics*, vol. 24, pp. 379-400, 1966.
- [169] A. N. Menendez and B. R. Ramaprian, "The use of flush-mounted hot-film gauges to measure skin friction in unsteady boundary layers," *Journal of Fluid Mechanics*, vol. 161, pp. 139-159, 1985.
- [170] J. Jimenez, R. Martinez-Val, and M. Rebollo, "Hot-film sensors calibration drift in water," *Journal of Physics E: Scientific Instruments*, vol. 14, pp. 569-572, 1981.
- [171] D. B. Spalding, "A single formula for the law of the wall," *Journal of Applied Mechanics, Transactions of the ASME, Series E*, vol. 83, pp. 455-458, 1961.
- [172] A. Musker, "Explicit Expression for the Smooth Wall Velocity Distribution in a Turbulent Boundary Layer," *AIAA Journal*, vol. 17, pp. 655-657, 1979.
- [173] F. Durst, H. Kikura, I. Lekakis, J. Jovanovic, and Q. Ye, "Wall shear stress determination from near-wall mean velocity data in turbulent pipe and channel flows," *Experiments in Fluids*, vol. 20, pp. 417-428, 1996.

- [174] T. von Kármán, "Mechanische Ähnlichkeit und turbulenz," In *Third International Congress of Applied Mechanics*, Stockholm, vol., pp. 85-105, 1930.
- [175] L. Brandt, "Numerical studies of the instability and breakdown of a boundary-layer low-speed streak," *European Journal of Mechanics - B/Fluids*, vol. 26, pp. 64-82, 2007.
- [176] J. Jeong and F. Hussain, "On the identification of a vortex," *Journal of Fluid Mechanics*, vol. 285, pp. 6-94, 1995.
- [177] J. Jeong, F. Hussain, W. Schoppa, and J. Kim, "Coherent structures near the wall in a turbulent channel flow," *Journal of Fluid Mechanics*, vol. 332, pp. 185-214, 1997.
- [178] J. C. R. Hunt and P. A. Durbin, "Perturbed vortical layers and shear sheltering," *Fluid Dynamics Research*, vol. 24, pp. 375-404, 1999.
- [179] H. Schlichting and K. Gersten, *Boundary-layer theory*: Springer, 2000.
- [180] P. E. Roach and D. H. Brierley, "The influence of a turbulent free-stream on zero pressure gradient transitional boundary layer development part I: test cases T3A and T3B," *Numerical simulation of unsteady flows and transition to turbulence*, pp. 319-347, 1992.
- [181] B. E. Launder and D. B. Spalding, "The numerical computation of turbulent flows," *Computer Methods in Applied Mechanics and Engineering*, vol. 3, pp. 269-289, 1974.
- [182] W. P. Jones and B. E. Launder, "The calculation of low-Reynolds-number phenomena with a two-equation model of turbulence," *International Journal of Heat and Mass Transfer*, vol. 16, pp. 1119-1130, 1973.
- [183] M. A. Cotton and J. D. Jackson, "Vertical tube air flow in the turbulent mixed convection regime calculated using a low-Reynolds-number  $k\text{-}\epsilon$  model," *International Journal of Heat and Mass Transfer*, vol. 33, pp. 275-286, 1990.
- [184] S. He, P.-X. Jiang, Y.-J. Xu, R.-F. Shi, W. S. Kim, and J. D. Jackson, "A computational study of convection heat transfer to CO<sub>2</sub> at supercritical pressures in a vertical mini tube," *International Journal of Thermal Sciences*, vol. 44, pp. 521-530, 2005.
- [185] J. D. Jackson, O. Büyükalaca, and S. He, "Heat transfer in a pipe under conditions of transient turbulent flow," *International Journal of Heat and Fluid Flow*, vol. 20, pp. 115-127, 1999.
- [186] J. G. M. Eggels, F. Unger, M. H. Weiss, J. Westerweel, R. J. Adrian, R. Friedrich, *et al.*, "Fully developed turbulent pipe flow: a comparison between direct numerical simulation and experiment," *Journal of Fluid Mechanics*, vol. 268, pp. 175-209, 1994.
- [187] B. J. Boersma, "Direct numerical simulation of turbulent pipe flow up to a Reynolds number of 61,000," *Journal of Physics: Conference Series*, vol. 318, pp. 042045-042045, 2011.
- [188] X. Wu and P. Moin, "A direct numerical simulation study on the mean velocity characteristics in turbulent pipe flow," *Journal of Fluid Mechanics*, vol. 608, pp. 81-112, 2008.

# List of publications

The following publications have been produced as part of the present study:

1. A. Mathur, M. Seddighi, S. He, "Turbulence in decelerating channel flows." (drafted)
2. A. Mathur, M. Seddighi, S. He, "Transition in high-Reynolds number ratio transient flows in a channel." (drafted)
3. S. He, A. Mathur, M. Seddighi, S. Gorji, "Observation of a laminar to turbulent transition in an already turbulent flow." (drafted)
4. A. Mathur, M. Seddighi, S. He, "Effect of high Reynolds number-ratio on transition of transient channel flow," In *8<sup>th</sup> International Symposium on Turbulence, Heat and Mass Transfer*, Sarajevo, 2015.
5. S. He, M. Seddighi, S. Gorji, A. Mathur, "Transition of transient turbulent channel flow," In *7<sup>th</sup> International Conference on Fluid Mechanics, Procedia Engineering*, vol. 126, pp. 34-38, 2015.
6. A. Mathur, S. He, "Performance and implementation of the Launder-Sharma low-Reynolds number turbulence model," *Computers & Fluids*, vol. 79, pp. 134-139, 2013.

# Appendix A

This section provides the transient development for friction coefficient, bulk and turbulence quantities for the ramp-like accelerating cases, E4-E7, discussed in Chapter 6.

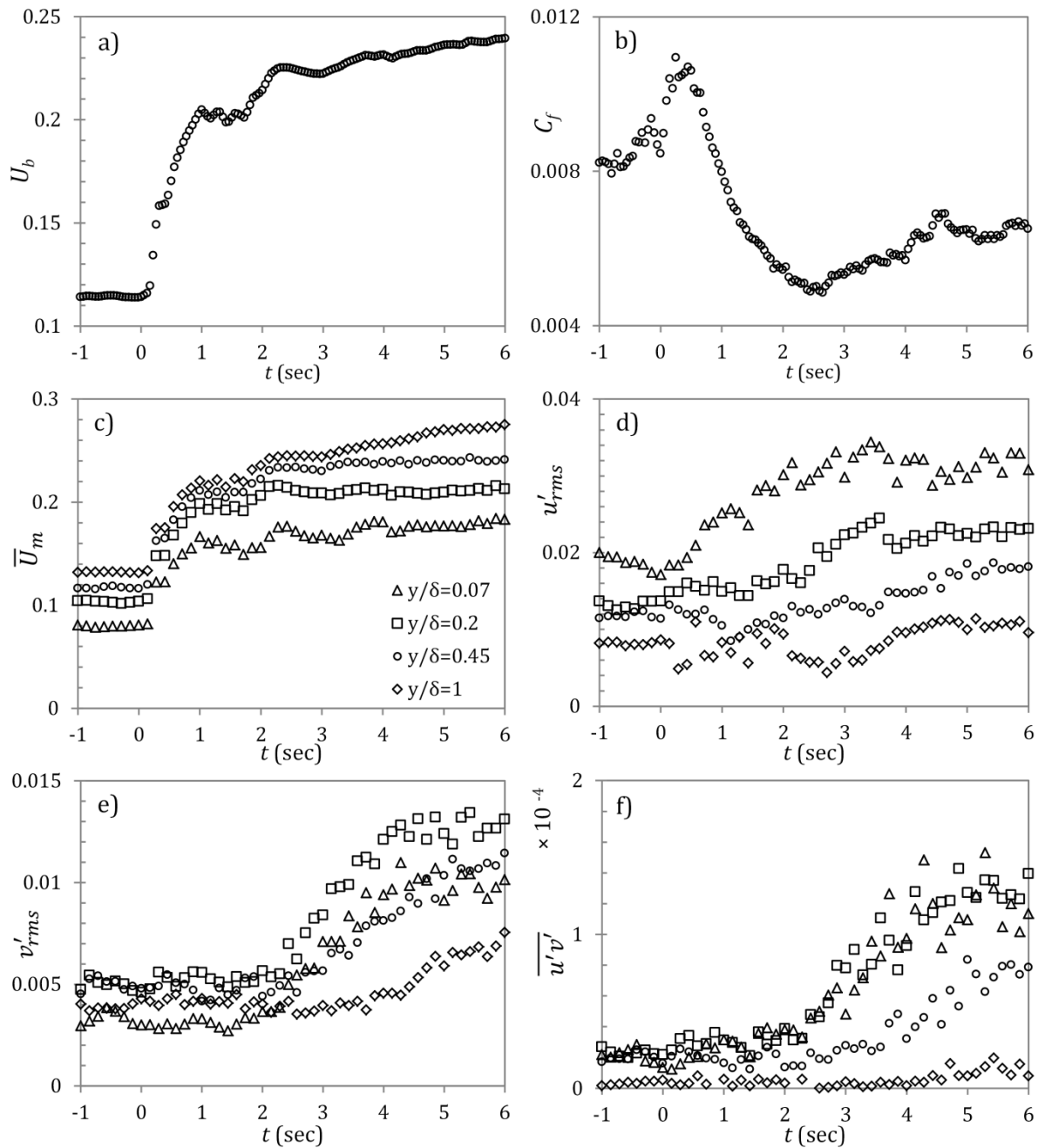


Figure A.1. Transient development of friction coefficient, mean, fluctuating and Reynolds stress components for case E4. All quantities are in absolute units:  $m/s$  for (a, c-f); and  $m^2/s^2$  for (f). Subplots (c-f) share the legend.

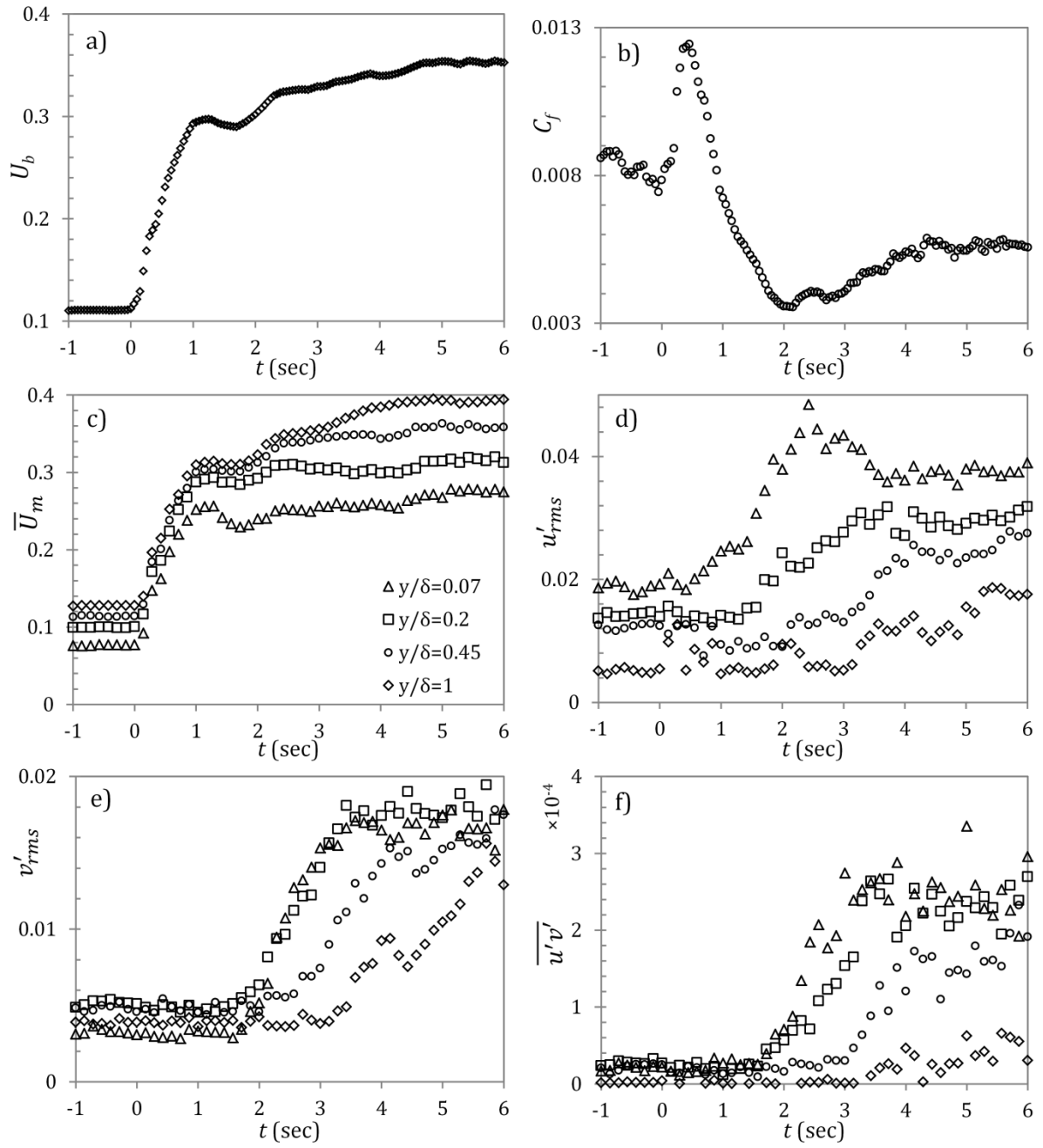


Figure A.2. Transient development of friction coefficient, mean, fluctuating and Reynolds stress components for case E5. All quantities are in absolute units:  $m/s$  for (a, c-f); and  $m^2/s^2$  for (f). Subplots (c-f) share the legend.

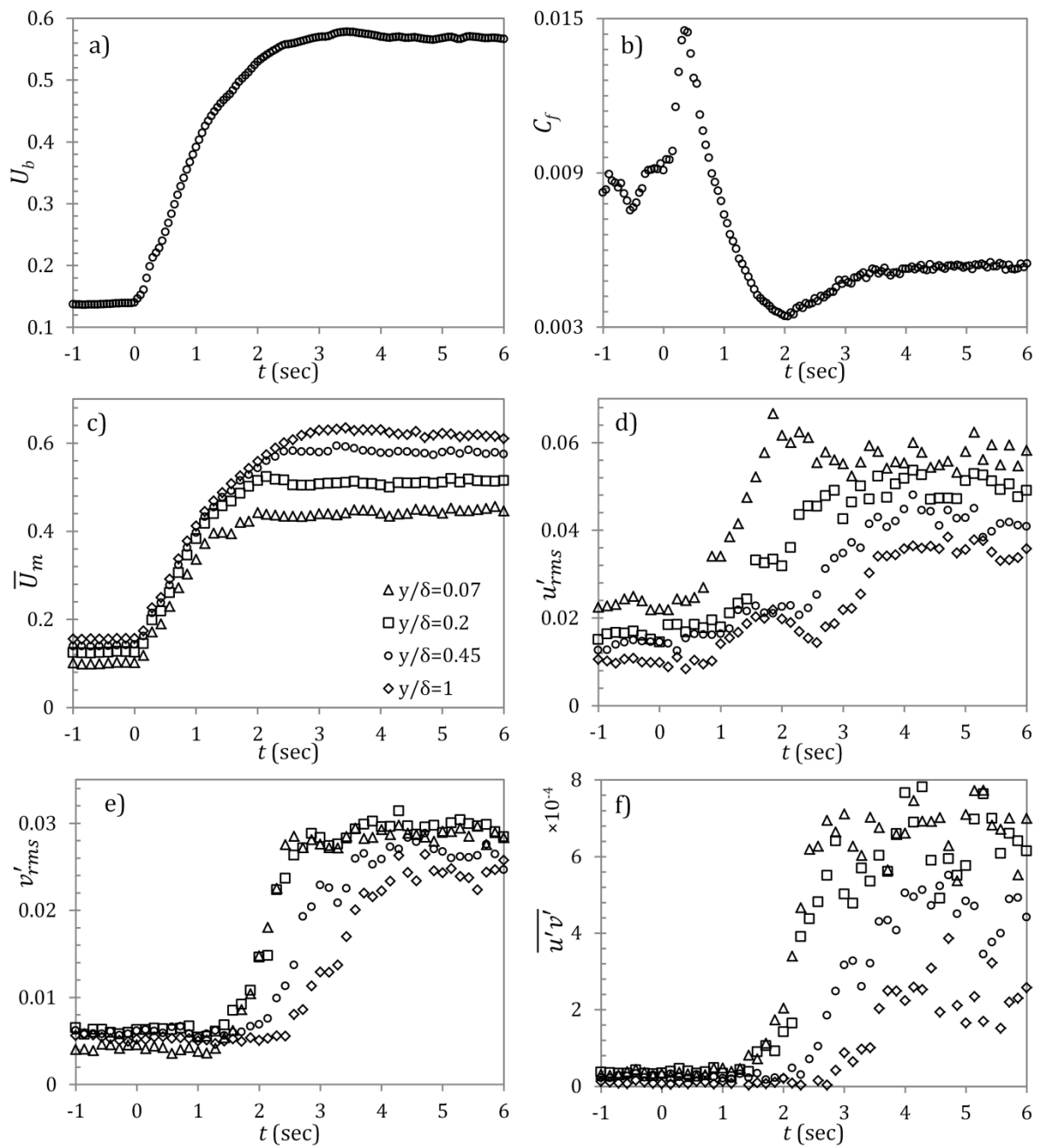


Figure A.3. Transient development of friction coefficient, mean, fluctuating and Reynolds stress components for case E6. All quantities are in absolute units:  $m/s$  for (a, c-f); and  $m^2/s^2$  for (f). Subplots (c-f) share the legend.

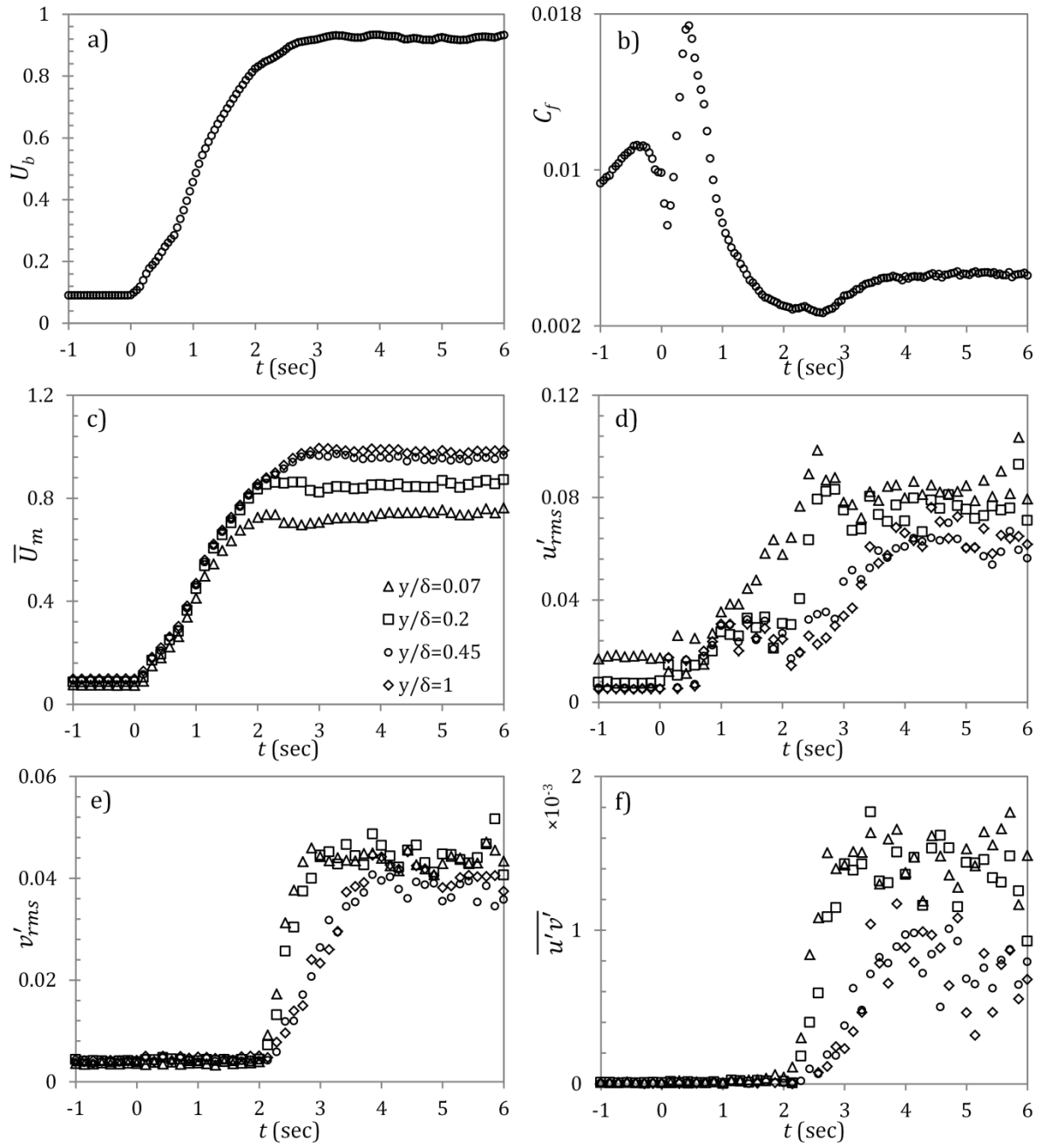


Figure A.4. Transient development of friction coefficient, mean, fluctuating and Reynolds stress components for case E7. All quantities are in absolute units:  $m/s$  for (a, c-f); and  $m^2/s^2$  for (f). Subplots (c-f) share the legend.

# Appendix B

This section provides the source code of the Launder-Sharma model implementation in ANSYS Fluent (UDF-LS) for the investigations presented in Chapter 8. Firstly, the steps to compile and load the UDF onto the CFD solver are listed, followed by the UDF-LS code.

*Steps to load and compile UDF:*

1. Set up the case with the *Spalart-Allmaras* model.  
(This option is switched on for enabling some mesh-related calculations – `C_WALL_DIST()` – in the UDF; The inbuilt model equations will not be actually used, as shown in Step 6 below).
2. Save the case file. Copy files '*UDF-LS.c*', '*udf.h*' and '*FlowData.dat*' to the same directory as the Fluent case file.
3. Go to *Define > User-Defined > Scalars*. Increase the 'Number of User-Defined Scalars' to 4.
4. Go to *Define > User-Defined > Memory*. Increase the 'Number of User-Defined Memory Locations' to 3.
5. Go to *Solve > Controls*. Set the Under-Relaxation Factors of 'User Scalar 0' and 'User Scalar 1' to 0.5 each.
6. Go to *Solve > Controls > Equations*. Turn off the equations for 'Modified Turbulent Viscosity', 'User Scalar 2' and 'User Scalar 3'.
7. Go to *Define > User-Defined > Functions > Compiled*. Add '*UDF-LS.c*' as source file and '*udf.h*' as header file. (Make sure the case file, source and header files are in the same directory.)
8. Give an appropriate Library Name for the case. Click Build. Click 'OK'. The text interface should show the following message on successful compilation:

```
Creating library libudf.lib and object libudf.exp  
Done.
```

9. Click 'Load' to finish loading the UDF. The text interface should show the following message on successful load:

```
Library "libudf\win64\2ddp\libudf.dll" opened  
k_src1  
k_src2  
d_src  
ke_diff  
turb_vis  
adj_func  
init_func
```

*k\_prof*  
*d\_prof*  
*flowdata*  
 Done.

10. Go to *Models > Viscous (Spalart-Allmaras)*. For User-Defined Functions of 'Turbulent Viscosity' select function '*turb\_vis*'.
11. Go to *Define > Materials*. Select the fluid, and click 'Edit'. For 'UDS Diffusivity', select 'user-defined' from the drop-down menu. Select the function '*ke\_diff*'.
12. Got to *Define > Cell Zone Conditions*. Select the fluid zone and click 'Edit'. Switch on 'Source Terms' through the check box. Go to the 'Source Terms' tab.
  - For User Scalar 0, click 'Edit'. Increase the 'Number of User-Scalar sources' to 2. Select function *k\_src1* for the first source and *k\_src2* for the second source. Click 'OK'.  
 (Make sure the order of the two sources is the same as above!)
  - For User Scalar 1, click 'Edit'. Increase the 'Number of User-Scalar sources' to 1. Select function *d\_src*. Click 'OK'.
13. Go to *Define > User-Defined > Function Hooks*.
  - For 'Initialization', click 'Edit'. Select the function '*init\_func*' and click 'Add'. Click OK.
  - For 'Adjust', click 'Edit'. Select the function '*adj\_func*' and click 'Add'. Click OK.
14. Go to *Define > Boundary Conditions*.
  - Select wall zone: Click 'Edit'. Go to 'UDS' tab. Change 'User-Defined Scalar Boundary Condition' of 'User Scalar 0' and 'User Scalar 1' to '*Specified Value*'. Ensure that 'User-Defined Scalar Boundary Value' for both scalars is 0.
  - Select velocity inlet zone: Click 'Edit'. Switch the 'Turbulence Specification Method' to 'Modified Turbulent Viscosity' and set its value to zero.  
 Go to 'UDS' tab. Change 'User-Defined Scalar Boundary Contidion' of 'User Scalar 0' and 'User Scalar 1' to '*Specified Value*'.
    - For User Scalar 0, select '*k\_prof*' from the drop down menu, as the 'User-Defined Scalar Boundary Value'.
    - For User Scalar 1, select '*d\_prof*' from the drop down menu, as the 'User-Defined Scalar Boundary Value'.
 Alternatively, provide appropriate constant values for inlet B.C. for *k* (User Scalar 0) and  $\epsilon$  (User Scalar 1).
15. Before Initialisation, make sure the appropriate data has been edited in *FlowData.dat*. (In case of transient simulation, write the initial bulk velocity in the aforementioned file. See instructions below.)

Go to *Solution Initialization*. Ensure that the Initial Value of 'Modified Turbulent Viscosity' is zero.

16. Initialise the domain. The text interface should display the values assigned in *FlowData.dat* on successful initialization.
17. Proceed to calculations.

NOTE –

1. Instructions for writing *FlowData.dat* (an ASCII text file) – The following flow specifications (in the specified units) must be entered in single line with a single blank spaces in between: Molecular viscosity [ $kgm^{-1}s^{-1}$ ]; Density [ $kgm^{-3}$ ]; Bulk velocity [ $ms^{-1}$ ]; Hydraulic Diameter [ $m$ ]; Turbulent Intensity [%]. e.g. “0.001 1000 0.9 0.05 5”  
(Parameters 1-3 are used for initialization; and 3-5 are used for turbulent inlet boundary conditions)
2. If continuing the calculations from a previously saved solution, execute the on-demand function 'flowdata' for loading the data from *FlowData.dat*, before reading the Fluent data file.
  - Read only the case file (\*.cas).
  - Setup the UDF as shown above (Steps 3-14).
  - Go to Define > User-Defined > Execute On Demand. Select the function flowdata from the drop-down menu. Click 'Execute'. On successful execution, the text interface should display the values assigned in FlowData.dat.
  - Now read only the previously saved data file (\*.dat) from where the calculations need to be continued.
  - Proceed with calculations.
3. If the UDF needs to be compiled again for the same case, make sure the previous library(s) have been unloaded first.

Go to *Define > User-Defined > Functions > Manage*. Select the previous library(s) and click 'Unload'.

4. New variables: Turbulent Kinetic Energy,  $k$  = User Scalar 0  
 Modified Dissipation Rate,  $\tilde{\varepsilon}$  = User Scalar 1  
 True Dissipation Rate,  $\varepsilon (= \tilde{\varepsilon} + D_\varepsilon) =$  User Scalar 1 + (User Memory 0/density)  
 Turbulent Viscosity,  $\mu_t =$  User Memory 1  
 Turbulent Reynolds Number,  $Re_t =$  User Memory 2

**UDF-LS code:**

```

#include "udf.h"
#define C_MU 0.09
#define SIG_K 1.0
#define SIG_D 1.3
#define C1_D 1.44
#define C2_D 1.92
float MU_L, DEN, MVEL, DH, IN; //global variables defined as in fileread()

enum // UD Scalars
{
    TKE, TDR, RK, SRM,
    N_REQUIRED_UDS
};

enum // UD Memory
{
    DE, MUT, RET,
    N_REQUIRED_UDM
};

double f_mu(cell_t c, Thread *t)
{ return exp(-3.4/SQR(1+C_UDMI(c,t,RET)/50)); }

float f_1(cell_t c, Thread *t)
{ return 1.0; }

double f_2(cell_t c, Thread *t)
{ return (1.-0.3*exp(-C_UDMI(c,t,RET)*C_UDMI(c,t,RET))); }

DEFINE_SOURCE(k_src1, c, t, dS, eqn) // k Production Term
{ C_UDSI(c,t,SRM) = C_STRAIN_RATE_MAG(c,t);
  C_UDSI(c,t,RK) = sqrt(C_UDSI(c,t,TKE));
  dS[eqn] = -
  2.*C_R(c,t)*C_R(c,t)*C_MU*f_mu(c,t)*C_UDSI(c,t,TKE)/C_UDMI(c,t,MUT);
  return -
  C_R(c,t)*C_R(c,t)*C_MU*f_mu(c,t)*SQR(C_UDSI(c,t,TKE))/C_UDMI(c,t,MUT);
}

DEFINE_SOURCE(k_src2, c, t, dS, eqn) // k Source Term -- D_e
{ double G_k;
  C_UDMI(c,t,DE) = 2.*C_MU_L(c,t)*NV_MAG2(C_UDSI_G(c,t,RK));
  G_k = C_UDMI(c,t,MUT)*SQR(C_STRAIN_RATE_MAG(c,t));
  dS[eqn] = 0;
  return G_k - C_UDMI(c,t,DE);
}

DEFINE_SOURCE(d_src, c, t, dS, eqn) // Epsilon source terms
{ double G_d, E_d;
  G_d =
  C1_D*f_1(c,t)*C_UDMI(c,t,MUT)*SQR(C_STRAIN_RATE_MAG(c,t))/C_UDSI(c,t,TKE);
  E_d =
  2.*C_UDMI(c,t,MUT)*C_MU_L(c,t)*(NV_MAG2(C_UDSI_G(c,t,SRM)))/C_R(c,t);
}

```

```

    dS[eqn] = G_d - 2.*C2_D*f_2(c,t)*C_R(c,t)*
C_UDSI(c,t,TDR)/C_UDSI(c,t,TKE);
    return G_d*(C_UDSI(c,t,TDR)) -
C2_D*f_2(c,t)*C_R(c,t)*SQR(C_UDSI(c,t,TDR))/C_UDSI(c,t,TKE) + E_d;
}

DEFINE_DIFFUSIVITY(ke_diff, c, t, eqn) // k and epsilon effective viscosity
{ switch(eqn)
  { case TKE: return C_UDMI(c,t,MUT)/SIG_K + C_MU_L(c,t); break;
    case TDR: return C_UDMI(c,t,MUT)/SIG_D + C_MU_L(c,t); break;
    default: return C_UDMI(c,t,MUT) + C_MU_L(c,t); }
}

DEFINE_TURBULENT_VISCOSITY(turb_vis, c, t) // Turbulent viscosity
{ return C_UDMI(c,t,MUT); }

DEFINE_ADJUST(adj_func,d) // Executed after every iteration -- calculation
of mu_t, Re_t, strain rate and sqrt(k)
{ Thread *t;
  cell_t c;
  thread_loop_c(t,d)
  { begin_c_loop(c,t)
    { C_UDMI(c,t,MUT) =
C_R(c,t)*C_MU*f_mu(c,t)*SQR(C_UDSI(c,t,TKE))/C_UDSI(c,t,TDR);
      C_UDMI(c,t,RET) =
C_R(c,t)*SQR(C_UDSI(c,t,TKE))/C_MU_L(c,t)/(C_UDSI(c,t,TDR));
      C_UDSI(c,t,SRM) = C_STRAIN_RATE_MAG(c,t);
      C_UDSI(c,t,RK) = sqrt(C_UDSI(c,t,TKE)); }
    end_c_loop(c,t) }
}

DEFINE_INIT(init_func,d) // Initialization Macro
{ cell_t c;
  face_t f;
  Thread *t;
  real temp,tempa,tempb,ustar,yplus,a,b,RE;
  fileread();
  RE=MVEL*DH*DEN/MU_L;
  temp = 0.079*pow(RE,-0.25);
  ustar = 0.70711*MVEL*sqrt(temp);
  a = 2.*pow(DEN/MU_L,2)*pow(ustar,5)*DH/2;
  b = 4.734*pow(ustar,3)/DH;
  thread_loop_c(t,d)
  { begin_c_loop(c,t)
    { yplus = C_WALL_DIST(c,t)*ustar* DEN/MU_L;
      if(yplus < 7.5) C_U(c,t) = ustar*yplus;
      else C_U(c,t) = ustar*(2.5*log(yplus)+5.5);
      if(yplus < 17.5) temp = 1.5+1.5*sin(3.141/17.5*(yplus-8.75));
      else temp = 3;
      temp = temp*ustar*ustar;
      C_UDSI(c,t,TKE) = temp;
      C_UDSI(c,t,RK) = sqrt(C_UDSI(c,t,TKE));
      temp = 2.*C_WALL_DIST(c,t)/DH;

```

```

        tempa=a*temp;
        tempb=b/temp;
        if (tempa < tempb) temp = tempa;
        else temp = tempb;
        C_UDSI(c,t,TDR) = temp;
        C_UDMI(c,t,MUT) = DEN*C_MU*f_mu(c,t)*
SQR(C_UDSI(c,t,TKE))/(C_UDSI(c,t,TDR));
        C_UDMI(c,t,RET) = DEN*SQR(C_UDSI(c,t,TKE))/MU_L/(C_UDSI(c,t,TDR)); }
    end_c_loop(c,t) }
}

DEFINE_PROFILE(k_prof,t,i) // k inlet B.C.
{ cell_t c;
  real temp = 1.5*MVEL*MVEL*IN*IN;
  begin_c_loop(c,t)
  { F_PROFILE(c,t,i) = temp; }
  end_c_loop(c,t)
}

DEFINE_PROFILE(d_prof,t,i) // epsilon inlet B.C.
{ cell_t c;
  real temp = 4.31242*MVEL*MVEL*MVEL*IN*IN*IN/DH;
  begin_c_loop(c,t)
  { F_PROFILE(c,t,i) = temp; }
  end_c_loop(c,t)
}

DEFINE_ON_DEMAND(flowdata)
{ fileread(); }

void fileread()
{ float tempc;
  FILE *fp;
  fp=fopen("FlowData.dat","r");
  if (fp==NULL) Message("\n\nError reading FlowData.dat !!\n");
  else
  { fscanf(fp,"%e",&tempc);
    MU_L=tempc;
    fscanf(fp,"%e",&tempc);
    DEN=tempc;
    fscanf(fp,"%e",&tempc);
    MVEL=tempc;
    fscanf(fp,"%e",&tempc);
    DH=tempc;
    fscanf(fp,"%e",&tempc);
    IN=tempc/100;
    Message("\nViscosity = %f\n",MU_L);
    Message("Density= %f\n",DEN);
    Message("Mean Velocity = %f\n",MVEL);
    Message("Hydraulic Diameter = %f\n",DH);
    Message("Intensity = %f\n",IN);
    fclose(fp); }
}

```